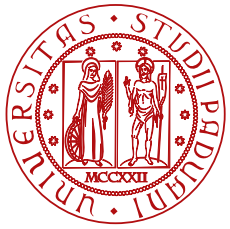

Università
degli Studi
di Padova

Master Thesis in Mathematical Engineering

Periodic Orbits in the Circular Restricted Three-Body Problem and Transfers from the Lunar Gateway to Lunar Repeating Ground Track Orbits

Master Candidate

Giulio Macrì

Student ID 2029061

Supervisor

Prof. Stefano Casotto

University of Padua

Co-supervisor

Dr. Nicola Baresi

University of Surrey

Academic Year
2022-2023

Contents

Chapter 1

Introduction

The study of the Circular Restricted Three-Body Problem (CR3BP) has a long history in the field of Celestial Mechanics. This simplified model of gravitational interaction between three bodies has been applied to a variety of problems, ranging from predicting the motions of celestial bodies to designing spacecraft trajectories. Of particular interest are the periodic orbits that exist within the CR3BP; these are trajectories that a spacecraft can follow indefinitely under the sole influence of the two primary bodies. These orbits have significant implications for the planning and execution of space missions, as they offer opportunities for fuel-efficient travel between different regions of space.

The first part of this thesis deals with the main concepts of the CR3BP, such as the Jacobi constant, the zero-velocity surfaces and the existence and stability of the five Lagrangian equilibrium points (see Section 2.4). We then proceed to introducing differential corrections (DC) techniques. These will be used along with continuation methods, to compute families of periodic orbits. Indeed, as we will see, periodic orbits are not isolated in the CR3BP, but lie in a cylinder of periodic orbits that is parametrized by the Jacobi constant. In particular we show how to compute the Lyapunov, Halo, Axial and Vertical families of periodic orbits, originating in the vicinity of the collinear Lagrangian points L_1, L_2 and L_3, as well as the families of the lunar Distant Prograde Orbits (DPO), Distant Retrograde Orbits (DRO) and Low Prograde Orbits (LPO). We also address the stability of these orbits and the presence of different types of bifurcations that exists along the families of periodic orbits, e.g., tangent and period multiplying bifurcations, using the Broucke diagrams.

In this work we also present the concept of stable and unstable invariant manifolds. The stable manifolds of a periodic orbit constitute paths along which a spacecraft asymptotically approaches the given orbit without the need for additional energy. On the other hand, unstable manifolds consist of trajectories along which the spacecraft locally diverges from the orbit, again without the need for external energy. This feature of invariant manifolds offers a significant advantage, as it can be utilized to design low-energy orbital transfers. In particular we show how the Poincaré maps of the invariant manifolds, associated with appropriate planes in phase space, i.e., Poincaré sections, can be leveraged to compute homoclinic and heteroclinic transfers between L_1 and L_2 Lyapunov orbits in the Earth-Moon system. In particular, these transfer orbits have the remarkable property of requiring virtually zero thrust. Furthermore, the thesis introduces a CR3BP model that incorporates the spherical harmonic expansion of the lunar gravitational potential using the gravitational coefficients from the GRAIL Gravity Model

(GL0660B) [24]. This model allows to compute families of lunar Repeat Ground Track (RGT) orbits (see Section 5.3) in a high fidelity lunar gravitational field. Finally, the thesis explores different possibilities for impulsive transfers departing from various Near Rectilinear Halo Orbits (NRHOs) towards RGT orbits at different altitudes and inclinations (see Section 5.4). In order to do this we again exploit the presence of unstable manifolds. The NRHOs of interest include the $4:1$ and the $9:2$ resonant Southern L_2 NRHO, in particular the latter constitutes the reference trajectory for the Lunar Gateway, the first planned extraterrestrial space station. Strong motivation in this research is provided by the renewed global interest in lunar exploration, including various ambitious lunar programs, such as the NASA's Artemis program, of which the Gateway constitutes a vital component, and the European Space Agency's (ESA) plan for a Lunar Navigation and Communication System (LNCS). In particular such an infrastructure would provide vital support for missions, facilitating communication and precise navigation, serving as an enabler for both institutional and commercial lunar missions. In this framework, our investigation aims at providing insights into the design of efficient trajectories for future lunar missions. Indeed, RGT orbits, especially those with nearly polar inclination, could be of interest for missions that focus on lunar surface coverage. For instance a Synthetic Aperture Radar (SAR), or similar technology on a RGT orbit could provide radar imaging for high-resolution detection and mapping with day-night imaging capabilities, providing detailed observations of the lunar surface [32].

1.1 Some history of the N-Body Problem

As we shall explore in the next chapter, the Circular Restricted Three-Body Problem represents a specialized variant of the broader Three-Body Problem, and by extension of the N-Body Problem. Given the significance of the N-Body Problem, it is important to understand its historical origins and development.

The N-Body Problem can be stated as the problem of uniquely determining the position and velocities as functions of time of N bodies subject to their mutual gravitation forces, given their initial conditions. This problem dates back to Newton's *Principia Mathematica* (1687) [36], where he made the first attempts at studying the motion of the Earth and Moon around the Sun. However, while by that time he had already solved the Two-Body Problem, it was clear that to consider more than two bodies added a whole new level of difficulty. In his *Principia* Newton writes:

"And hence it is that the attractive force is found in both bodies. The Sun attracts Jupiter and the other planets, Jupiter attracts its satellites, and similarly the satellites act on one another and on Jupiter, and all the planets on one another. And although the actions of each of a pair of planets on the other can be distinguished from each other and can be considered as two actions by which each attracts the other, yet inasmuch as they are between the same two bodies they are not two but a single operation between two termini.

After Newton, contributions on the N-Body Problem were made by some of the greatest mathematicians of the 18th and 19th century, such as Euler, Lagrange, Laplace, Hamilton, Liouville, Jacobi, D'Alembert and Poincaré. The quest to discover a general solution for N-Body Problem was regarded as highly significant, daunting. to the point that, in the latter part of the 19th century, King Oscar II of Sweden, instituted a reward

for anyone who could unravel this enigma. The specifications of the challenge were quite explicit:

" Given a system of arbitrarily many mass points that attract each according to Newton's law, under the assumption that no two points ever collide, try to find a representation of the coordinates of each point as a series in a variable that is some known function of time and for all of whose values the series converges uniformly."

In the event that the original problem remained unsolved, any other notable advancement in the field of classical mechanics would be deemed worthy of the prize. Hence, even though Poincaré did not provide a solution to the original problem, the prize was still awarded to him. His groundbreaking work laid the foundations for the emergence of chaos theory. In his words [39]:

"It may happen that small differences in the initial conditions produce very great ones in the final phenomena. A small error in the former will produce an enormous error in the latter. Prediction becomes impossible, and we have the fortuitous phenomenon."

The ideas present in Poincaré's work on the Three-Body Problem have laid the foundations for chaos theory. However, if on one side chaos means that long term evolution become impossible to predict, on the other hand it unfolds the possibilities for traveling towards different destination at very low energy cost, as we will show later in this thesis.

1.1.1 On the solutions of the Three-Body Problem

Ultimately, the original problem was solved by Sundman for the case $N = 3$ [48]. Sundman has shown that an analytical solution expressed in terms of power series of $t^{2/3}$ exists. Unfortunately, this solution converges so incredibly slowly that it is completely useless from a practical point of view. Moreover, it is known today that the general N-Body Problem, for $N \geq 3$, does not admit a closed-form solution. However, special solutions can be found for some special cases of the Three-Body Problem. However, special classes of solutions for the Three-Body Problem have been known to exist for a long time. In fact in 1767 Euler proved that three collinear bodies of arbitrary finite masses, with appropriate initial conditions would remain collinear indefinitely, while the line on which they lie rotates around their center of mass describing Keplerian orbits of which the center of mass is one focus. A second class of periodic solutions was found by Lagrange in 1772, when he showed that three bodies forming an equilateral triangle with suitable initial conditions would describe ellipses such that the triangle formed by the three bodies will remain equilateral at all times.

More recently a new remarkable solution to the three-body problem, known as the *figure-eight* solution, was discovered numerically by Alain Chenciner and Richard Montgomery [9]. In the figure-eight solution, three bodies of equal mass follow a single looping trajectory that resembles the shape of an eight. Each body moves smoothly along this shared path, never colliding with the others, and after one full cycle, each body returns to its original position and the pattern repeats indefinitely, in what may be regarded as an orbital dance. Surprisingly this eight-shaped orbit appears to be stable [22] and to persist for small perturbation of both the masses and the initial conditions, moreover it has been proven numerically to be a possible, albeit rather rare, outcome of a planar binary-binary scattering [18].

Since the discovery of the figure-eight solution, many solutions to the N-body problem

in which N equal masses chase each other around a fixed closed curve, equally spaced in phase along the curve, have been found. These solutions are known as N-body choreographies, and have already been found for many different values of N.

As we close this short overview of the general Three-Body Problem and its intriguing solutions, we turn our attention to the Circular Restricted Three-Body Problem and its many interesting aspects, particularly the existence of periodic solutions, which are not isolated, but rather come in families of orbits that are parametrized by the Jacobi constant, an energy-like first integral. We want to emphasize that these solutions, apart from being fascinating mathematical constructs, also bear significant implications for space mission planning.

Chapter 2

The Circular Restricted Three-Body Problem

The Circular restricted Three-Body problem (CR3BP) is a simplification of the general Three-Body problem, in which one of the masses is assumed to be much smaller than the to the other two, which we shall call the primaries, so that the force exerted by this body on the primaries can be neglected. In this case the motion of the primaries can be simply described by the Two-Body problem, whose analytical solution is known, in particular we will assume that the primaries describe circular orbits around their center of mass. This approximation allows for more tractable solutions and it has proven to be of large practical interest in the field of celestial mechanics and spacecraft trajectory design.

2.1 Motion of the primaries

Let's start by considering N point masses in an inertial reference frame, subject only to their mutual gravitational interaction and label them $P_1, P_2, \dots P_N$. Their equations of motion read

$$\ddot{\boldsymbol{r}}_i = G \sum_{\substack{j=i \\ i \neq j}}^{N} \frac{m_j}{r_{ij}^3} \boldsymbol{r}_{ij}, \quad i = 1, 2, 3, \tag{2.1}$$

where we have let:

$$\boldsymbol{r}_i = (x_i, y_i), \quad \boldsymbol{r}_{ij} = \boldsymbol{r}_j - \boldsymbol{r}_i, \quad r_{ij} = \|\boldsymbol{r}_{ij}\|, \tag{2.2}$$

so that $\boldsymbol{r}_{ij}$ is the relative position vector of the bodies P_i and P_j. Suppose now for simplicity that there are only two bodies in our system, for instance this may be the Earth and the Moon, so that the gravitational interactions with the Sun as well as those with all the other planets are neglected. We label these two bodies P_1 and P_2. In this case, we can rewrite the equation (2.1) in a more explicit form as shown below:

$$\ddot{\boldsymbol{r}}_1 = G \frac{m_2}{r_{12}^3} \boldsymbol{r}_{12}, \quad \ddot{\boldsymbol{r}}_2 = G \frac{m_1}{r_{21}^3} \boldsymbol{r}_{21}. \tag{2.3}$$

Let $\boldsymbol{r}_b$ be the position vector of the center of mass of the system, that is:

$$\boldsymbol{r}_b = \frac{m_1 \boldsymbol{r}_1 + m_2 \boldsymbol{r}_2}{m_1 + m_2}. \tag{2.4}$$

Then (2.3) can be rewritten in the form:

$$\ddot{\boldsymbol{r}}_b = 0, \quad \ddot{\boldsymbol{r}}_{12} = -\frac{G(m_1+m_2)}{r_{12}^3}\boldsymbol{r}_{12}. \tag{2.5}$$

The first equation in (2.5) implies in particular that the center of mass moves of uniform linear motion. While the second equation implies that the motion of the relative position vector $\boldsymbol{r}_{12}$ is determined by the Kepler problem with mass $m_1 + m_2$. From now on, let $\boldsymbol{r} = \boldsymbol{r}_{12}$ and $r = \|\boldsymbol{r}\|$, for simplicity. We define the specific angular momentum vector as

$$\boldsymbol{h} = \boldsymbol{r} \times \dot{\boldsymbol{r}}. \tag{2.6}$$

Then it is easy to show that $\boldsymbol{h}$ is a first integral of motion, i.e., it remains constant along a solution of our differential equation, indeed:

$$\frac{d\boldsymbol{h}}{dt} = \boldsymbol{r} \times \ddot{\boldsymbol{r}} + \dot{\boldsymbol{r}} \times \dot{\boldsymbol{r}} = 0 \tag{2.7}$$

Where we used the fact that $\boldsymbol{r}$ and $\ddot{\boldsymbol{r}}$ are parallel because of (2.5). As a consequence of the conservation of the angular momentum, we find that the motion of P_1 and P_2 in the reference frame centered in the center of mass of the system takes place in a plane. This follows from the fact that $\boldsymbol{h}$ is a fixed vector which by construction, is perpendicular both to the $\boldsymbol{r}$ and $\dot{\boldsymbol{r}}$. In this way the three-dimensional dynamics is reduced to dynamics on a plane. This observations justify the choice of a planar inertial reference frame with origin in the center of mass of the system and orthogonal to $\boldsymbol{h}$. In this new reference frame the relative position vector of P_1 and P_2 can be expressed in terms of the polar coordinates r, θ, as:

$$\boldsymbol{r} = (x, y) = (r\cos\theta, r\sin\theta). \tag{2.8}$$

Now define the specific kinetic energy

$$T(= \frac{1}{2}\dot{\boldsymbol{r}}^2 = \frac{1}{2}(\dot{r}^2 + r^2\dot{\theta}^2), \tag{2.9}$$

and the potential energy

$$V = -\frac{G(m_1+m_2)}{r}. \tag{2.10}$$

This allows us to express Lagrangian of the system as follows:

$$\mathcal{L}(r, \theta, \dot{r}, \dot{\theta}) = T - V = \frac{1}{2}(\dot{r}^2 + r^2\dot{\theta}^2) + \frac{G(m_1+m_2)}{r}. \tag{2.11}$$

Now we can compute:

$$\frac{\partial \mathcal{L}}{\partial \dot{r}} = \dot{r}, \quad \frac{\partial \mathcal{L}}{\partial \dot{\theta}} = r^2\dot{\theta}, \tag{2.12}$$

$$\frac{\partial \mathcal{L}}{\partial r} = r\dot{\theta}^2 - \frac{\partial V}{\partial r}, \quad \frac{\partial \mathcal{L}}{\partial \theta} = 0, \tag{2.13}$$

$$\frac{d}{dt}\left(\frac{\partial \mathcal{L}}{\partial \dot{r}}\right) = \ddot{r}, \quad \frac{d}{dt}\left(\frac{\partial \mathcal{L}}{\partial \dot{\theta}}\right) = 2r\dot{r}\dot{\theta} + r^2\ddot{\theta}. \tag{2.14}$$

Finally the Lagrange equations read [17]:

$$\ddot{r} = r\dot{\theta}^2 - \frac{\partial V}{\partial r} \tag{2.15}$$

$$2r\dot{r}\dot{\theta} + r^2\ddot{\theta} = 0. \tag{2.16}$$

At this point we can compute the conjugate momenta p_r and p_θ of the polar coordinates r and θ respectively. This is done via the Legendre transform, which yields

$$p_r = \frac{\partial \mathcal{L}}{\partial \dot{r}} = \dot{r}, \quad p_\theta = \frac{\partial \mathcal{L}}{\partial \dot{\theta}} = r^2\dot{\theta}. \tag{2.17}$$

Now we can so express the Hamiltonian of the system, which can be written in the form:

$$\mathcal{H}(r, \theta, p_r, p_\theta) = T + V = \frac{p_r^2}{2} + \frac{p_\theta^2}{2r^2} - \frac{G(m_1 + m_2)}{r}. \tag{2.18}$$

Then the Hamilton equations hold, i.e.,

$$\dot{p_r} = -\frac{\partial \mathcal{H}}{\partial r}, \quad \dot{r} = \frac{\partial \mathcal{H}}{\partial p_r}, \tag{2.19}$$

$$\dot{p_\theta} = -\frac{\partial \mathcal{H}}{\partial \theta}, \quad \dot{\theta} = \frac{\partial \mathcal{H}}{\partial p_\theta}. \tag{2.20}$$

From the Hamilton equations (2.19), we rediscover that the angular momentum p_θ is a first integral of motion, alongside the Hamiltonian $\mathcal{H}$. This follows immediately from the fact that the Hamiltonian does not depend explicitly on θ, indeed it is:

$$\dot{p_\theta} = -\frac{\partial \mathcal{H}}{\partial \theta} = 0. \tag{2.21}$$

In particular we are interested in the circular orbits solution. This can be found by imposing that r minimizes the effective potential V^*, defined as the sum of the potential energy angular kinetic energy:

$$V^*(r) = \frac{p_\theta^2}{2r^2} + V = \frac{p_\theta^2}{2r^2} - \frac{G(m_1 + m_2)}{r}, \tag{2.22}$$

This is the same as requiring that $\dot{p_r} = 0$ [17], from which find:

$$\dot{p_r} = -\frac{\partial \mathcal{H}}{\partial r} = -\frac{dV^*}{dr} = -\frac{p_\theta^2}{r^3} + \frac{G(m_1 + m_2)}{r^2} = 0. \tag{2.23}$$

Equation (2.23) can now be solved for r, yielding the fixed relative distance $\bar{r}$ between P_1 and P_2 for circular orbits:

$$r = \bar{r} = \frac{p_\theta^2}{G(m_1 + m_2)}. \tag{2.24}$$

Moreover we can obtain the following expression for the angular velocity $\dot{\theta}$ in the case of circular motion:

$$\dot{\theta} = \frac{\partial \mathcal{H}}{\partial p_\theta} = \frac{p_\theta}{\bar{r}^2}. \tag{2.25}$$

At this stage, we can define a set of normalized units to further simplify our description. We choose the unit distance to be equal to the relative distance for circular motion, i.e, $L = \bar{r} = 1$. Now assume that $m_2 \leq m_1$, and let μ be the relative mass of the smaller primary, i.e.,

$$\mu = \frac{m_2}{m_1 + m_2}, \quad 0 < \mu \leq \frac{1}{2}, \tag{2.26}$$

moreover we choose the unit of mass to be the total mass of the primaries, so that we can write:

$$m_1 + m_2 = 1 \quad \Longrightarrow \quad m_2 = \mu, \quad m_1 = 1 - \mu. \tag{2.27}$$

The unit of time is chosen so that the period of the orbit of P_1 around P_2 is $T = 2\pi$. With this choice it must be that the angular velocity is $\dot{\theta} = 1$, and using (2.24) and (2.25) we obtain also $G = 1$. Since the inertial frame reference frame has origin in the center of mass, and the orbits are circular, i.e., the distance from the origin for each of the two bodies remains constant, it must be $r_1 = -\mu$ and $r_2 = 1 - \mu$. Finally we can write an expression for the position vectors of the two bodies as a function of time. Assuming that P_1 and P_2 are aligned on the x axis at $t = 0$, we find:

$$\boldsymbol{r}_1(t) = -\mu(\cos t, \sin t), \tag{2.28}$$

$$\boldsymbol{r}_2(t) = (1 - \mu)(\cos t, \sin t). \tag{2.29}$$

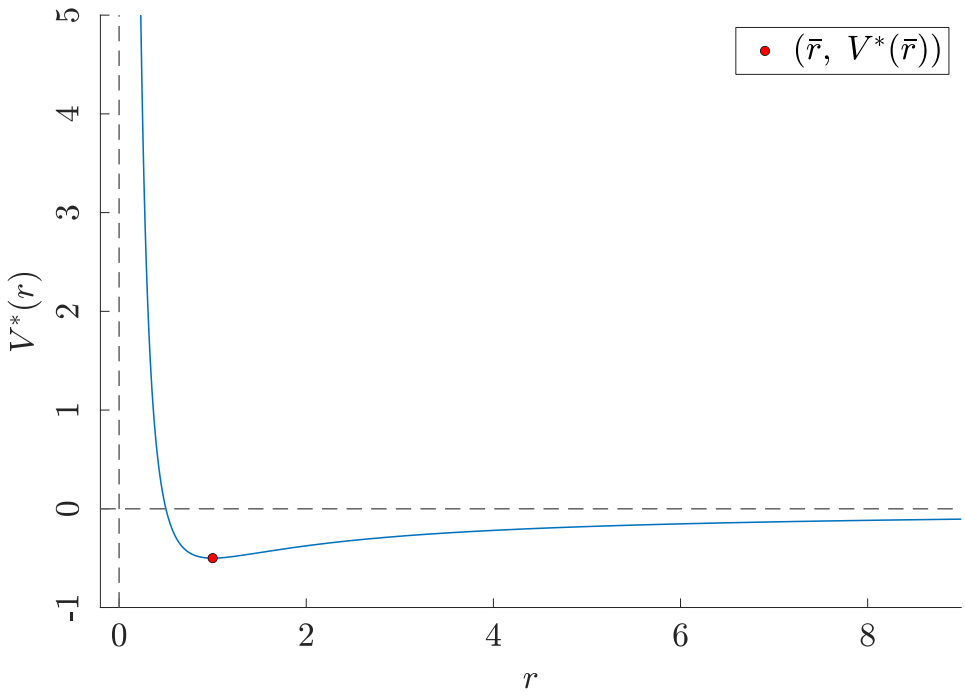

Figure 2.1: Plot of the effective potential $V^*(r)$. The value $\bar{r}$ corresponds to the global minimum V^*. At this value of the potential the orbits are circular, and $\bar{r}$ is the fixed distance that separates P_1 and P_2.

2.2 Equations of motion in the synodic frame

Since we are interested in studying the motion of the third body it is convenient to perform all the calculations in the synodic reference frame, that is the orthogonal reference frame

such that the primaries lie on the x axis oriented towards the smaller of the primaries, with the origin coinciding with the center of mass and with the z axis normal to the ecliptic plane, so that it ha the same direction of the angular momentum vector, finally the y axis is chosen as to complete the right handed triad. Clearly in this frame the positions of the primaries are fixed, and it is:

$$P_1 = (-\mu, 0, 0), \quad P_2 = (1-\mu, 0, 0). \tag{2.30}$$

In the following we will denote the positions and velocity of the massless particle P as

$$\boldsymbol{r} = (x, y, z), \quad \dot{\boldsymbol{r}} = (\dot{x}, \dot{y}, \dot{z}) \tag{2.31}$$

The equations of motion for P, using vector notation, can be written as

$$\ddot{\boldsymbol{r}} + 2\boldsymbol{\omega} \times \dot{\boldsymbol{r}} + \boldsymbol{\omega} \times (\boldsymbol{\omega} \times \boldsymbol{r}) = \frac{\partial \mathcal{U}_G}{\partial \boldsymbol{r}}, \tag{2.32}$$

where $\boldsymbol{\omega} = (0, 0, \omega)$ is the angular momentum vector, and $\mathcal{U}_G$ is the gravitational potential:

$$\mathcal{U}_G(\boldsymbol{r}; \mu) = \frac{1-\mu}{r_1} + \frac{\mu}{r_2}. \tag{2.33}$$

Here r_1 and r_2 are the distances from the massive bodies:

$$r_1 = \sqrt{(x+\mu)^2 + y^2 + z^2}, \qquad r_2 = \sqrt{(x-1+\mu)^2 + y^2 + z^2}. \tag{2.34}$$

It should be clear that in the limiting case $\mu = 0$ the problem is just the Kepler problem in rotating coordinates [31]. Let us define we define the centrifugal potential:

$$\mathcal{U}_C(\boldsymbol{r}) = \frac{1}{2}(\boldsymbol{\omega} \times \boldsymbol{r})^2 = \frac{1}{2}(x^2 + y^2), \tag{2.35}$$

We can then define the effective potential $\mathcal{U}$:

$$\mathcal{U}(\boldsymbol{r}; \mu) = \mathcal{U}_C(\boldsymbol{r}) + \mathcal{U}_G(\boldsymbol{r}) = \frac{1-\mu}{r_1} + \frac{\mu}{r_2} + \frac{1}{2}(x^2 + y^2). \tag{2.36}$$

Finally we can rewrite the the equations of motion as

$$\ddot{\boldsymbol{r}} + 2\boldsymbol{\omega} \times \dot{\boldsymbol{r}} = \frac{\partial \mathcal{U}}{\partial \boldsymbol{r}}, \tag{2.37}$$

which is just a more compact way of writing (2.40).

Alternatively we can proceed using Lagrangian formalism, by introducing the Lagrangian of the massless particle in the synodic frame is given by [25]:

$$\mathcal{L}(\boldsymbol{r}, \dot{\boldsymbol{r}}) = \frac{1}{2}\left(\dot{x}^2 + \dot{y}^2 + \dot{z}^2\right) + (x\dot{y} - \dot{x}y) - \mathcal{U}(\boldsymbol{r}; \mu). \tag{2.38}$$

Then the equations of motion in the synodic reference frame for the massless particle P can be obtained from the Euler-Lagrange equations

$$\frac{d}{dt}\frac{\partial \mathcal{L}}{\partial \dot{\boldsymbol{r}}} = \frac{\partial \mathcal{L}}{\partial \boldsymbol{r}}, \tag{2.39}$$

which can be written more explicitly as a set of three second order ordinary differential equations (ODEs), that is the most common form of the equations of motion for the spatial Circular Restricted Three-Body Problem, i.e.,

$$\ddot{x} - 2\dot{y} = \frac{\partial \mathcal{U}}{\partial x}, \qquad \ddot{y} + 2\dot{x} = \frac{\partial \mathcal{U}}{\partial y}, \qquad \ddot{z} = \frac{\partial \mathcal{U}}{\partial z}, \tag{2.40}$$

and the explicit expression of the partial derivatives of $\mathcal{U}$ are given by:

$$\frac{\partial \mathcal{U}}{\partial x} = x - \frac{1-\mu}{r_1^3}(x+\mu) - \frac{\mu}{r_2^3}(x-1+\mu), \tag{2.41}$$

$$\frac{\partial \mathcal{U}}{\partial y} = y - \frac{1-\mu}{r_1^3}y - \frac{\mu}{r_2^3}y, \tag{2.42}$$

$$\frac{\partial \mathcal{U}}{\partial z} = -\frac{1-\mu}{r_1^3}z - \frac{\mu}{r_2^3}z. \tag{2.43}$$

It is worth noting that the equations of motion (2.40) do not explicitly depend on time, and we say that the system in $t-$invariant. Finally we give one more form of the equations of motion which will be useful later. We can rewrite the vector form of the equations of motion:

$$\ddot{\boldsymbol{r}} = 2\Omega\dot{\boldsymbol{r}} + \frac{\partial \mathcal{U}}{\partial \boldsymbol{r}}, \tag{2.44}$$

where we have let

$$\Omega = \begin{pmatrix} 0 & 1 & 0 \\ -1 & 0 & 0 \\ 0 & 0 & 0 \end{pmatrix}. \tag{2.45}$$

Moreover let $\boldsymbol{x} = (\boldsymbol{r}, \dot{\boldsymbol{r}})$. Then the equations of motion can be written as a first order vector ODE:

$$\dot{\boldsymbol{x}} = g(\boldsymbol{x};\mu), \qquad g(\boldsymbol{x};\mu) = \begin{pmatrix} 0_{3\times3} & I_{3\times3} \\ 0_{3\times3} & 2\Omega \end{pmatrix} \boldsymbol{x} + \begin{pmatrix} 0_{3\times1} \\ \mathcal{U}_{\boldsymbol{r}}^T \end{pmatrix}, \tag{2.46}$$

where we denoted $\mathcal{U}_{\boldsymbol{r}} = \partial\mathcal{U}/\partial\boldsymbol{r}$. Additionally we denote the flow associated to the dynamical system (2.46) as $\varphi(\boldsymbol{x}(t_i), t)$, i.e.,

$$\varphi(\boldsymbol{x}(t), t) = \boldsymbol{x}(t) + \int_{t_0}^{t} g(\boldsymbol{x}(\tau);\mu)\, d\tau. \tag{2.47}$$

For completeness we report here the explicit expression of the second order derivatives of $\mathcal{U}$, which will need later on. This are given by:

$$\mathcal{U}_{xx} = 1 - \frac{1-\mu}{r_1^3} - \frac{\mu}{r_2^3} + 3(1-\mu)\frac{(x-x_1)^2}{r_1^5} + 3\mu\frac{(x-x_2)^2}{r_2^5}, \tag{2.48}$$

$$\mathcal{U}_{yy} = 1 - \frac{1-\mu}{r_1^3} - \frac{\mu}{r_2^3} + 3\left[\frac{1-\mu}{r_1^5} + \frac{\mu}{r_2^5}\right]y^2, \tag{2.49}$$

$$\mathcal{U}_{zz} = -\frac{1-\mu}{r_1^3} - \frac{\mu}{r_2^3} + 3\left[\frac{1-\mu}{r_1^5} + \frac{\mu}{r_2^5}\right]z^2, \tag{2.50}$$

$$\mathcal{U}_{xy} = 3\left[(1-\mu)\frac{x-x_1}{r_1^5} + \mu\frac{x-x_2}{r_2^5}\right]y, \tag{2.51}$$

$$\mathcal{U}_{xz} = 3\left[(1-\mu)\frac{x-x_1}{r_1^5} + \mu\frac{x-x_2}{r_2^5}\right]z, \tag{2.52}$$

$$\mathcal{U}_{yz} = 3\left[\frac{1-\mu}{r_1^5} + \frac{\mu}{r_2^5}\right]yz. \tag{2.53}$$

System	μ	L [km]	V [km/s]	T [s]
Sun-Jupiter	9.537×10^{-4}	7.784×10^{8}	13.102	3.733×10^{8}
Sun-(Earth+Moon)	3.036×10^{-6}	1.496×10^{8}	29.784	3.147×10^{7}
Earth-Moon	1.215×10^{-2}	3.844×10^{5}	1.022	2.357×10^{6}
Mars-Phobos	1.667×10^{-8}	9.380×10^{3}	2.144	2.749×10^{4}
Jupiter-Io	4.704×10^{-5}	4.218×10^{5}	17.390	1.524×10^{5}
Jupiter-Europa	2.528×10^{-5}	6.711×10^{5}	13.780	3.060×10^{5}
Jupiter-Ganymede	7.804×10^{-5}	1.070×10^{6}	10.909	6.165×10^{5}
Jupiter-Callisto	5.667×10^{-5}	1.883×10^{6}	8.226	1.438×10^{6}
Saturn-Mimas	6.723×10^{-8}	1.856×10^{5}	14.367	8.117×10^{4}
Saturn-Titan	2.366×10^{-4}	1.222×10^{6}	5.588	1.374×10^{6}
Neptune-Triton	2.089×10^{-4}	3.548×10^{5}	4.402	5.064×10^{5}
Pluto-Charon	1.097×10^{-1}	1.941×10^{4}	0.222	5.503×10^{5}

Table 2.1: Approximate values of the μ parameter for different systems inside the Solar systems, as well as the dimensional mean values of the unit distance between the primaries L, unit velocity V, and period of the orbit of the primaries $T = 2\pi$. The values are from the Jet Propulsion Laboratory's solar system dynamics website: http://ssd.jpl.nasa.gov/.

We now note the presence of three kinds of symmetries in the CR3BP, this is remarkable in that they allow us to find new solutions when some are already known, this will be useful later on, e.g., we can immediately recover the initial conditions for a Southern Halo orbit, once the corresponding Northern Halo is given. The symmetries are the following [13]:

- Symmetry with respect to the xy plane, i.e., if $(x(t), y(t), z(t))$ is a solution of (2.40), then the mapping
$$(x(t), y(t), z(t)) \mapsto (x(t), y(t), -z(t)), \tag{2.54}$$
yields another solution.

- Symmetry with respect to time, i.e., if $(x(t), y(t), z(t))$ is a solution of (2.40), then the mapping
$$(x(t), y(t), z(t)) \mapsto (x(-t), -y(-t), z(-t)), \tag{2.55}$$
yields another solution.

- Symmetry with respect to the mass parameter, i.e., if $(x(t), y(t), z(t))$ is a solution of (2.40), for μ, then the mapping
$$(x(t), y(t), z(t); \mu) \mapsto (-x(t), -y(t), z(t); 1-\mu), \tag{2.56}$$
yields another solution, but for mass parameter $1 - \mu$.

2.3 The Jacobi constant

In general the Lagrange equation of a time independent Lagrangian $\mathcal{L}(\boldsymbol{r}, \dot{\boldsymbol{r}})$ admit a first integral of the form:
$$\mathcal{C} = \dot{\boldsymbol{r}} \cdot \frac{\partial \mathcal{L}}{\partial \dot{\boldsymbol{r}}} - \mathcal{L}(\boldsymbol{r}, \dot{\boldsymbol{r}}). \tag{2.57}$$

Parameter	Symbol	Value
Earth gravitational parameter	Gm_E	398.6004415 km^3/s^2
Moon gravitational parameter	Gm_M	4.902801076 km^3/s^2
Moon radius	R_M	1738.0 km
Earth n radius	R_E	6371.0 km
Earth-Moon distance	L	384400 km
Moon relative mass	μ	0.01215058655960256
Time unit	$T/2\pi$	375190.258663027 s

Table 2.2: Earth-Moon system parameters. The Earth and Moon gravitational parameter and radius are those used in the Earth Gravity Model (EGM96) and the GRAIL Gravity Model (GL0660B) [24], respectively. The mass parameter μ is derived from (2.26). The remaining data is borrowed from [45] and Jet Propulsion Laboratory's solar system dynamics website.

We arrive to the same conclusion by noting that (2.40) can be recast as system of 6 first order ordinary differential equations, moreover the system is autonomous and as such admits one energy-like first integral. A simple way of finding the explicit form of the first integral is to scalar multiply equation (2.37) by $\dot{\boldsymbol{r}}$, this yields

$$\dot{\boldsymbol{r}} \cdot \left(\ddot{\boldsymbol{r}} + 2\boldsymbol{\omega} \times \dot{\boldsymbol{r}}\right) = \dot{\boldsymbol{r}} \cdot \frac{\partial \mathcal{U}}{\partial \boldsymbol{r}}, \tag{2.58}$$

which can be rewritten as

$$\frac{1}{2}\frac{d\dot{\boldsymbol{r}}^2}{dt} = \frac{d\mathcal{U}}{dt}. \tag{2.59}$$

This last equation can be integrated to obtain

$$\dot{\boldsymbol{r}}^2 = 2\mathcal{U}(\boldsymbol{r}) - \mathcal{C}. \tag{2.60}$$

Then the constant of integration $\mathcal{C}$, is the first integral we were looking for, usually known as the Jacobi constant, which can be thought as a function of the positions and velocities as

$$\mathcal{C}(\boldsymbol{r}, \dot{\boldsymbol{r}}) = 2\mathcal{U}(\boldsymbol{r}) - (\dot{x}^2 + \dot{y}^2 + \dot{z}^2). \tag{2.61}$$

It can be shown that it is actually the only first integral of the CR3BP, thus we are not able to reduce further the number of degrees of freedom of the system. However as we will see the Jacobi constant can be used to recover important information on the dynamics of the system.

2.3.1 Hamiltonian formulation

Up until this point, we have expressed the equations of motion using the state variables x, y, z and their corresponding time derivatives $\dot{x}$, $\dot{y}$, $\dot{z}$. As we move to a discussion of the Hamiltonian formalism, it is useful to introduce a new set of variables. These are the generalized coordinates q_i and the generalized momenta p_i. In our current context, the q_i variables correspond to the positional state variables x, y, and z, so that:

$$q_1 = x, \quad q_2 = y, \quad q_3 = z. \tag{2.62}$$

The generalized momenta p_i are defined as the partial derivatives of the Lagrangian $\mathcal{L}$ with respect to the time derivatives of q_i, which in this case correspond to $\dot{x}$, $\dot{y}$, $\dot{z}$. Then

the expressions for the generalized momenta p_i are given by:

$$p_1 = \frac{\partial \mathcal{L}}{\partial \dot{x}} = \dot{x} - y, \tag{2.63}$$

$$p_2 = \frac{\partial \mathcal{L}}{\partial \dot{y}} = \dot{y} + x, \tag{2.64}$$

$$p_3 = \frac{\partial \mathcal{L}}{\partial \dot{z}} = \dot{z}. \tag{2.65}$$

If we now denote $\boldsymbol{q} = (q_1, q_2, q_3)$, $\boldsymbol{p} = (p_1, p_2, p_3)$, the Hamiltonian function can be written as:

$$\mathcal{H}(\boldsymbol{q}, \boldsymbol{p}) = \sum_{i=1}^{3} p_i \dot{q}_i - \mathcal{L}(\boldsymbol{q}, \dot{\boldsymbol{q}}), \tag{2.66}$$

more explicitly we can write:

$$\mathcal{H} = \frac{1}{2}(\dot{x}^2 + \dot{y}^2 + \dot{z}^2) - \frac{1-\mu}{r_1} - \frac{\mu}{r_2} - \frac{1}{2}(x^2 + y^2). \tag{2.67}$$

The Hamiltonian has then the same expression of the Jacobian constant up to a constant factor -2. This is an alternative proof that $\mathcal{C}$ is constant since $\mathcal{H}$ is the energy of the system which, in absence of external and dissipative forces, is conserved. Finally the equations of motion can be retrieved once again, from the Hamilton equations:

$$\dot{q}_i = \frac{\partial \mathcal{H}}{\partial p_i}, \quad i = 1, 2, 3, \tag{2.68}$$

$$\dot{p}_i = -\frac{\partial \mathcal{H}}{\partial q_i}, \quad i = 1, 2, 3. \tag{2.69}$$

2.4 Lagrangian points

The equations of motion (2.40) admit exactly five stationary points, known as Lagrangian points and denoted by L_i, $i = 1, \ldots, 5$, that are the solutions of

$$\nabla \mathcal{U} = \left(\frac{\partial \mathcal{U}}{\partial x}, \frac{\partial \mathcal{U}}{\partial y}, \frac{\partial \mathcal{U}}{\partial z} \right) = 0. \tag{2.70}$$

Indeed this condition guarantees that if the massless particle P is placed in $L_i = (x_i, y_i, z_i)$ with zero-velocity, then the accelerations will also be zero, and P will remain in L_i forever (in the synodic frame of reference). Clearly in the non-rotating frame P will move in a circular orbit with the same frequency of the primaries. With this idea in mind we will now find the critical points of $\mathcal{U}$ explicitly. We notice immediately from (2.43) that it needs be $z = 0$, thus the Lagrangian points all lie on the orbital plane xy. That said, we now distinguish two cases.

If $y = 0$, then (2.42) is solved for any value of x while from (2.41) we obtain:

$$f(x) \equiv \left. \frac{\partial \mathcal{U}}{\partial x} \right|_{y,z=0} = x - (1-\mu)\frac{x+\mu}{|x+\mu|^3} - \mu \frac{x-1+\mu}{|x-1+\mu|^3} = 0. \tag{2.71}$$

That is equivalent to finding the zeros of the function $f(x)$. In Figure 2.2 we show the plot of $f(x)$ obtained for the Earth-Moon system, and we observe that $f(x)$ has three zeros, which we label x_{L_1}, x_{L_2}, x_{L_3}, so that

$$x_{L_3} < -\mu < x_{L_1} < 1 - \mu < x_{L_2}. \tag{2.72}$$

Therefore we have found three critical points for $\mathcal{U}$, that go under the name of collinear Lagrangian points $L_1,\ L_2,\ L_3$. These corresponds to the collinear solutions for the general three body problem, found by Euler in 1767, the remaining two equilibria correspond instead to the equilateral solutions for the three body problem, discovered by Lagrange in 1772. The approximate positions of the collinear points for the Earth-Moon system are:

$$L_1 = (x_{L_1}, y_{L_1}, z_{L_1}) = (0.8369, 0, 0), \tag{2.73}$$
$$L_2 = (x_{L_2}, y_{L_2}, z_{L_2}) = (1.1557, 0, 0), \tag{2.74}$$
$$L_3 = (x_{L_3}, y_{L_3}, z_{L_3}) = (-1.0051, 0, 0). \tag{2.75}$$

If instead we let $y \neq 0$, from (2.42), dividing both members by y, after rearranging we obtain:

$$\frac{1-\mu}{r_1^3} = 1 - \frac{\mu}{r_2^3}. \tag{2.76}$$

On the other hand, if we now substitute (2.76) into (2.41), we get:

$$x - (1 - \frac{\mu}{r_2^3})(x+\mu) - \frac{\mu}{r_2^3}(x - 1 + \mu) = 0, \tag{2.77}$$

finally implying:

$$\mu(1 - \frac{1}{r_2^3}) = 0. \tag{2.78}$$

Clearly (2.78) is satisfied only for $r_2 = 1$, moreover substituting in (2.76) we get

$$\frac{1-\mu}{r_1^3} = 1 - \mu. \tag{2.79}$$

Implying that it must also be $r_1 = 1$. Substituting $r_1 = r_2 = 1$, into (2.34)we obtain:

$$x = \frac{1}{2} - \mu, \qquad y = \pm\frac{\sqrt{3}}{2}. \tag{2.80}$$

Thus we have found two more critical points of $\mathcal{U}$, that are those forming an equilateral triangle with P_1 and P_2, known as the equilateral Lagrangian points L_4 and L_5, with coordinates

$$L_4 = (x_{L_4}, y_{L_4}, z_{L_4}) = \big(\frac{1}{2} - \mu, \frac{\sqrt{3}}{2}, 0\big), \tag{2.81}$$
$$L_5 = (x_{L_5}, y_{L_5}, z_{L_5}) = \big(\frac{1}{2} - \mu, -\frac{\sqrt{3}}{2}, 0\big). \tag{2.82}$$
$$\tag{2.83}$$

Recall that by convention we assumed $m_2 \leq m_1$ so that $0 < \mu \leq \frac{1}{2}$. Then it holds:

$$\mathcal{U}(L_1) > \mathcal{U}(L_2) \geq \mathcal{U}(L_3) > \mathcal{U}(L_4) = \mathcal{U}(L_5), \tag{2.84}$$

and the equality $\mathcal{U}(L_2) = \mathcal{U}(L_3)$ holds only in the limit case $\mu = \frac{1}{2}$. In the following we will use the notation

$$\boldsymbol{x}_{L_i} = (x_{L_i}, y_{L_i}, z_{L_i}, 0, 0, 0), \quad i = 1, 2, \dots 5 \tag{2.85}$$

In Figure 2.2 we show the positions of the Lagrangian points for the value of μ corresponding to the Earth-Moon system.

2.5 The zero-velocity surfaces

The presence of a first integral of motion allows us to grasp some insight on the dynamics of the massless particle, by defining the so called zero-velocity surfaces. These are regions in phase space where the velocity of a particle goes to zero, thus not allowing the particle to go trough them, thus confining the regions of space where the particle is confined. The starting point for understanding these surfaces is defining the energy surface of the system, we define this as the level set:

$$\mathcal{M}(\mathcal{C};\mu) = \{(x,y,z,\dot{x},\dot{y},\dot{z}) : \ 2\mathcal{U} - \dot{\boldsymbol{r}}^2 = \mathcal{C}\}, \tag{2.86}$$

this is a 5 dimensional hypersurface embedded in $\mathbb{R}^6$. In particular we are interested in its projection in the physical space, two this aim consider the auxialiary function

$$f(\boldsymbol{r};\mu,\mathcal{C}) = 2\mathcal{U} - \mathcal{C}. \tag{2.87}$$

Since it is obvious that the velocity components must be real, it needs be $\dot{\boldsymbol{r}}^2 \geq 0$. As a consequence, along any trajectory, it needs be also $f(\boldsymbol{r};\mu,\mathcal{C}) \geq 0$. This means that by solving

$$f(\boldsymbol{r};\mu,\mathcal{C}) = 0, \tag{2.88}$$

we are able to get insight on the regions of space in which the massless particle P is confined. Indeed we can define the admissible region, i.e., the projection of $\mathcal{M}(\mathcal{C};\mu)$ as

$$\mathcal{A}(\mathcal{C};\mu) = \{(x,y,z) : \ f(\boldsymbol{r};\mu,\mathcal{C}) \geq 0\}. \tag{2.89}$$

The reason is that for the definition of f above, P can reach the boundary of $\mathcal{A}(\mathcal{C};\mu)$ only with zero-velocity, i.e., $\dot{\boldsymbol{r}} = 0$, and hence P cannot cross it. For the same reason the boundaries of $\mathcal{A}(\mathcal{C};\mu)$, are called zero-velocity surfaces i.e.,

$$\mathcal{S}(\mathcal{C};\mu) \equiv \partial\mathcal{A}(\mathcal{C};\mu) = \{(x,y,z) : \ f(\boldsymbol{r};\mu,\mathcal{C}) = 0\}, \tag{2.90}$$

and their intersections with the coordinate planes are known as zero-velocity curves. Moreover we call the complement of $\mathcal{A}(\mu,\mathcal{C})$ the forbidden region, i.e.,

$$\mathcal{F}(\mathcal{C};\mu) \equiv \mathbb{R}^3 \setminus \mathcal{A}(\mathcal{C};\mu). \tag{2.91}$$

For simplicity we will denote $\mathcal{C}_i = \mathcal{C}(L_i),\ i = 1,\dots,5$. If we restrict the motion to the xy plane we can distinguish the following five scenarios depending on the value the Jacobi constant [25], and hence on the shape of the zero-velocity curves.

- $\mathcal{C} > \mathcal{C}_1$: If the Jacobi constant is above $\mathcal{C}_1$, the particle is trapped either in the region surrounding P_1 or P_2 depending on the initial state.
- $\mathcal{C}_2 < \mathcal{C} < \mathcal{C}_1$: If the Jacobi constant is just below $\mathcal{C}_1$, a tunnel between the regions around P_1 and P_2 opens up, allowing the massless particle to move between the two.
- $\mathcal{C}_3 < \mathcal{C} < \mathcal{C}_2$: This is the case the most interesting case, when the Jacobi constant is just below C_2. The particle can now move not only between the regions in the vicinity of P_1 and P_2 but it is also allowed to reach the exterior region via a tunnel near L_2.

- $\mathcal{C}_4 = \mathcal{C}_5 < \mathcal{C} < \mathcal{C}_3$: In this case, the Jacobi constant is above $\mathcal{C}_3$ but below that of $\mathcal{C}_4 = \mathcal{C}_5$. The particle can now move from the vicinity of P_1 into the exterior region also trough a gap around L_3.
- $\mathcal{C} < \mathcal{C}_5$: If the Jacobi constant is below $\mathcal{C}_5$, the forbidden realm disappears, so that the particle is free to move in the entire xy plane.

In Figure 2.4 we show the zero-velocity curves $\mathcal{S}(\mathcal{C};\mu)$ on the xy and xz plane, and the corresponding forbidden regions $\mathcal{F}(\mathcal{C};\mu)$ for different values of the Jacobi constant for the Earth-Moon system.

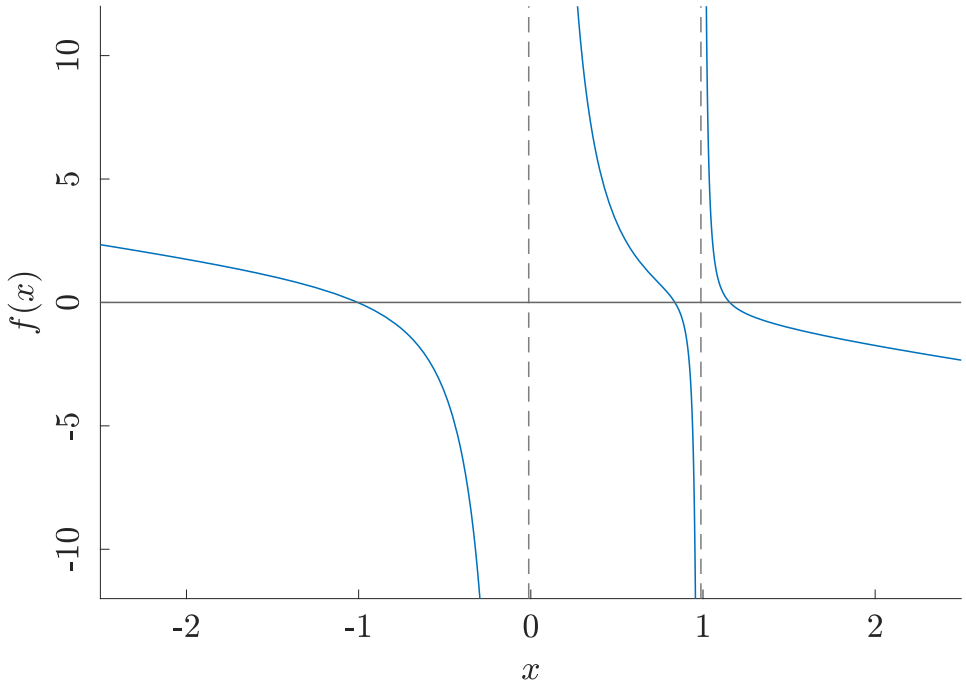

Figure 2.2: Plot of $f(x) \equiv \partial\mathcal{U}/\partial x$ for the Earth-Moon system. The intersections with the x axis are the abscissae of the critical points of $\mathcal{U}$. The two vertical asymptotes have equations $x = -\mu$ and $x = 1 - \mu$.

2.6 Linearization near the Lagrangian points

This section investigates the stability of the equilibrium points, i.e., the behavior of a particle initially placed in an equilibrium point, after a small perturbation in its position and/or velocity. The nonlinear system of differential equations is linearized relative to the equilibrium solutions, i.e., yielding linear variational equations. Stability is defined in terms of a reference solution, and if a disturbance remains in the small neighborhood of an equilibrium point, the reference solution is considered stable. The stability criteria used here is Lyapunov stability, which is valid only if the reference solution is constant, i.e., an equilibrium point. In a later section the stability of non constant periodic orbits will be investigated after introducing further concepts.

Then if we consider a perturbation of the state by a quantity $\delta\boldsymbol{x}$, we obtain, after linearization the variational equations:

$$\frac{d}{dt}\delta\boldsymbol{x} = \Lambda(\boldsymbol{x})\delta\boldsymbol{x} \tag{2.92}$$

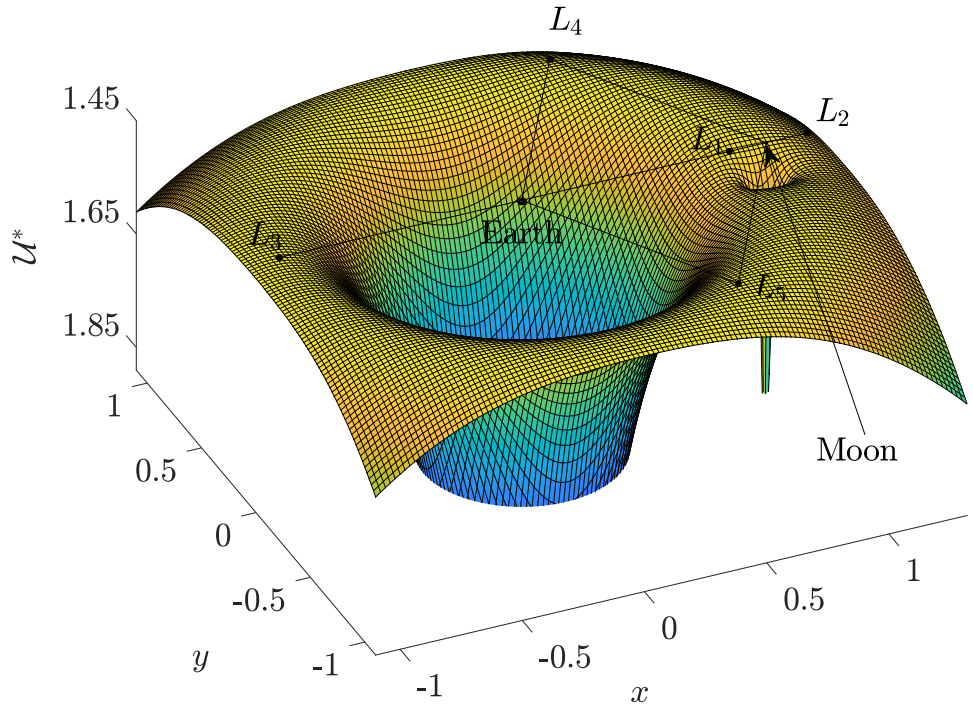

Figure 2.3: The position of the Lagrangian points and the effective potential $\mathcal{U}$, for the Earth-Moon system on the xy plane.

where $\Lambda(\boldsymbol{x})$ is the 6×6 matrix defined as:

$$\Lambda(\boldsymbol{x}) = \frac{\partial g(\boldsymbol{x};\mu)}{\partial \boldsymbol{x}} = \begin{pmatrix} 0_{3\times3} & I_{3\times3} \\ \mathcal{U}_{\mathbf{rr}} & 2\Omega \end{pmatrix}, \quad \mathcal{U}_{\mathbf{rr}} = \begin{pmatrix} \mathcal{U}_{xx} & \mathcal{U}_{xy} & \mathcal{U}_{xz} \\ \mathcal{U}_{xy} & \mathcal{U}_{yy} & \mathcal{U}_{yz} \\ \mathcal{U}_{xz} & \mathcal{U}_{yz} & \mathcal{U}_{zz} \end{pmatrix}, \tag{2.93}$$

where I is the 3×3 identity matrix. The general solution to (2.92) is of the form

$$\delta\boldsymbol{x}(t) = e^{\Lambda(t-t_0)}\delta\boldsymbol{x}(t_0), \tag{2.94}$$

which can be expanded as:

$$\delta\boldsymbol{x}(t) = \sum_{j=1}^{6} c_j e^{\lambda_j(t-t_0)}\boldsymbol{v}_j, \tag{2.95}$$

where c_j are coefficients determined from the initial conditions, and λ_j and $\boldsymbol{v}_j$ are the eigenvalues and eigenvectors associated with matrix Λ. Note that this solution assumes that the matrix Λ has $n = 6$ linearly independent eigenvectors. If this is not the case, the solution process becomes more complicated and may involve generalized eigenvectors [38]. The eigenvalues λ_j provide important information regarding the stability of the linearized system, and in some special cases also for the nonlinear system. Before proceeding we provide the definition of Lyapunov stability [17].

Definition 1. *An equilibrium point $\boldsymbol{x}_{\text{eq}}$ is stable (in the future), in the sense of Lyapunov, if for every neighborhood U of $\boldsymbol{x}_{\text{eq}}$ there exists a neighborhood V such that any solution to the Cauchy problem associated to 2.40 and initial condition in V does not exit from U, i.e.,*

$$\boldsymbol{x}_{\text{eq}} \in V \quad \Longrightarrow \quad \varphi(\boldsymbol{x}_{\text{eq}}, t) \in U, \quad \forall t \geq 0. \tag{2.96}$$

An equilibrium point $\boldsymbol{x}_{\text{eq}}$ is unstable if it is not stable.

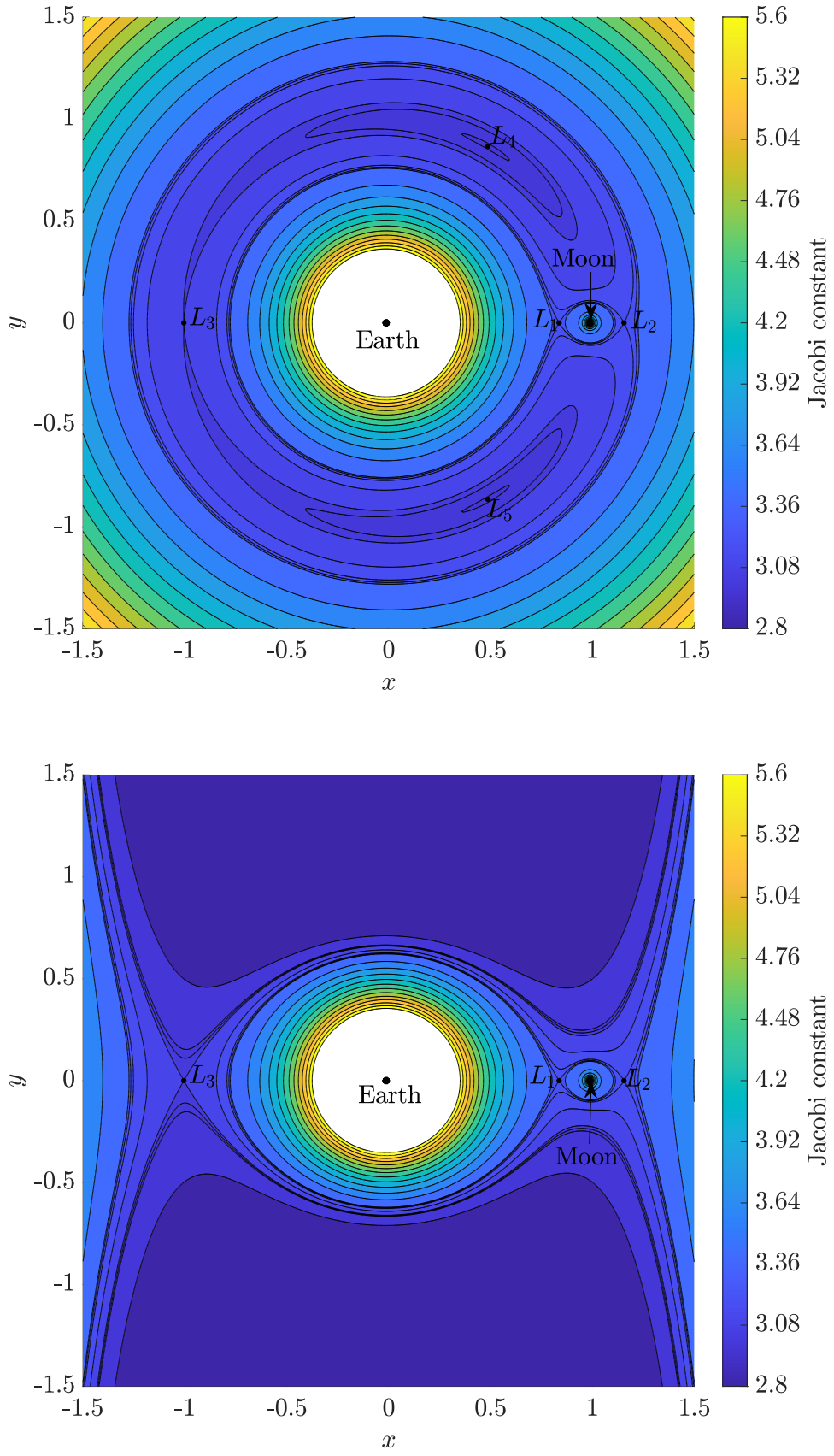

Figure 2.4: Zero-velocity curves on the xy plane (top) and xz plane (bottom) for the Earth-Moon system, corresponding to different values of the Jacobi constant. The coloured area corresponds to the forbidden region $\mathcal{F}(\mathcal{C};\mu)$.

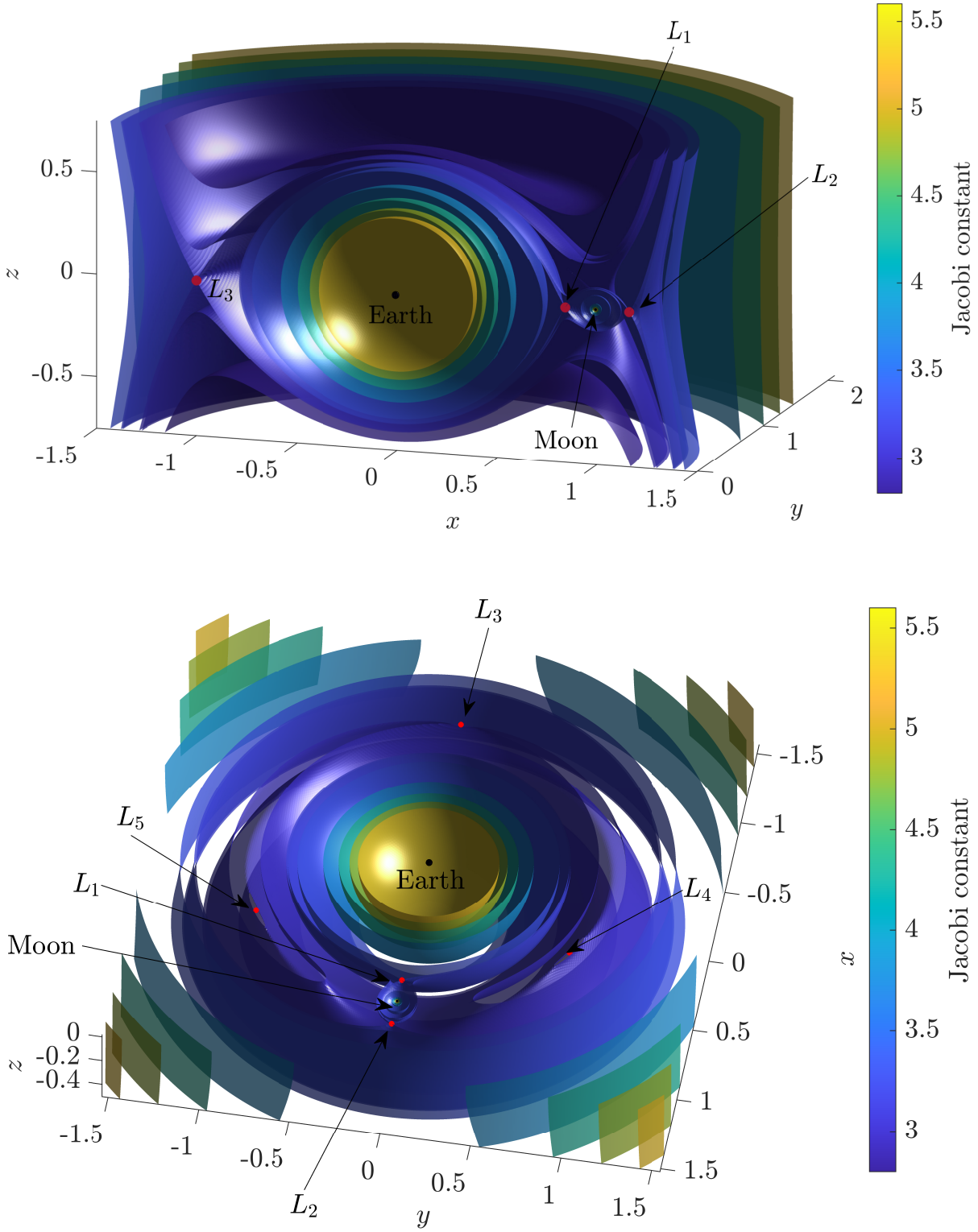

Figure 2.5: Zero-velocity surfaces corresponding to different values of the Jacobi constant. In the top panel we show a cut through the xz plane and the $z = \pm 0.75$ planes. In the bottom panel we show a cut through the xy plane.

We have indeed the following theorem due to Lyapunov [17].

Theorem 1 (Lyapunov's Theorem)**.** *Let $\boldsymbol{x}_{\text{eq}}$ be an equilibrium point for the nonlinear system, $\dot{\boldsymbol{x}} = g(\boldsymbol{x})$. If all the eigenvalues of the Jacobian matrix $\Lambda(\boldsymbol{x}_{\text{eq}})$, have strictly negative real part, then the equilibrium point $\boldsymbol{x}_{\text{eq}}$, is a stable equilibrium point, for the nonlinear system. If $\Lambda(\boldsymbol{x}_{\text{eq}})$ has at least one eigenvalue with strictly positive real part, then $\boldsymbol{x}_{\text{eq}}$ is an unstable equilibrium point the non linear system.*

Thus in the two scenarios considered by Lyapunov's Theorem, the stability properties of the equilibrium point $\boldsymbol{x}_{\text{eq}}$, for the nonlinear system (2.40), and in the linearized system (2.92), are the same. Under all the other circumstances, the theorem does not apply and it is not guaranteed that the stability properties of in the linearized dynamics carry over to the nonlinear system. In summary the stability properties of the equilibrium points as is then determined by the characteristics of the eigenvalues, are as follows λ_j [49, 52]:

- **Complex eigenvalues:** If all λ_j have negative real parts, then sufficiently small perturbations tend to zero as time approaches infinity, and the equilibrium point is Lyapunov stable. If any of the λ_j have a positive real part, then the perturbation will grow in time, and the equilibrium point is unstable.
- **Real eigenvalues:** Similarly to the previous case, if any of the λ_j are positive real integers, the solution is unstable. If all are negative real integers, the solution is stable.
- **Purely imaginary eigenvalues:** If all λ_j are imaginary, the motion is oscillatory and the solution is only linearly stable. If there are multiple roots, the solution is unstable.

Additionally if the equilibrium point $\boldsymbol{x}_{\text{eq}}$ possesses eigenvalues λ_i and λ_j such that the associated real parts have opposite signs, then $\boldsymbol{x}_{\text{eq}}$ is called a saddle point. A stable or unstable equilibrium point with no complex eigenvalues is labeled a node, and an equilibrium point is hyperbolic if all eigenvalues possess non-zero real parts [52].

2.7 Invariant manifolds of equilibrium points

Let $\boldsymbol{x}_{\text{eq}}$ be an equilibrium point, and suppose that the Jacobian matrix $\Lambda(\boldsymbol{x}_{\text{eq}})$ possess n_s eigenvalues with positive real parts, n_u eigenvalues with negative real parts, and n_c eigenvalues with zero real parts. The eigenvectors associated with these eigenvalues are linearly independent, thus, they span $\mathbb{R}^n$, so that $n = \text{rank}(\Lambda) = n_s + n_u + n_c$. Moreover $\mathbb{R}^n$ can be decomposed as the direct sum of three fundamental subspaces: the stable subspace E^s, the unstable subspace E^u, and the center subspace E^c. These subspaces are those generated by the eigenvectors associated to eigenvalues with positive real part, negative real part and, and purely imaginary respectively. Then we can write:

$$E^s \oplus E^c \oplus E^u = \mathbb{R}^n, \tag{2.97}$$

These are the invariant subspaces associated with the linear variational equations in equation (2.92). A solution initially in a specific subspace remains in that subspace for at all subsequent times, hence the name of invariant manifolds.

The Stable Manifold Theorem [16], states that if all eigenvalues, λ_j, associated with the constant Jacobian matrix $\Lambda(\boldsymbol{x}_{\text{eq}})$ possess non-zero real parts, then $\boldsymbol{x}_{\text{eq}}$ is an hyperbolic equilibrium point, and does not possess a center manifold. Moreover in a neighborhood $N(\boldsymbol{x}_{\text{eq}})$, there exists local stable and unstable invariant manifolds W^s_{loc} and W^u_{loc}, of the equilibrium point, that are related to the invariant subspaces E_s and E_u associated with the linear system.

Theorem 2 (Stable Manifold Theorem)**.** *Suppose the nonlinear first order system of differential equations $\dot{\boldsymbol{x}} = g(\boldsymbol{x})$, possesses a hyperbolic equilibrium point $\boldsymbol{x}_{\text{eq}}$. Then in a neighborhood $N(\boldsymbol{x}_{\text{eq}})$ there exist local stable and unstable manifolds,*

$$W^s_{\text{loc}}(\boldsymbol{x}_{\text{eq}}) = \{\boldsymbol{x} \in N \mid d(\varphi(\boldsymbol{x},t),\boldsymbol{x}_{\text{eq}}) \to 0 \text{ as } t \to \infty, \quad \varphi(\boldsymbol{x},t) \in N,\ \forall t \geq 0\}\,, \tag{2.98}$$

$$W^u_{\text{loc}}(\boldsymbol{x}_{\text{eq}}) = \{\boldsymbol{x} \in N \mid d(\varphi(\boldsymbol{x},t),\boldsymbol{x}_{\text{eq}}) \to 0 \text{ as } t \to -\infty, \quad \varphi(\boldsymbol{x},t) \in N,\ \forall t \leq 0\}\,, \tag{2.99}$$

of the same dimension n_s, n_u, as those of the eigenspaces E^s, E^u, of the linearized system (2.92), and tangent to E^s and E^u at $\boldsymbol{x}_{\text{eq}}$. Moreover W^s_{loc} and W^u_{loc} are as smooth as the function g.

The local invariant manifolds W^s_{loc} and W^u_{loc} can be extended into the global stable and unstable manifolds W^s and W^u. This can be computed by propagating the flow backward and forward in time, for W^s and W^u respectively.

We now present another result. If $\boldsymbol{x}_{\text{eq}}$, is a non-hyperbolic equilibrium point, that is, n_s, n_u, and n_c are all non-zero, the structure of the local flow is governed by the Center Manifold Theorem for Flows [16]:

Theorem 3 (Center Manifold Theorem for Flows)**.** *Let g be a vector field on $\mathbb{R}^n$ vanishing at the equilibrium point $g(\boldsymbol{x}_{\text{eq}}) = 0$, let $\Lambda(\boldsymbol{x}_{\text{eq}})$ be the Jacobian matrix of g at the equilibrium $\boldsymbol{x}_{\text{eq}}$. Then the spectrum of $\Lambda(\boldsymbol{x}_{\text{eq}})$ can be decomposed into three subsets n_s, n_c, and n_u, such that:*

$$Re[\lambda] < 0, \lambda \in n_s \tag{2.100}$$

$$Re[\lambda] = 0, \lambda \in n_c \tag{2.101}$$

$$Re[\lambda] > 0, \lambda \in n_u \tag{2.102}$$

Let the generalized eigenspaces be E^s, E^c, and E^u, respectively. Then, there exist stable and unstable invariant manifolds W^s and W^u tangent to the E^u and E^s at $\boldsymbol{x}_{\text{eq}}$, and a center manifold W^c, tangent to the center subspace E^c at $\boldsymbol{x}_{\text{eq}}$. The manifolds W^s, W^u, and W^c are all invariant for the flow g. The stable and unstable manifolds are unique, but W^c need not be.

The existence of a center manifold implies that the structure of the flow near the equilibrium point, possessing at least one zero eigenvalue, is more diverse than an equilibrium point with no center subspace. The solutions initially in the center manifold neither grow nor decay over time, relative to $\boldsymbol{x}_{\text{eq}}$. In Section 2.7.3 we will show how the center manifold can be leveraged to obtain an initial guess for a Lyapunov periodic orbit in the vicinity of the collinear points.

2.7.1 Stability of the collinear points L_1, L_2, L_3

In particular we are interested in studying the stability near the Lagrangian points. We begin by considering the collinear ones. Since $L_i = (x_{L_i}, 0, 0)$, $i = 1, 2, 3$, from equations (2.51-2.53) we obtain:

$$\mathcal{U}_{xx}(L_i) = 1 + \frac{2(1-\mu)}{r_1^3} + \frac{2\mu}{r_2^3}, \tag{2.103}$$

$$\mathcal{U}_{yy}(L_i) = 1 - \frac{1-\mu}{r_1^3} - \frac{\mu}{r_2^3}, \tag{2.104}$$

$$\mathcal{U}_{zz}(L_i) = -\frac{1-\mu}{r_1^3} - \frac{\mu}{r_2^3}, \tag{2.105}$$

$$\mathcal{U}_{xy}(L_i) = \mathcal{U}_{xz}(L_i) = \mathcal{U}_{yz}(L_i) = 0. \tag{2.106}$$

Then the linearized equation (2.92) can be rewritten explicitly as:

$$\delta\ddot{x} - 2\delta\dot{y} = \mathcal{U}_{xx}(L_i)\delta x, \qquad \delta\ddot{y} + 2\delta\dot{x} = \mathcal{U}_{yy}(L_i)\delta y, \qquad \delta\ddot{z} = \mathcal{U}_{zz}(L_i)\delta z. \tag{2.107}$$

We observe that the the third equation in (2.107) is uncoupled from the first two and it is the equation of an harmonic motion of frequency $\sqrt{|\mathcal{U}_{zz}(L_i)|}$. Thus the motion is stable with respect to the z direction. Now we can assume that the solution to the remaining set of two second order linear ODE's is of the form

$$\delta x = \alpha e^{\lambda t}, \qquad \delta y = \beta e^{\lambda t}. \tag{2.108}$$

Then substituting in (2.107), we obtain a linear system in the unknowns α and β:

$$\begin{cases} [\lambda^2 - \mathcal{U}_{xx}(L_i)]\alpha - 2\lambda\beta = 0, \\ 2\lambda\alpha + [\lambda^2 - \mathcal{U}_{yy}(L_i)]\beta = 0. \end{cases} \tag{2.109}$$

This is an homogeneous system, and as such it admits the trivial solution $\alpha = \beta = 0$. We are interested in non-trivial solutions, according to Kramer's rule we then require that

$$\begin{vmatrix} \lambda^2 - \mathcal{U}_{xx}(L_i) & -2\lambda \\ 2\lambda & \lambda^2 - \mathcal{U}_{yy}(L_i) \end{vmatrix} = 0, \tag{2.110}$$

this leads to the characteristic equation

$$\lambda^4 + 2A\lambda^2 - B = 0, \tag{2.111}$$

where we have let

$$A = 2 - \frac{1}{2}[\mathcal{U}_{xx}(L_i) + \mathcal{U}_{yy}(L_i)], \tag{2.112}$$

$$B = -\mathcal{U}_{xx}(L_i)\mathcal{U}_{yy}(L_i). \tag{2.113}$$

Equation (2.111) is a biquadratic equation in λ, with solutions given by

$$\lambda = \pm\sqrt{-A \pm \sqrt{A^2 + B}}. \tag{2.114}$$

It is immediate from (2.103) that $\mathcal{U}_{xx}(L_i) > 0$, moreover it can be shown that for the collinear points it is $\mathcal{U}_{yy}(L_i) < 0$. Hence it holds $B > 0$, implying that the characteristic equation (2.111) admits a pair of real eigenvalues with opposite sign:

$$\lambda_{1,2} = \pm\sqrt{-A + \sqrt{A^2 + B}} \in \mathbb{R}, \tag{2.115}$$

and a pair of conjugate, purely imaginary eigenvalues:

$$\lambda_{3,4} = \pm i\sqrt{-A - \sqrt{A^2 + B}} \in \mathbb{C} \setminus \mathbb{R}. \tag{2.116}$$

2.7.2 Stability of the equilateral points L_4, L_5

We will now study the stability of the equilateral points. In order to do this we substitute the coordinates of the equilateral points given by (2.81 − 2.82), in the linearized equations of motion (2.107), obtaining

$$\delta\ddot{x} - 2\delta\dot{y} = \frac{3}{4}\delta x + \frac{\sqrt{27}}{4}(1-2\mu)\delta y, \tag{2.117}$$

$$\delta\ddot{y} + 2\delta\dot{x} = \frac{\sqrt{27}}{4}(1-2\mu)\delta x + \frac{9}{4}\delta y, \tag{2.118}$$

$$\delta\ddot{z} = -\delta z. \tag{2.119}$$

We observe that also in this case the z equation is uncoupled from the first two, and it is easily seen that it leads to 2π periodic motion, proving stability in the z direction. At this point we can proceed as before to investigate stability in the xy plane for the equilateral points. This leads to the characteristic equation

$$\lambda^4 + \lambda^2 + \frac{27}{4}\mu(1-\mu) = 0. \tag{2.120}$$

This has solutions

$$\lambda_{1,2,3,4} = \pm\sqrt{\frac{-1 \pm \sqrt{1-27\mu(1-\mu)}}{2}}. \tag{2.121}$$

It turns out that if

$$1 - 27\mu(1-\mu) \geq 0, \tag{2.122}$$

we have two pairs of purely imaginary eigenvalues, implying that the equilateral points are stable and non attracting in the linear approximation. Otherwise the eigenvalues will have non-zero real part, thus the solution will be unstable. Since we assumed by convention that $0 < \mu \leq 0.5$, the inequality (2.122) is verified for

$$\mu \leq \mu^* = \frac{1}{2} - \sqrt{\frac{23}{108}} \approx 0.0385, \tag{2.123}$$

the threshold μ^* is known as Routh's critical mass ratio. In particular for $\mu = \mu^*$, we find the repeated eigenvalues $\lambda_1 = \lambda_2 = i\sqrt{2}/2$, and $\lambda_3 = \lambda_4 = -i\sqrt{2}/2$. The condition (2.123) is satisfied for many systems of interest, e.g., Earth-Moon, Sun-Earth and in particular for Sun-Jupiter pairs, explaining the existence of the Greek and Trojan families of asteroids that surrounds the L_4 and L_5 points of the system.

The eigenvalues associated with the collinear points have real and imaginary parts. At least one eigenvalue includes a positive real part, thus, L_1, L_2, and L_3 are unstable. Moreover for the values of μ satisfying (2.123) the Lagrangian equilibria are all non hyperbolic, i.e., the center space has non zero dimension, and in particular the linearized system at L_1, L_2, L_3 has a stable space E^s of dimension $n_s = 1$, an unstable space E^u of dimension $n_u = 1$ and center space E^c of dimension $n_c = 4$, while for L_4 and L_5 the center space coincides with the entire phase space. Its worth noting however that whenever an equilibrium point is unstable, with appropriate initial conditions, the divergent motion can be suppressed in the linear system, resulting in an ellipse about the libration point. These ellipses are not periodic in the real system, and the motion will quickly diverge if propagated in the nonlinear equations of motion (see Section 2.7.3). However as we will see in more detail later, a periodic solution in the nonlinear system can be determined employing a differential correction scheme to obtain an orbit of the Lyapunov family.

Collinear point	j	λ_j	$\boldsymbol{v}_j$					
L_1	1	$+2.3344i$	$(-0.1058,$	$-0.3793i,$	$0,$	$-0.2469i,$	$+0.8854,$	$0)$
	2	$-2.3344i$	$(-0.1058,$	$+0.3793i,$	$0,$	$+0.2469i,$	$+0.8854,$	$0)$
	3	$+2.2688i$	$(0,$	$0,$	$-0.4033i,$	$0,$	$0,$	$+0.9151)$
	4	$-2.2688i$	$(0,$	$0,$	$+0.4033i,$	$0,$	$0,$	$+0.9151)$
	5	-2.9321	$(-0.2932,$	$-0.1349,$	$0,$	$+0.8598,$	$+0.3956,$	$0)$
	6	$+2.9321$	$(-0.2932,$	$+0.1349,$	$0,$	$-0.8598,$	$+0.3956,$	$0)$
L_2	1	$+1.8626i$	$(-0.1536,$	$-0.4474i,$	$0,$	$-0.2861i,$	$+0.8333,$	$0)$
	2	$-1.8626i$	$(-0.1536,$	$+0.4474i,$	$0,$	$+0.2861i,$	$+0.8333,$	$0)$
	3	$+1.7862i$	$(0,$	$0,$	$+0.4885i,$	$0,$	$0,$	$-0.8726)$
	4	$-1.7862i$	$(0,$	$0,$	$-0.4885i,$	$0,$	$0,$	$-0.8726)$
	5	-2.1587	$(+0.3556,$	$+0.2241,$	$0,$	$-0.7676,$	$-0.4838,$	$0)$
	6	$+2.1587$	$(-0.3556,$	$+0.2241,$	$0,$	$-0.7676,$	$+0.4838,$	$0)$
L_3	1	$+1.0104i$	$(-0.3145,$	$-0.6292i,$	$0,$	$-0.3178i,$	$+0.6357,$	$0)$
	2	$-1.0104i$	$(-0.3145,$	$+0.6292i,$	$0,$	$+0.3178i,$	$+0.6357,$	$0)$
	3	$+1.0053i$	$(0,$	$0,$	$-0.7052i,$	$0,$	$0,$	$+0.7090)$
	4	$-1.0053i$	$(0,$	$0,$	$+0.7052i,$	$0,$	$0,$	$+0.7090)$
	5	-0.1779	$(-0.1163,$	$-0.9776,$	$0,$	$+0.0207,$	$+0.1739,$	$0)$
	6	$+0.1779$	$(+0.1163,$	$-0.9776,$	$0,$	$+0.0207,$	$-0.1739,$	$0)$

Table 2.3: Eigenvalues and eigenvectors of $\Lambda(L_i)$, $i = 1, 2, 3$, obtained for the Earth-Moon system.

2.7.3 Center space initial guess

Notice that it is always possible to choose initial conditions such that the contribution of the stable and unstable manifold is null leaving only the periodic components of the solution due to the purely imaginary exponents [7]. This observation indicates the existence of periodic orbits near the collinear equilibrium points L_i, that live inside their respective center space E^c. Thus the idea is to use an approximation of the center manifold near the collinear points to generate an initial guess for a periodic orbit, then we will need to apply iteratively a differential correction a scheme, the detailed procedure will be discussed in the next Section. An approximation of the center space near L_i is given by the eigenvectors of the four purely imaginary eigenvalues of the matrix $\Lambda(L_i)$ [30]. Then an initial guess for the initial conditions of a periodic orbit near L_i is given by:

$$\boldsymbol{x}_0 = \boldsymbol{x}_{L_i} + \sum_{j=1}^{4} w_j \boldsymbol{v}_j \tag{2.124}$$

where $\boldsymbol{v}_j \in \mathbb{R}^6$, $j = 1, 2, 3, 4$ are the eigenvectors associated to the four purely imaginary eigenvalues of $\Lambda(L_i)$, i.e., and $w_j \in \mathbb{C}$ are coefficients such that $w_2 = \overline{w}_1$, $w_4 = \overline{w}_3$. Then if we choose $\boldsymbol{w} = (w_1, w_2, w_3, w_4)$ such that $\|\boldsymbol{w}\|$ is small enough, a periodic orbit can be generated via a differential correction scheme. In particular the initial guess obtained for $\boldsymbol{w} = k(1, 1, 0, 0)$ with small k, e.g., $k = 10^{-2}$ can be used to obtain a small amplitude, planar periodic orbit homeomorphic to the $1-$sphere $\mathcal{S}^1$, in the vicinity of the collinear point L_i, $i = 1, 2, 3$. We call this an L_i Lyapunov orbit. Moreover each L_i Lyapunov orbit will be unique for a given value of the Jacobi constant $\mathcal{C}$.

Chapter 3

Periodic orbits

A periodic orbit is a special type of solution for a dynamical system, that has the property of repeating itself after a given time T, known as the period of the orbit. The existence of periodic motion in the CR3BP is well-known, and the following sections will mainly deal with the computation of periodic orbits and studying the dynamical behavior in the vicinity of these solutions. As we have seen, the CR3BP admits exactly five equilibrium points, and it holds in general for autonomous Hamiltonian systems that the elementary equilibrium points $\boldsymbol{x}_{\text{eq}}$, i.e., those for which $\Lambda(\boldsymbol{x}_{\text{eq}})$ is non singular, are isolated. In this chapter we will see that this is not at all true for non constant periodic orbits, which come in families of solutions parametrized by the Hamiltonian integral or equivalently, in our case, by the Jacobi constant. Later in the chapter we will deal with families of periodic orbits that can be found in the vicinity of the collinear equilibrium points and the Moon, offering valuable insight on the dynamical behavior in these regions.

Let φ be the flow of (2.46), as defined in (2.47). Then a generic periodic orbit $\boldsymbol{\gamma}$ in the CR3BP with initial conditions $\boldsymbol{x}_0$ and period T, can be represented as

$$\boldsymbol{\gamma} = \{\varphi(\boldsymbol{x}_0, t) | t \in \mathbb{R}\}, \quad \varphi(\boldsymbol{x}_0, T) = \boldsymbol{x}_0. \tag{3.1}$$

Then any point on $\boldsymbol{\gamma}$ can be computed as $\boldsymbol{x}(t_i) = \varphi(\boldsymbol{x}_0, t_i)$, for some $t_i \in [0, T]$.

3.1 Poincaré maps

In the realm of dynamical systems, a pivotal concept named after the eminent mathematician Henri Poincaré, is the first recurrence map, also known as the Poincaré map. This map is essentially the intersection of the flow in phase space of a continuous dynamical system with a given lower-dimensional subspace, known as the Poincaré section, which is transversal to the system's flow. The construction of a Poincaré map eliminates at least one variable in the problem, thus leading to the analysis of a lower-dimensional system. In these lower-dimensional problems, numerically computed Poincaré maps provide an illuminating view of the system's global dynamics. They highlight the existence of periodic, quasi-periodic, and chaotic behaviors, making Poincaré maps a powerful tool in the analysis of dynamical systems.

More precisely, consider the flow $\varphi(\boldsymbol{x}(t_i), t)$ associated to some dynamical state $\boldsymbol{x}(t_i)$, and assume that the Poincaré section is simply a generic plane in physical space:

$$\pi : \; ax + by + cz = d, \quad (a, b, c) \in \mathbb{R}^3 \setminus \{0\}, \; d \in \mathbb{R}. \tag{3.2}$$

We want to emphasize that π could be an higher dimensional manifold in phase space with and need not be defined in physical space. Then for our purposes, we can define the Poincaré map associated to the flow $\varphi(\boldsymbol{x}(t_i), t)$ as:

$$\Gamma_\pi(\boldsymbol{x}(t_i)) = \{\varphi(\boldsymbol{x}(t_i), t) : (x(t), y(t), z(t)) \in \pi,\ t \in \mathbb{R}\}, \tag{3.3}$$

that is the set of points in phase space that belongs to the flow of $\boldsymbol{x}(t_i)$ at some time t, such that their projection in physical space lies on the plane π. Note that we have already used the concept of Poincaré sections, without explicitly mentioning it, in Section 3.3 when dealing with the technique of differential corrections.

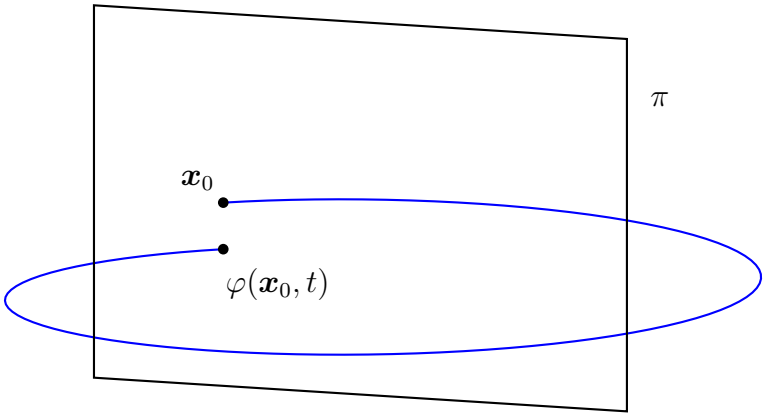

Figure 3.1: Visualization of the Poincaré map.

3.1.1 Computation of the crossing time

In the following we will need to compute the time of the first crossing with a given Poincaré plane, which will be denoted by t_f. In order compute t_f and dynamical state $\boldsymbol{x}(t_f)$ at the crossing with the xz or xy plane, the equations of motion are integrated using a fixed time step fourth-order Runge-Kutta method until $y(t)$ or $z(t)$, respectively, changes sign, then the time step is reduced and the integration is restarted from the last known dynamical state before the crossing. This procedure is iterated until we find $y(t_f) < \varepsilon$ or $z(t_f) < \varepsilon$ respectively, e.g., $\varepsilon = 10^{-11}$. More in general we can compute the time at which the a given trajectory crosses a generic plane π in physical space defined as in (3.2). To do this we simply have to check for a change in sign of the quantity $f_\pi = ax + by + cz - d$, and decrease the time step iteratively as before.

3.2 The Mirror Theorem

In this section we present the Mirror Theorem [44]. This fundamental result provide us with sufficient conditions that guarantees the periodicity of a given trajectory and lays the basis for the symmetry-based differential correction schemes that will be presented in Section 3.3. The Mirror Theorem for the general $N-$Body Problem can be stated as follows:

Theorem 4 (Mirror Theorem)**.** *Given N point masses, subject only to mutual gravitational forces, i.e., they obey (2.1), if at a certain time, each radius vector from the center of mass of the system is perpendicular to every velocity vector, then the orbit of each mass*

after that point is a mirror image of its orbit prior to that point, and we call this a mirror configuration. There are two possible mirror configurations:

- *All the point masses lie in a plane, with all velocity vectors at right angles to the plane and therefore parallel to each other,*
- *All the point masses lie on a straight line, with all velocity vectors at right angles to that line, but not necessarily parallel to each other.*

A rigorous proof of this theorem, can be found in [44]. As a corollary we have that if at two separate points in time, a mirror configuration occurs, then the orbits of the N point masses are periodic. The proof of the periodicity corollary is straightforward [43], indeed if two mirror configurations $\boldsymbol{x}_A$ and $\boldsymbol{x}_B$ occur at $t = -t_f$ and $t = 0$, then $\boldsymbol{x}_A$ occurs again at $t = t_f$, $\boldsymbol{x}_B$ at $t = 2t_f$ and so on. Hence the orbits are periodic, with period $T = 2t_f$.

3.3 Differential corrections

To obtain highly accurate initial conditions and compute periodic orbits in the CR3BP, a differential correction scheme becomes necessary. This iterative method adjusts the initial conditions of an orbit until a mirror configuration is achieved, thereby ensuring the orbit's periodicity according to the Mirror Theorem (Theorem 4). Note that for successful convergence, the algorithm necessitates an initial guess that is nearly periodic.

In this chapter we will illustrate various types of differential correction schemes. These will be employed to generate periodic orbits exhibiting symmetry with respect to the xz plane (for instance, Lyapunov and Halo orbit families), symmetry with respect to the x axis (such as the Axial orbit families), or symmetry relative to both the xz and xy planes (like the Vertical orbit families).

3.3.1 The state transition matrix $\Phi(t, t_0)$

Before proceeding we need to introduce the concept of state transition matrix, denoted as $\Phi(t, t_0)$. This matrix is defined as the partial derivative of the flow $\varphi(\boldsymbol{x}_0, t)$ with respect to the initial state vector $\boldsymbol{x}_0$, expressed as follows:

$$\Phi(t, t_0) = \frac{\partial \varphi(\boldsymbol{x}_0, t)}{\partial \boldsymbol{x}_0}, \tag{3.4}$$

In practice $\Phi(t, t_0)$ can be computed integrating the system of differential equations:

$$\frac{d\Phi(t, t_0)}{dt} = \Lambda(\boldsymbol{x})\Phi(t, t_0), \quad \Phi(t_0, t_0) = I_{6\times 6}. \tag{3.5}$$

where $\Lambda(\boldsymbol{x})$ is defined as in equation (2.93). It's noteworthy to point out that equations (2.46) and (3.5) together constitute a system of 42 first-order ODEs. These can be integrated numerically, e.g., using an high order method of the Runge-Kutta family, to finally obtain the state transition matrix $\Phi(t, t_0)$.

3.3.2 Symmetry with respect to the xz plane

Suppose that the initial state is perpendicular xz plane:

$$\boldsymbol{x}_0 = (x_0, 0, z_0, 0, \dot{y}_0, 0)^T. \tag{3.6}$$

Then the Mirror Theorem guarantees that if another perpendicular crossing occurs at time $t_f = T/2$, i.e.,

$$\boldsymbol{x}(T/2) = (x, 0, z, 0, \dot{y}, 0)^T, \tag{3.7}$$

the orbit will be periodic with period T. In general we must expect that at the time of the second crossing t_f, the dynamical state will not be orthogonal to the xz plane due to small but non zero components of the velocity along the plane i.e.,

$$\boldsymbol{x}(t_f) = \boldsymbol{x}_f = (x_f, 0, z_f, \dot{x}_f, \dot{y}_f, \dot{z}_f)^T. \tag{3.8}$$

Then the idea is to find the corrections $\delta\boldsymbol{x}_0$ that we need to impose to the initial dynamical state $\boldsymbol{x}_0$, for a perpendicular crossings to occur. Let $\boldsymbol{x}_f^s = (x_f^s, 0, z_f^s, 0, \dot{y}_f^s, 0)^T$ be a mirror state and define the deviation $\delta\boldsymbol{x}_f = \boldsymbol{x}_f - \boldsymbol{x}_f^s$. Then we can express $\delta\boldsymbol{x}_f$ as:

$$\delta\boldsymbol{x}_f = \Phi(t_f, t_0)\delta\boldsymbol{x}_0 + \dot{\boldsymbol{x}}(t_f; \boldsymbol{x}_0)\delta t_f. \tag{3.9}$$

Clearly the desired changes are $\delta\dot{x}_f = -\dot{x}_f$ and $\delta\dot{z}_f = -\dot{z}_f$. Now we show two strategies proposed in [19], that can be used to compute the desired changes in the initial conditions $\delta\boldsymbol{x}_0$. Imposing that $\delta y_f = 0$, if we fix x_0 then from equation (3.9), we obtain:

$$\begin{pmatrix} \delta\dot{x}_f \\ \delta\dot{z}_f \end{pmatrix} = \left[\begin{pmatrix} \Phi_{43} & \Phi_{45} \\ \Phi_{63} & \Phi_{65} \end{pmatrix} - \frac{1}{\dot{y}_f} \begin{pmatrix} \ddot{x}_f \\ \ddot{z}_f \end{pmatrix} \begin{pmatrix} \Phi_{23} & \Phi_{25} \end{pmatrix} \right] \begin{pmatrix} \delta z_0 \\ \delta\dot{y}_0 \end{pmatrix}. \tag{3.10}$$

Alternatively we can fix z_0 and let x_0 and $\dot{y}_0$ vary, in which case we obtain:

$$\begin{pmatrix} \delta\dot{x}_f \\ \delta\dot{z}_f \end{pmatrix} = \left[\begin{pmatrix} \Phi_{41} & \Phi_{45} \\ \Phi_{61} & \Phi_{65} \end{pmatrix} - \frac{1}{\dot{y}_f} \begin{pmatrix} \ddot{x}_f \\ \ddot{z}_f \end{pmatrix} \begin{pmatrix} \Phi_{21} & \Phi_{25} \end{pmatrix} \right] \begin{pmatrix} \delta x_0 \\ \delta\dot{y}_0 \end{pmatrix}. \tag{3.11}$$

These procedure usually requires less than five iterations to obtain the dynamical state that leads to a periodic orbit up to ten significant digits [4]. Once the convergence has been achieved to obtain the desired periodic orbit the equations of motion are integrated starting from $\boldsymbol{x}_0$ the over the period $T = 2t_f$.

3.3.3 Symmetry with respect to the x axis

Suppose that at the initial dynamical state the massless body is lying on the x axis with velocity orthogonal to it, i.e.,

$$\boldsymbol{x}_0 = (x_0, 0, 0, 0, \dot{y}_0, \dot{z}_0)^T. \tag{3.12}$$

We can choose to fix either the $\dot{y}_0$ or $\dot{z}_0$ component of the initial velocity. If we fix $\dot{y}_0$ then from equation (3.9), we obtain:

$$\begin{pmatrix} \delta y_f \\ \delta z_f \\ \delta\dot{x}_f \end{pmatrix} = \begin{pmatrix} \Phi_{21} & \Phi_{26} & \dot{y}_f \\ \Phi_{31} & \Phi_{36} & \dot{z}_f \\ \Phi_{41} & \Phi_{46} & \ddot{x}_f \end{pmatrix} \begin{pmatrix} \delta x_0 \\ \delta\dot{z}_0 \\ \delta t_f \end{pmatrix}. \tag{3.13}$$

Alternatively if $\dot{z}_0$ is fixed, then from (3.9), we obtain:

$$\begin{pmatrix} \delta y_f \\ \delta z_f \\ \delta \dot{x}_f \end{pmatrix} = \begin{pmatrix} \Phi_{21} & \Phi_{25} & \dot{y}_f \\ \Phi_{31} & \Phi_{35} & \dot{z}_f \\ \Phi_{41} & \Phi_{45} & \ddot{x}_f \end{pmatrix} \begin{pmatrix} \delta x_0 \\ \delta \dot{y}_0 \\ \delta t_f \end{pmatrix}. \tag{3.14}$$

In this case the time t_f can be chosen to be either the time of the crossing with the xz plane as before, in which case $y(t_f) = 0$, or as the crossing with the xy plane, so that $z(t_f) = 0$. In this way two types of mappings are obtained, by imposing in equations (3.13) and (3.14), either $\delta y_f = 0$ or $\delta z_f = 0$ respectively. The other required changes are $\delta z_f = -z_f$ or $\delta y_f = -y_f$, respectively, depending on the mapping chosen, and $\delta \dot{x}_f = -\dot{x}_f$. Finally the complete orbit is obtained integrating the equations of motion over a period $T = 2t_f$ starting from $\boldsymbol{x}_0$.

3.3.4 Symmetry with respect to xz and xy planes

The orbits belonging to the L_1, L_2 and L_3 Vertical families are symmetric with respect to both the xz and xy plane. We present here a procedure to exploit this double symmetry. Suppose we have an initial dynamical state $\boldsymbol{x}_0$ defined as in 3.12, and let t_f be the time of the first crossing with the xz plane. If we let x_0 and $\dot{z}_0$ vary, using equation (3.9) we can write [14]:

$$\begin{pmatrix} 0 \\ \delta \dot{x}_f \\ \delta \dot{z}_f \end{pmatrix} = \begin{pmatrix} \Phi_{21} & \Phi_{26} & \dot{y}_f \\ \Phi_{41} & \Phi_{46} & \dot{z}_f \\ \Phi_{61} & \Phi_{66} & \ddot{x}_f \end{pmatrix} \begin{pmatrix} \delta x_0 \\ \delta \dot{z}_0 \\ \delta t_f \end{pmatrix}. \tag{3.15}$$

Then we impose $\delta \dot{x}_f = -\dot{x}_f$ and $\delta \dot{z}_f = -\dot{z}_f$. Once convergence has been obtained, the complete periodic orbit can be obtained by integrating the equations of motion over the period $T = 4t_f$ starting from dynamical state $\boldsymbol{x}_0$.

3.4 Families of periodic orbits

Our search of periodic orbits is justified by the Cylinder Theorem [31]. This theorem is a general result for Hamiltonian system, that guarantees that if a periodic orbit is elementary, i.e., its monodromy matrix has exactly two unit eigenvalues, the trivial ones, then a cylinder of periodic orbits exists that are parametrized by the Hamiltonian integral. Recalling as we have seen in Section 2.3.1, that in the CR3BP the Hamiltonian is equal to the Jacobi constant up to a constant factor, we can state the theorem as follows.

Theorem 5 (Cylinder Theorem)**.** *Let $\boldsymbol{\gamma}$ be periodic orbit such that its monodromy matrix $\Phi(T, t_0)$, has exactly two unity eigenvalues, then there exist a unique cylinder of periodic orbits passing through $\boldsymbol{\gamma}$, that are parametrized by the Jacobi constant $\mathcal{C}$.*

The proof of this result uses the Poincaré map of the periodic orbit. If the orbit is elementary then applying the implicit function theorem gives a one parameter branch of fixed points for the map, that vary with energy (see [31] for the details). Moreover the hypotheses of the theorem on the monodromy matrix are true in the generic case and the periodic orbits are isolated at any fixed value of the Jacobi constant [46].

3.5 Invariant manifolds of periodic orbits

In Section 2.7 we introduced the concept of invariant manifolds of an equilibrium point. Here we want to extend this definition to a non constant periodic orbit. Like their analogues for equilibrium points, the stable manifolds of a periodic orbit constitute paths where a probe will asymptotically approach the given orbit without the need for additional energy. On the other hand, unstable manifolds consist of trajectories where the probe will asymptotically diverge from the orbit, also without the need for external energy. This feature of invariant manifolds offers a significant advantage, as it can be utilized to engineer low-energy orbital transfers. However the extension of the concept to a periodic orbit comes with some additional difficulties, as the linearized variational equation (2.92) now leads to a non constant Jacobian matrix Λ. In order to reduce the dimensionality of the problem Poincaré maps can be used. The Poincaré map retains most properties of the original system's periodic and quasi-periodic trajectories, making it an effective tool for stability analysis of these orbits. The stability of a periodic orbit in the original system is closely associated with the fixed point's stability of the corresponding Poincaré map, providing insights into stability and invariant manifold representations. Therefore, a general background concerning the phase space near periodic orbits in the CR3BP is key and a necessary component for the understanding of resonant orbits and their associated manifolds. In addition to this basic theoretical background in invariant manifold theory, a method for the numerical computation of the unstable and stable manifolds is also detailed. The following theorem, which we present as in [38], provides the conditions under which the stable and unstable manifolds of a periodic orbit exists.

Theorem 6 (Stable Manifold Theorem for Periodic Orbits)**.** *Let A be an open subset of $\mathbb{R}^n$ that contains a periodic orbit $\boldsymbol{\gamma}$ of period T and denote the flow as usual by $\varphi(\boldsymbol{x}, t)$. If k characteristic exponents of $\boldsymbol{\gamma}$ have a negative real part where $0 \leq K \leq n-1$ and $n-K-1$ of them have a positive real part, then there exists a neighborhood $N(\boldsymbol{\gamma}) \in A$ such that the local stable manifold of $\boldsymbol{\gamma}$,*

$$W^s_{\text{loc}}(\boldsymbol{\gamma}) = \{\boldsymbol{x} \in N \mid d(\varphi(\boldsymbol{x}, t), \boldsymbol{\gamma}) \to 0 \text{ as } t \to \infty, \quad \varphi(\boldsymbol{x}, t) \in N, \ \forall t \geq 0\}, \tag{3.16}$$

a $(K+1)$-dimensional, differentiable manifold which is positively invariant under the flow $\varphi(\boldsymbol{x}, t)$, and the unstable manifold of $\boldsymbol{\gamma}$,

$$W^u_{\text{loc}}(\boldsymbol{\gamma}) = \{\boldsymbol{x} \in N \mid d(\varphi(\boldsymbol{x}, t), \boldsymbol{\gamma}) \to 0 \text{ as } t \to -\infty, \quad \varphi(\boldsymbol{x}, t) \in N, \ \forall t \leq 0\}, \tag{3.17}$$

is an $(n-K)$-dimensional, differentiable manifold which is negatively invariant under the flow $\varphi(\boldsymbol{x}, t)$. Furthermore, the stable and unstable manifolds of $\boldsymbol{\gamma}$ intersect transversally in $\boldsymbol{\gamma}$.

For the existence of stable and unstable manifolds of a periodic orbit, the monodromy matrix must possess at least one stable and one unstable eigenvalue. However, not all the members in a given family of periodic orbits in the CR3BP possess a stable and unstable eigenvalue. Therefore, it is beneficial to devise a method to identify which members in the family do possess stable and unstable eigenvalues, and thus, stable and unstable manifolds.

3.5.1 Stability of periodic orbits

Here we deal with assessing the stability of a non constant periodic orbit. Unlike what we have done for the Lagrangian points, the stability of a periodic orbit can be assessed

by investigating the eigenvalues of the corresponding monodromy matrix, i.e., the state transition matrix computed after one full period of the orbit, $\Phi(T, t_0)$. It is worth noting that the values eigenvalues remain the same regardless of the point of the orbit at which the monodromy matrix is computed, allowing us to introduce a well defined set of stability indices associated to the periodic orbit. In the following sections we will study the behavior of the eigenvalues of the monodromy matrix along different families of periodic orbits. As we will see this will give us insights not only on the stability properties of the orbits but on the presence of bifurcations along the families as well.

It can be shown that $\Phi(T, t_0)$ is a symplectic matrix [46], that is:

$$\Phi^T \begin{pmatrix} 0 & I \\ -I & 0 \end{pmatrix} \Phi = \begin{pmatrix} 0 & I \\ -I & 0 \end{pmatrix}. \tag{3.18}$$

Moreover it holds that the determinant of a symplectic matrix is always equal to unity.As we will see, the monodromy matrix has always two eigenvalues that are equal to unity due to the periodicity, and as a consequence of the symplectic property [46, 31], the other four are found in reciprocal pairs. This last property is stated in Lyapunov's Theorem [53].

Theorem 7 (Lyapunov's Theorem)**.** *If λ_j is an eigenvalue of the monodromy matrix $\Phi(T, t_0)$, of a $t-$invariant system, then λ_j^{-1} is also an eigenvalue of $\Phi(T, t_0)$, with the same structure of elementary divisors.*

Moreover it can be shown that $\lambda = 1$ is always a characteristic multiplier of a periodic orbit, in particular we have the following result [31].

Proposition 1. *Let $\boldsymbol{\gamma}$ be a periodic orbit of period T and let $\boldsymbol{x} \in \boldsymbol{\gamma}$, so that $\varphi(\boldsymbol{x}_0, T) = \boldsymbol{x}_0$. Then $\lambda = 1$ is always an eigenvalue of its monodromy matrix $\Phi(T, t_0)$. In particular $g(\boldsymbol{x})$ is an eigenvector of the monodromy matrix corresponding to the eigenvalue $\lambda = 1$.*

Proof. From the definition of flow it holds $\varphi(\varphi(\boldsymbol{x}, t), \tau) = \varphi(\boldsymbol{x}, t+\tau)$. Then differentiating both sides of this equation with respect to $\boldsymbol{x}$ and setting $\tau = T$ and $t = t_0$, we obtain

$$\frac{\partial \varphi(\boldsymbol{x}, T)}{\partial \boldsymbol{x}} \dot{\varphi}(t_0, \boldsymbol{x}) = \dot{\varphi}(T, \boldsymbol{x}), \tag{3.19}$$

which can be rewritten as

$$\Phi(T, t_0) g(\boldsymbol{x}) = g(\boldsymbol{x}). \tag{3.20}$$

Since we are assuming $\boldsymbol{\gamma}$ is a non constant periodic orbit, it must be $g(\boldsymbol{x}) \neq 0$, hence the thesis. □

It follows from Proposition 1 and Lyyapunov's Theorem that the algebraic multiplicity of the eigenvalue $+1$ needs to be at least two in virtue, since both $\lambda = \lambda^{-1} = 1$. In the following we will refer to the two unit characteristic multipliers of a periodic orbit as its trivial eigenvalues. The trivial eigenvalues can be thought as representing one mode along the periodic orbit, and one mode along the family of periodic orbits. [15].

Then the eigenvalues of the monodromy matrix $\Phi(T, t_0)$ associated to a periodic orbit, often referred to as its characteristic multipliers, always have the following form:

$$\lambda_1,\ \lambda_3 = \lambda_1^{-1}, \quad \lambda_2,\ \lambda_4 = \lambda_2^{-1}, \quad \lambda_5 = \lambda_6 = 1. \tag{3.21}$$

Then the four non trivial eigenvalues allow to define two stability indices, plus a third trivial one, as the sum of each reciprocal pair:

$$\nu_1 = \frac{1}{2}(\lambda_1 + \frac{1}{\lambda_1}), \quad \nu_2 = \frac{1}{2}(\lambda_2 + \frac{1}{\lambda_2}), \quad \nu_3 = 1. \tag{3.22}$$

The the stability indices can be then used to assess the stability of the orbit. Clearly, since the stability index that corresponds to the two unity eigenvalues is always equal to unity, we can consider just the other two indices ν_1, ν_2. In particular the orbit is said to be linearly stable if both $|\nu_1| < 1$, $|\nu_2| < 1$, in which case we say the linear instability of the orbit is order zero. Otherwise, if either $|\nu_i| > 1$, $i = 1, 2$, we say that the orbit is unstable [3, 2], in which case stable and unstable invariant manifolds will exist. Furthermore we say that the linear instability of the orbit is either order one or two, if just one or both the non trivial stability indices are greater than one, respectively [28]. When dealing with planar orbits, one of the stability indices measures the in-plane stability, whereas the other, can be thought as a measure of the out-of-plane stability of the periodic orbit [21, 26, 40].

For families of orbits that are symmetric with respect to the xz plane such as the Lyapunov, DRO and Halo families, in the interest of numerical accuracy, we can proceed as in [3] to compute the monodromy matrix $\Phi(T, t_0)$, using $\Phi(t_f, t_0)$, i.e., the state transition matrix at half a period, therefore without the need to integrate past $t = t_f$. If we define $\tilde{\Phi}(t, t_0)$ as:

$$\tilde{\Phi}(t, t_0) = \begin{pmatrix} I & 0 \\ -\Omega & I \end{pmatrix} \Phi(t, t_0) \begin{pmatrix} I & 0 \\ \Omega & I \end{pmatrix}, \tag{3.23}$$

then $\tilde{\Phi}(t, t_0)$ is a symplectic matrix [20]. Using the symplectic property of $\tilde{\Phi}$ and the invariance under transformations (2.55), it can be shown [3] that:

$$\Phi(t_0, -t_f) = B\Phi(t_0, t_f)B = B \begin{pmatrix} 0 & I \\ -I & 2\Omega \end{pmatrix} \Phi^T(t_f, t_0) \begin{pmatrix} 2\Omega & I \\ -I & 0 \end{pmatrix} B \tag{3.24}$$

where we B is a diagonal 6×6 matrix, with main diagonal elements $B_{jj} = (-1)^{j+1}$. Finally we can write:

$$\Phi(T, t_0) = \Phi(2t_f, t_0) = \Phi(2t_f, t_f)\Phi(t_f, t_0) = \Phi(t_0, -t_f)\Phi(t_f, t_0) \tag{3.25}$$

3.5.2 Numerical computation of the invariant manifolds

More specifically, let $\boldsymbol{\gamma}$ be a generic periodic orbit in the CR3BP, defined as in (3.1). If $\boldsymbol{\gamma}$ is linearly stable, i.e., all its stability indices are less or equal to unity, then $\boldsymbol{\gamma}$ possesses neither stable nor unstable manifolds. For simplicity we now suppose that $\boldsymbol{\gamma}$ has instability of order one, so that its monodromy matrix $\Phi(T, t_i)$ of $\boldsymbol{\gamma}$ admits four real eigenvalues and a complex conjugate pair, i.e., it has a pair non-trivial real eigenvalues, which we denote by

$$\lambda_s < 1, \qquad \lambda_s^{-1} = \lambda_u > 1, \tag{3.26}$$

identify the stable and unstable unit eigenvectors, which we denote by $\boldsymbol{v}_s(t_i)$, $\boldsymbol{v}_u(t_i)$ respectively. These eigenvectors locally span the two-dimensional stable and unstable invariant manifolds of $\boldsymbol{\gamma}$, $W^s(\boldsymbol{\gamma})$ and $W^u(\boldsymbol{\gamma})$. It is worth noting that the hypothesis above

is satisfied by most, although not all, the orbits in the L_1 and L_2 Lyapunov and Halo families. In general the stable and unstable manifolds $W^s(\boldsymbol{\gamma})$ and $W^u(\boldsymbol{\gamma})$, associated with the periodic orbit $\boldsymbol{\gamma}$, are of dimension $n_s + 1$ and $n_u + 1$, respectively, where we denoted by n_s and n_u the dimension of the stable and unstable spaces E^s, E^u associated to the periodic orbit $\boldsymbol{\gamma}$ [52].

We now describe the numerical procedure to compute the stable and unstable manifolds. Let $\boldsymbol{x}(t_i)$ be the dynamical state of a generic point on $\boldsymbol{\gamma}$, and consider a perturbation of this initial state in the direction of $\boldsymbol{v}_s$ and $\boldsymbol{v}_u$, by a small displacement $\varepsilon > 0$:

$$\boldsymbol{x}_u(t_i) = \boldsymbol{x}(t_i) \pm \varepsilon \boldsymbol{v}_u(t_i), \tag{3.27}$$

$$\boldsymbol{x}_s(t_i) = \boldsymbol{x}(t_i) \pm \varepsilon \boldsymbol{v}_s(t_i). \tag{3.28}$$

where $\pm$ determines which of the two branches of the stable or unstable manifold is computed, while the value of ϵ should be small enough, for the linear approximation to remain valid, and it can be chosen as $\varepsilon \approx 10^{-6}$, following the discussion in [51, 12]. Then propagating (3.28) backward in time, and (3.27) forward in time, and letting vary $t_i \in [0, T]$ the manifolds $W^s(\boldsymbol{\gamma})$ and $W^u(\boldsymbol{\gamma})$ are obtained. Then recalling the definition of flow given (2.47), we can write

$$W^u(\boldsymbol{\gamma}) = \bigcup_{t_i \in [0,T]} \varphi\big(\boldsymbol{x}(t_i) \pm \varepsilon \boldsymbol{v}_u(t_i), t \geq 0\big), \tag{3.29}$$

$$W^s(\boldsymbol{\gamma}) = \bigcup_{t_i \in [0,T]} \varphi\big(\boldsymbol{x}(t_i) \pm \varepsilon \boldsymbol{v}_s(t_i), t \leq 0\big). \tag{3.30}$$

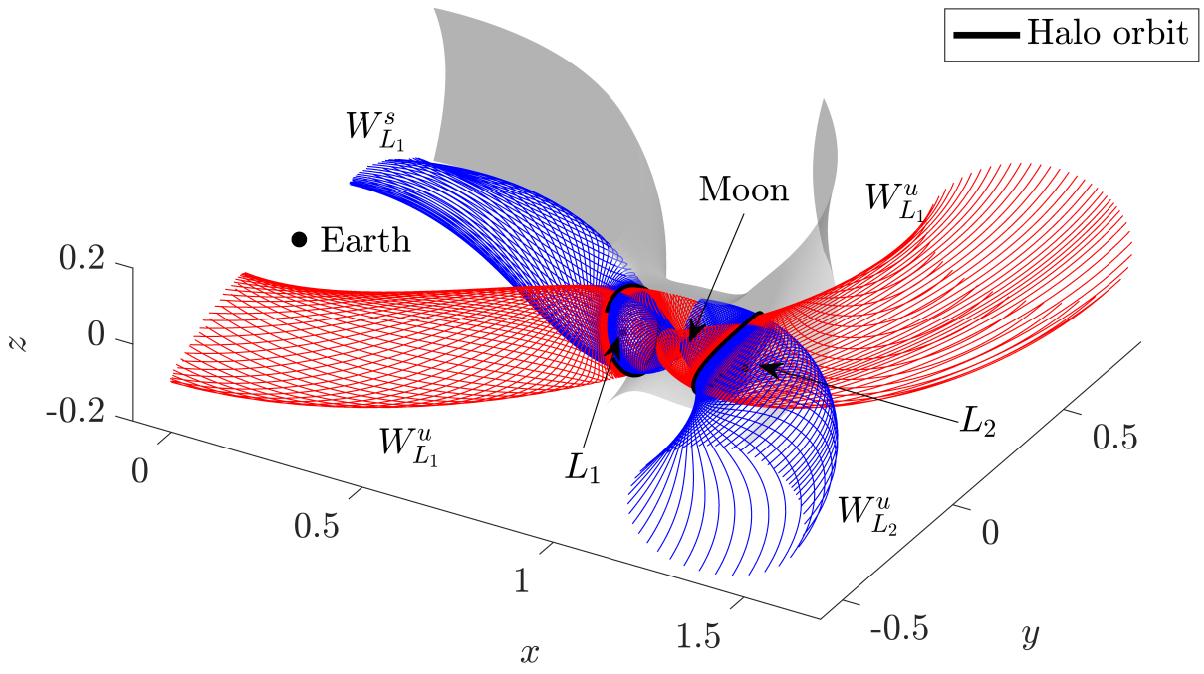

Figure 3.2: Invariant manifolds of an L_1 and L_2 northern Halo orbits at $\mathcal{C} = 3.1$, in the Earth-Moon system. A section of the the zero-velocity surface $\mathcal{S}(\mathcal{C}; \mu)$ is show in gray.

3.6 The Broucke diagram

An alternative method to identify bifurcations was introduced by Roger Broucke in [4], this based on changes in the eigenstructure of the monodromy matrix. In this technique, the four non-trivial eigenvalues of the monodromy matrix for each family member are recast in terms of only two parameters α and β. The following arguments follow closely the derivation found in [15].

3.6.1 The characteristic equation

Consider the characteristic equation for the monodromy matrix $\Phi(T, t_0)$, this reads:

$$\det(\Phi - \lambda I) = 0. \tag{3.31}$$

The roots of the characteristic equation are the eigenvalues of $\Phi(T, t_0)$. Since the eigenvalues come in reciprocal pairs and two are equal to unity, then the characteristic equation must be of the form

$$(\lambda - 1)^2(\lambda - \lambda_1)(\lambda - \frac{1}{\lambda_1})(\lambda - \lambda_2)(\lambda - \frac{1}{\lambda_2}) = 0. \tag{3.32}$$

The last equation can be expanded in the form

$$(\lambda - 1)^2(\lambda^4 + \alpha\lambda^3 + \beta\lambda^2 + \alpha\lambda + 1) = 0. \tag{3.33}$$

with

$$\alpha = -(\lambda_1 + \frac{1}{\lambda_1} + \lambda_2 + \frac{1}{\lambda_2}) = -2(\nu_1 + \nu_2), \tag{3.34}$$

$$\beta = 2 + \lambda_1\lambda_2 + \frac{1}{\lambda_1\lambda_2} + \frac{\lambda_1}{\lambda_2} + \frac{\lambda_2}{\lambda_1} = 2 + 4\nu_1\nu_2. \tag{3.35}$$

We will now show that α and β can be computed directly from $\Phi(T, t_0)$, without the need of explicitly computing the eigenvalues. Thus reducing the numerical errors involved in the computation of the eigenvalues. Since $\Phi(T, t_0)$ is diagonalizable, we can write:

$$D = V^{-1}\Phi(T, t_0)V. \tag{3.36}$$

Therefore, $\Phi(T, t_0)$ and D are similar matrices and both matrices have the same trace, i.e.,

$$\mathrm{Tr}(\Phi(T, t_0)) = \mathrm{Tr}(D) = 2 + \lambda_1 + \frac{1}{\lambda_1} + \lambda_2 + \frac{1}{\lambda_2} \tag{3.37}$$

Similarly we have

$$D^2 = V^{-1}\Phi(T, t_0)VV^{-1}\Phi(T, t_0)V = V^{-1}(\Phi(T, t_0))^2V, \tag{3.38}$$

thus we can write

$$\mathrm{Tr}((\Phi(T, t_0))^2) = \mathrm{Tr}(D^2) = 2 + \lambda_1^2 + \frac{1}{\lambda_1}^2 + \lambda_2^2 + \frac{1}{\lambda_2}^2. \tag{3.39}$$

Therefore, using equation (3.38), the expressions for α and β can be given as

$$\alpha = 2 - \mathrm{Tr}(\Phi(T, t_0)), \tag{3.40}$$

$$\beta = \frac{1}{2}\left(\alpha^2 + 2 - \mathrm{Tr}((\Phi(T, t_0))^2)\right). \tag{3.41}$$

The relevance if the parameters α and β arise from the fact that they uniquely determine the non trivial eigenvalues of the monodromy matrix, and thus they contain all the information relative to the stability of the periodic orbit for which they are computed. We will now show this fact.

Eliminating ν_2 in equations (3.34 – 3.35), yields

$$4\nu_1^2 + 2\alpha\nu_1 + (\beta - 2) = 0. \tag{3.42}$$

Then, by the quadratic formula we obtain

$$\nu_1 = \frac{-\alpha \pm \sqrt{\Delta/4}}{4}, \quad \frac{\Delta}{4} = \alpha^2 - 4(\beta - 2). \tag{3.43}$$

At this point, without loss of generality, we can set $\nu_1 = \frac{-\alpha+\sqrt{\Delta/4}}{4}$, and from (3.34 – 3.35) it must be $\nu_2 = \frac{-\alpha-\sqrt{\Delta/4}}{4}$. Using the definition of the stability indices, we can write:

$$\lambda_1^2 - 2\nu_1\lambda_1 + 1 = 0, \tag{3.44}$$
$$\lambda_2^2 - 2\nu_2\lambda_2 + 1 = 0, \tag{3.45}$$
$$\tag{3.46}$$

Each of these admits exactly to solutions, i.e.,

$$\lambda_1 = \nu_1 \pm \sqrt{\nu_1^2 - 1}, \tag{3.47}$$
$$\lambda_2 = \nu_2 \pm \sqrt{\nu_2^2 - 1}. \tag{3.48}$$

Then we can assign either of the two to λ_1 and λ_2, then the discarded solution will correspond to the remaining non trivial eigenvalues, i.e., $\lambda_3 = \lambda_1^{-1}$, $\lambda_4 = \lambda_2^{-1}$. Moreover it is trivially $\lambda_5 = \lambda_6 = 1$. Thus all eigenvalues of the monodromy matrix are uniquely determined by α and β.

3.6.2 Stability regions

As noted by Broucke in [4], stability boundaries are found in the $\alpha\beta$ plane corresponding to $\Delta = 0$ in 3.43 and to either $\nu_1^2 - 1 = 0$ or $\nu_2^2 - 1 = 0$ in (3.47) and (3.48), respectively. In particular when $\Delta = 0$, we find

$$\beta = \frac{\alpha^2}{4} + 2. \tag{3.49}$$

In the $\alpha\beta$ plane, equation (3.49) corresponds to a parabola with vertex at $(\alpha, \beta) = (0, 2)$ (see Figure 3.4). On the other hand when it is either $\nu_1^2 - 1 = 0$ or $\nu_2^2 - 1 = 0$, we obtain

$$\left(-\alpha \pm \sqrt{\Delta/4}\right)^2 = 16. \tag{3.50}$$

After expanding the expression and rearranging, we finally obtain

$$\beta = \pm 2\alpha - 2. \tag{3.51}$$

In the $\alpha\beta$ plane, equation (3.51) corresponds to two lines with slopes $+2$ and -2, intersecting in the point $(\alpha, \beta) = (0, -2)$. Moreover the parabola defined by (3.49), is tangent to these lines at the points $(\alpha, \beta) = (\pm 4, 6)$. The parabola and lines determine seven distinct regions of stability, as shown in Figure 3.4. Additionally in each of these regions we find a different eigenstructure. This different structures will now described in detail [4, 15].

- **Region I: Local Stability.** For this region the nontrivial eigenvalues are all complex and lie on the unit circle. In particular it is

$$\mathrm{Im}(\lambda_1) < 0, \quad \mathrm{Im}(\lambda_2) < 0, \quad \lambda_3 = \lambda_1^{-1} = \bar{\lambda}_1, \quad \lambda_4 = \lambda_2^{-1} = \bar{\lambda}_2. \tag{3.52}$$

  Where the $\bar{\lambda}$ denotes the complex conjugate of λ. The asterisk indicates complex-conjugate. As a consequence the stability indices satisfy

$$-1 < \nu_1 < 1, \quad -1 < \nu_2 < 1, \tag{3.53}$$

  and we have stability. Since two different modes are complex and on the unit-circle, the periodic orbit is surrounded by two different of invariant tori [15].

- **Region II: Complex Instability.** For this region The nontrivial eigenvalues are all complex, but in this case do not lie on the unit circle. In particular it is:

$$\mathrm{Im}(\lambda_1) > 0, \quad |\nu_1| < 1, \quad \lambda_2 = \bar{\lambda}_1, \quad \lambda_3 = \lambda_1^{-1} = \bar{\lambda}_2^{-1}, \quad \lambda_4 = \lambda_2^{-1} = \bar{\lambda}_1^{-1}. \tag{3.54}$$

  As a consequence ν_1 and ν_2 are complex and it holds $\nu_2 = \bar{\nu}_1$.

- **Region III: Even-Odd Instability.** For this region the nontrivial eigenvalues are all real and they satisfy

$$\lambda_1 < -1, \quad 0 < \lambda_2 < 1, \quad -1 < \lambda_3 = \lambda_1^{-1} < 0, \quad \lambda_4 = \lambda_2^{-1} > 1. \tag{3.55}$$

  Consequently also ν_1 and ν_2 are real, and it is:

$$\nu_1 < -1, \quad \nu_2 > 1. \tag{3.56}$$

  The four modes correspond to invariant stable and unstable manifolds. Moreover, the negative real modes correspond to manifolds that locally have double the period of the associated periodic orbit [15].

- **Region IV: Even-Even Instability.** This region is bounded by the parabola $\beta = \alpha^2/4 + 2$ and the line $\beta = -2\alpha - 2$. The nontrivial eigenvalues are all real and satisfy

$$0 < \lambda_1 < 1, \quad 0 < \lambda_2 < 1, \quad \lambda_3 = \lambda_1^{-1} > 1, \quad \lambda_4 = \lambda_2^{-1} > 1. \tag{3.57}$$

  As a consequence ν_1 and ν_2 are real, and it is:

$$\nu_1 > 1, \quad \nu_2 > 1. \tag{3.58}$$

  The periodic orbit possesses two unstable and two stable invariant manifolds. The eigenvalue with the largest magnitude correspond to the unstable manifolds that is quickest in leaving the vicinity of the periodic orbit, while its reciprocal corresponds to the stable manifold that is the quickest in asymptotically approaching the periodic orbit.

- **Region V: Odd-Odd Instability.**

  This region is bounded by the parabola $\beta = \alpha^2/4 + 2$ and the line $\beta = 2\alpha - 2$. The nontrivial eigenvalues are all real and satisfy

  $$\lambda_1 < -1, \quad \lambda_2 < -1, \quad -1 < \lambda_3 = \lambda_1^{-1} < 0, \quad -1 < \lambda_4 = \lambda_2^{-1} < 0. \tag{3.59}$$

  As a consequence ν_1 and ν_2 are real, and it is:

  $$\nu_1 < -1, \quad \nu_2 < -1. \tag{3.60}$$

  The periodic orbit possesses two unstable and two stable invariant manifolds, that locally have double the period of the associated periodic orbit.

- **Region VI: Even Semi-Instability.** For this region the eigenvalue λ_2 is complex and lies on the unit-circle while λ_1 is real. Then the nontrivial eigenvalues satisfy

  $$\mathrm{Im}(\lambda_1) < 0, \quad 0 < \lambda_2 < 1, \quad \lambda_3 = \lambda_1^{-1} = \bar{\lambda}_1, \quad \lambda_4 = \lambda_2^{-1} > 1. \tag{3.61}$$

  Then ν_1 and ν_2 are real, and it is:

  $$-1 < \nu_1 < 1, \quad \nu_2 > 1. \tag{3.62}$$

  The the real positive modes corresponds to invariant stable and unstable manifolds, while the complex one signals the presence of an invariant tori in the vicinity of the periodic orbit.

- **Region VII: Odd Semi-Instability.** For this region the eigenvalue λ_2 is complex and lies on the unit-circle while λ_1 is real. Then the nontrivial eigenvalues satisfy

  $$\mathrm{Im}(\lambda_1) < 0, \quad 0 < \lambda_2 < 1, \quad \lambda_3 = \lambda_1^{-1} = \bar{\lambda}_1, \quad \lambda_4 = \lambda_2^{-1} > 1. \tag{3.63}$$

  Then ν_1 and ν_2 are real, and it is:

  $$-1 < \nu_1 < 1, \quad \nu_2 < -1. \tag{3.64}$$

  The the real positive modes corresponds to invariant stable and unstable manifolds, while the complex one signals the presence of an invariant tori in the vicinity of the periodic orbit.

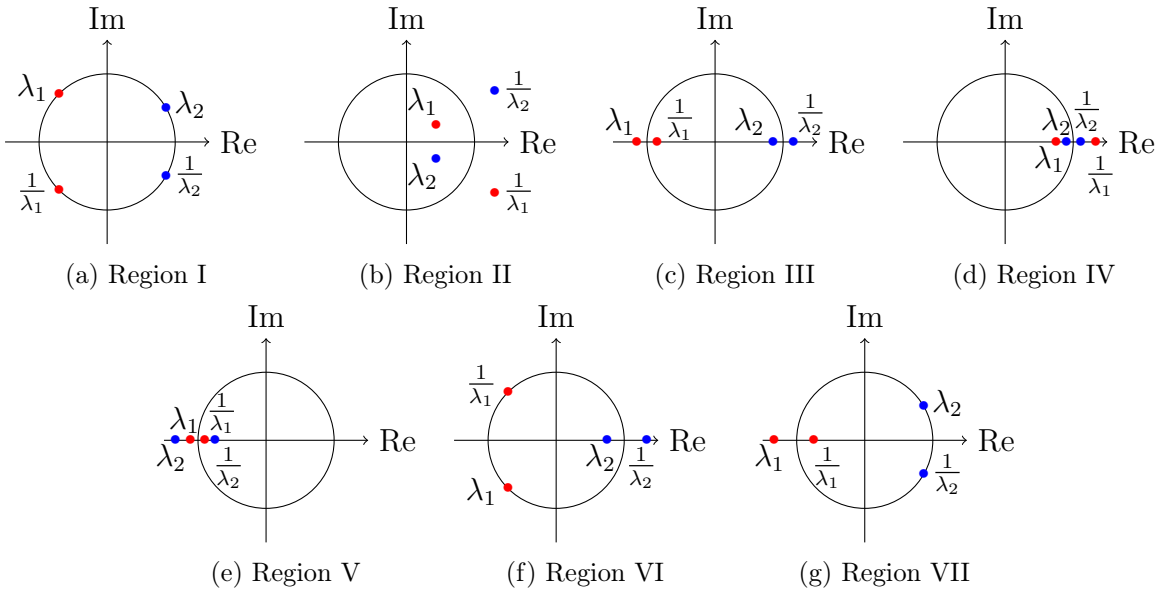

(a) Region I (b) Region II (c) Region III (d) Region IV

(e) Region V (f) Region VI (g) Region VII

Figure 3.3: Eingenvalue configuration in the different regions of the Broucke diagram (see Figure 3.4).

3.6.3 Bifurcations

In some cases changes in the value of the Jacobi constant may result in a change in the qualitative behaviour of trajectories close to a periodic orbit, in which case we say that a local bifurcation occurs [2]. Bifurcations may result in a change in the stability of the periodic orbits along a family, the formation of a new family of periodic orbits, or termination of the current family [47].

For instance, in the Section 3.8 we will show a practical procedure for computing the family of Lyapunov originating from L_1, L_2 and L_3. Along each of the Lyapunov families it will be possible to determine a tangent bifurcation, that give rise to the corresponding Axial and Halo families. We will now make a brief overview of different type of bifurcations, and then illustrate how the Broucke diagram can be used to detect them.

As we have seen the stability of periodic orbit can be studied by looking at the stability indexes ν_i, $i = 1, 2$ that we derived from the non trivial eigenvalues of the monodromy matrix, then, since the stability of an orbit reflects the behavior of nearby orbits, we can detect local bifurcations by monitoring when the stability indices, ν_i, $i = 1, 2$ pass through some critical values. Here we briefly summarize the main types of bifurcations that we can encounter.

- **Tangent bifurcation:** This type of local bifurcation occur when one pair of non-trivial eigenvalues transition from the real axis to the unit circle through the critical values $\lambda_i = 1/\lambda_i = +1$. Then at the same time, the corresponding stability index ν_i passes through $+1$. In the $\alpha\beta$ plane this type of bifurcation correspond to a crossing of the line $\beta = -2\alpha - 2$. Notice that in this case the hypothesis of the Cylinder Theorem on the unit eigenvalue having geometric multiplicity equal to 1 fails to be true, so that the cylinder of orbits is not necessarily unique. The tangent bifurcation is further classified into three subtypes [47, 1]:

  - **Fold bifurcation:** A change of stability occurs along a single family of orbits, without originating nor intersecting other families.
  - **Pitchfork bifurcation:** A change in stability is accompanied with the formation of two additional families of similar period, with stability properties similar to those of the orbits in the original family prior to the bifurcation.
  - **Transcritical bifurcation:** A family of stable orbits intersects a family of unstable orbits, i.e., there exists a common orbit belonging to both families is correspondence of which a stability change occurs.

- **Period-multiplying bifurcations:** A period-multiplying bifurcation of multiplying factor $m \in \mathbb{N}$ occurs when two nontrivial eigenvalues evolve such that $\lambda_{j,k} = \sqrt[m]{1} = \cos(2k\pi/m) \pm i\sin(2k\pi/m)$ [1]. In this scenario it is possible to find, in the vicinity of a periodic orbit with period T, a different periodic orbit of period mT that belongs to a new family of periodic orbits. A period doubling bifurcation, i.e., $m = 2$, corresponds to a crossing of the line $\beta = 2\alpha - 2$, that is one of the boundaries of the stability regions. Thus the bifurcation is accompanied by a change in stability. For $m \neq 2$, however this type of bifurcation generally occurs can a change in orbital stability [1].

- **Secondary Hopf and modified secondary Hopf bifurcations:** These occur when two eigenvalues collide either on the unit circle or the real line and depart into the complex plane, respectively, with a change in stability occurring only in the first scenario. These bifurcations corresponds to a crossing with the parabola $\beta = \alpha^2/4+2$, thus a passage from or towards the complex stability region (Region II in Figure 3.4). Thus the eigenvalues become complex but with a magnitude greater than unity, indicating the existence of the so called spiral manifolds, which is given by a combination of both oscillatory as well as departing/approaching flow [5, 55].

The presence of bifurcations along a family of periodic orbits, can be detected by looking for crossings of special lines in the $\alpha\beta$ plane. The equations of the lines corresponding to the tangent bifurcation, period multiplying bifurcations up to $m = 5$, and secondary Hopf bifurcation are show in Table 3.1 [55, 28].

Type of bifurcation	**Equation**
Tangent	$\beta = -2\alpha - 2$
Period doubling	$\beta = 2\alpha - 2$
Period tripling	$\beta = \alpha + 1$
Period quadrupling	$\beta = 2$
Period quintupling	$\beta = \alpha/(2\cos(4k\pi/5)) - (\cos(8k\pi/5) + 1)/\cos(4k\pi/5), \quad k = 1, 2$
Secondary Hopf	$\beta = \alpha^2/4 + 2, \quad \alpha \in (-4, 4)$
Modified secondary Hopf	$\beta = \alpha^2/4 + 2, \quad \alpha \in (-\infty, 4] \cup [4, \infty]$

Table 3.1: Equations of the lines defining the different types of bifurcations in the Broucke diagram. Notice that the secondary Hopf bifurcation and the modified secondary Hopf bifurcation both correspond to crossings with the same parabola but in different regions of the $\alpha\beta$ plane.

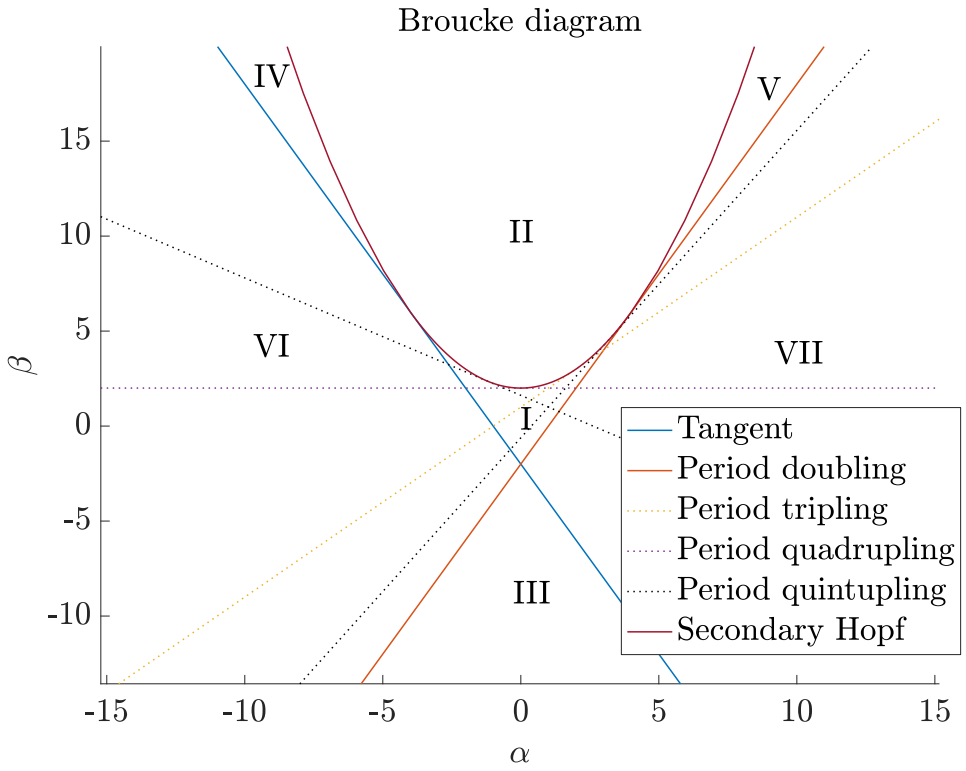

Figure 3.4: The Broucke diagram and the seven stability regions. The solid lines correspond to the bifurcation lines that constitute also boundaries of the stability region, while the dotted lines correspond to lines that only correspond to a bifurcation to bifurcation.

3.7 Resonance

We say that a periodic orbit $\boldsymbol{\gamma}$ of period T is $p : q$ resonant if it completes p orbits in the same time that the primaries complete q, recalling that the in normalized units the period of the primaries is 2π, we have the following resonance condition:

$$\frac{p}{q} = \frac{2\pi}{T}, \quad p, q \in \mathbb{N}. \tag{3.65}$$

Since the families of periodic orbits are continuous in time and the set of rationals $\mathbb{Q}$ is dense in $\mathbb{R}$, according to our definition, near any periodic orbit there exist countably many resonant orbits arbitrarily close it. However we are interested only in the resonant orbits with p and q reasonably small.

3.8 Lyapunov families of orbits

In Section 2.7.3 we described the procedure to obtain the initial guess for a Lyapunov orbit with small amplitude around the collinear Lagrangian point L_i, $i = 1, 2, 3$. Here we show in further detail a computational procedure that can be used to correct the initial guess into an orbit that is periodic to numerical precision. Then the newly computed periodic orbit can be used as an initial guess itself to compute an orbit with larger (or smaller) amplitude, by moving along the cylinder of Lyapunov orbits parametrized by the Jacobi constant that exists in virtue of Theorem 5. In the following we will refer to this cylinder, as the family of L_i Lyapunov periodic orbits.

In order to compute the Lyapunov family around any of the collinear points, as anticipated, we start by generating an initial guess from equation (2.124) with $\boldsymbol{w} = k(1,1,0,0)$. The Lyapunov orbits have the property of being symmetric with respect to the xz plane, then we can employ the differential correction method described in Section 3.3.2, which should converge to a periodic orbit in just a few iterations. Note that it is useful to choose $k > 0$ for L_1 and L_3 and $k < 0$ for L_2, by doing so $\boldsymbol{x}_0$ will be on the opposite side of L_i with respect to the nearest major body, in our case either the Earth or the Moon. At this point we suppose that we have the initial conditions for a small amplitude Lyapunov orbit, which will be of the form

$$\boldsymbol{x}_0 = (x_0, 0, 0, 0, \dot{y}_0, 0)^T, \tag{3.66}$$

and choose a small fixed step size Δx_0 that we use to generate an initial guess for a new Lyapunov orbit as:

$$\boldsymbol{x}_0 + (\Delta x_0, 0, 0, 0, 0, 0)^T. \tag{3.67}$$

We then use equation (3.10), that is the differential correction method at fixed x_0, and if Δx_0 is small enough the procedure will converge in just a few iterations to a new periodic Lyapunov orbit at a slightly lower or larger value of the Jacobi constant, depending on the sign the sign of Δx_0. Note that a lower Jacobi constant corresponds to larger amplitude, and vice versa. In general choosing Δx_0 with sign opposite to that of k, above, will result in a larger amplitude orbit.

In Figures 3.5, 3.7 and 3.9 we show the plots of selected orbit belonging to the L_1, L_2 and L_3 Lyapunov families, respectively. The Earth and Moon are plotted to scale to put the size of the orbits into perspective and the value of the Jacobi constant is shown as a color gradient. Along the L_i Lyapunov family, we find tangential bifurcations corresponding to an intersection with the L_i Halo family and with the L_i Axial families. These new families of periodic orbits will be described in detail in Sections 3.10 and 3.11, respectively. Along the L_3 Lyapunov family, we find also tangent bifurcation with the L_4/L_5 Planar families. These however are not symmetric, with the exception of the Lyapunov orbit from which they bifurcate, and cannot be computed with the differential correction scheme presented here (see e.g., [14]). In Figures 3.6, 3.8 and 3.10, we show the evolution of the orbital period along each of the Lyapunov families and highlight the presence of some of the relevant resonances along the family. Interestingly the orbits of L_3 Lyapunov families have an orbital period close to 27 days across the entire family, i.e., from the small amplitude orbits near L_3 to the largest amplitude orbits intersecting the Earth surface. The periods of the L_1 and L_2 Lyapunov orbits, starts from around 11 days and 15 days, respectively, for the smallest amplitude orbits near the corresponding Lagrangian point and go up to over 30 days, for the large amplitude orbits. In Figures 3.11, 3.12 and 3.13, we show the stability indices and the Broucke diagrams corresponding each of the Lyapunov families. It is worth noting that all orbits in the L_1 and L_2 families of orbits are unstable, as one of the stability indices has modulus larger than unity through the entire family. The same can be said for most of the orbits in the L_3 Lyapunov family, with the exception of the orbits with the largest amplitudes.

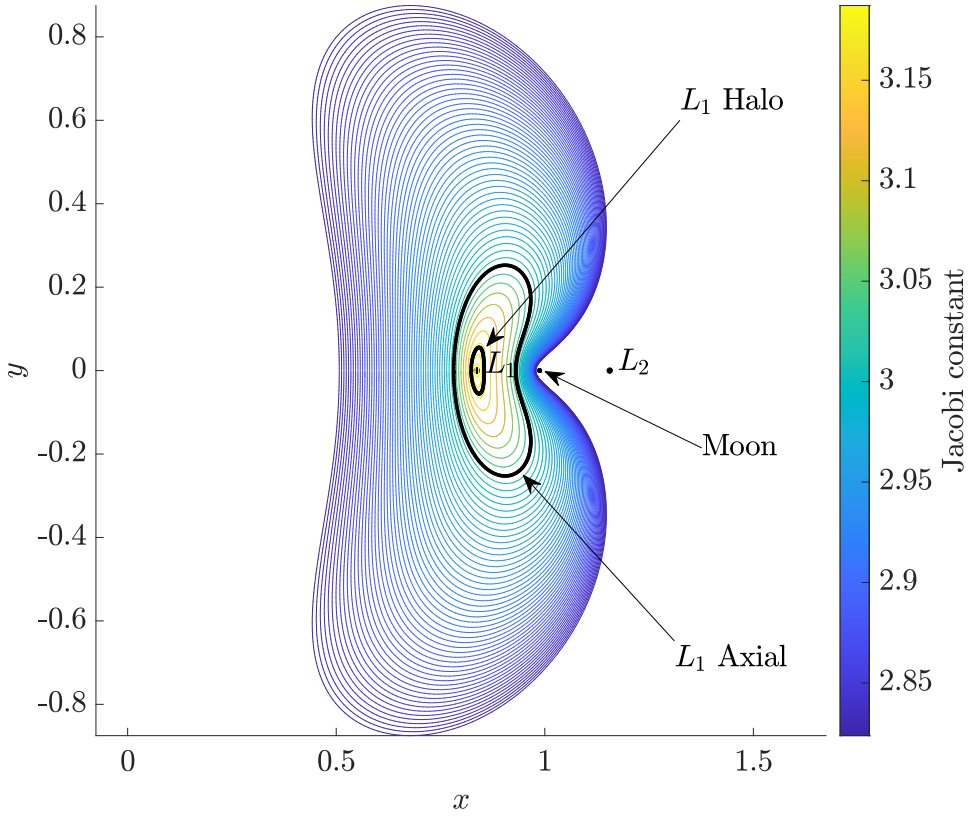

Figure 3.5: Family of Lyapunov orbits emanating from L_1.

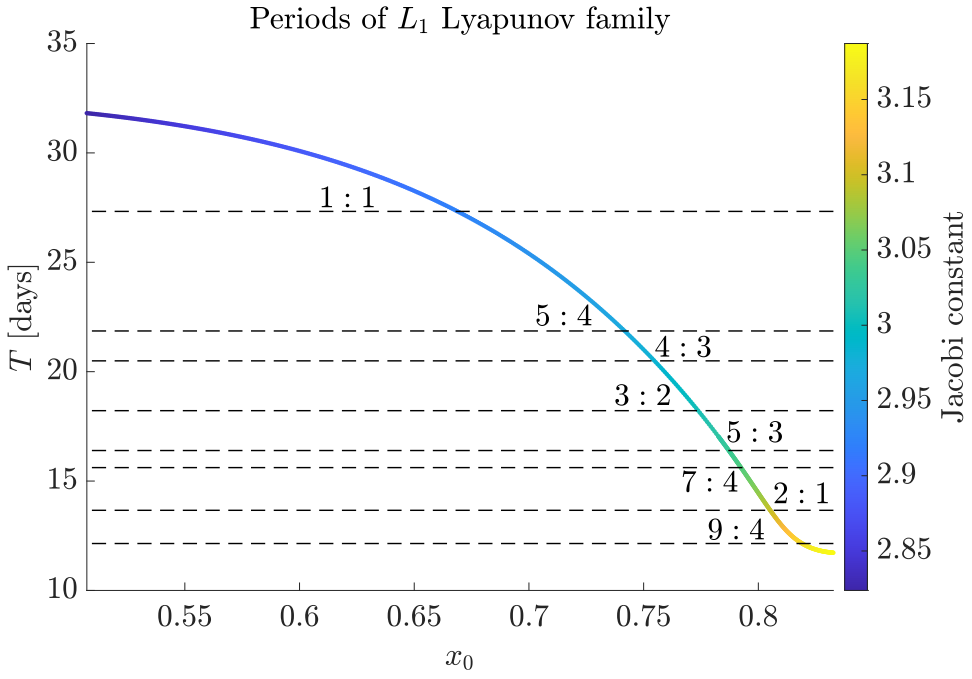

Figure 3.6: Periods in units of days and some of the relevant resonances of the orbits of the L_1 Lyapunov family.

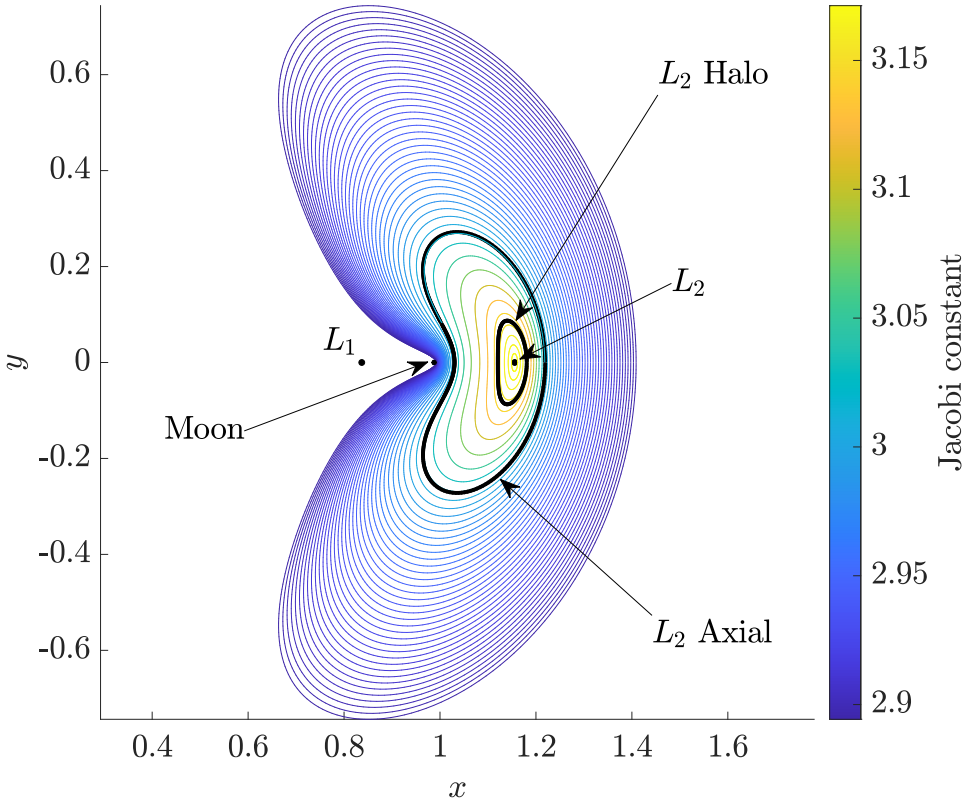

Figure 3.7: Family of Lyapunov orbits emanating from L_2.

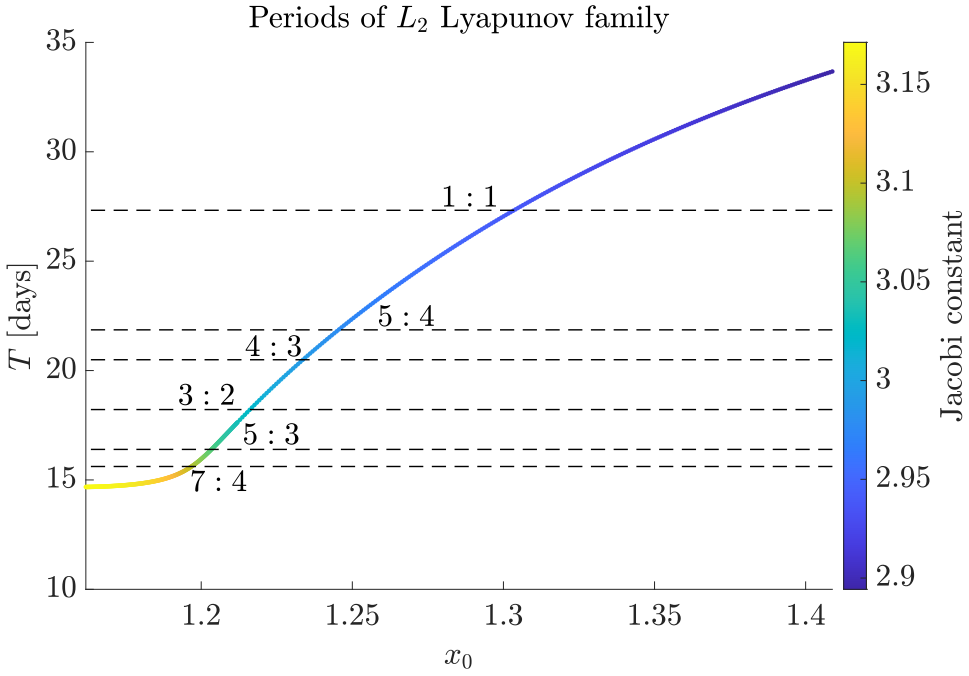

Figure 3.8: Periods in units of days and some of the relevant resonances of the orbits of the L_2 Lyapunov family.

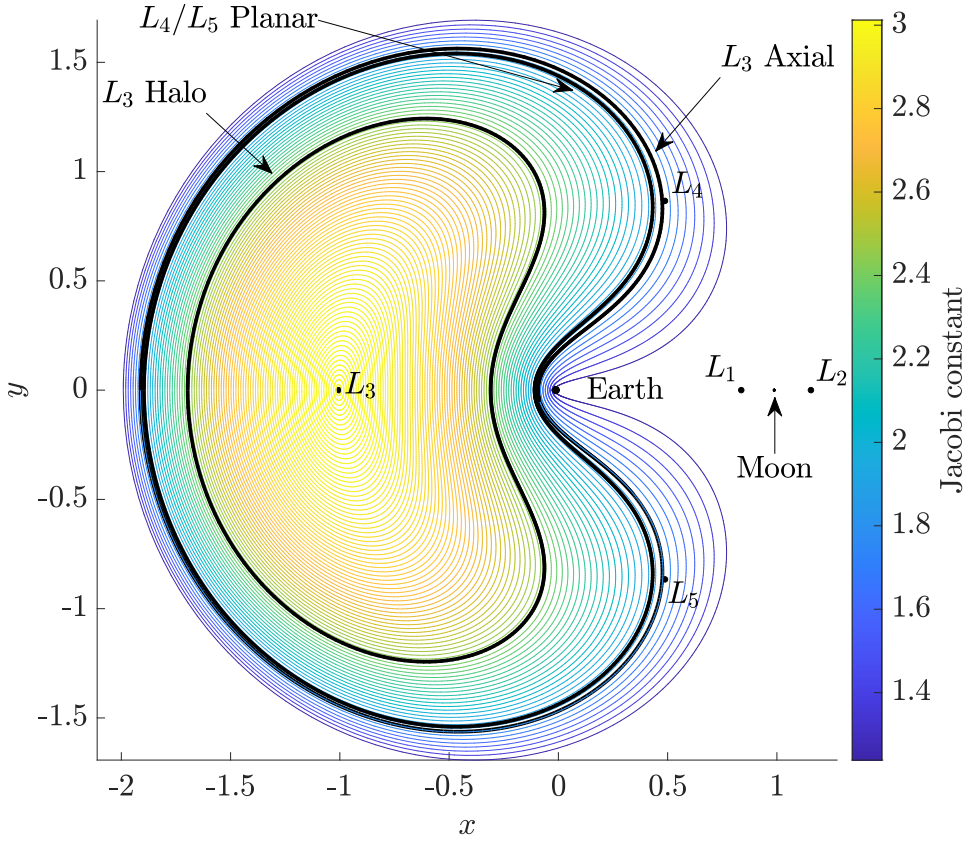

Figure 3.9: Family of Lyapunov orbits emanating from L_3.

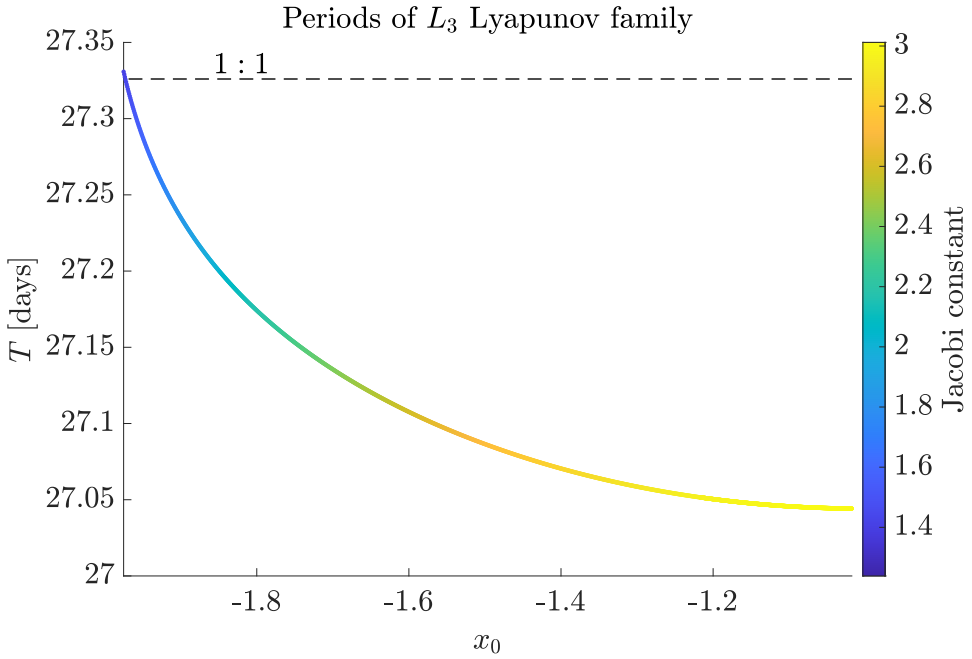

Figure 3.10: Periods in units of days and some of the relevant resonances of the orbits of the L_3 Lyapunov family.

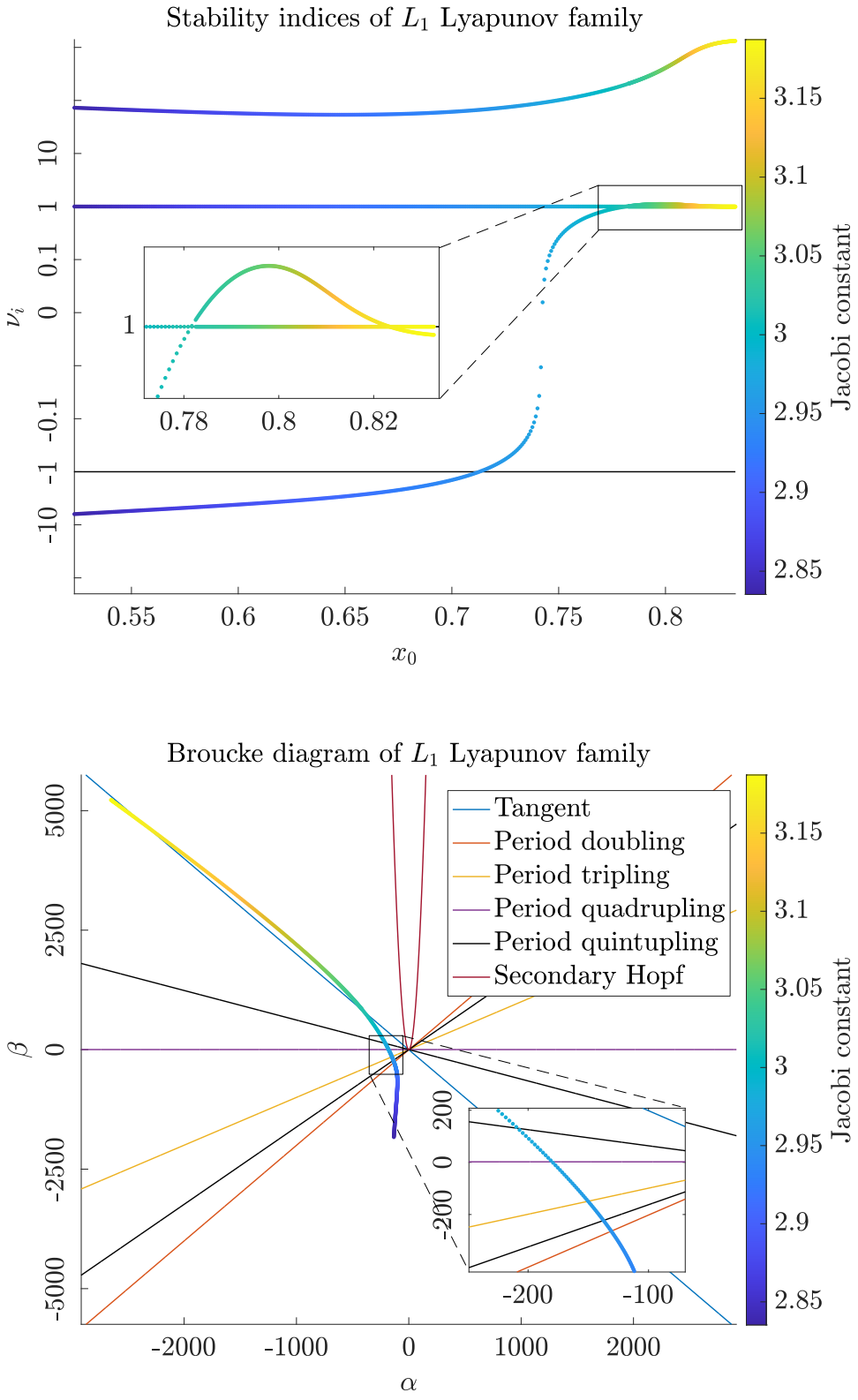

Figure 3.11: Plots showing the stability indices (top), and Broucke diagram (bottom) of the L_1Lyapunov families plotted against the value of x_0 used to identify the different Lyapunov orbits.

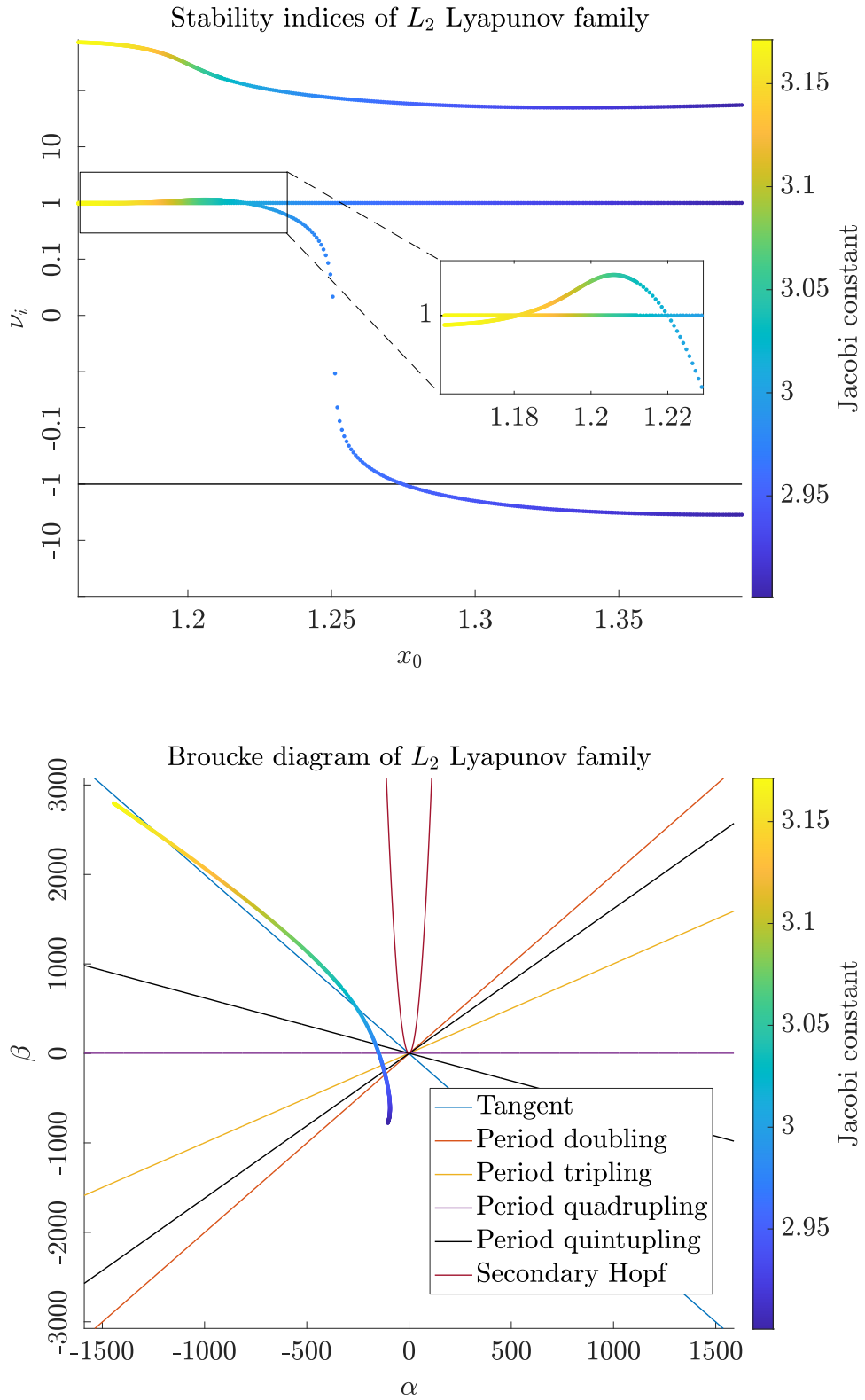

Figure 3.12: Plots showing the stability indices (top), and Broucke diagram (bottom) of the L_2 Lyapunov families plotted against the value of x_0 used to identify the different Lyapunov orbits.

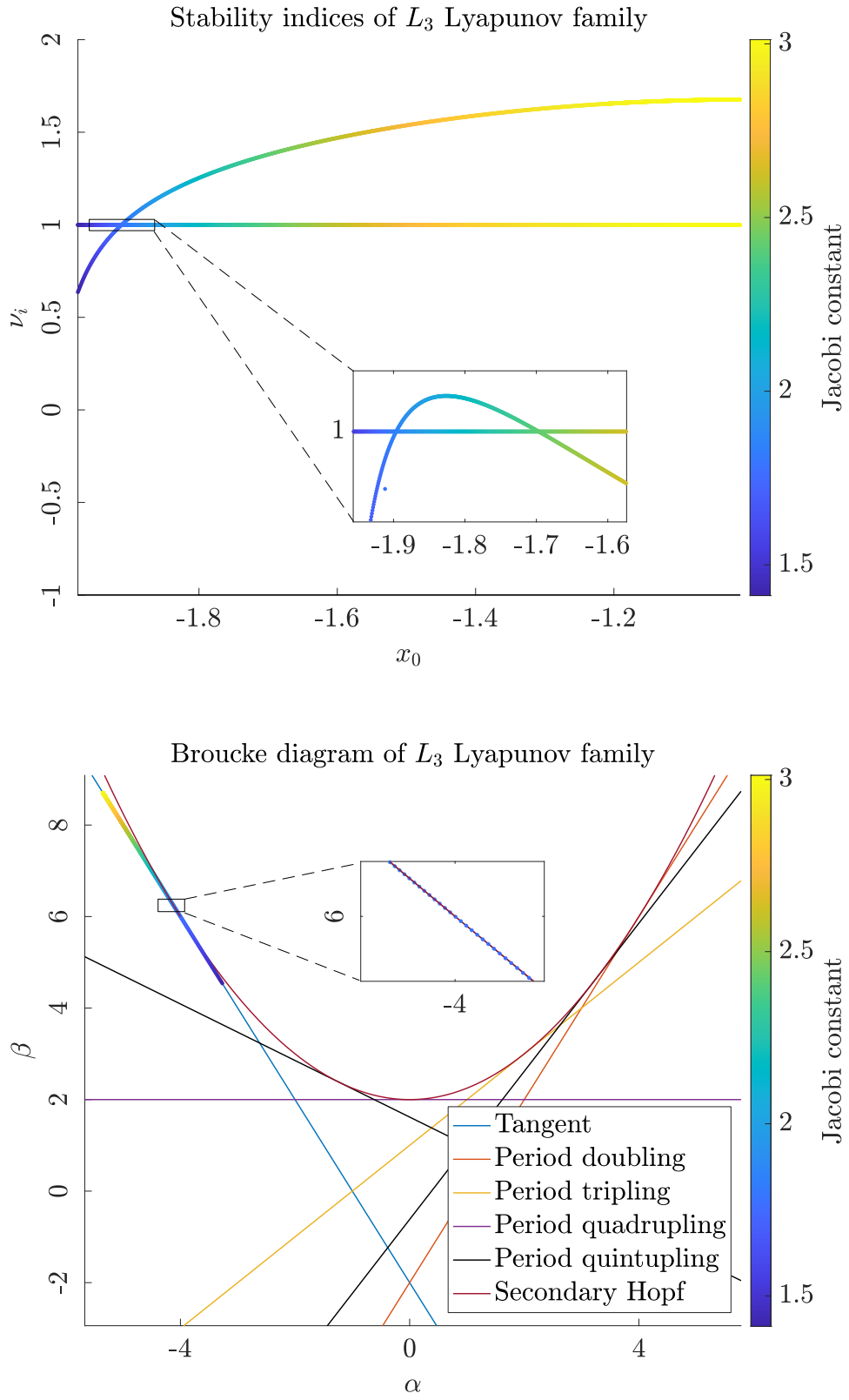

Figure 3.13: Plots showing the stability indices (top), and Broucke diagram (bottom) of the L_3 Lyapunov families plotted against the value of x_0 used to identify the different Lyapunov orbits.

3.9 DRO, DPO and LPO families of orbits

Using the same technique that we have already seen for the Lyapunov families, we now compute four more families periodic orbits, known as the Distant Retrograde Orbit (DRO) family, the Distant Prograde Orbit (DPO) family and the Western and Eastern Low Prograde Orbit families (LPO). The initial guesses for starting the DRO and Western LPO families can be determined easily by taking planar nearly circular orbits close to the Moon's surface, while for the Eastern LPO and the DPO family we refer to the data provided by Jet Propulsion Laboratory's solar system dynamics website. In any case the initial conditions will be of the type:

$$\boldsymbol{x}_0 = (x_0, 0, 0, 0, \dot{y}_0, 0)^T, \tag{3.68}$$

where for the DRO and Western LPO family x_0 is taken on the left side of the Moon, i.e., $x_0 < 1 - \mu$, and the sign of $\dot{y}_0$ determines whether the prograde or the retrograde family of orbits is computed. In particular we find the DRO family by setting $\dot{y}_0 > 0$, and the Western LPO family with the choice $\dot{y}_0 < 0$. For the Western LPO and the DPO family we take $x_0 > 1-\mu$, that is on the right side of the Moon, and $\dot{y}_0 > 0$, while for the Eastern LPO we take initial condition on the left side of the Moon, i.e., $x_0 < 1-\mu$. Then we can proceed exactly as for the Lyapunov case by choosing appropriate Δx_0, and after applying the differential correction scheme the initial guess for the next orbit is again of the form:

$$\boldsymbol{x}_0 + (\Delta x_0, 0, 0, 0, 0, 0)^T. \tag{3.69}$$

In particular with the above conventions regarding the choice of $\boldsymbol{x}_0$, it must be $\Delta x_0 > 0$ for the DRO and Western LPO family, and $\Delta x_0 < 0$ for the Eastern LPO family. In the case of the Eastern LPO family, we find that the differential correction scheme sometimes corrects the the guess for an Eastern LPO orbit into an orbit of the Lyapunov family at the same value of x_0 that differs only in he $\dot{y}_0$ component of the velocity. To overcome this issue it suffices to constrain the maximum value of $\delta\dot{y}_0$, thus forcing the continuation algorithm to remain on the LPO family.

In Figures 3.14, 3.16 and 3.20 we show the plots of selected orbit belonging to the DRO, DPO and LPO families of periodic orbits, respectively. In Figures 3.15, 3.17 and 3.21, we show the evolution of the periods of the DRO, LPO and DPO families, respectively, and highlight the presence of some of the relevant resonances. Lastly, in Figures 3.22, 3.23 and 3.25, we show the stability indices and the Broucke diagrams corresponding to the DRO, LPO and DPO families, respectively. It is worth noting that most of the orbits in the DRO family are linearly stable, with the exception of the portion of the DRO family with the largest amplitudes. Moreover the orbital periods of the DRO orbits span from just a few hours, corresponding to the nearly-circular orbits are close to the Moon's surface, up to periods close to the $1:1$ resonance with the Moon, i.e., about 27.3 days, that are found for the large amplitude orbits. Large stability regions are found also for the Western and Eastern LPO families. On the other hand all the orbits of the DPO family are unstable, as one of the stability indices has modulus always larger than unity.

We conclude by mentioning that recently a lunar DRO has been used employed by the Orion spacecraft. Orion was launched as part of NASA's Artemis 1 mission via the Space Launch System on November 16 2022. After performing a lunar flyby Orion was injected into a lunar DRO on November 25. Orion then remained on the DRO for a total of six days before performing a second lunar flyby and finally reentering the Earth atmosphere. [33, 34]

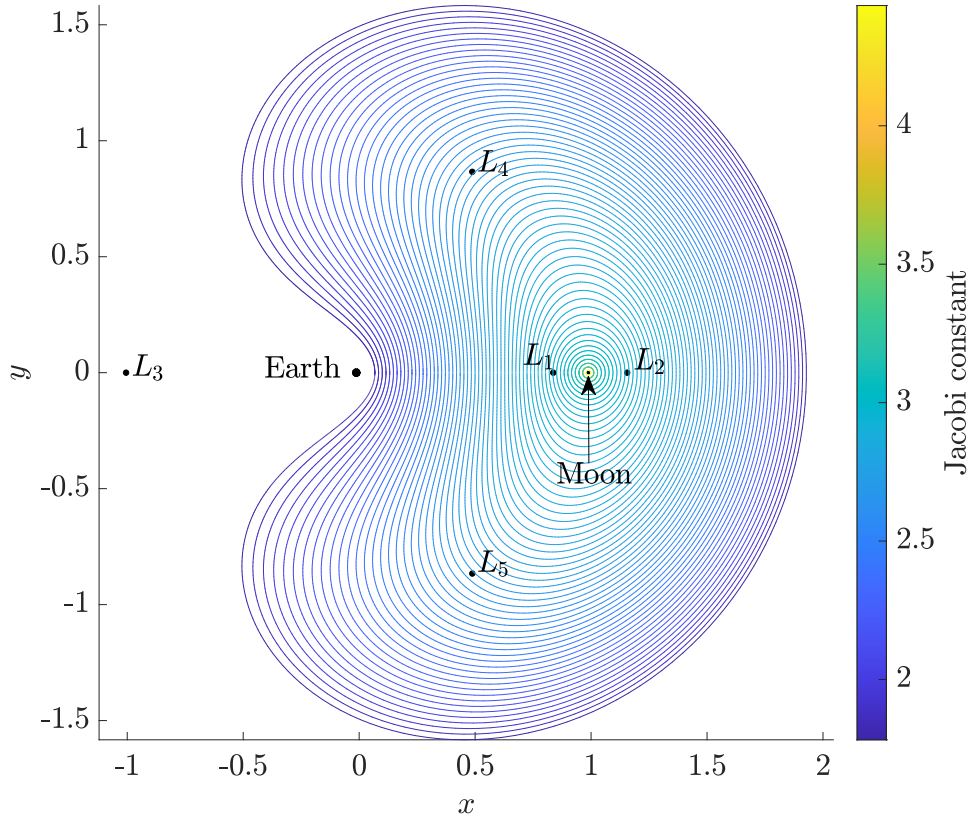

Figure 3.14: Family of DRO orbits. The colours of the orbits correspond to the Jacobi constant. Here only the portion of the family that does not intersect the Earth's surface is shown.

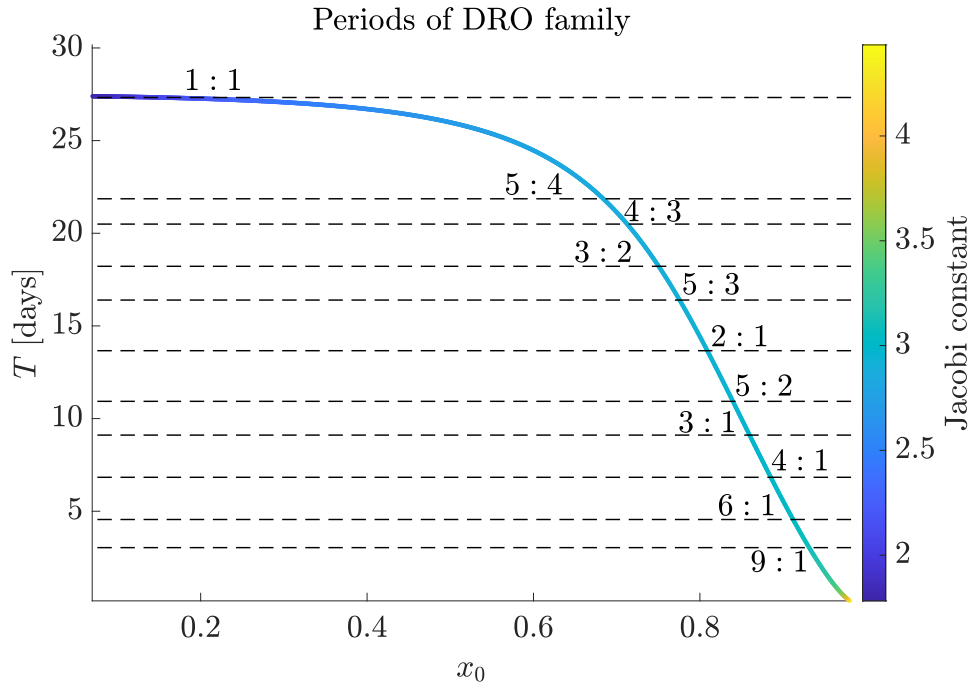

Figure 3.15: Periods in units of days and some of the relevant resonances of the orbits of the DRO family.

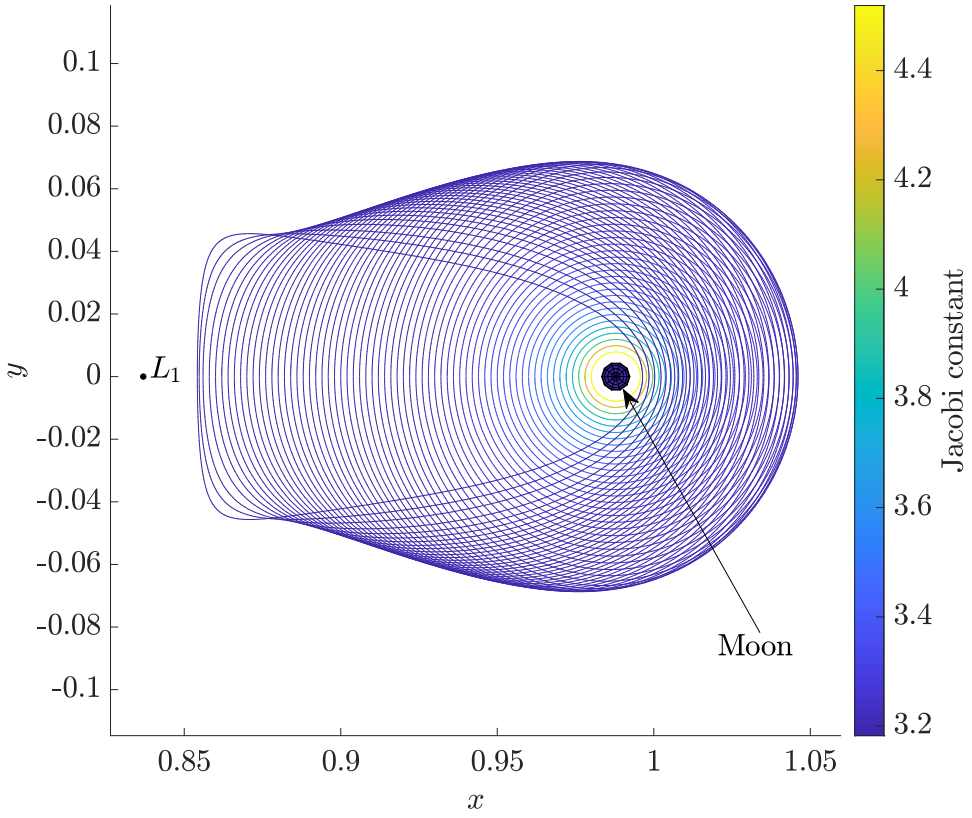

Figure 3.16: Family of Western LPO orbits. The colours of the orbits correspond to the Jacobi constant. Here only the portion of the family that does not intersect the Moon's surface is shown.

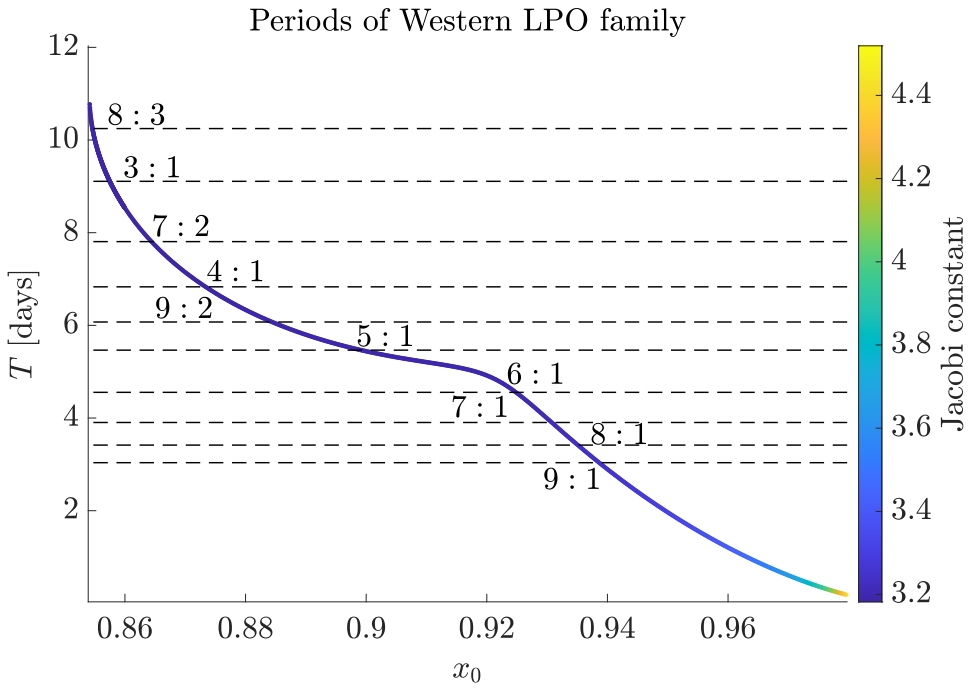

Figure 3.17: Periods in units of days and some of the relevant resonances of the orbits of the Western LPO family.

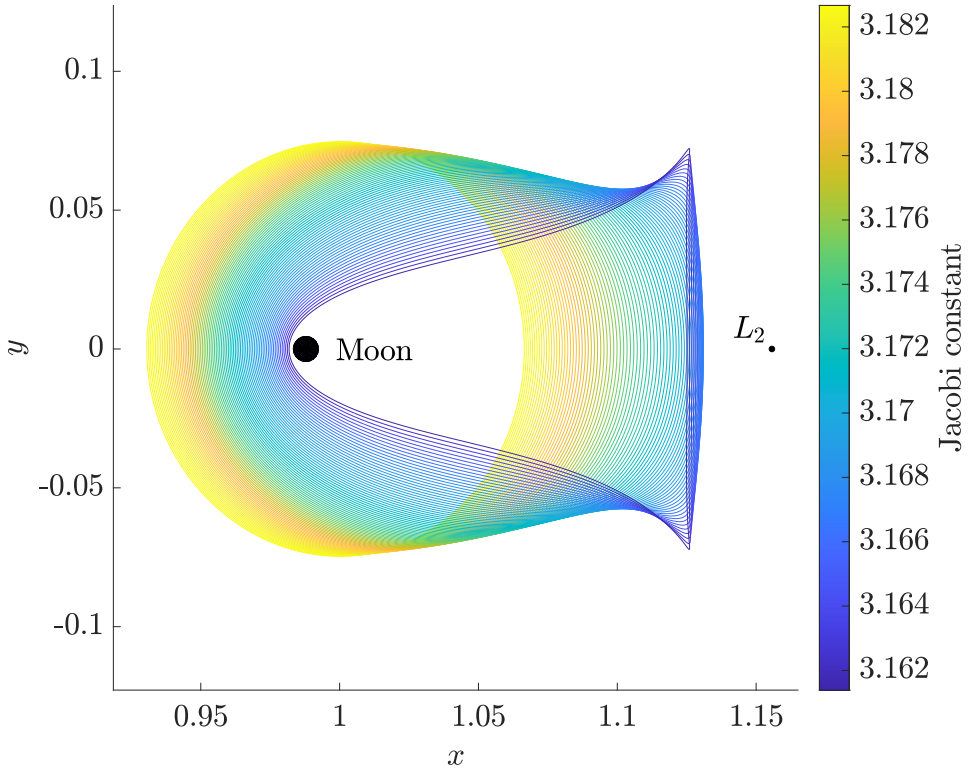

Figure 3.18: Family of Eastern LPO orbits. The colours of the orbits correspond to the Jacobi constant. Here only the portion of the family that does not intersect the Moon's surface is shown.

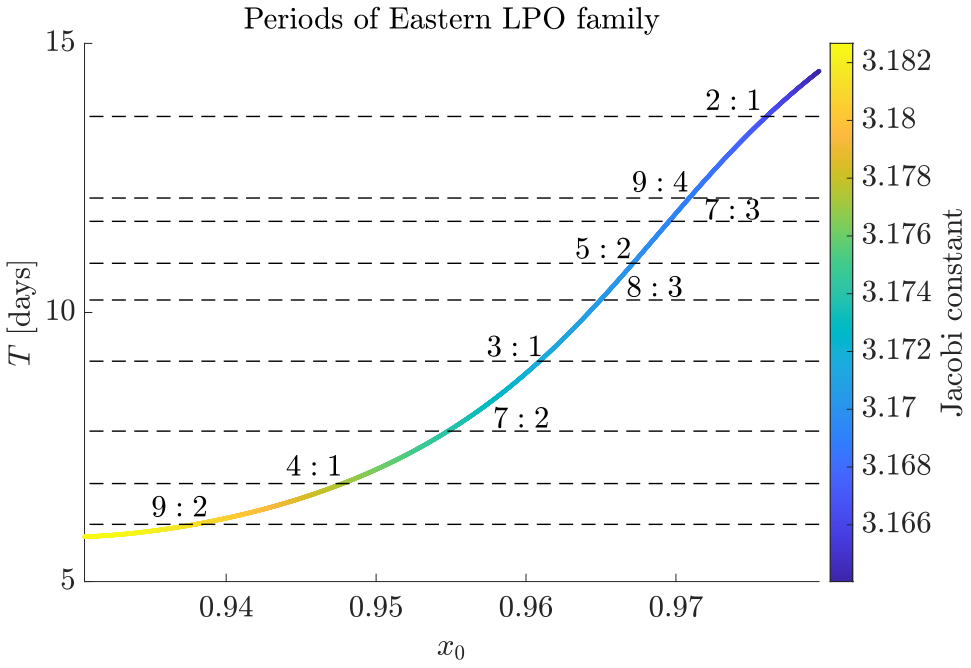

Figure 3.19: Periods in units of days and some of the relevant resonances of the orbits of the Eastern LPO family.

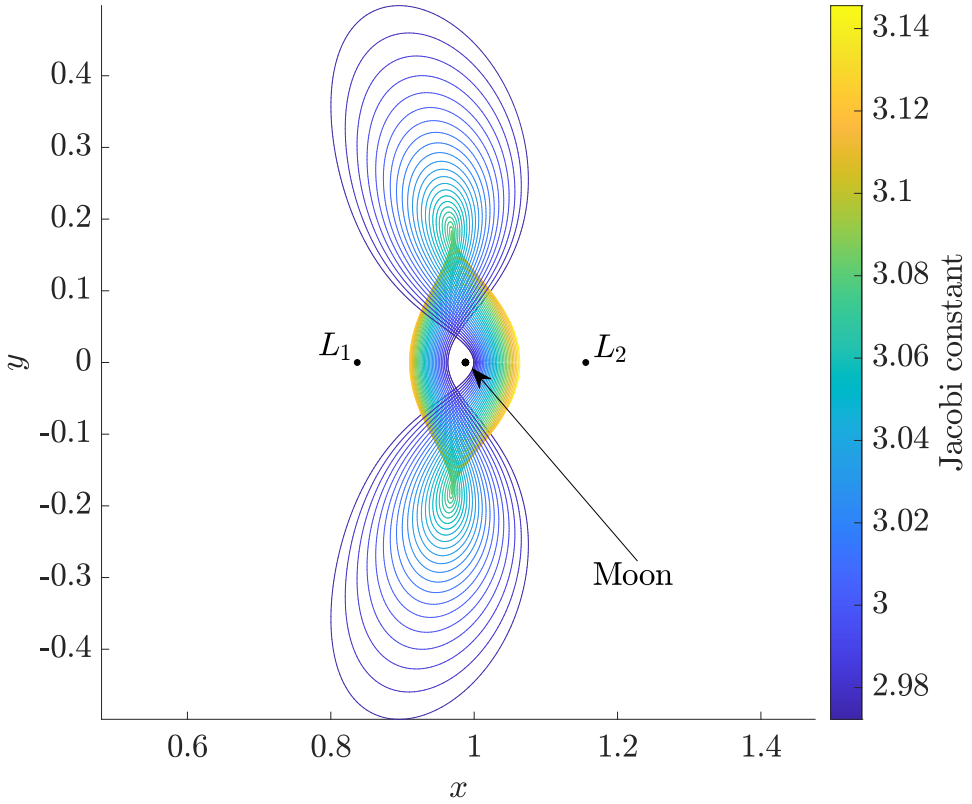

Figure 3.20: Family of DPO orbits. The colours of the orbits correspond to the Jacobi constant.

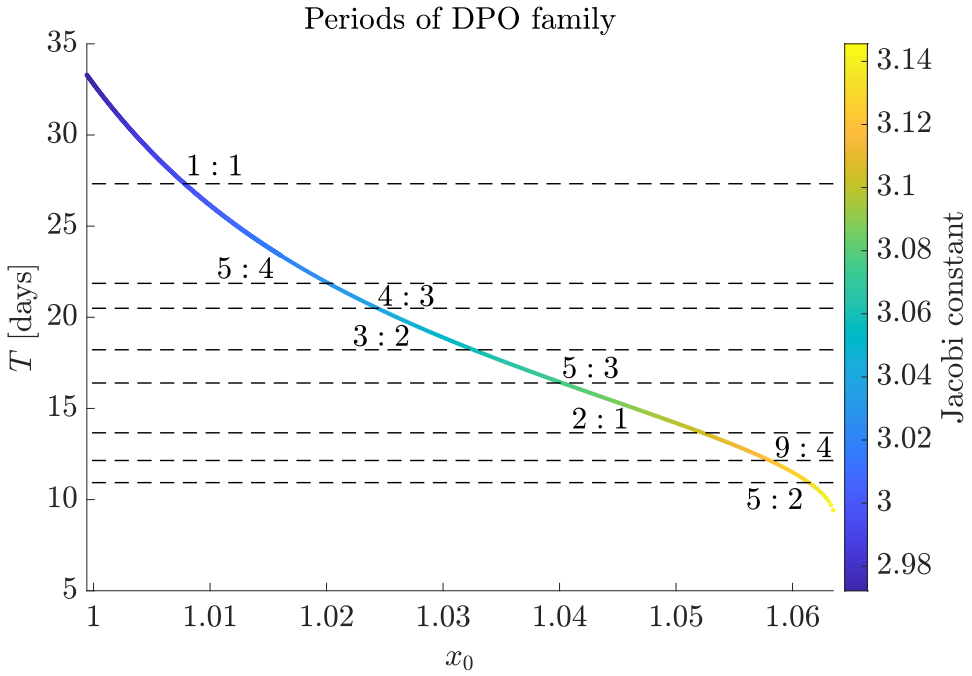

Figure 3.21: Periods in units of days and some of the relevant resonances of the orbits of the DPO family.

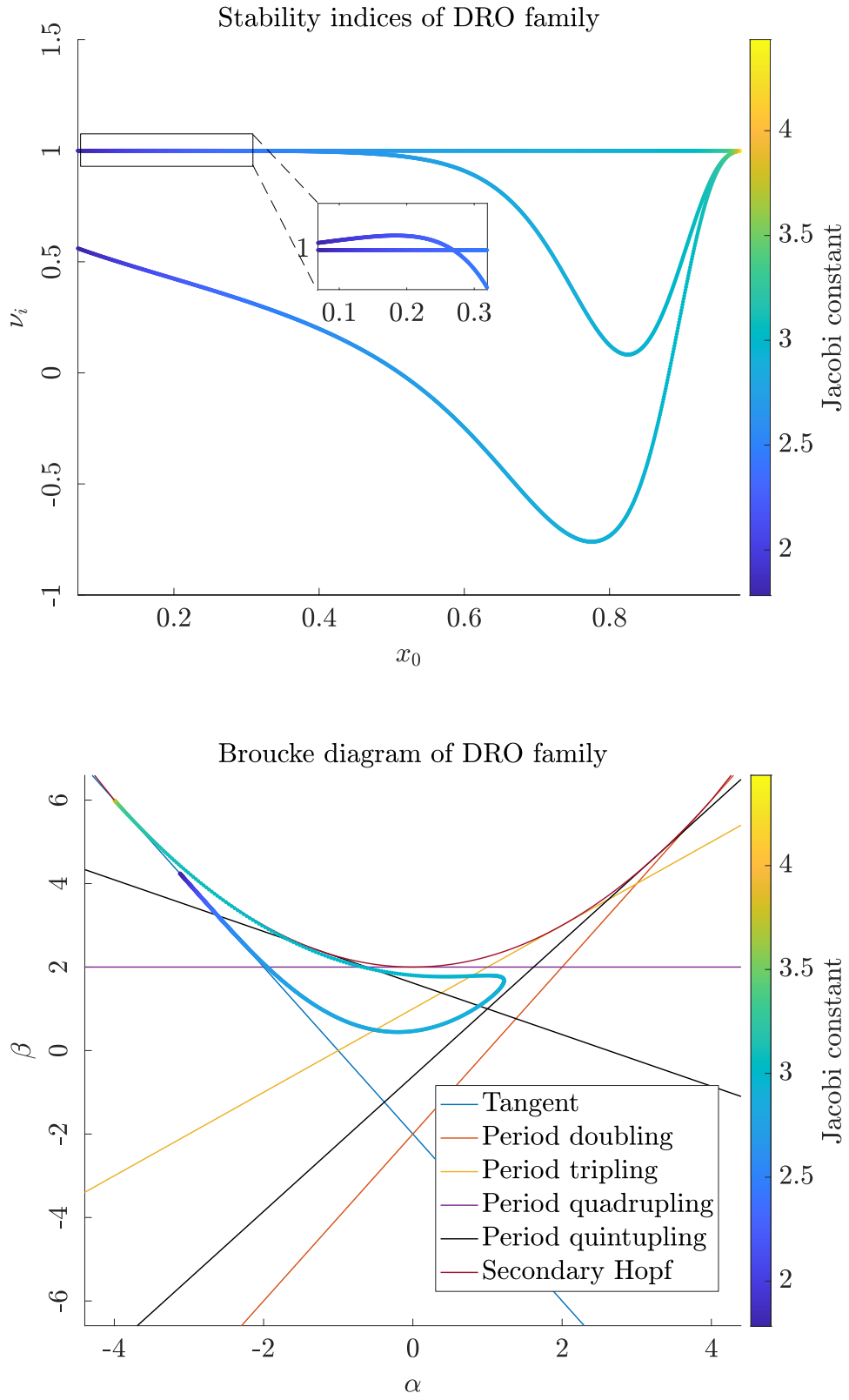

Figure 3.22: Plots showing the stability indices (top), and Broucke diagram (bottom) of the DRO family plotted against the value of x_0 used to identify the different DRO orbits.

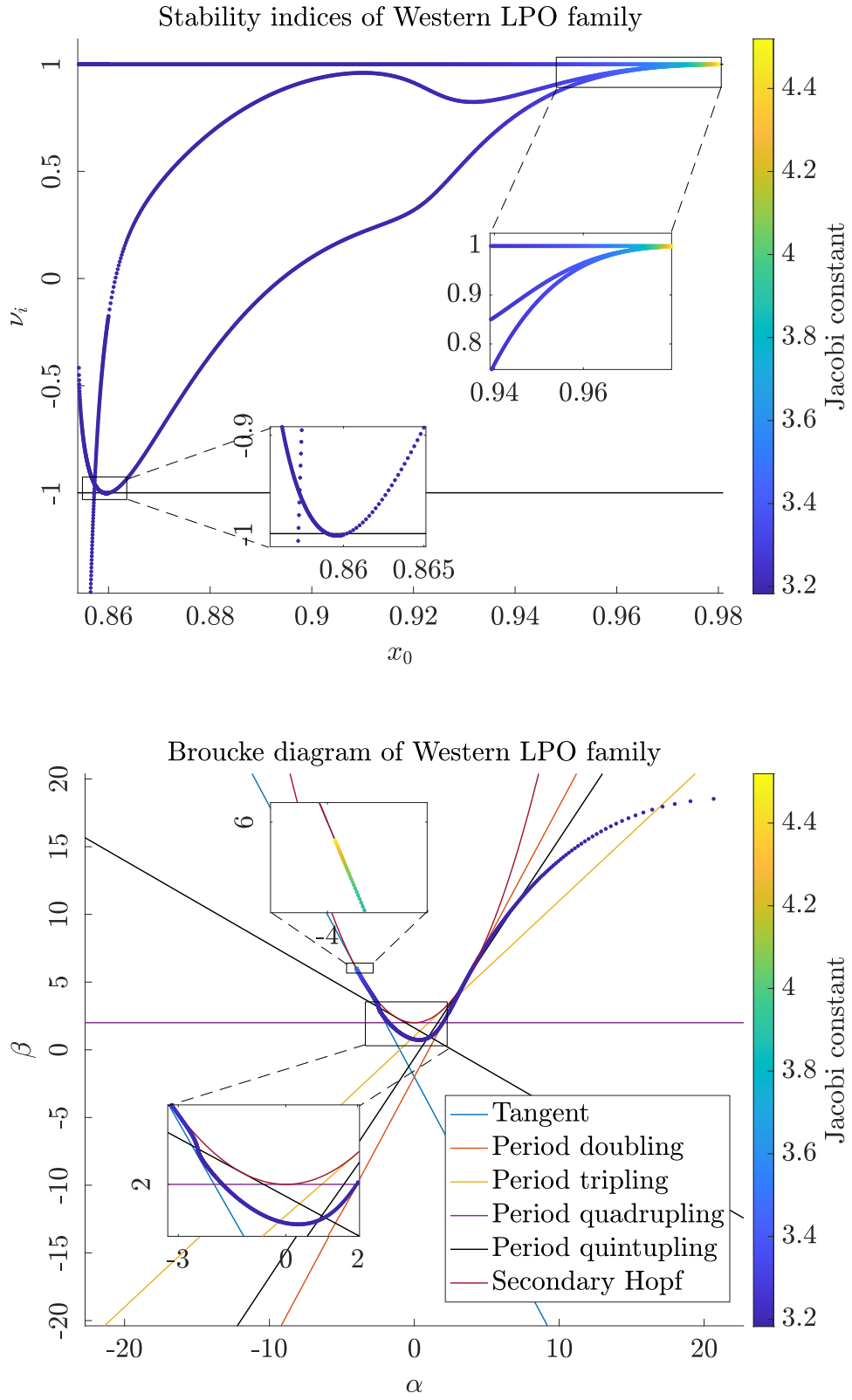

Figure 3.23: Plots showing the stability indices (top), and Broucke diagram (bottom) of the Western LPO family plotted against the value of x_0 used to identify the different LPO orbits.

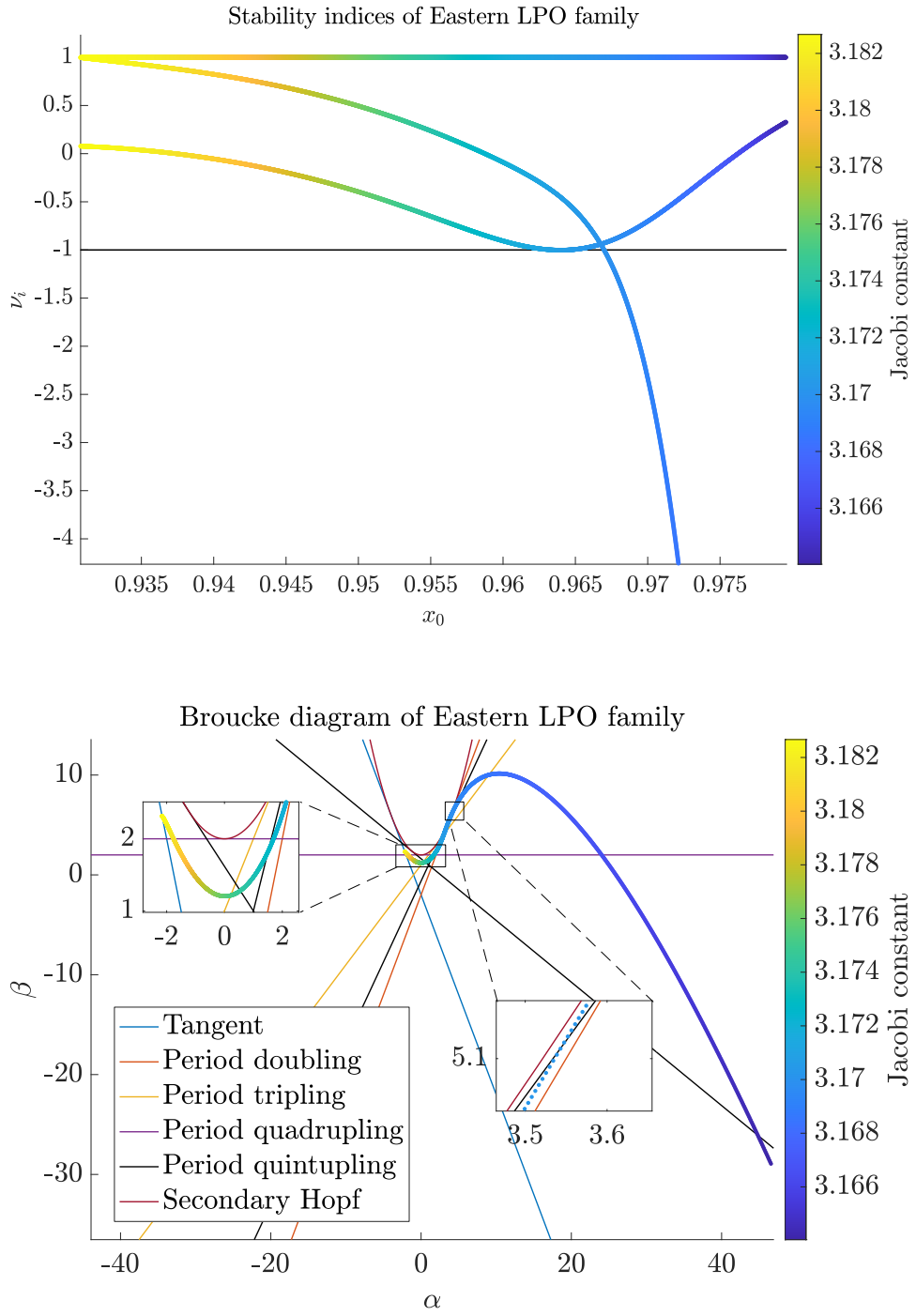

Figure 3.24: Plots showing the stability indices (top), and Broucke diagram (bottom) of the Eastern LPO family plotted against the value of x_0 used to identify the different LPO orbits.

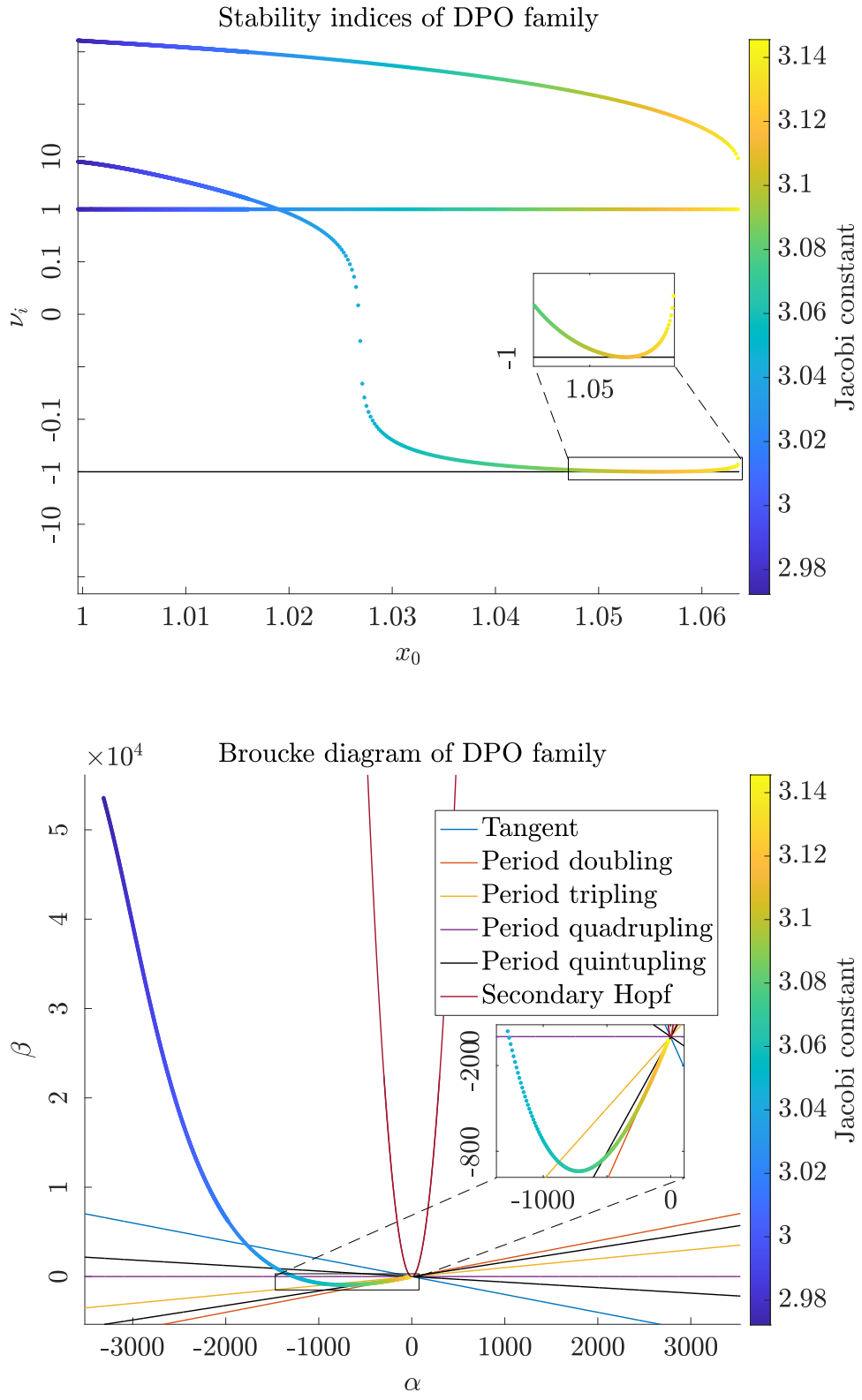

Figure 3.25: Plots showing the stability indices (top), and Broucke diagram (bottom) of the Western DPO family plotted against the value of x_0 used to identify the different DPO orbits.

3.10 Halo families of orbits

The family of Halo orbits in the vicinity of the collinear point L_i, emanates from the corresponding bifurcation orbit found along the family of L_i Lyapunov orbits. To accurately compute the bifurcation orbit, it is necessary to employ some correction algorithm, e.g., a bisection method with respect to the initial conditions that converges when the nontrivial eigenvalues associated to the bifurcation are within some specified tolerance from the bifurcation value. We note however that the exact position of the bifurcation along the Lyapunov family is not necessary to compute the family of Halo orbits. In fact, we find that the differential correction scheme presented in Section 3.3, is powerful enough to converge to a Halo orbit even if the Lyapunov orbit used to start the Halo family is only fairly close but not exactly on the bifurcation point.

With this idea in mind, we now describe the procedure that we adopted to compute families of Halo orbits that bifurcate from L_1, L_2 and L_3 Lyapunov orbits. Note that because of the symmetries in the equations of motion, actually there exists two families of Halo orbits bifurcating from the L_i Lyapunov family. We call these the Northern and Southern families of Halo orbits. In particular, each orbit in the Northern Halo family is the mirror image of its Southern counter part with respect to the xy plane. We anticipate that given a Northern Halo orbits the initial conditions for its Southern counterpart can be determined simply by inverting the sign of z_0 in the corresponding initial dynamical state $\boldsymbol{x}_0$, i.e., by applying the symmetry transformation (2.54), consequently both orbits will lie at the same value of the Jacobi constant $\mathcal{C}$.

That said the procedure to compute the L_i Halo family of orbits is as follows. First of all we need to select a Lyapunov orbit computed in Section 3.8 of initial condition $\boldsymbol{x}_0$, that is located in the vicinity of the bifurcation. Then we need to choose a small fixed step size Δz_0, the sign of which determines whether the Northern or Southern Halo family is sought, and generate the initial guess for a new orbit with out of plane component as:

$$\boldsymbol{x}_0 + (0, 0, \Delta z_0, 0, 0, 0)^T. \tag{3.70}$$

We then use equation (3.11), that is the differential correction method at fixed z_0, and if Δz_0 is small enough the procedure will converge to a Halo orbit with small out of plane component. We then iterate the procedure until:

$$|x_0^{n+1} - x_0^n| < |z_0^{n+1} - z_0^n|, \tag{3.71}$$

as suggested in [14]. After that x_0 is fixed instead and equation (3.67) is applied. This is done in order to avoid the necessity of using smaller and smaller step in the z direction as the family grows out of plane.

In Figure 3.26, 3.28 and 3.30 we show selected periodic orbits belonging to the L_1, L_2 and L_3 Northern Halo families. In Figures 3.27, 3.29 and 3.31, we show the evolution of the orbital period along each of the Northern Halo families and highlight the presence of some of the most relevant resonances along the family. Lastly, in Figures 3.32, 3.33 and 3.34, we show the stability indices and the Broucke diagrams corresponding each of the Northern Halo families. In particular wa want to draw attention to the zoomed-in area in Figure 3.34, as this correspond to the L_2 NRHO region. In this region eight bifurcations are found. In particular these are: two period doubling, two period quadrupling, three period quintupling bifurcations, and one tangent bifurcation. The latter however is a

fold type bifurcation and as such gives rise to no other family. The last period doubling bifurcation (following the curve from the Lyapunov bifurcation) gives rise to the family of the Butterfly orbits. A more detailed overview of the L_2 NRHO bifurcations — with the exception of the period quintupling ones — is given in [55, 56].

It appears evident that starting from the Lyapunov bifurcation each of the Halo families tends toward orbits which have a large out of plane component z and increasingly smaller in plane components. As we move towards the end of the Halo families, closer to one of the two major bodies, we find that the periodic orbits become thin, almost perpendicular to the plane of motion of the primaries. These are known as the Near Rectilinear Halo Orbits (NRHOs). Of particular interest are the L_2 NRHO in $4:1$ and $9:2$ resonance with the Moon's orbit around the Earth (see Figure 3.29). The latter in particular is the reference orbit for the NASA Lunar Gateway concept. Additionally in 2022, the Cislunar Autonomous Positioning System Technology Operations and Navigation Experiment (CAPSTONE) become the first spacecraft to be be deployed in an L_2 NRHO, with the aim of validating the mission design and operations of NASA's Gateway [8]. Finally we observe that the Halo orbits bifurcating near L_1 and L_2 grow larger, but shorter in period, as they shift towards the Moon. In both cases a narrow band of stable orbits can be found roughly at half distance from the Moon. We conclude by mentioning that historically the name *Halo* was first used by Farquhar in 1966, when he proposed the use of such an orbit as a communications relay station for an Apollo mission to the far side of the Moon, i.e., in the vicinity of L_2. However this idea was brought to life only in 2018, when China placed the first communications relay satellite, Queqiao, in an L_2 Halo orbit [54]. We conclude by mentioning the International Sun-Earth Explorer-3 (ISEE-3), a collaborative mission by ESA and NASA launched in 1978 with the goal of surveying the Earth magnetic tail. ISEE-3 was the first mission to operate in a Halo orbit near the Sun-Earth L_1 point [35].

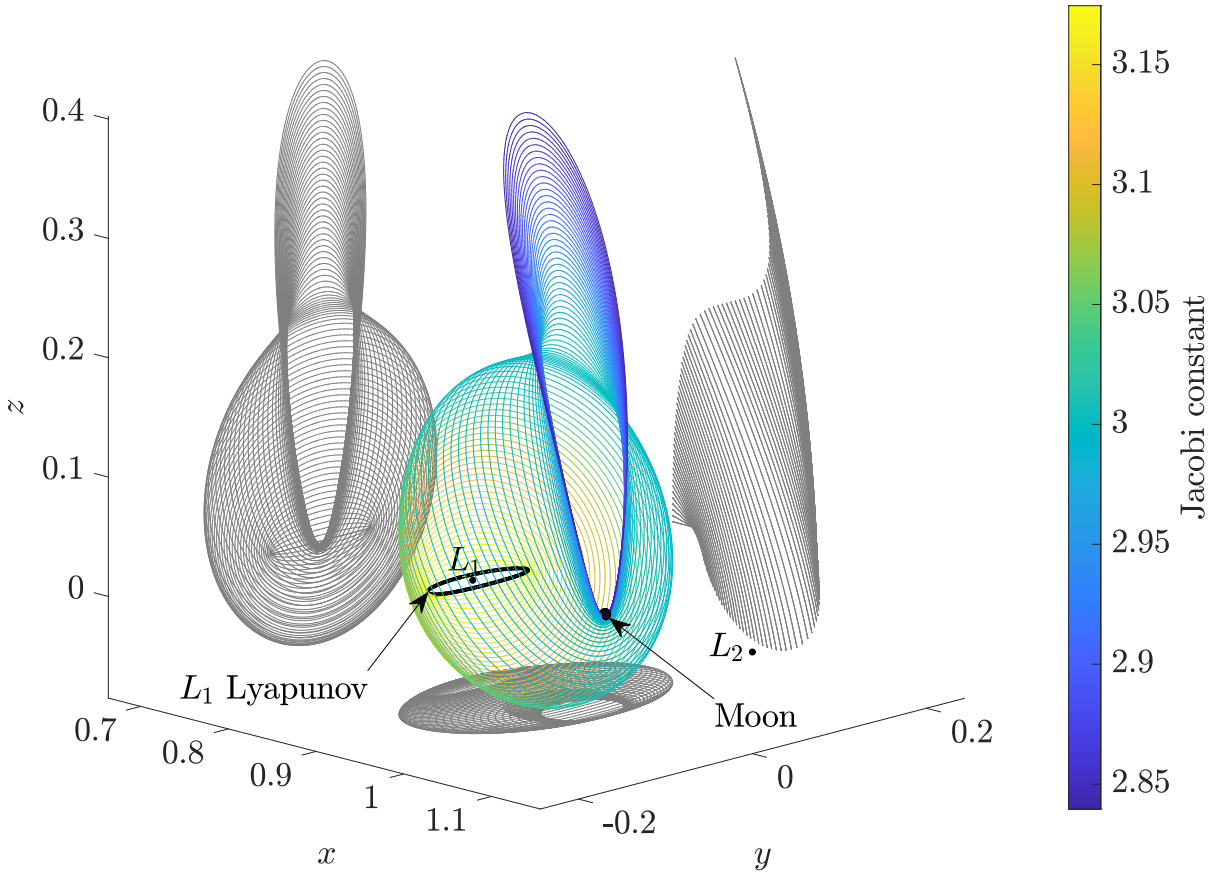

Figure 3.26: Family of Northern Halo orbits bifurcating from Lyapunov orbits near L_1. Note that the portion of the family with the lowest values of $\mathcal{C}$ intersects the Moon's surface, moreover the family continues to grow much further than shown here (see [15]).

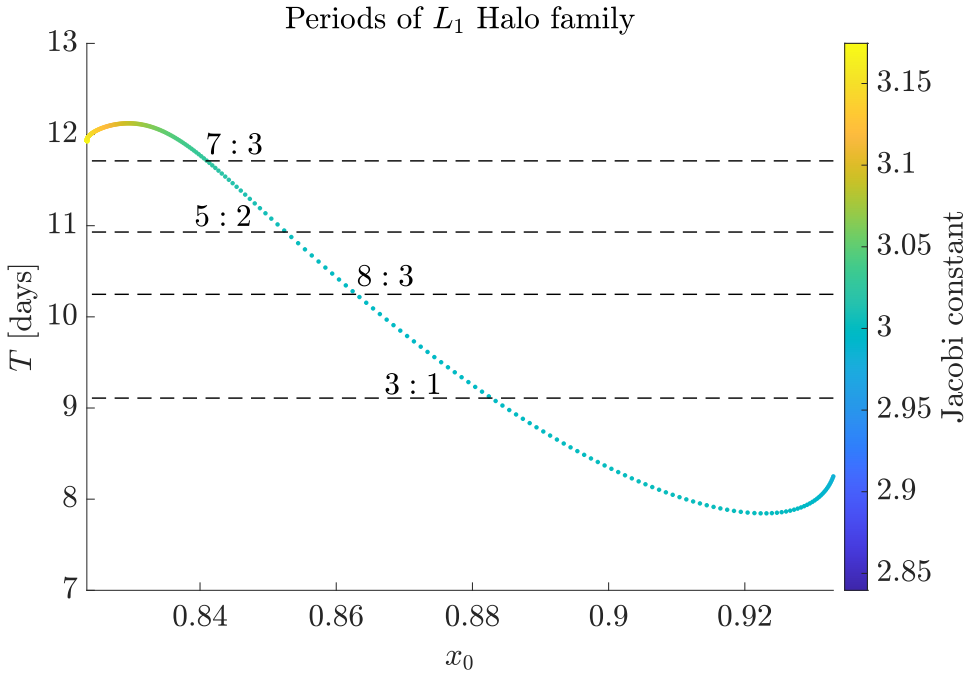

Figure 3.27: Periods in units of days and some of the relevant resonances of the orbits of the L_1 Halo family. Only the data of orbits not intersecting the Moon surface is shown.

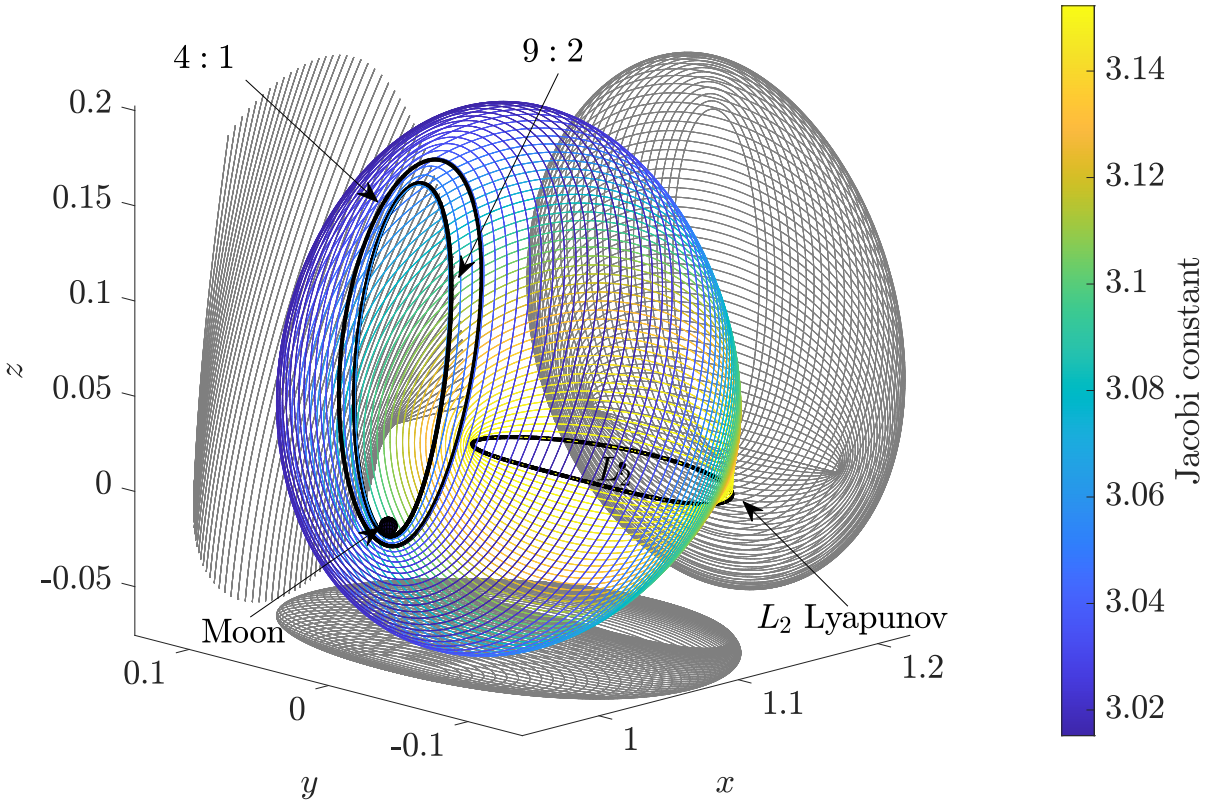

Figure 3.28: Family of Northern Halo orbits bifurcating from Lyapunov orbits near L_2. The 4 : 1 and 9 : 2 resonant NRHOs are highlighted.

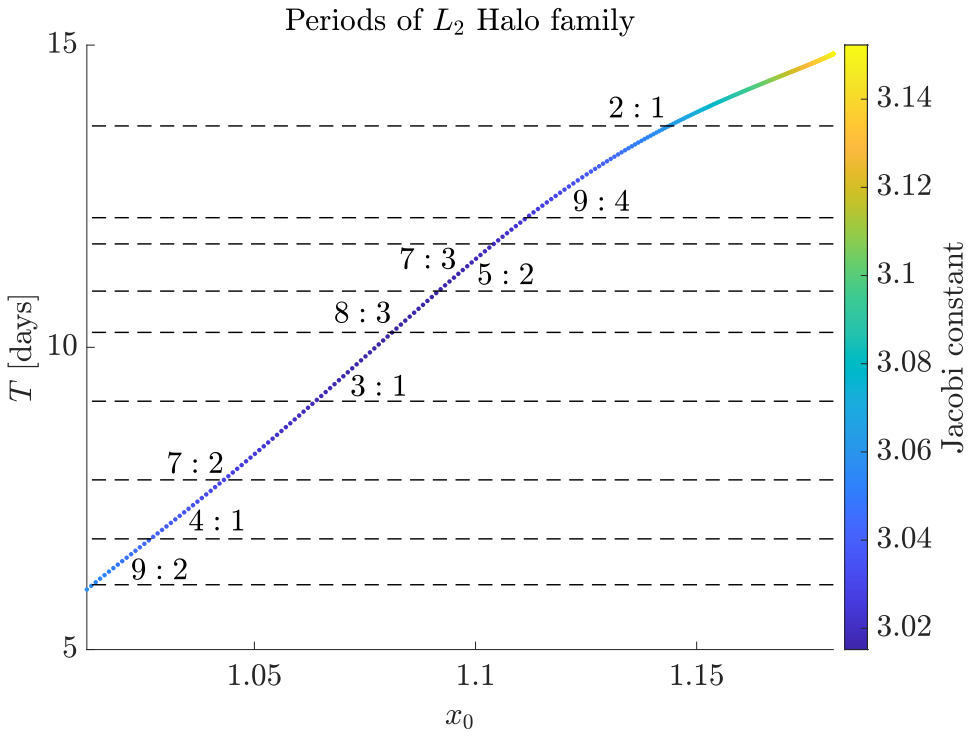

Figure 3.29: Periods in units of days and some of the relevant resonances of the orbits of the L_2 Halo family.

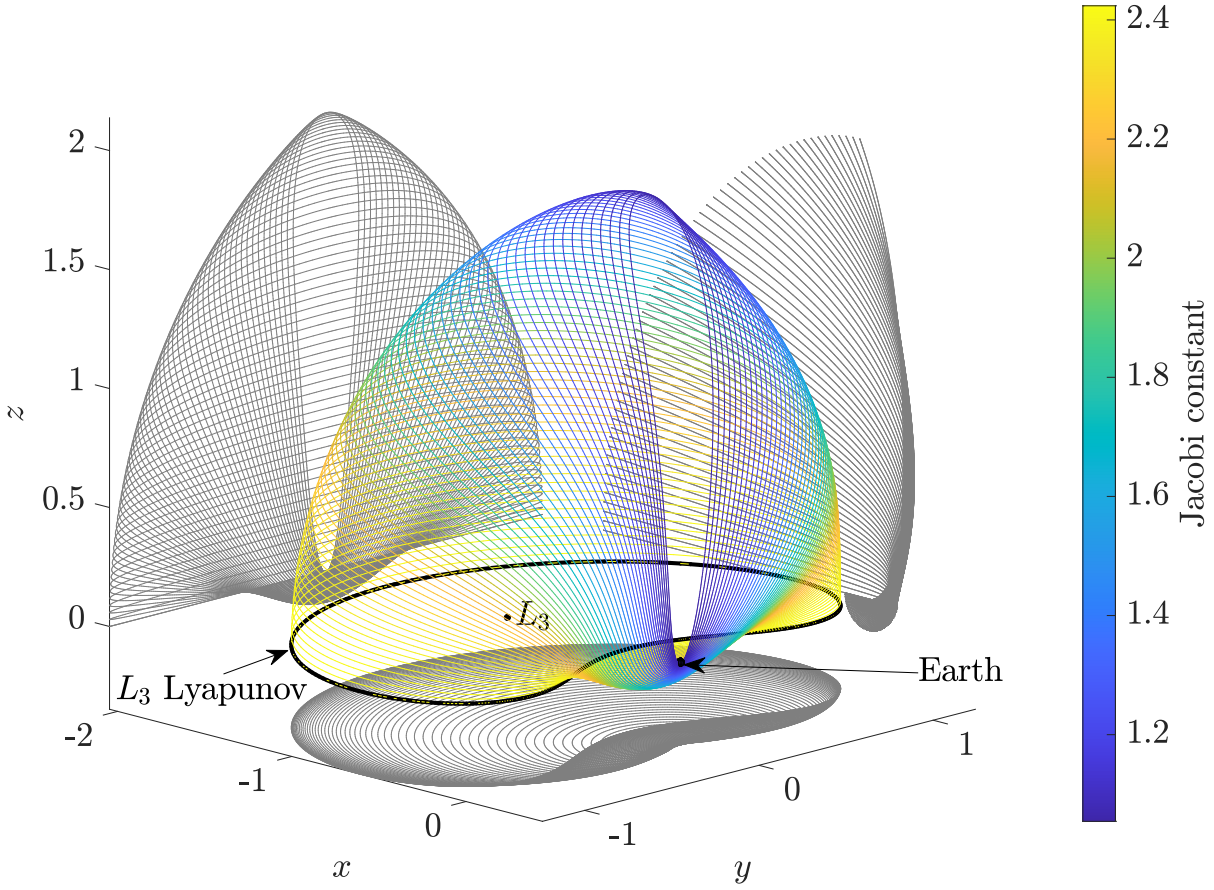

Figure 3.30: Family of Northern Halo orbits bifurcating from Lyapunov orbits near L_3.

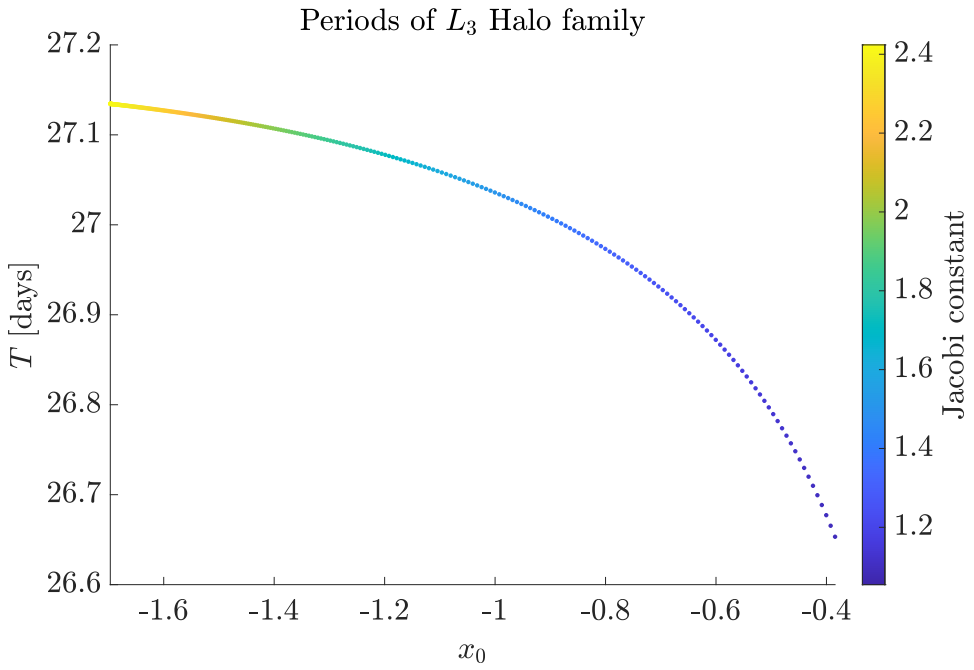

Figure 3.31: Periods in units of days and some of the relevant resonances of the orbits of the L_3 Halo family.

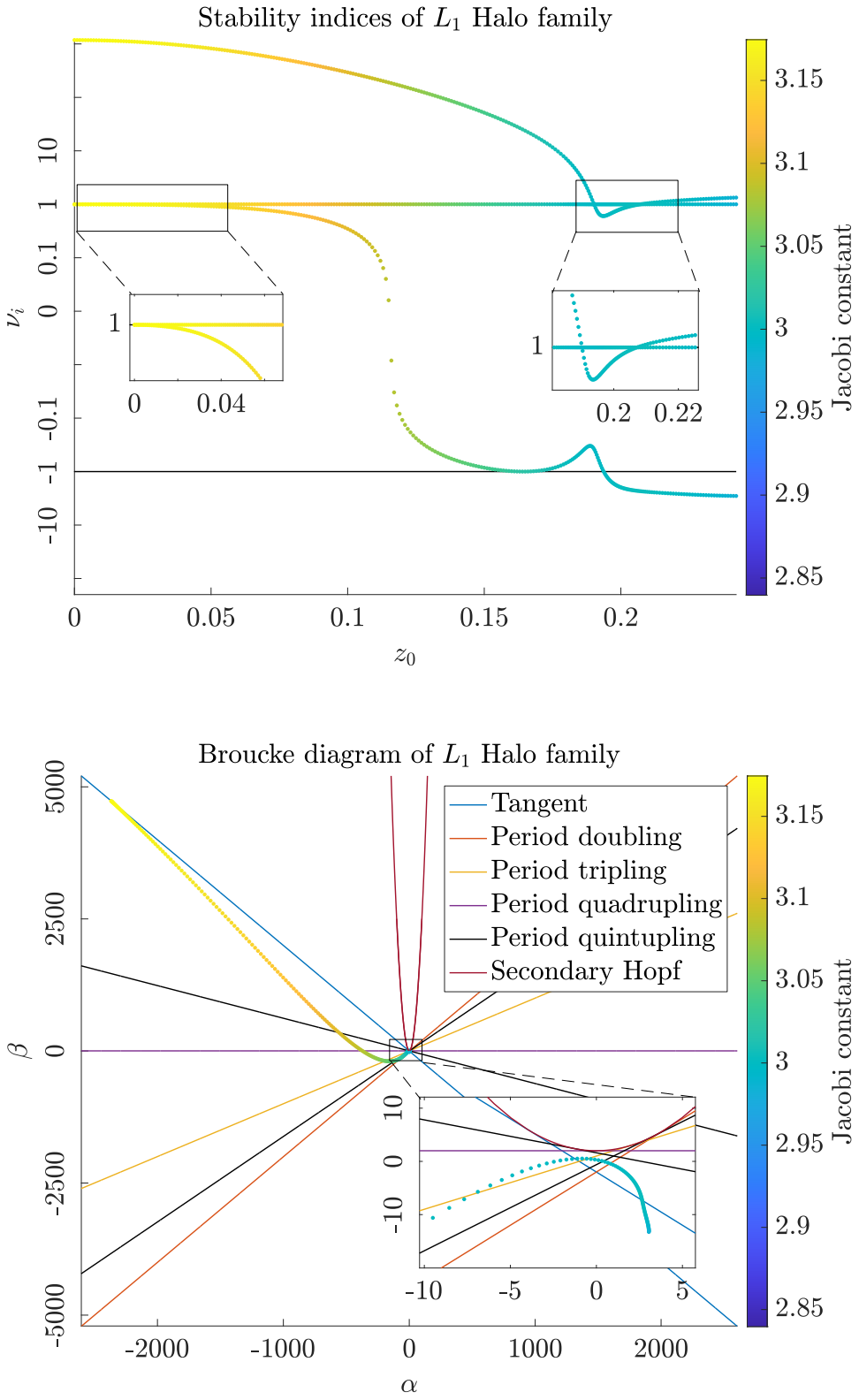

Figure 3.32: Plots showing the stability indices (top), and Broucke diagram (bottom) of the L_1 Halo family plotted against the value of x_0 used to identify the different Halo orbits. Only the data of orbits not intersecting the Moon surface is shown.

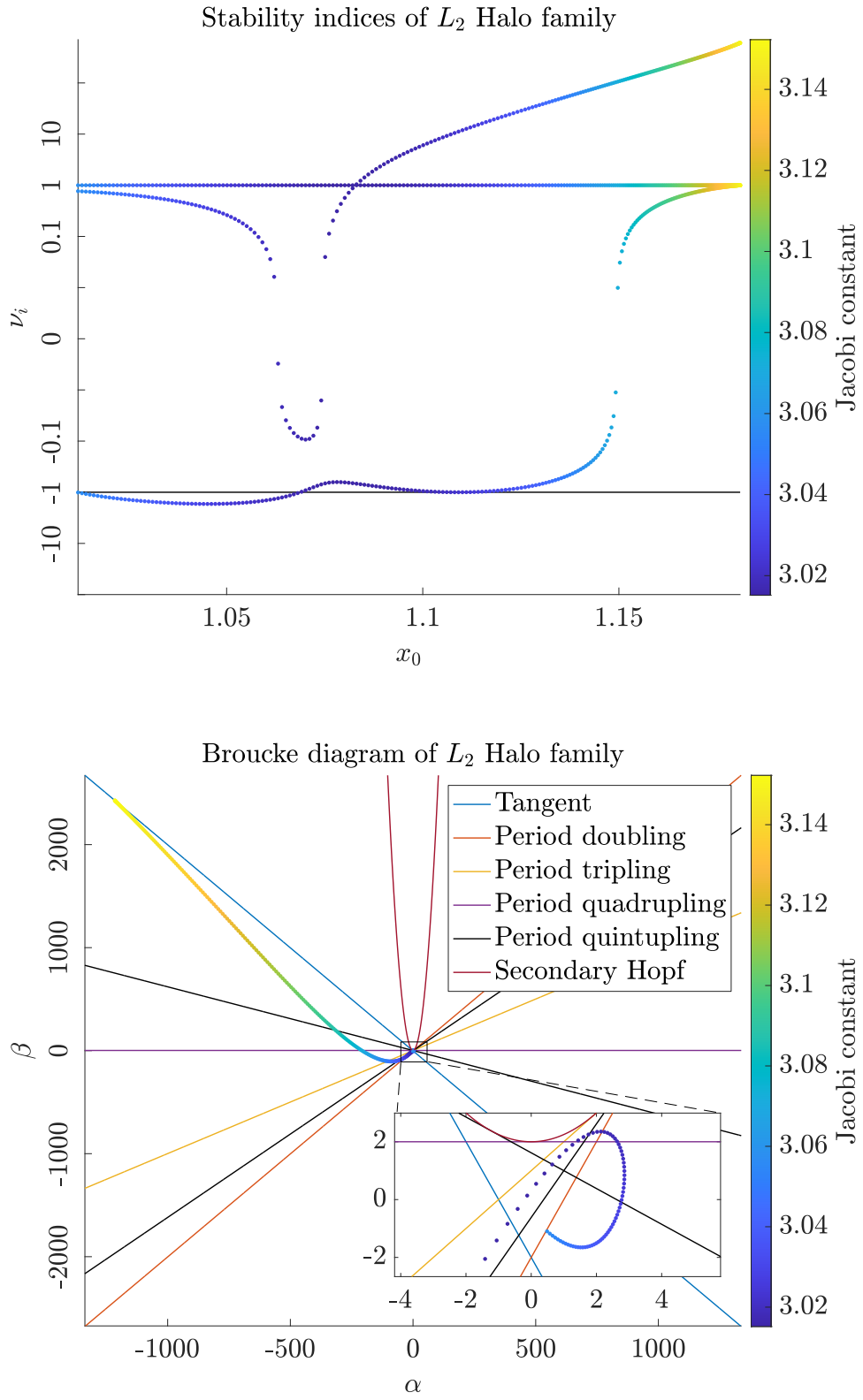

Figure 3.33: Plots showing the stability indices (top), and Broucke diagram (bottom) of the L_2 Halo family plotted against the value of x_0 used to identify the different Halo orbits. The zoomed area of the diagram corresponds to the NRHO region.

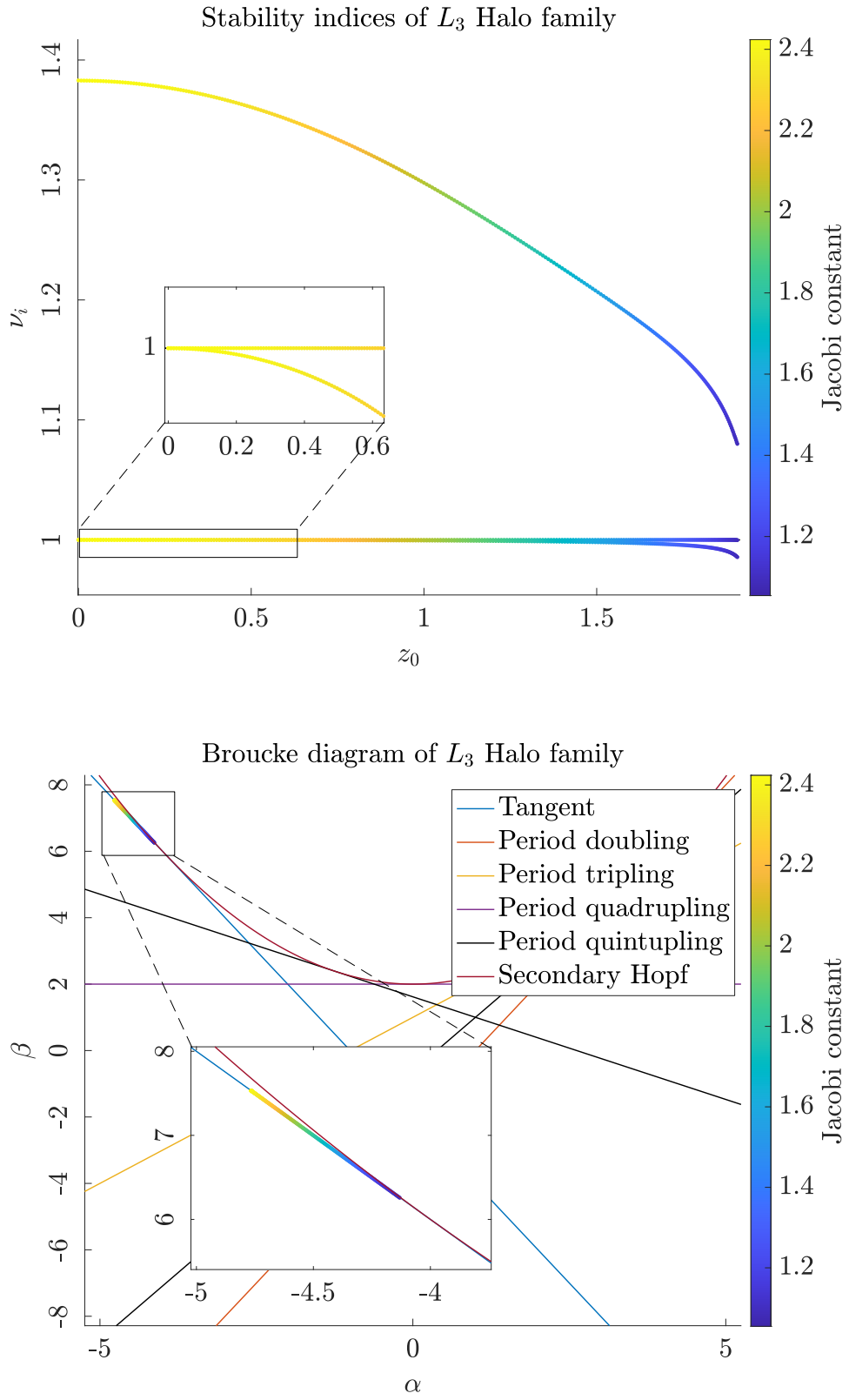

Figure 3.34: Plots showing the stability indices (top), and Broucke diagram (bottom) of the L_3 Halo family plotted against the value of x_0 used to identify the different Halo orbits.

3.11 Axial families of orbits

Similarly to the Halo families of orbits the Axial families near L_1, L_2 and L_3 are three dimensional orbits that emanate from bifurcation points found along the respective Lyapunov families. However the Axial families are symmetric with respect to the x axis so that the differential correction technique outlined in Section 3.3.3 has to be used. Similarly to what we have already seen for the Northern and Southern Halo families of orbits, there exists actually two families of L_i Axial families originating from the same bifurcation on the corresponding L_i Lyapunov family. Following the literature we will refer to these as the Northeastern and Northwestern L_i Axial families. In this case, given a Northwestern Axial orbit, the initial conditions for its Northeastern counterpart can be determined simply by inverting the sign of z_0 in the corresponding initial dynamical state $\boldsymbol{x}_0$, consequently both orbits will lie at the same value of the Jacobi constant $\mathcal{C}$.

That said the procedure to compute the L_i Halo family of orbits is as follows. First of all we need to select a Lyapunov orbit near the bifurcation that was previously computed in Section 3.8 of initial condition $\boldsymbol{x}_0$, that is located in the vicinity of the bifurcation. Then we need to choose a small fixed step size $\Delta\dot{z}_0$, the sign of which determines whether the Northeastern or Northwestern Axial family is computed, and we generate the initial guess for a new orbit with out of plane velocity component as:

$$\boldsymbol{x}_0 + (0, 0, 0, 0, 0, \Delta\dot{z}_0)^T. \tag{3.72}$$

At this point we can use equation (3.14), that is the differential correction method at fixed $\dot{z}_0$. Initially, and as long as the out of plane component is relatively small, we employ the mapping associated to the crossing with the xz plane, i.e., so that $y_f = 0$, and if $\Delta\dot{z}_0$ is small enough the procedure will converge to an Axial orbit with small out of plane velocity component. As the family grows vertically, the procedure will eventually break. Then we will need to switch to the mapping associated to the crossing with the xy plane, i.e., so that $z_f = 0$.

In Figures 3.35, 3.37 and 3.39 we show selected periodic orbits belonging to the L_1, L_2 and L_3 Axial families. In Figures 3.36, 3.38 and 3.40, we show the evolution of the orbital period along L_1, L_2 and L_3 Axial families, respectively. Lastly, in Figures 3.41, 3.42 and 3.43, we show the stability indices and the Broucke diagrams corresponding to L_1, L_2 and L_3 Axial families, respectively. It is worth noting that each of the Axial families terminates with a tangent bifurcation that gives rise to the L_1, L_2 and L_3 Vertical families of orbit, at the same time the Northeastern Axial family reunites with the Northwestern Axial family. Finally we note that the Vertical bifurcation is the only other bifurcation present along each Axial family, together with the tangent bifurcation with the corresponding Lyapunov family from which the Axial family originates. Additionally, all Axial orbits turn out to be linearly unstable.

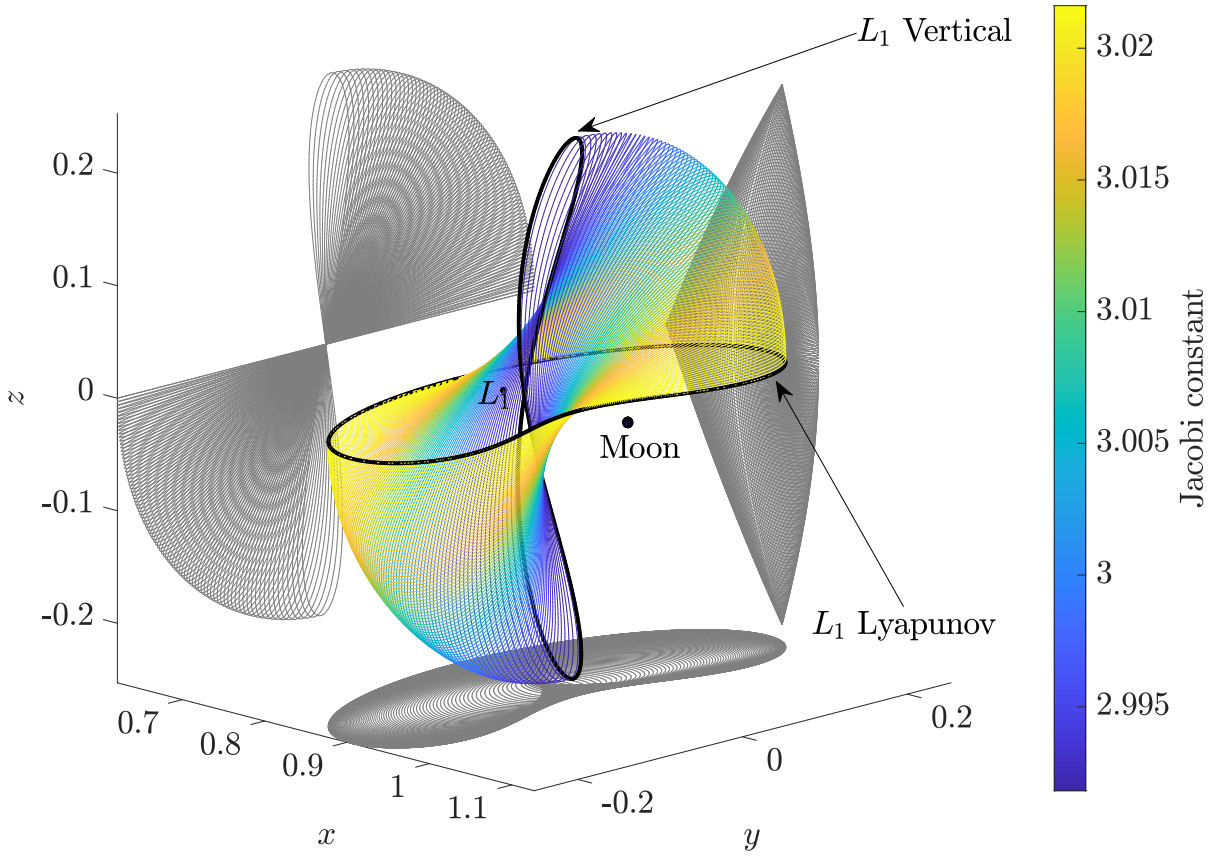

Figure 3.35: Family of Northeastern Axial orbits bifurcating from Lyapunov orbits near L_1.

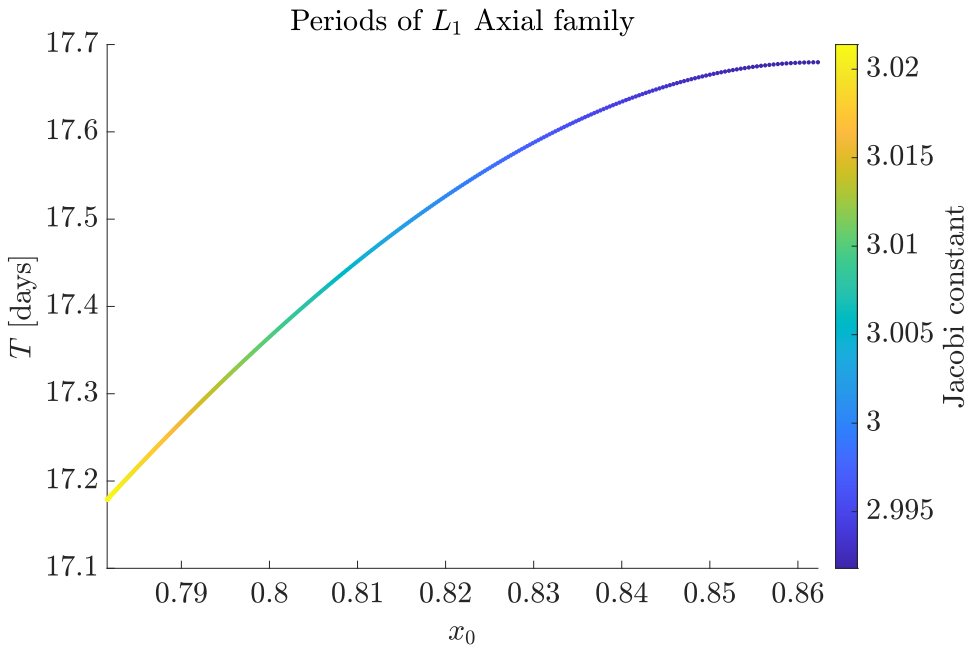

Figure 3.36: Periods in units of days and some of the relevant resonances of the orbits of the L_1 Axial family.

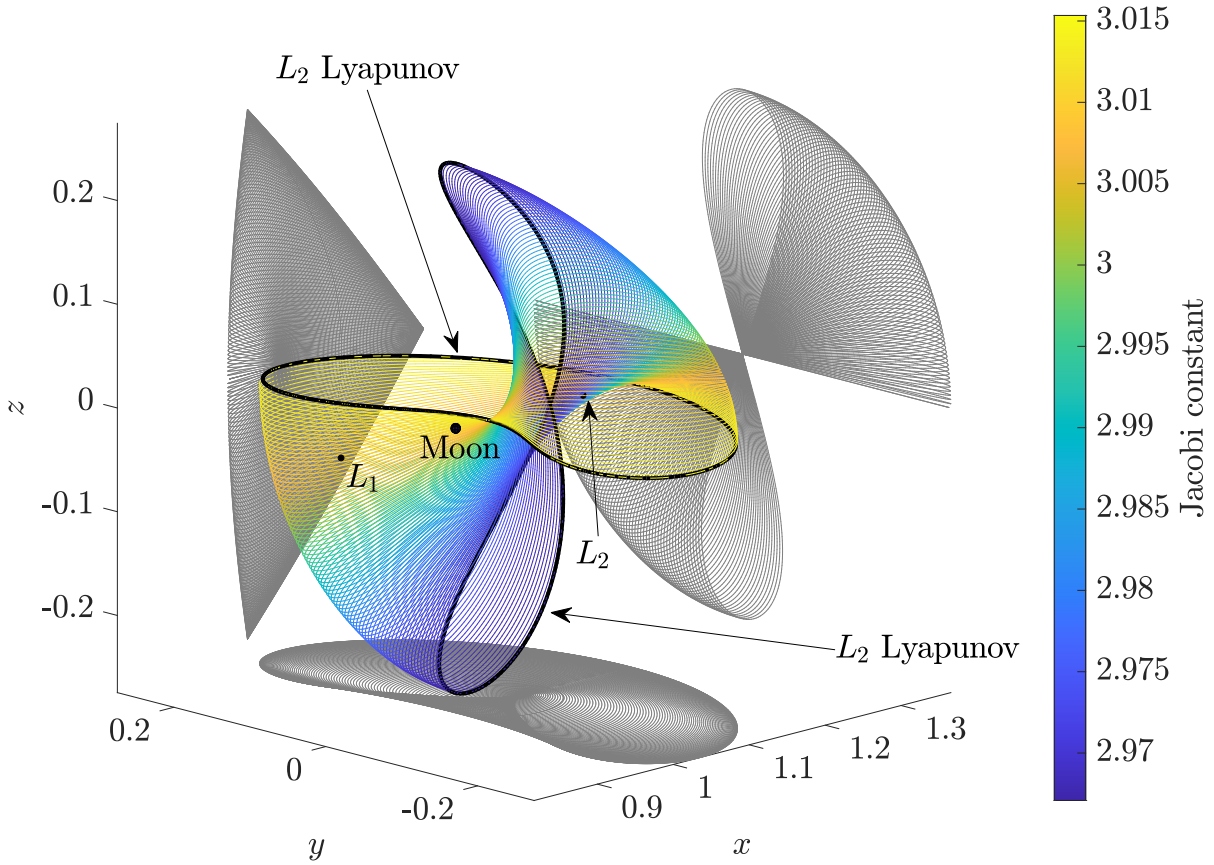

Figure 3.37: Family of Northwestern Axial orbits bifurcating from Lyapunov orbits near L_2.

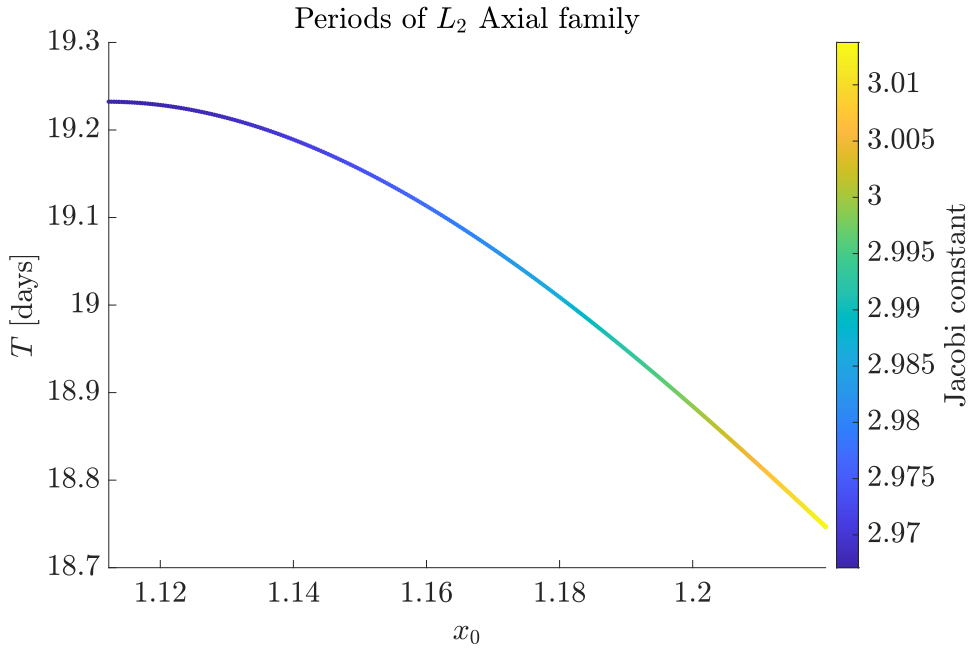

Figure 3.38: Periods in units of days and some of the relevant resonances of the orbits of the L_2 Axial family.

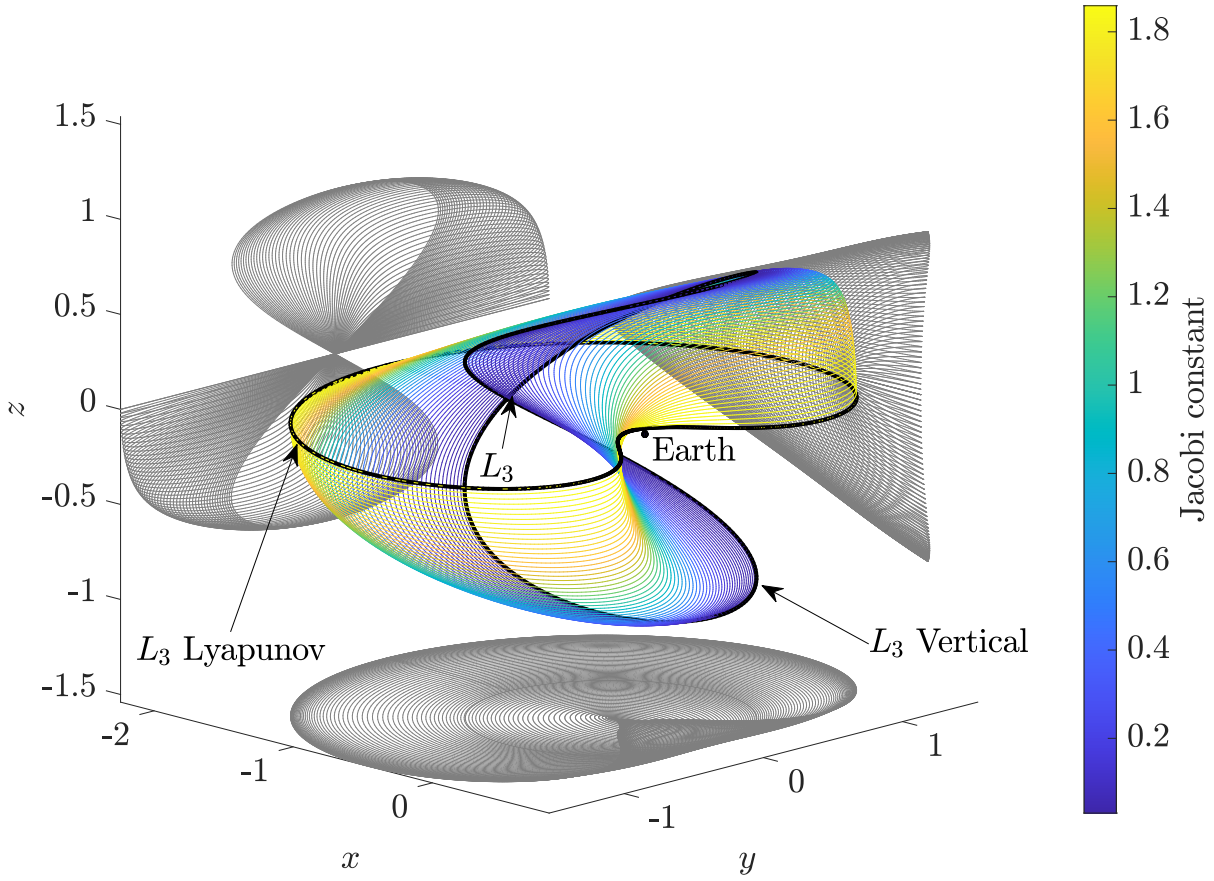

Figure 3.39: Family of Northeastern Axial orbits bifurcating from Lyapunov orbits near L_3.

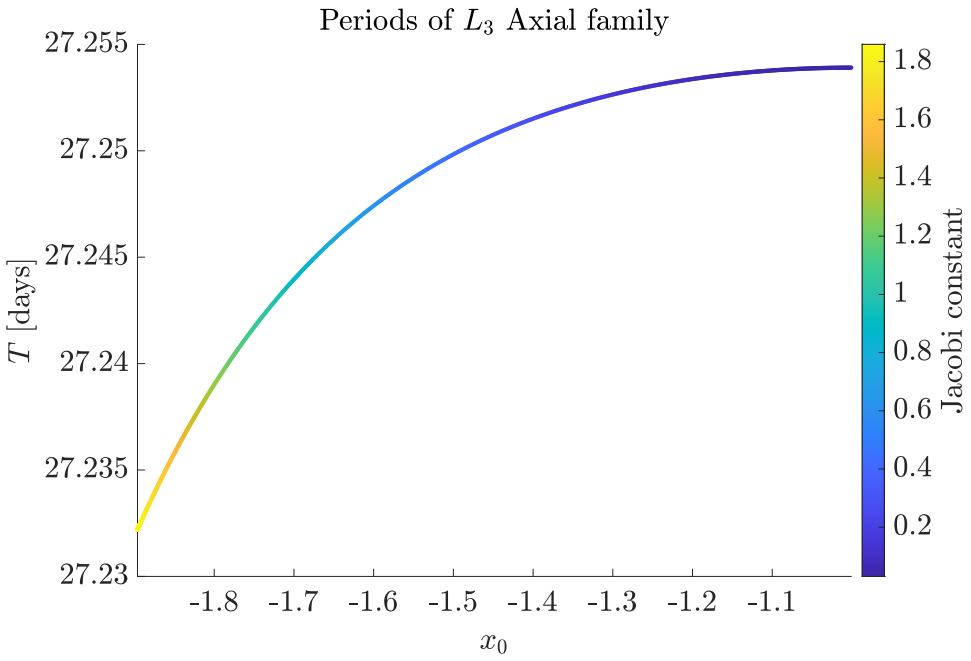

Figure 3.40: Periods in units of days and some of the relevant resonances of the orbits of the L_3 Axial family.

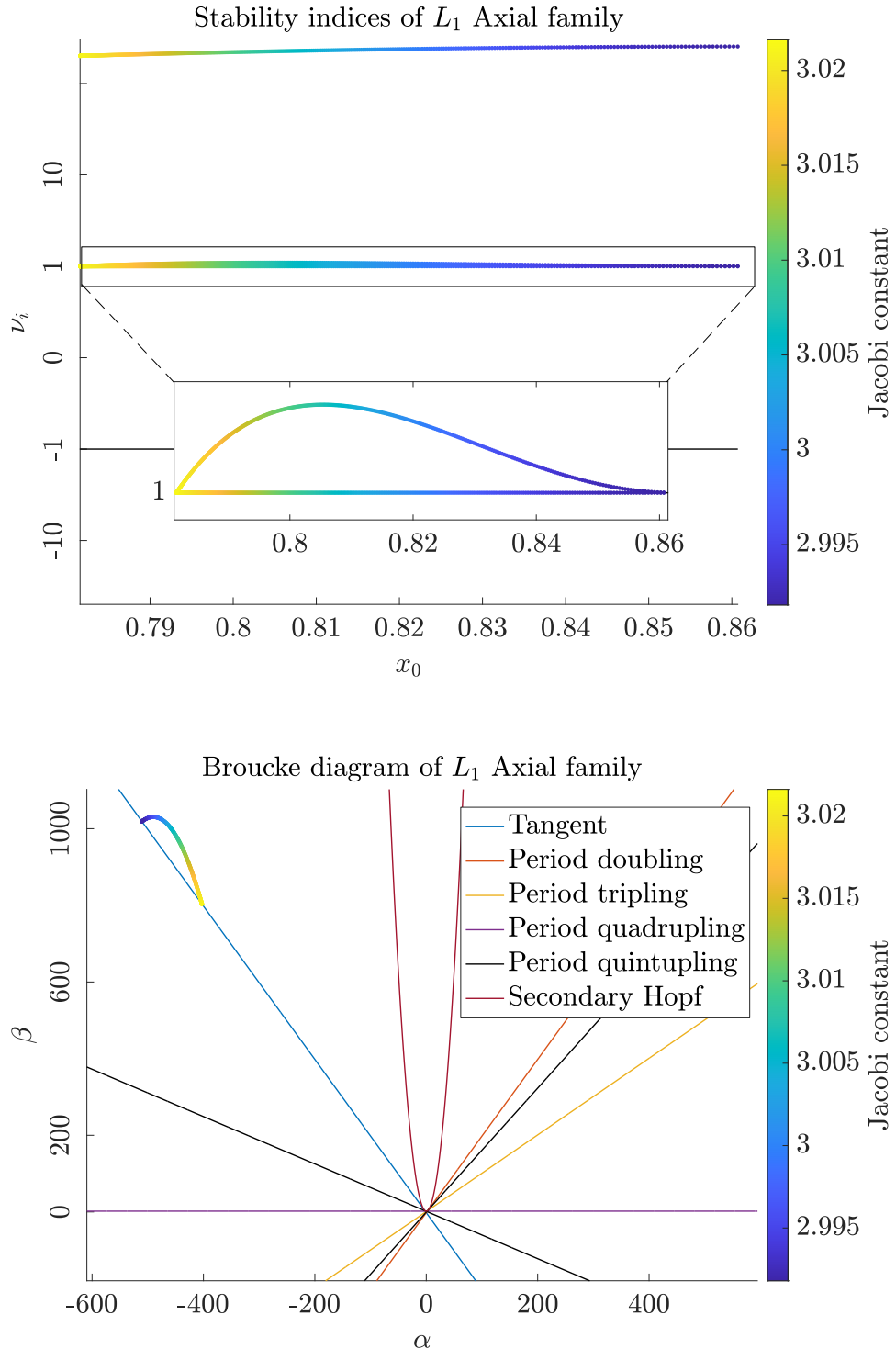

Figure 3.41: Plots showing the stability indices (top), and Broucke diagram (bottom) of the L_1 Axial family plotted against the value of x_0 used to identify the different Axial orbits.

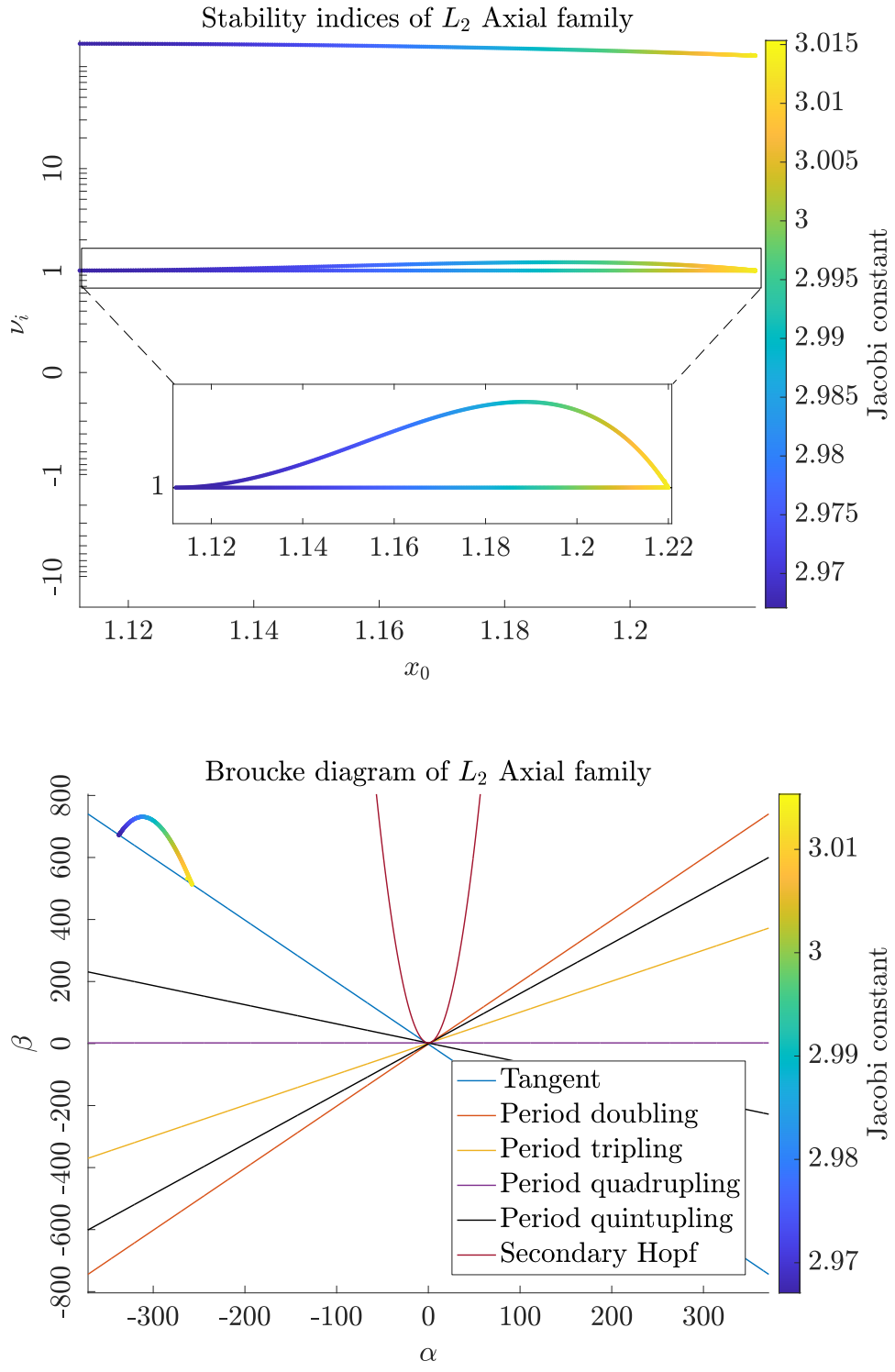

Figure 3.42: Plots showing the stability indices (top), and Broucke diagram (bottom) of the L_2 Axial family plotted against the value of x_0 used to identify the different Axial orbits.

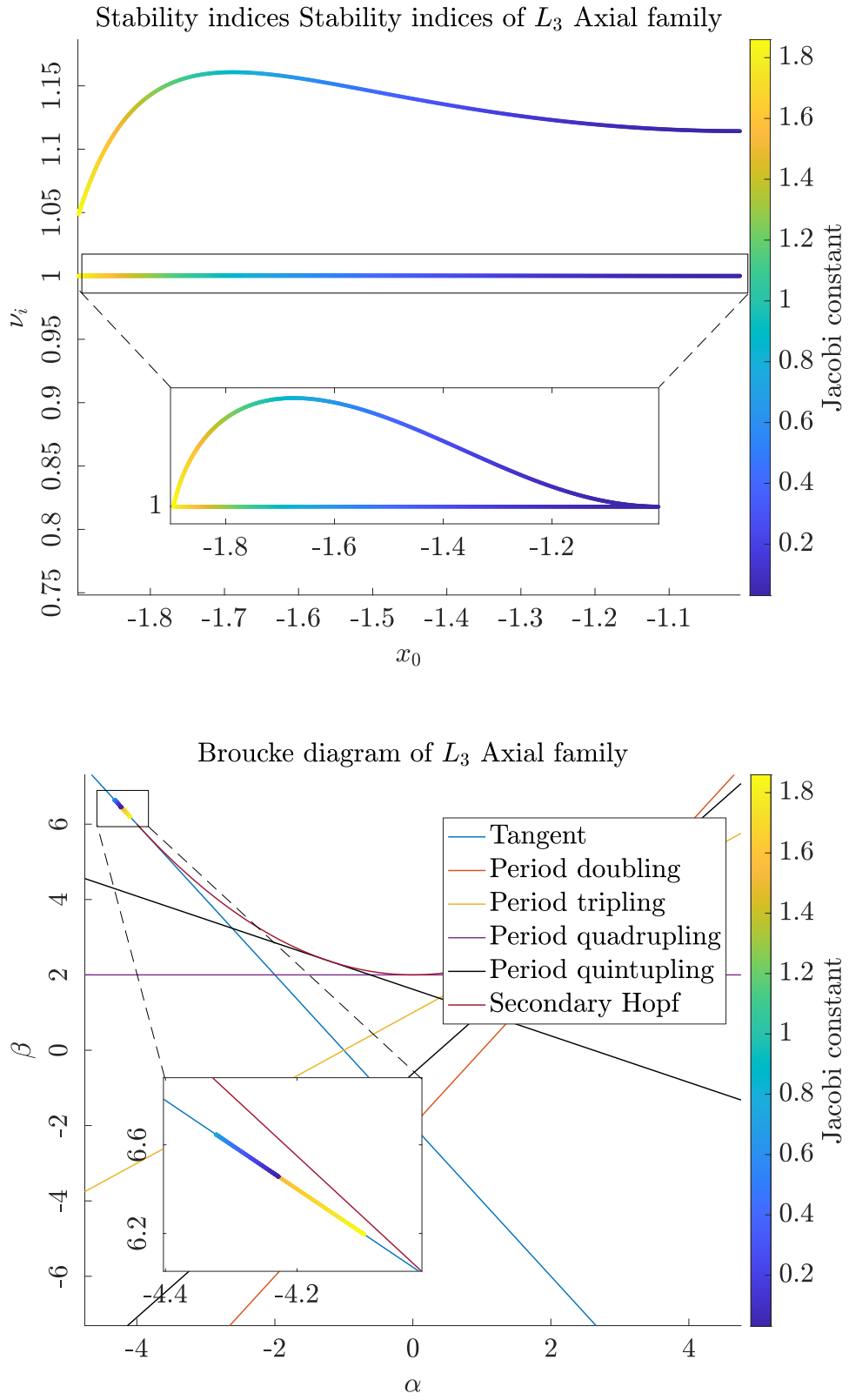

Figure 3.43: Plots showing the stability indices (top), and Broucke diagram (bottom) of the L_3 Axial family plotted against the value of x_0 used to identify the different Axial orbits.

3.12 Vertical families of orbits

The L_1, L_2 and L_3 Vertical families of orbits emanate from the bifurcations found at the end of the respective Axial families. The Vertical families are symmetric with respect to both the xz and xy plane, and as such it is also symmetric with respect to the x axis (obviously the vice versa is not true). Therefore in principle both the differential correction techniques, previously used for the Halo and Axial families can be employed. However a better way of proceeding is to exploit the symmetry with respect to both planes as described in Section 3.3.4, which also prevent the differential correction scheme to fall back into the Axial family when near to the bifurcation. Notice however that for the specific case of the L_1 Vertical family, and in particular for the branch that is obtained when walking in the negative $\mathcal{C}$ direction from the L_1 Axial bifurcation, the mapping that works with fixed $\dot{y}_0$, as described in Section 3.3.4, will eventually break down. This is due to the fact that $\dot{y}_0$ does not monotonically decrease along the entire branch. As a workaround, it is possible compute the initial part of this branch using the same mapping technique used for the L_1 Axial family, and then switch to the differential correction scheme of Section 3.3.4, when we are past the local minimum in $\dot{y}_0$.

That said, the procedure can be summarized as follows. First of all we select the Axial orbit, with initial dynamical state $\boldsymbol{x}_0$, from which the Vertical family bifurcates, that was already computed in Section 3.11. Then we choose a small fixed step size $\Delta\dot{y}_0$, the sign of which determines in which direction we walk through the family. To compute the complete families both negative and positive steps have to be employed starting from the bifurcation orbit. Then we can generate the initial guess for a new Vertical orbit as:

$$\boldsymbol{x}_0 + (0, 0, 0, 0, \Delta\dot{y}_0, 0)^T. \tag{3.73}$$

We then use equation (3.15), where t_f is the time of the crossing with the xz plane, i.e., so that $y_f = 0$, and if $\Delta\dot{y}_0$ is small enough the procedure will converge to Vertical orbit.

In Figure 3.44, 3.46 and 3.48 we show selected periodic orbits belonging to the L_1, L_2 and L_3 Vertical families. In Figures 3.45, 3.47 and 3.49, we show the evolution of the orbital period along L_1, L_2 and L_3 Axial families, respectively. Lastly, in Figures 3.50, 3.51 and 3.52, we show the stability indices and the Broucke diagrams corresponding to L_1, L_2 and L_3 Vertical families, respectively. It is worth noting that each of the bifurcation orbits corresponding to the termination of the respective Vertical family of orbits is a planar orbit, i.e., lies the xy plane. Additionally all orbits of the L_1 and L_2 Vertical orbits are unstable, this hold also for most of the L_3 Vertical orbits, with the exception of a stable portion of the family that lives closest to the in-plane bifurcation.

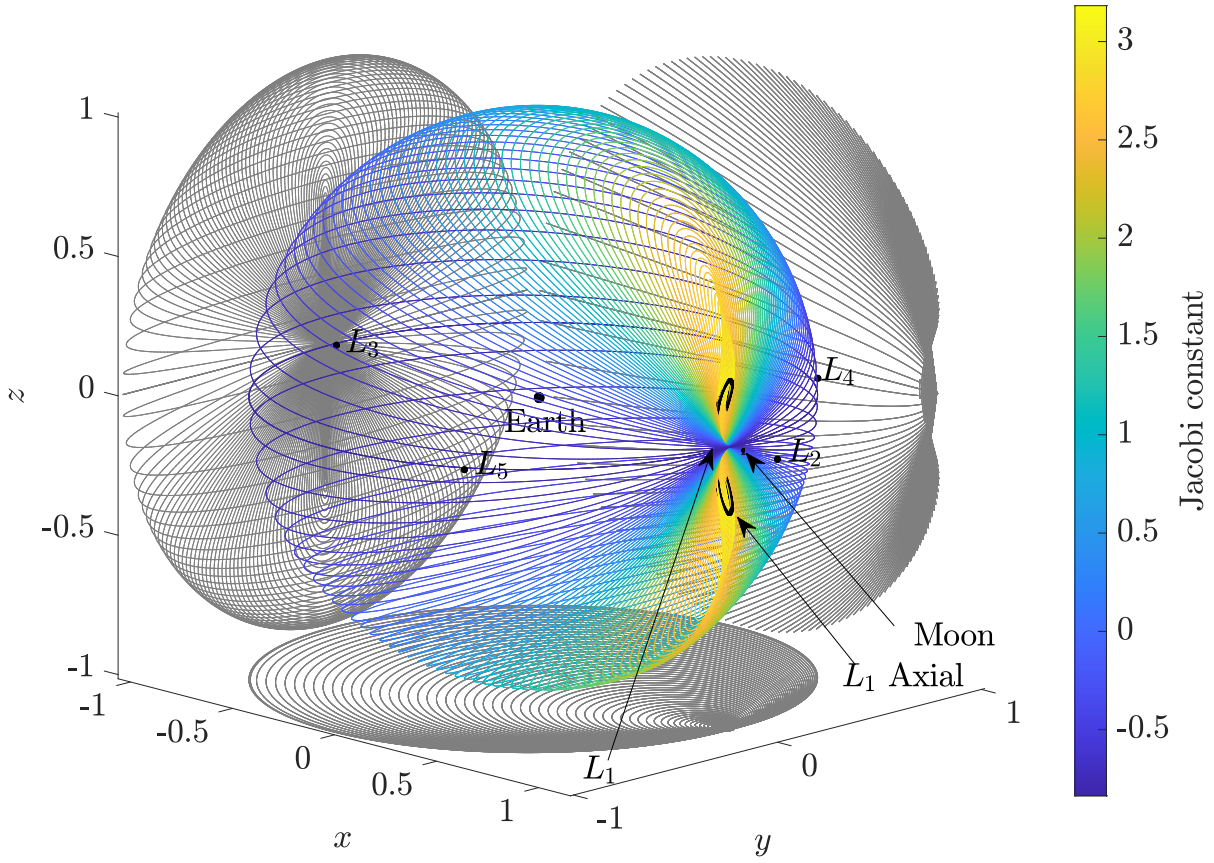

Figure 3.44: Family of L_1 Vertical orbits.

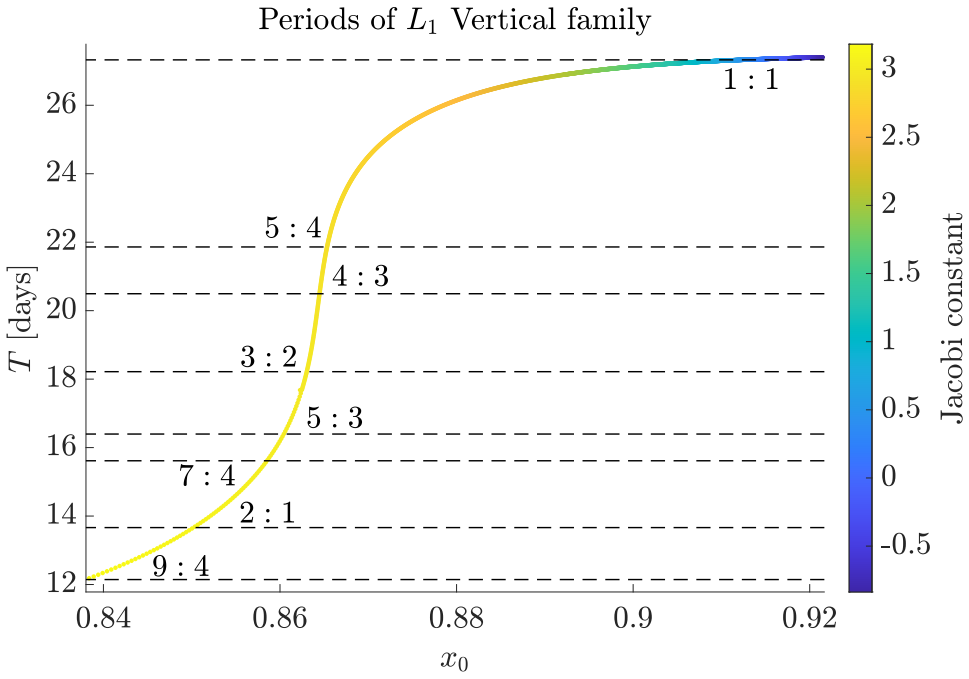

Figure 3.45: Periods in units of days and some of the relevant resonances of the orbits of the L_1 Vertical family.

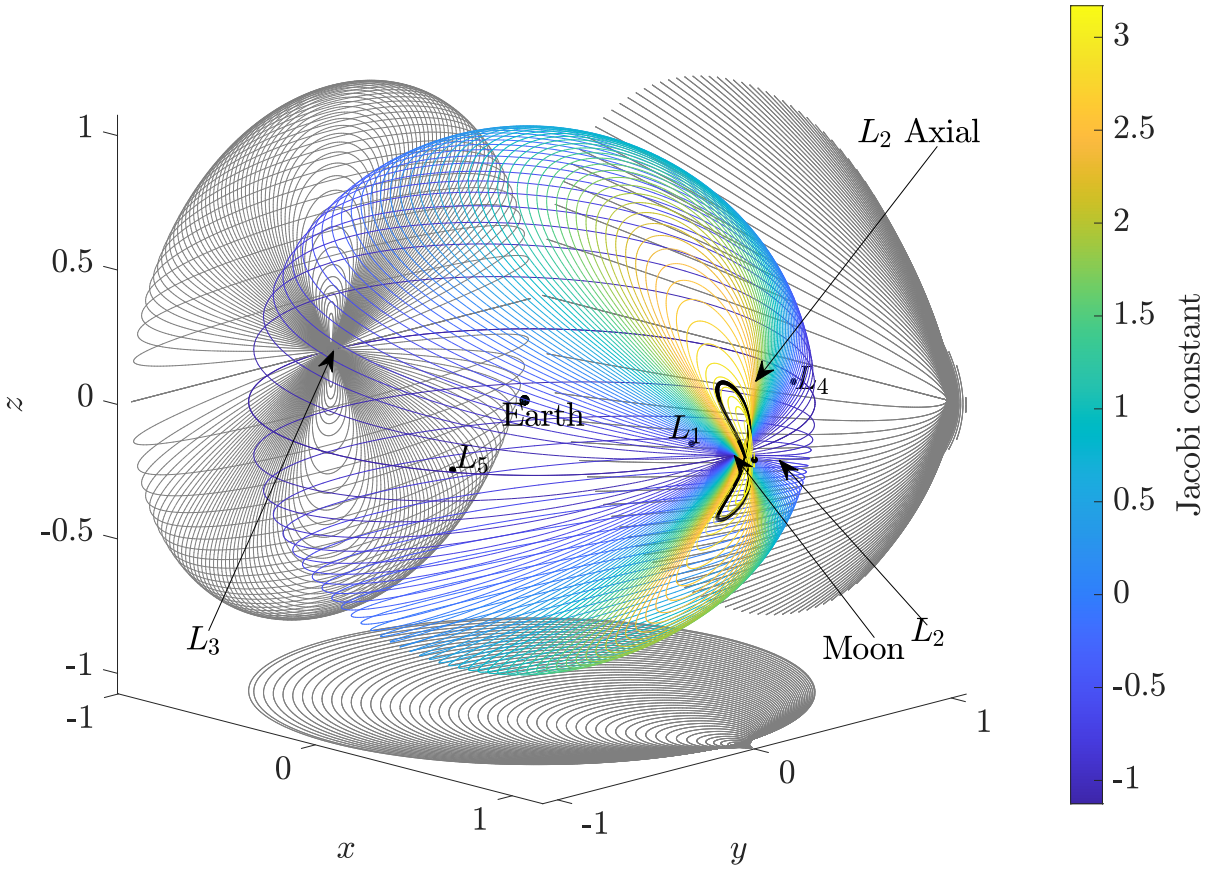

Figure 3.46: Family of L_2 Vertical orbits.

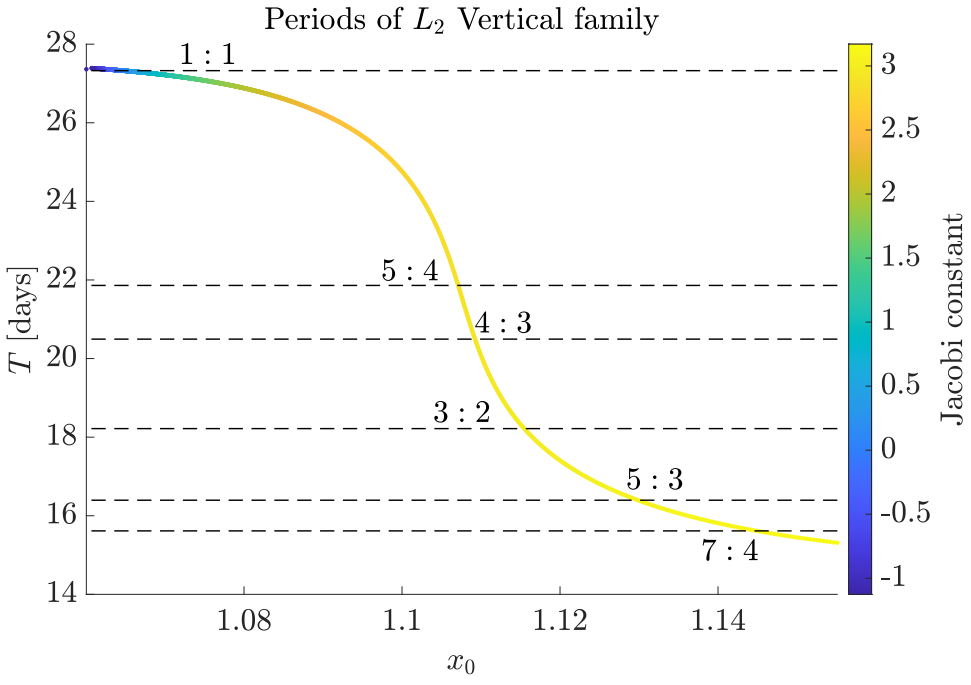

Figure 3.47: Periods in units of days and some of the relevant resonances of the orbits of the L_2 Vertical family.

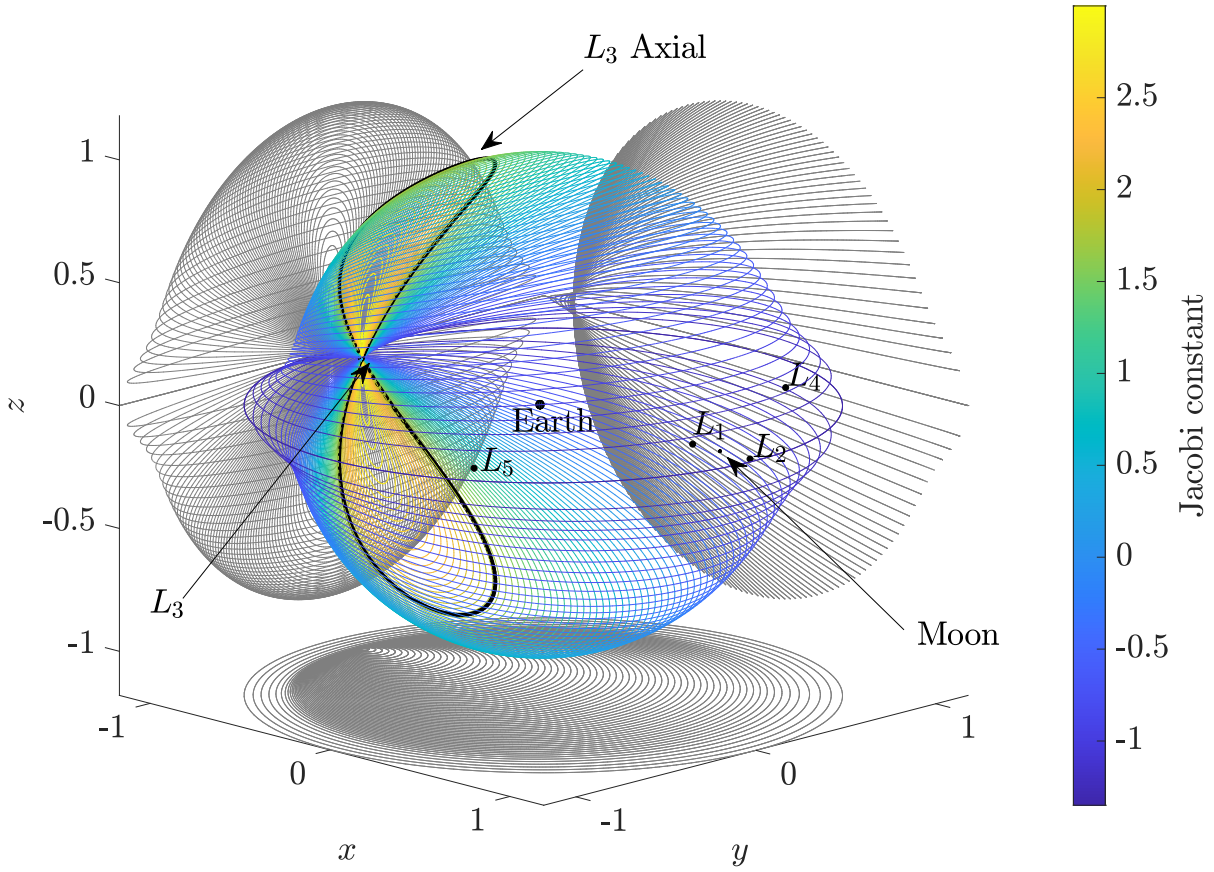

Figure 3.48: Family of L_3 Vertical orbits.

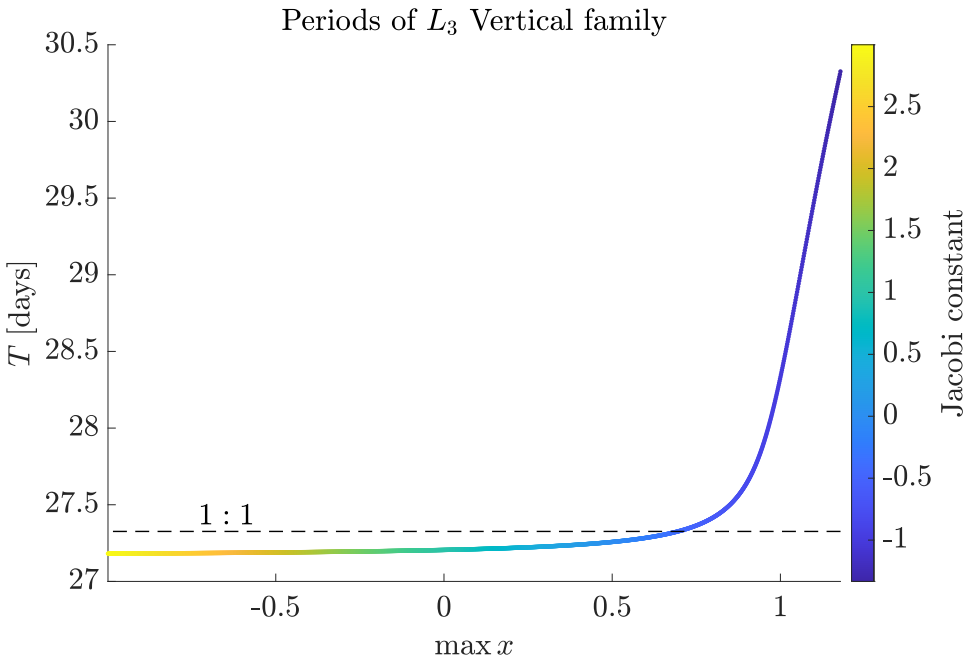

Figure 3.49: Periods in units of days and some of the relevant resonances of the orbits of the L_3 Vertical family.

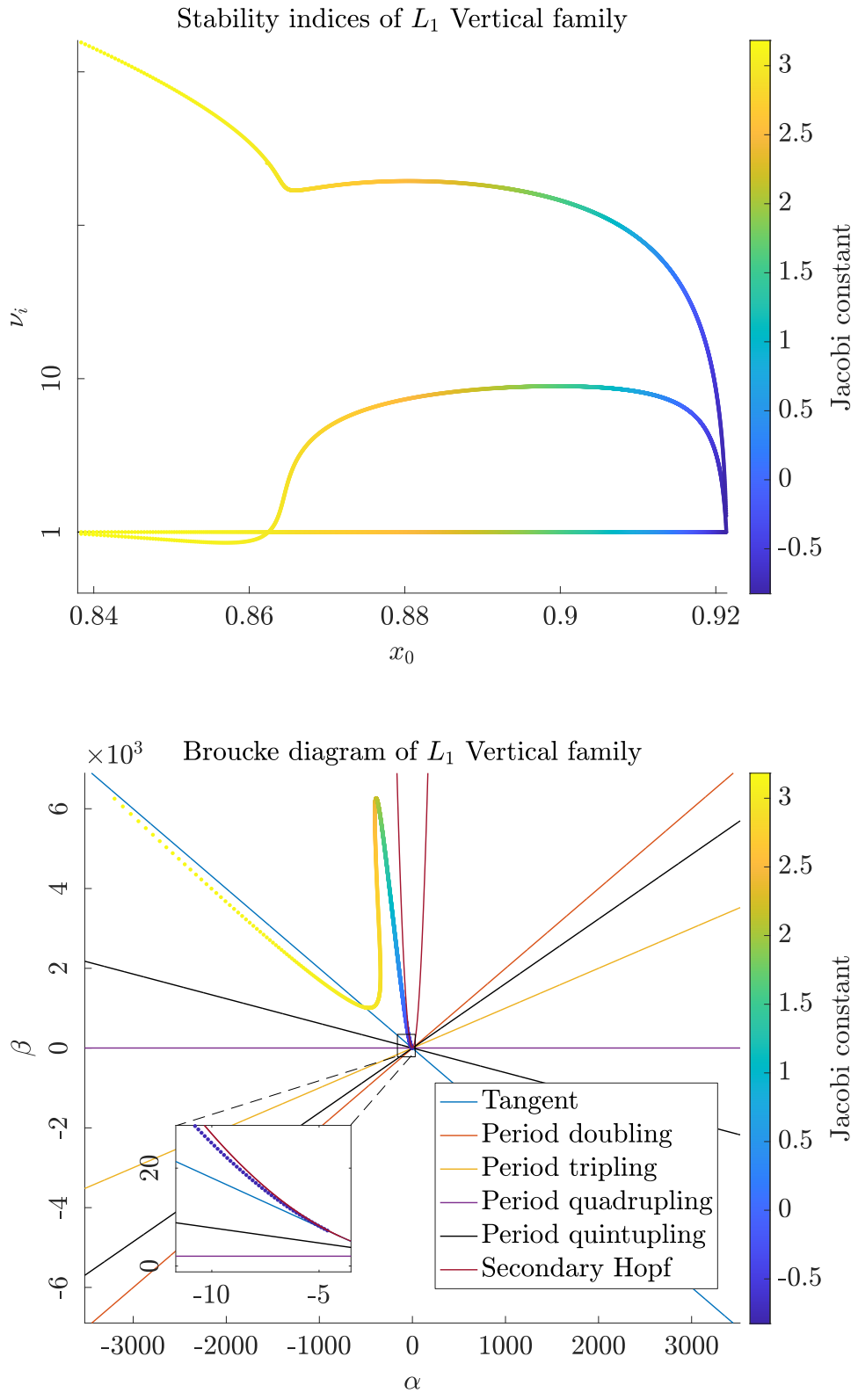

Figure 3.50: Plots showing the stability indices (top), and Broucke diagram (bottom) of the L_1 Vertical family plotted against the value of x_0 used to identify the different Vertical orbits.

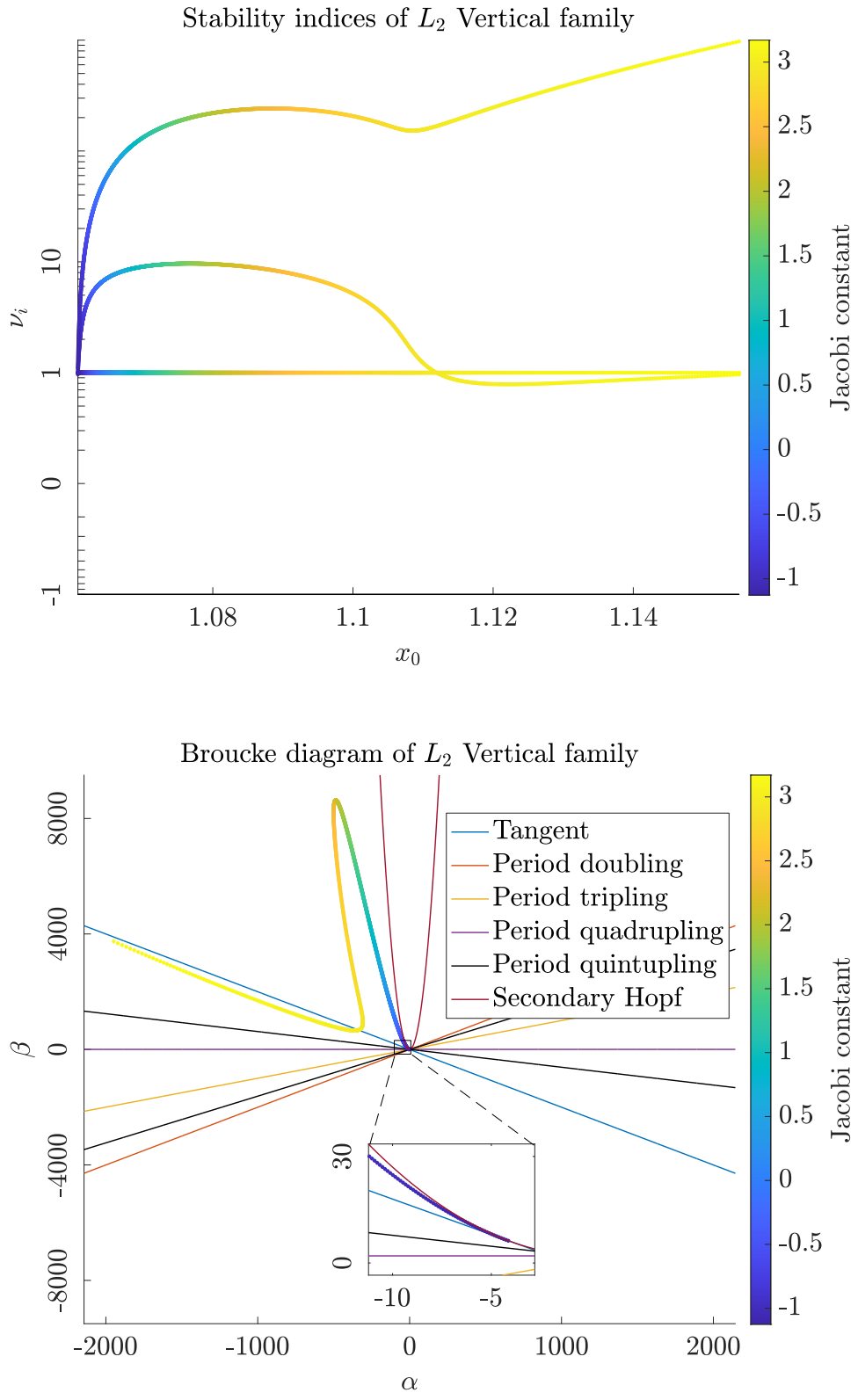

Figure 3.51: Plots showing the stability indices (top), and Broucke diagram (bottom) of the L_2 Vertical family plotted against the value of x_0 used to identify the different Vertical orbits.

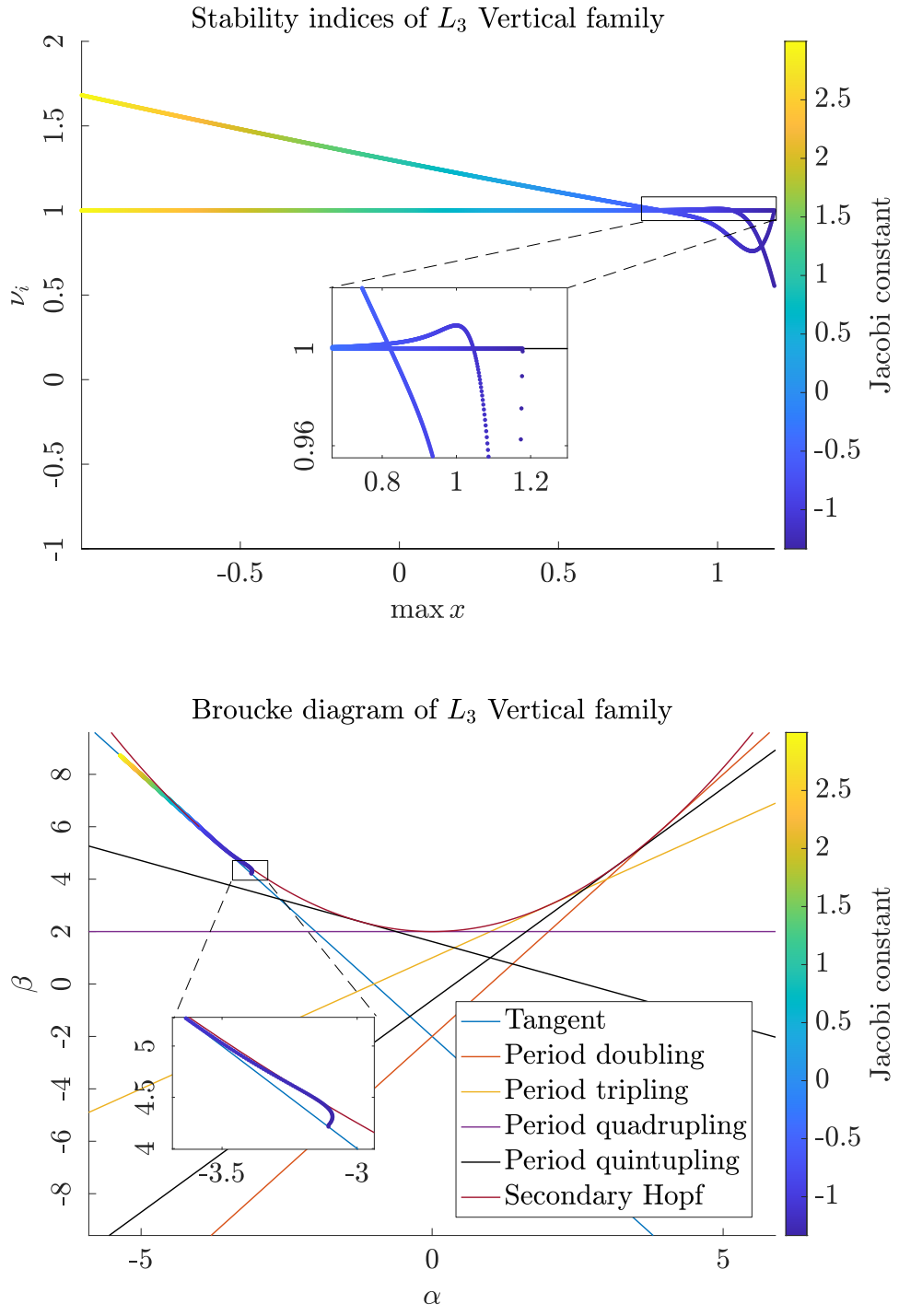

Figure 3.52: Plots showing the stability indices (top), and Broucke diagram (bottom) of the L_3 Vertical family plotted against the value of x_0 used to identify the different Vertical orbits.

Chapter 4

Homoclinic and heteroclinic connections

In this Section we will outline the procedure to find, if they exist, homoclinic and heteroclinic connections among Lyapunov orbits of the L_1 and L_2 families. In this context we call an homoclinc connection, a trajectory that connects a periodic orbit with itself, these depart along the unstable manifold and asymptotically approach the starting periodic orbit along its stable manifold after some period of time. On the other hand an heteroclinic connection is a trajectory that departs from one periodic orbits, e.g., an L_1 Lyapunov orbit, along its unstable manifold and then asymptotically approaches a different periodic orbit, e.g., an L_2 Lyapunov orbit along its stable manifold. Clearly for this to happen the two orbits need to lie at the same level of the Jacobi constant $\mathcal{C}$.

Throughout this section we will use the following notation. Let $\boldsymbol{\gamma}_{L_1}$ and $\boldsymbol{\gamma}_{L_2}$ be an L_1 and an L_2 Lyapunov orbit, respectively, and assume that they are associated to the same value of the Jacobi constant $\mathcal{C}$. We denote the stable and unstable manifolds of $\boldsymbol{\gamma}_{L_i}$, by $W^{s/u}(\boldsymbol{\gamma}_{L_i}) = W^{s/u}_{L_i}$, $i = 1, 2$. Moreover we introduce the following definitions. Let π be a Poincaré section, as defined in Section 3.1, and let $p \in \mathbb{N}$ be some positive integer. Then we define $\Gamma^{u,p}_{\pi}(\boldsymbol{x}(t))$, $\Gamma^{s,p}_{\pi}(\boldsymbol{x}(t))$, as the dynamical state at the time of the $p-$th intersection of the flow $\varphi(\boldsymbol{x}(t)$ with the plane π, in forward or backward time respectively, relative to some reference initial time t_0. Moreover given a periodic orbit $\boldsymbol{\gamma}$, with a little abuse of notation we can define:

$$\Gamma^{u,p}_{L_1} \equiv \Gamma^{u,p}_{\pi}(W^u(\boldsymbol{\gamma})) = \bigcup_{t_i \in [0,T]} \Gamma^{u,p}_{\pi}\big(\boldsymbol{x}(t_i) \pm \varepsilon \boldsymbol{v}_u(t_i)\big), \tag{4.1}$$

$$\Gamma^{s,q}_{L_1} \equiv \Gamma^{s,q}_{\pi}(W^s(\boldsymbol{\gamma})) = \bigcup_{t_i \in [0,T]} \Gamma^{u,q}_{\pi}\big(\boldsymbol{x}(t_i) \pm \varepsilon \boldsymbol{v}_s(t_i)\big). \tag{4.2}$$

The subscript π will be dropped when doing so will not cause any ambiguity.

Before showing how heteroclinic and homoclinic connections can be constructed numerically, we present some analytical results. In 1985, Llibre, Martinez, and Simó [29] devoted their efforts to show that under appropriate conditions, the invariant manifolds of the L_1 Lyapunov orbits intersect transversely. In particular they were able to prove two theorems that we report here [29, 25]. Together these two theorems imply that for sufficiently small mass parameter μ and for an appropriate range of the Jacobi constant $\mathcal{C} < \mathcal{C}_1$, the invariant manifolds $W^s_{L_1}$ and $W^u_{L_1}$ intersect transversely in the interior realm, i.e., the region surrounding P_1, the largest of the primaries . Recall that in our notation $\mathcal{C}_1$ is the Jacobi constant associated with the Lagrangian point L_1. Moreover, we want to

emphasize that L_1 Lyapunov orbits can only exist values of the Jacobi constant smaller than $\mathcal{C}_1$.

Theorem 8 (Llibre-Martinez-Simó)**.** *For μ sufficiently small, the branch of $W^u_{L_1}$ in the interior realm has a projection on position space given by*

$$d = \mu^{\frac{1}{3}} \left(3N^2\right)^{\frac{1}{6}} - 3 + M\cos t + o(1),$$
$$\theta = -\pi + \mu^{\frac{1}{3}}(Nt + 2M\sin t + o(1)),$$

where d is the distance to the zero velocity curve, θ is the angular coordinate, and N and M are constants. In particular, for a sequence of values of μ which have the following asymptotic expression:

$$\mu_k = \frac{1}{N^3 k^3}(1 + o(1)), \tag{4.3}$$

the first intersection of this projection with the x axis is orthogonal to that axis, giving a symmetric $(1,1)$-homoclinic orbit for L_1. The prefix (1,1) refers to the first intersection (with the Poincaré section defined by the plane $y = 0$, $x < 0$) of both the stable and unstable manifolds of L_1.

Theorem 9 (Llibre-Martinez-Simó)**.** *For μ and $\Delta\mathcal{C} = \mathcal{C}_1 - \mathcal{C}$ sufficiently small, the branch $W^u_{L_1}$ contained initially in the interior realm of the energy surface intersects the plane $y = 0$ for $x < 0$ in a curve diffeomorphic to a circle. In particular, for points in the $(\mu, \mathcal{C})$ plane such that there is a μ_k of Theorem 8 for which*

$$\Delta\mathcal{C} > L\mu^{\frac{4}{3}}(\mu - \mu_k)^2, \tag{4.4}$$

where L is a constant, there exist symmetric transversal $(1,1)$-homoclinic orbits.

Theorems 8 and 9 focus on studying the transversality of the invariant manifolds for the L_1 Lyapunov orbits with Jacobi constant slightly smaller than $\mathcal{C}_1$. Additionally in [29], formulas for this intersection as functions of μ and $\Delta\mathcal{C}$ were provided. However, these expression are rather complex and of difficult interpretation [25]. Then main idea behind these results is that if we have an expression for the first intersection of the unstable manifold with the plane $y = 0$, which we denote by $\Gamma^{u,1}_{L_1}$, and find an orthogonal intersection with the x axis, i.e., $\dot{x} = 0$, then by the symmetry (2.55) of the equations of motion, we would obtain also an intersection of the stable manifold $\Gamma^{s,1}_{L_1}$ with the same plane, and the intersection would correspond to the same point in phase space, providing a symmetric $(1,1)$-homoclinic connection for $\boldsymbol{\gamma}_{L_1}$.

4.0.1 Homoclinic and heteroclinic connections between Lyapunov orbits in the Moon region

We will now see how the ideas presented in the previous section can be applied to numerically construct different types of homoclinic and heteroclinic connections. Before proceeding we want to stress that at a fixed μ these trajectories may exist only for some values of the Jacobi constant $\mathcal{C}$.

We have seen in Section 3.8 that there exists a unique family of Lyapunov orbits in the vicinity of each of the collinear points, that is parametrized by the Jacobi constant $\mathcal{C}$. The idea now is to look for the zero energy transfers which connects $\boldsymbol{\gamma}_{L_i}$ to $\boldsymbol{\gamma}_{L_j}$,

as we anticipated if $i = j$ we call this an homoclinic connection, or an heteroclininc connection if if $i \neq j$. Homoclinic and heteroclinic connections can be found by looking for intersections between the stable manifold of $\boldsymbol{\gamma}_{L_i}$ with the unstable manifold of the $\boldsymbol{\gamma}_{L_j}$, indeed if such an intersection is found the corresponding trajectory will approach asymptotically $\boldsymbol{\gamma}_{L_i}$ in forward time and $\boldsymbol{\gamma}_{L_j}$ in backward time.

Suppose now that we are interested in finding an heteroclinic/homoclinic connections from $\boldsymbol{\gamma}_{L_i}$ to $\boldsymbol{\gamma}_{L_j}$ in the Moon region. Then we need to look for intersections between $\Gamma^{u,p}_{L_i}$ and $\Gamma^{s,q}_{L_j}$, i.e., the $p-$th and the $q-$th Poincaré cuts with the Moon plane $x = 1-\mu$ of the unstable manifold, $W^u_{L_i}$, and of the stable manifold $W^s_{L_j}$, respectively. To do this we can simply find the intersections between $\Gamma^{u,p}_{L_i}$ and $\Gamma^{s,q}_{L_j}$, in the $y\dot{y}$ plane, and assume them to be closed curves in this plane, then if an intersection exists at the point $A = (y_A, \dot{y}_A)$, we can recover the value of $|\dot{x}_A|$, by imposing that the intersection point has Jacobi constant equal to $\mathcal{C}$ and solving for $\dot{x}_A$, i.e.,

$$\mathcal{C} = 2\mathcal{U}(x_A, y_A, 0) - (\dot{x}_A^2 + \dot{y}_A^2), \tag{4.5}$$

then we can determine the sign of $|\dot{x}_A|$, by imposing that it is consistent with the direction from which the manifolds intersects the Moon plane. Finally we can integrate the trajectory that starts at

$$\boldsymbol{x}_A = (x_A, y_A, 0, \dot{x}_A, \dot{y}_A, 0)^T, \quad x_A = 1-\mu, \tag{4.6}$$

both forward and backward in time to find the (p, q)-homoclinic/heteroclinic connection $\varphi(\boldsymbol{x}_A, t)$.

In summary the possible types of connection in considerations are:

- (p, q)-homoclinic connection of $\boldsymbol{\gamma}_{L_i}$, if $\Gamma^{s,p}_{L_i} \cap \Gamma^{u,q}_{L_i} \neq \emptyset,\ i = 1, 2,$
- (p, q)-heteroclinic connection from $\boldsymbol{\gamma}_{L_i}$ to $\boldsymbol{\gamma}_{L_j}$, if $\Gamma^{s,p}_{L_i} \cap \Gamma^{u,q}_{L_j} \neq \emptyset,\ i = 1, 2,\ i \neq j.$

For homoclinic/heteroclinic connections in the Moon region, it is of interest the number of times the connecting orbit goes around the Moon. It turns out [6], that the number of loops n is:

- $n = (p + q - 1)/2,$ for (p, q)-homoclinic connections,
- $n = (p + q - 2)/2,$ for (p, q)-heteroclinic connections.

Consequently it must that $\kappa = p + q - 1$, i.e., the number of times the Moon plane is crossed, must be even for homoclinic connections and odd for the heteroclinic ones [6].

Additionally, because of the symmetry (2.55) of the equations of motion, for each heteroclinic connection $\varphi(\boldsymbol{x}_A, t)$ connecting $\boldsymbol{\gamma}_{L_1}$ to $\boldsymbol{\gamma}_{L_2}$, there exists one from $\boldsymbol{\gamma}_{L_2}$ to $\boldsymbol{\gamma}_{L_1}$ that is symmetric with respect to the xz plane. These two heteroclinic connections together form a symmetric heteroclinic cycle.

It is worth noting, that the homoclinic and heteroclinic orbits do not exist for all values of $\mathcal{C}$, as the invariant manifolds do not necessarily intersect (see e.g., Figure 4.6).

We conclude with some relevant details about the numerical procedure that we described above.

Note that In order to compute the intersection of the manifolds with the Moon plane, we need to compute the crossing with very high accuracy, this can be done as described in Section 3.1.1.

The closed curves in the Poincaré section plot are obtained by computing a number of trajectories on the order 10^3 belonging to each manifold. Then the intersection of the stable/unstable manifold is computed and projected onto the chosen Poincaré section (the Moon plane in our case). Lastly, the closed curves on the Poincaré section are obtained by and linearly interpolating the points corresponding to each of the trajectories of the stable/unstable manifold.

The procedure explained above requires that $\boldsymbol{\gamma}_{L_1}$ and $\boldsymbol{\gamma}_{L_2}$ have the same Jacobi constant $\mathcal{C}$, within some tight tolerance, e.g., $\tau = 10^{-8}$. In order to achieve this we use a bisection method, coupled with the same differential correction scheme that we used for computing the families of Lyapunov orbits in Section 3.8. More specifically, let $\boldsymbol{x}_0^+$ and $\boldsymbol{x}_0^-$, be the dynamical states of two Lyapunov orbit with Jacobi constants above and below larger the target value $\mathcal{C}$, and let $\Delta x_0 = x_0^- - x_0^+$. We then compute a new orbit at $\tilde{x}_0 = x_0^+ + \Delta x_0/2$, using a differential correction scheme, and check if the value $\tilde{\mathcal{C}}$ of its Jacobi constant is equal to $\mathcal{C}$ within the given tolerance τ, i.e.,

$$|\tilde{\mathcal{C}} - \mathcal{C}| < \tau, \tag{4.7}$$

otherwise, either x_0^+ or x_0^- is replaced with $\tilde{x}_0$ depending on whether $\tilde{\mathcal{C}} \lessgtr \mathcal{C}$. This procedure is reiterated until the condition (4.7) is satisfied.

In Figures 4.1 – 4.5 we show examples of $(1,1)$-homoclinic connections for both L_1 and L_2 Lyapunov orbits, as well as $(1,1)$-heteroclinic and $(1,2)$-heteroclinic connections among an L_1 to an L_2 Lyapunov orbits, at different values of $\mathcal{C}$.

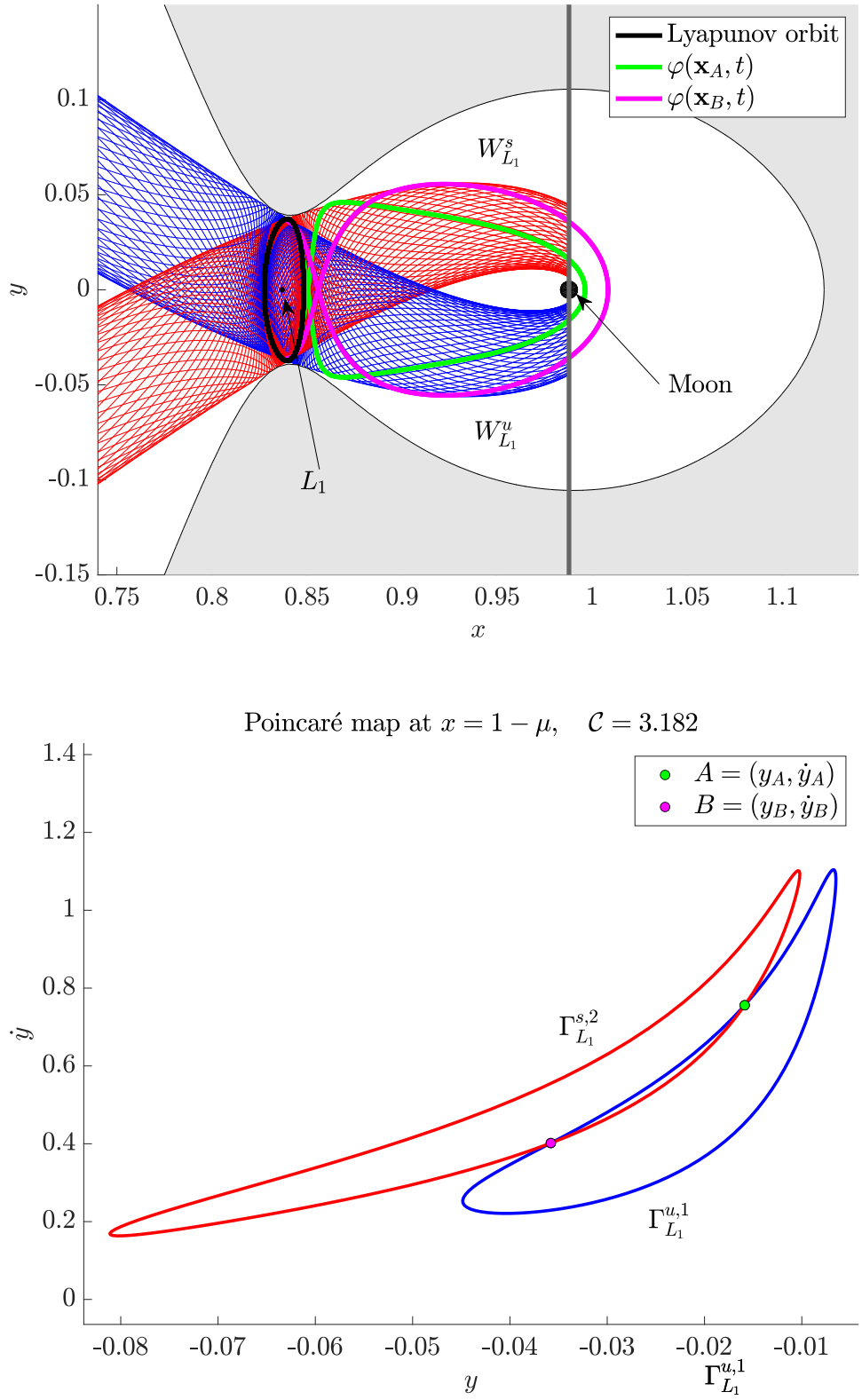

Figure 4.1: In the top panel we show two $(1, 2)$-homoclinic connections of an L_1 Lyapunov orbit at $\mathcal{C} = 3.182$, and their stable (red) and unstable (blue) manifolds. In the bottom panel we show the Poincaré map of the first and second crossing with the Moon plane of $W^u_{L_1}$ and $W^s_{L_1}$, respectively, and their intersection points.

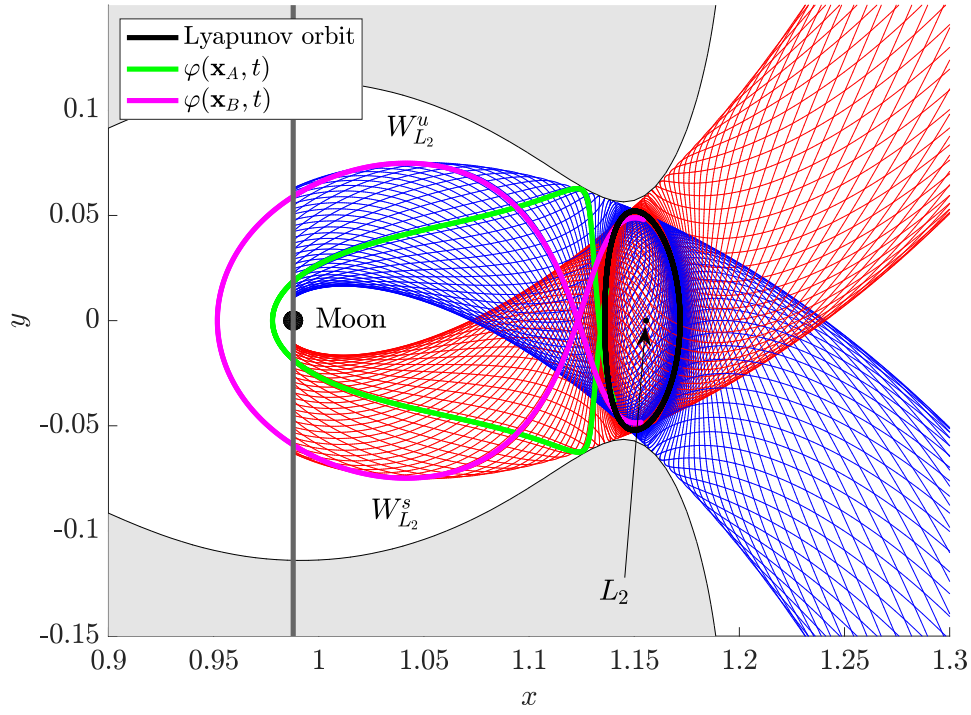

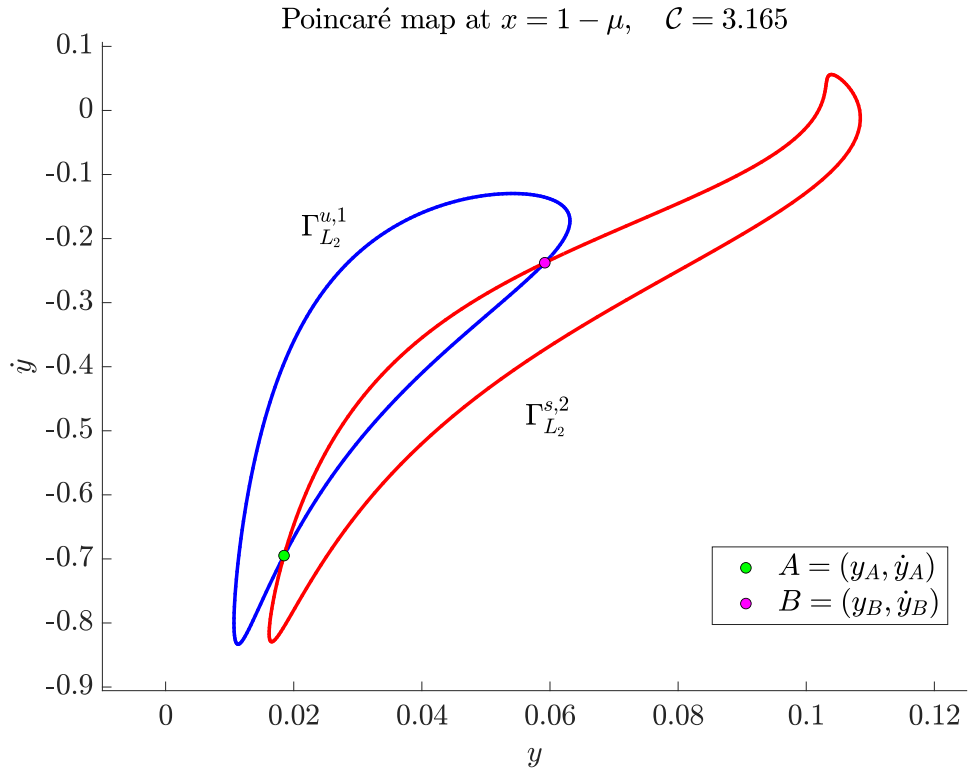

Figure 4.2: In the top panel we show two $(1,2)$-homoclinic connections of an L_2 Lyapunov orbit at $\mathcal{C} = 3.165$, and their stable (red) and unstable (blue) manifolds. In the bottom panel we show the Poincaré map of the first and second crossing with the Moon plane of $W^u_{L_1}$ and $W^s_{L_1}$, respectively, and their intersection points.

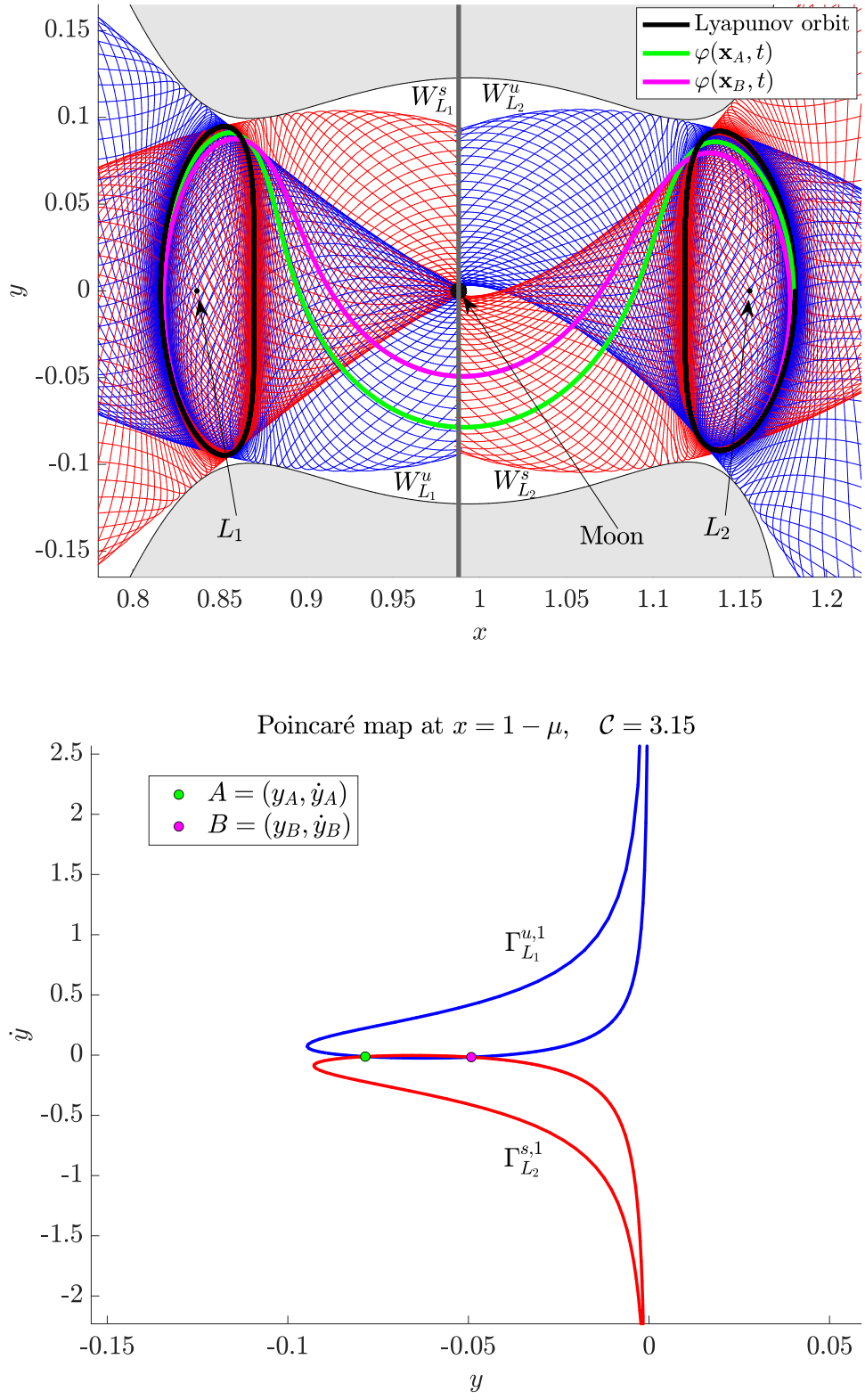

Figure 4.3: In the top panel we show two $(1,1)$-heteroclinic connections from an L_1 Lyapunov orbit to an L_2 Lyapunov orbit at $\mathcal{C} = 3.15$, and their stable (red) and unstable (blue) manifolds. In the bottom panel we show the Poincaré map of the first crossing with the Moon plane of $W^u_{L_1}$ and $W^s_{L_2}$ and their intersection points.

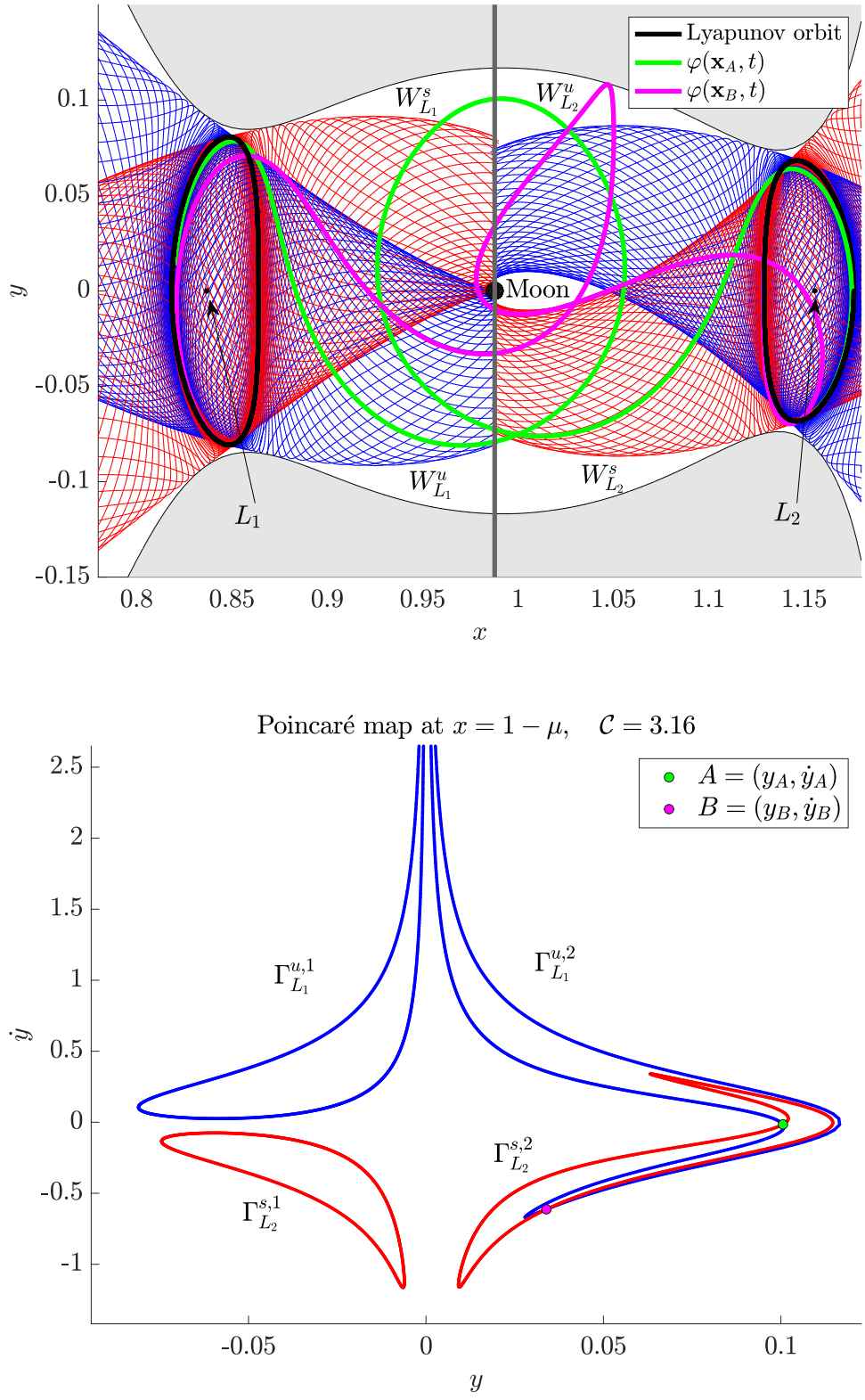

Figure 4.4: In the top panel we show two $(2,2)$-heteroclinic connections from an L_1 Lyapunov orbit to an L_2 Lyapunov orbit at $\mathcal{C} = 3.16$, and their stable (red) and unstable (blue) manifolds. In the bottom panel we show the Poincaré map of the first and second crossing with the Moon plane of $W^u_{L_1}$ and $W^s_{L_2}$ and their intersection points. Notice that in this case there exists no $(1,1)-$heteroclinic connection.

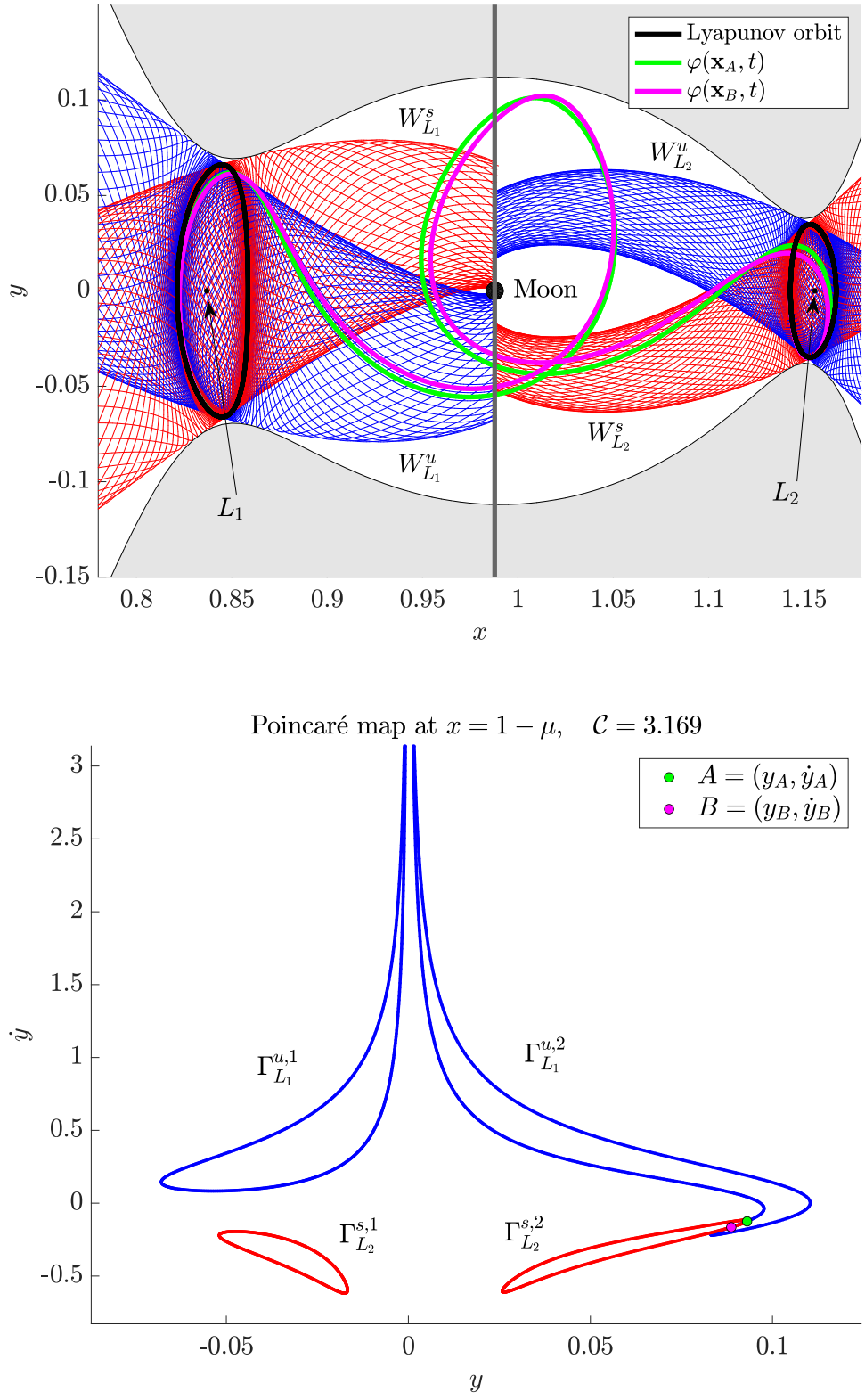

Figure 4.5: In the top panel we show two $(2, 2)$-heteroclinic connections from an L_1 Lyapunov orbit to an L_2 Lyapunov orbit at $\mathcal{C} = 3.169$, and their stable (red) and unstable (blue) manifolds. In the bottom panel we show the Poincaré map of the first and second crossing with the Moon plane of $W^u_{L_1}$ and $W^s_{L_2}$ and their intersection points.

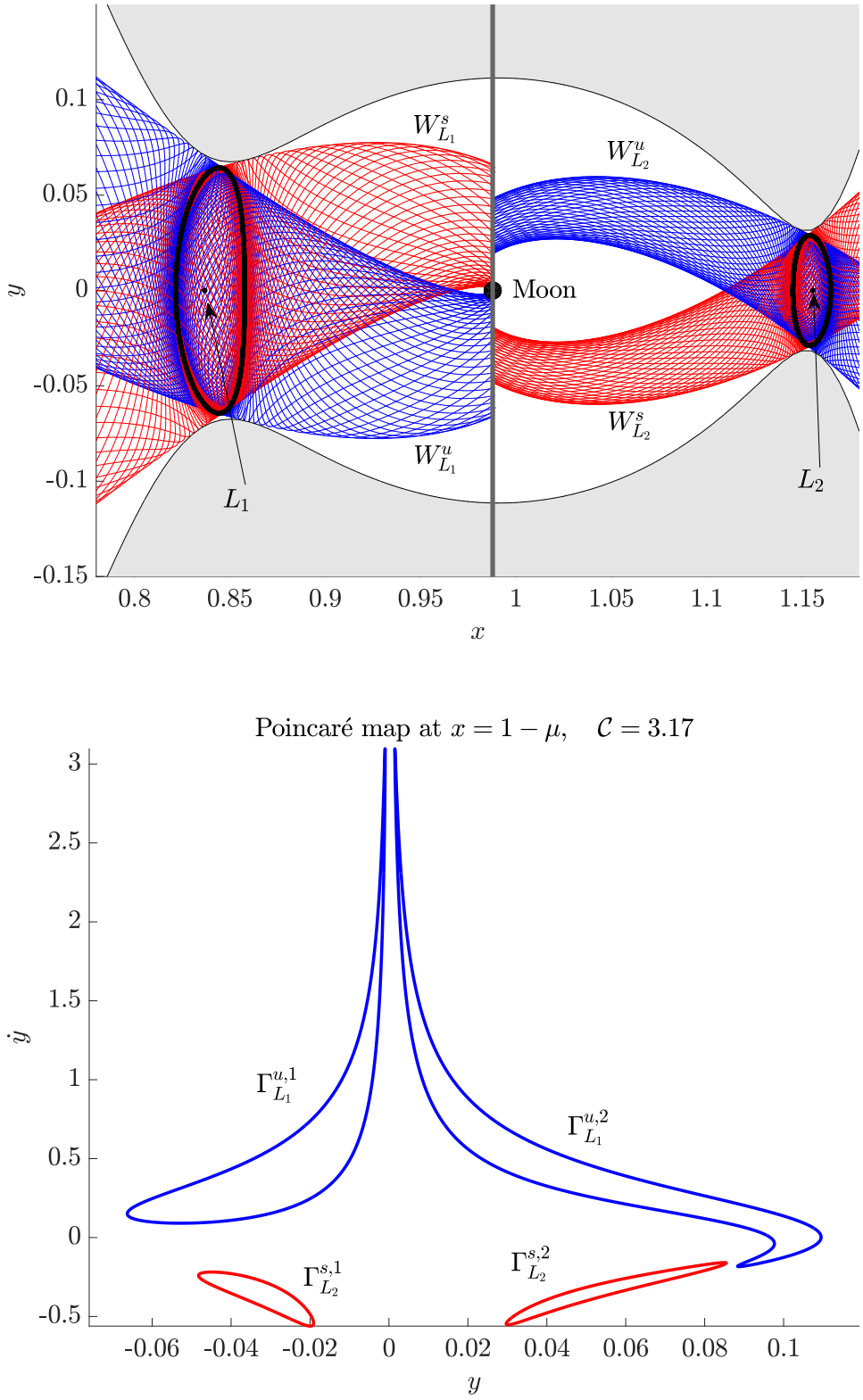

Figure 4.6: In the top panel we show the stable (red) and unstable (blue) manifolds of an L_1 and an L_2 Lyapunov orbit at $\mathcal{C} = 3.17$. In the bottom panel we show the Poincaré map of the first and second crossing with the Moon plane of $W^u_{L_1}$ and $W^s_{L_2}$. Unlike the precedent cases no intersection is found at this level of energy, and neither a $(2, 2)$-heteroclinic connection nor a $(1, 1)-$heteroclinic connection can be constructed.

4.0.2 Homoclinic connections among Lyapunov orbits in the interior and exterior regions

In the previous Section we have seen how homoclinic and heteroclinic connections among Lyapunov orbits can be found in the Moon region. Here we will instead show a similar procedure that can be used to construct homoclinic connections occurring in the interior region, i.e., the region surrounding the largest of the primaries, for the L_1 Lyapunov orbits and in the exterior region for L_2 Lyapunov orbits.

As usual, let $\boldsymbol{\gamma}_{L_i}$ be an L_1 or L_2 Lyapunov orbit. It In this case it will be more convenient to use the Poincaré cuts with the plane $y = 0$, and look for intersection between $\Gamma^{u,p}_{L_i}$ and $\Gamma^{s,q}_{L_i}$ in the $x\dot{x}$ plane. The intersections will be sought in the interior region for L_1 orbits and in the exterior region for L_2 orbits, as this is the most natural choice. Then if an intersection is found at the point $A = (x_A, \dot{x}_A)$, we can recover the value of $|\dot{y}_A|$, by imposing that the intersection point has Jacobi constant equal to $\mathcal{C}$ and solving (4.5) for $\dot{y}_A$. Finally we need again to determine the sign of $|\dot{y}_A|$, by imposing that it is consistent with the direction from which the manifolds intersects the $y = 0$ plane. Finally we can integrate the trajectory that starts at

$$\boldsymbol{x}_A = (x_A, y_A, 0, \dot{x}_A, \dot{y}_A, 0)^T \quad y_A = 0, \tag{4.8}$$

both forward and backward in time to find the desired homoclinic connection $\varphi(\boldsymbol{x}_A, t)$.

In Figures 4.7 and 4.8, we show two examples of $(1, 1)$-homoclinic connections for an L_1 and an L_2 Lyapunov orbit, that can be found in the interior and exterior regions, respectively, as we described above.

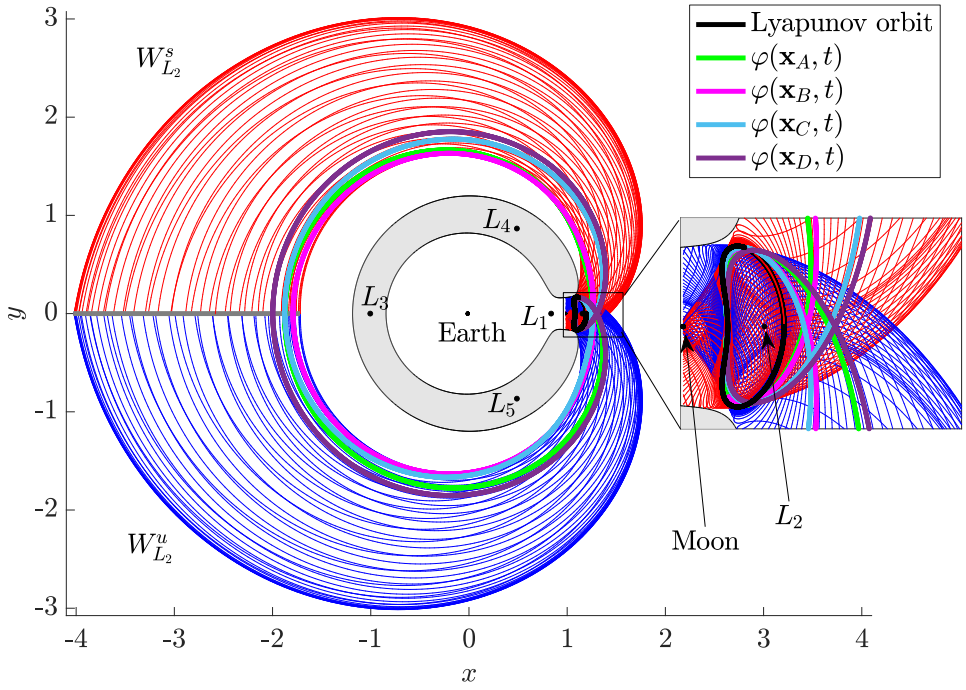

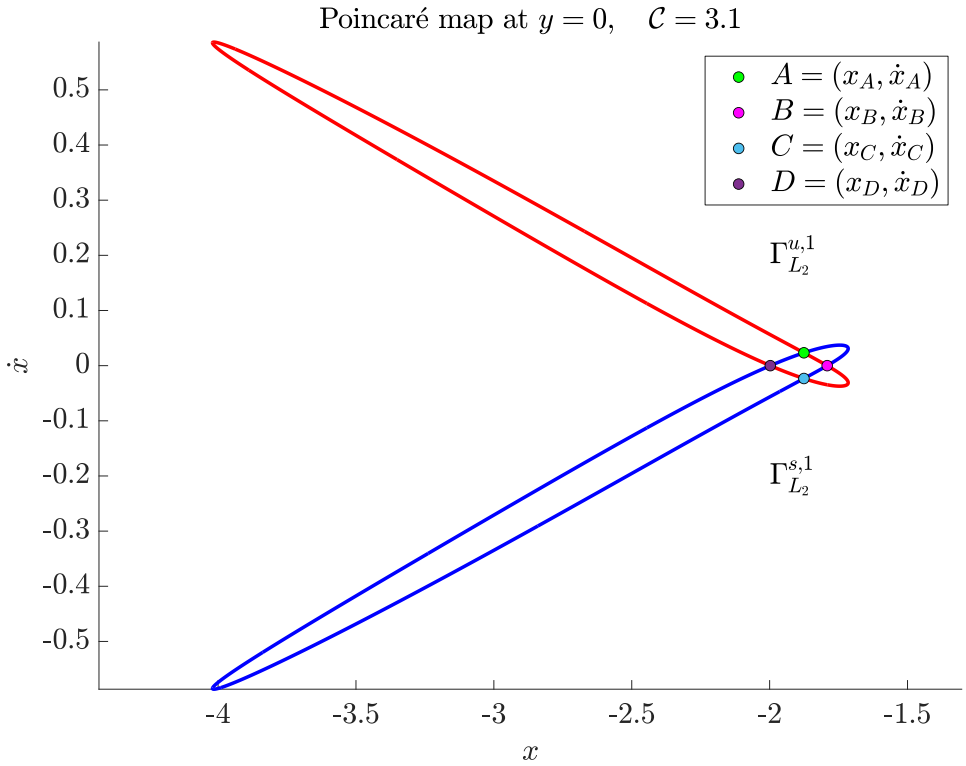

Figure 4.7: In the top panel we show the stable (red) and unstable (blue) manifolds of an L_1 Lyapunov orbit at $\mathcal{C} = 3.12$, in the interior region as well as four different $(1-1)$-homoclinic connections. Notice that the trajectories corresponding to the intersection points B and D are non-symmetric. In the bottom panel we show the Poincaré map of the first crossing with the $y = 0$ plane of $W^u_{L_2}$ and $W^s_{L_2}$ in the interior region.

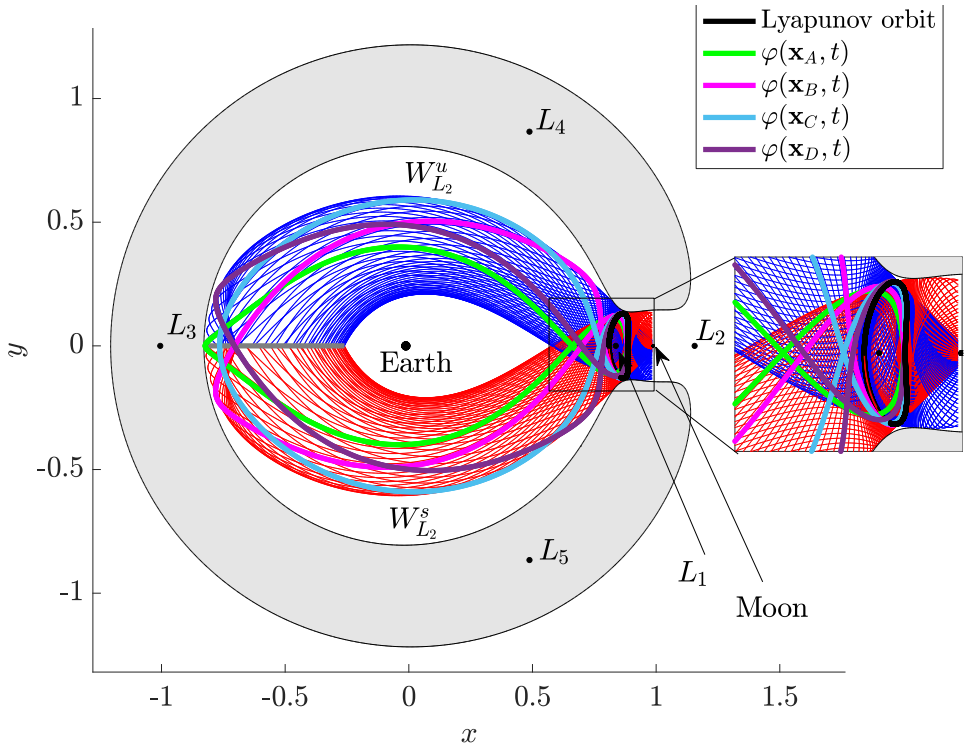

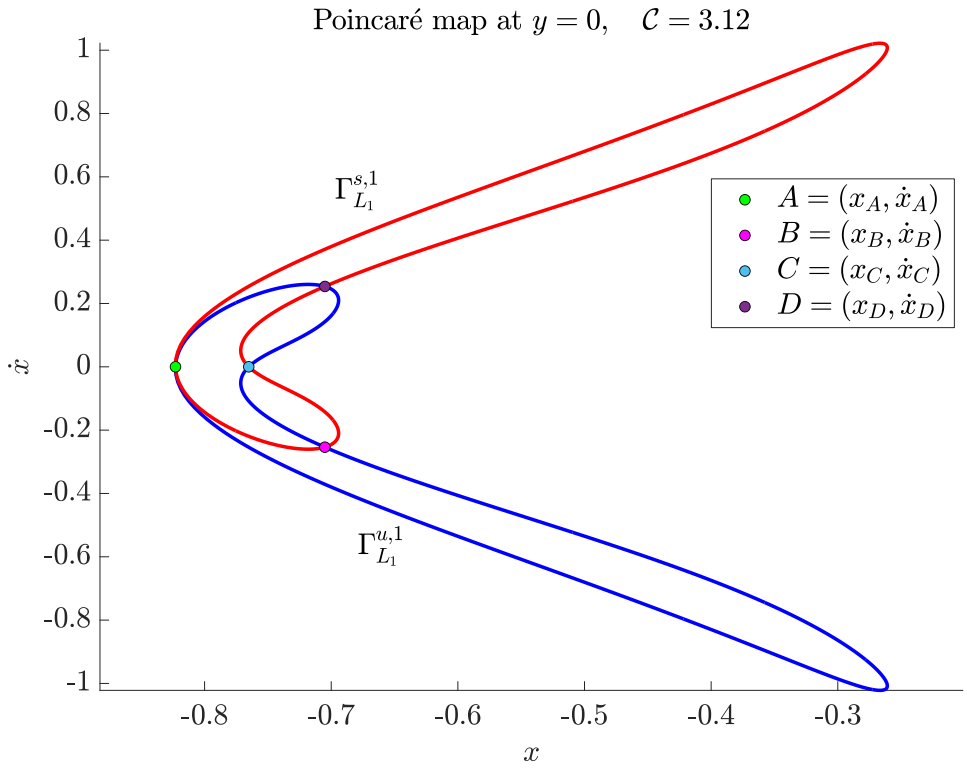

Figure 4.8: In the top panel we show the stable (red) and unstable (blue) manifolds of an L_2 Lyapunov orbit at $\mathcal{C} = 3.1$, in the exterior region as well as four different homoclinic connections. In the bottom panel we show the Poincaré map of the first crossing with the $y = 0$ plane of $W^u_{L_2}$ and $W^s_{L_2}$ in the exterior region.

Chapter 5

Motion in the Earth-Moon CR3BP with lunar gravitational field

We will now consider a model proposed by Russel & Lara in [45], to compute orbits in an high degree and order lunar gravity model that is superimposed to the Earth-Moon CR3BP in order to include also the third-body perturbation effects of the Earth. As in the CR3BP assume that the Earth and Moon follow circular orbits around their common center of mass, in reality the radius varies by ±5%. We also assume that the rotation of the Moon is synchronous with its orbital period, so that the lunar body-fixed reference frame coincides with the Moon centered frame, i.e., $P_2 = (0, 0, 0)$, in reality a ±8° libration results from the Moon's elliptic orbit and solar perturbations. Note that in this case we place the Earth on the positive side of the x axis, i.e., $P_1 = (1, 0, 0)$, to be consistent with the orientation of the lunar body-fixed frame in which the spherical harmonic coefficients are given. Moreover the lunar equatorial plane is inclined by 5.2° with respect to its orbital plane [42, 45].

The equations of motion of the CR3BP plus lunar gravitational field, in the Moon centered rotating frame are given by:

$$\ddot{x} - 2\dot{y} = \frac{\partial \mathcal{U}^*}{\partial x}, \qquad \ddot{y} + 2\dot{x} = \frac{\partial \mathcal{U}^*}{\partial y}, \qquad \ddot{z} = \frac{\partial \mathcal{U}^*}{\partial z}, \tag{5.1}$$

where

$$\mathcal{U}^*(\boldsymbol{r}) = \frac{(x - 1 + \mu)^2}{2} + \frac{y^2}{2} + \frac{(1 - \mu)}{r_E} + \frac{\mu}{r} + \mathcal{V}(\boldsymbol{r}), \tag{5.2}$$

$$r_E = \sqrt{(x-1)^2 + y^2 + z^2}, \qquad r = r_M = \sqrt{x^2 + y^2 + z^2}, \tag{5.3}$$

so that the potential $\mathcal{U}^*(\boldsymbol{r})$ is the sum of the effective potential of the CR3BP given in the Moon centered frame, and the Earth on the right relative to the Moon, i.e., $\mathcal{U}(x - 1 + \mu, y, z; 1 - \mu)$, plus the lunar gravitational field perturbation term due to the nonsphericity of the Moon $\mathcal{V}$, expressed in the standard spherical harmonic expansion [45], as explained in Section 5.1. As usual we can express the equations of motion as a vector ODE as:

$$\dot{\boldsymbol{x}} = g^*(\mu, \boldsymbol{x}), \qquad g^*(\mu, \boldsymbol{x}) = \begin{pmatrix} 0_{3\times3} & I_{3\times3} \\ 0_{3\times3} & 2\Omega \end{pmatrix} \boldsymbol{x} + \begin{pmatrix} 0_{3\times1} \\ \mathcal{U}_{\boldsymbol{r}}^{*T} \end{pmatrix}. \tag{5.4}$$

Notice that this system is again Hamiltonian, so that the same arguments of Section 2.3 hold. Hence there exists an integral of motion which we still call Jacobi constant and

denote it by $\mathcal{C}^*$, defined as:

$$\mathcal{C}^*(\boldsymbol{r}, \dot{\boldsymbol{r}}) = 2\mathcal{U}^*(\boldsymbol{r}) - \dot{\boldsymbol{r}}^2. \tag{5.5}$$

5.1 Spherical harmonic expansion of the gravitational field

Consider a volume V in physical space and let $\rho(x, y, z) \geq 0$ be the scalar function that describes the spatial mass density within V bounded by the closed surface $S = \partial V$. Then, indicating with

$$m(V) = \int_V \rho \, dV, \tag{5.6}$$

the total mass enclosed by the surface S, the gravitational acceleration $\boldsymbol{g}$ due to m at any point P of position external to the mass distribution is given by the vector field

$$\boldsymbol{g}(\boldsymbol{r}) = -G \int_V \frac{\rho(\mathbf{r}')(\boldsymbol{r} - \boldsymbol{r}')}{|\boldsymbol{r} - \boldsymbol{r}'|^3} \, dV, \tag{5.7}$$

where $\boldsymbol{r} - \boldsymbol{r}'$, represents the distance of $P(x, y, z)$ from the volume element dV of V, located at $\boldsymbol{r}'$.

We now prove a fundamental result known as Gauss's theorem. This result allows to express the flux of the gravitational acceleration field generated a massive body as a function of its mass only. The proof follows the one presented in [7].

Theorem 10. *Let $\mathcal{F}(S)$ be the flux of the vector field g through the surface S, this is given by*

$$\mathcal{F}(S) = \int_S \boldsymbol{g}(\boldsymbol{r}) \cdot \boldsymbol{n} \, dS, \tag{5.8}$$

where $\boldsymbol{n}$ denotes the outward normal unit vector to S at the surface element dS. Then $\mathcal{F}(S)$ depends only on the total mass bounded by the enclosing surface S, in particular it holds:

$$\mathcal{F}(S) = -4\pi G m. \tag{5.9}$$

Proof. Substituting (5.7) into (5.8) we obtain:

$$\mathcal{F}(S) = -G \int_S \left[\int_V \frac{\rho(\mathbf{r}')(\boldsymbol{r} - \boldsymbol{r}')}{|\boldsymbol{r} - \boldsymbol{r}'|^3} \, dV \right] \cdot \boldsymbol{n} \, dS. \tag{5.10}$$

We can now apply Fubini's theorem to rewrite this as:

$$\mathcal{F}(S) = -G \int_V \left[\int_S \frac{(\boldsymbol{r} - \boldsymbol{r}')}{|\boldsymbol{r} - \boldsymbol{r}'|^3} \cdot \boldsymbol{n} \, dS \right] \rho(\mathbf{r}') \, dV. \tag{5.11}$$

The term inside square brackets is just the integral of the solid angle Ω represents the subtended at $\boldsymbol{r}'$ by the surface element dS, of position $\boldsymbol{r}$. It follows that as the surface element varies over the entire surface, the integral will asume the value of entire solid angle, hence we have

$$\int_S \frac{(\boldsymbol{r} - \boldsymbol{r}')}{|\boldsymbol{r} - \boldsymbol{r}'|^3} \cdot \boldsymbol{n} \, dS = \int_\Omega d\Omega = 4\pi. \tag{5.12}$$

Finally from (5.6) it follows the thesis. □

Next we want tho show that the gravitational potential $\mathcal{V}^*$ exerted by a massive body is an harmonic function in the space not occupied by it. In order to show this it suffices to apply the divergence theorem in (5.8), this yields

$$\int_S \boldsymbol{g}(\boldsymbol{r}) \cdot \boldsymbol{n}\, dS = \int_V \nabla \cdot \boldsymbol{g}(\boldsymbol{r}) dV, \tag{5.13}$$

then from (5.9) and (5.6 we obtain)

$$\int_V \nabla \cdot \boldsymbol{g}(\boldsymbol{r}) dV = -4\pi G \int_V \rho\, dV. \tag{5.14}$$

Since the volume V is arbitrary, this equation can be rewritten in differential form as

$$\nabla \cdot \boldsymbol{g} = -4\pi G\rho. \tag{5.15}$$

Now let $\mathcal{V}^*$ be the gravitational potential associated to the mass distribution ρ, so that $\boldsymbol{g} = \nabla\mathcal{V}^*$. Then at a point in space not occupied by the body, i.e., $\rho = 0$, the gravitational potential satisfies the Laplace equation:

$$\nabla \cdot \nabla\mathcal{V}^* = \Delta\mathcal{V}^* = 0, \tag{5.16}$$

where $\Delta(\cdot)$ denotes the Laplacian operator. A solution to the Laplace equation is called a *harmonic* function. Moreover, a harmonic function that is homogeneous of degree n, i.e., it satisfies Euler's identity, is called a *spherical harmonic*. This special class of functions has the additional property of forming an orthonormal basis. This will allow us to represent the Moon's gravitational potential as a series expansion in terms of spherical harmonics.

For convenience we will now switch to a polar coordinate representation. Let us denote $\boldsymbol{\sigma} = (r, \phi, \lambda)$, the spherical coordinates vector, where ϕ and λ represent the geocentric latitude and longitude angle respectively, and they are related with the Cartesian position vector $\boldsymbol{r} = (x, y, z)$ by

$$\sin\phi = z/r, \quad \sin\lambda = y/\sqrt{x^2+y^2}, \quad \cos\lambda = x/\sqrt{x^2+y^2}. \tag{5.17}$$

Note that in spherical coordinates the Laplace operator now has the expression:

$$\Delta\mathcal{V} = \frac{1}{r^2}\frac{\partial}{\partial r}\left(r^2\frac{\partial\mathcal{V}}{\partial r}\right) + \frac{1}{r^2\cos\phi}\frac{\partial}{\partial\phi}\left(\cos\phi\frac{\partial\mathcal{V}}{\partial\phi}\right) + \frac{1}{r^2\cos^2\phi}\frac{\partial^2\mathcal{V}}{\partial\lambda^2}. \tag{5.18}$$

Before proceeding, it is worth noting that for a body that is spherically symmetric, and with homogeneous mass density ρ, Newton's Shell Theorem holds. Hence, in a reference frame with origin coinciding with the center of mass of the body, and at radial distance r greater than the body's radius, the gravitational potential acts as if all of the mass were concentrated at its center, i.e. the potential is simply μ/r. Now let $P_{n,m}$ denote the associated Legendre function of degree n, and order m, as defined in Section 5.1.1. Then, the spherical harmonic expansion of the gravitational potential due only to the asphericity of the Moon, i.e., $\mathcal{V} = \mathcal{V}^* - \mu/r$, can be written in terms of the Stokes coefficients $C_{n,m}$, $S_{n,m}$ of degree n and order m as in [50]:

$$\mathcal{V}(\boldsymbol{\sigma}) = \frac{\mu}{r}\sum_{n=2}^{\infty}\sum_{m=0}^{n}\left(\frac{R_M}{r}\right)^n \big(C_{n,m}\cos m\lambda + S_{n,m}\sin m\lambda\big)P_{n,m}(\sin\phi). \tag{5.19}$$

Parameter	Value
$\bar{C}_{2,0}$	$-9.088083466222 \times 10^{-5}$
$\bar{C}_{2,1}$	$1.232336842695 \times 10^{-10}$
$\bar{S}_{2,1}$	$1.013126827836 \times 10^{-9}$
$\bar{C}_{2,2}$	$3.467379822995 \times 10^{-5}$
$\bar{S}_{2,2}$	$-2.489004351630 \times 10^{-10}$
$\bar{C}_{3,0}$	$-3.197467349260 \times 10^{-6}$
$\bar{C}_{3,1}$	$2.636804553722 \times 10^{-5}$
$\bar{S}_{3,1}$	$5.454519551956 \times 10^{-6}$
$\bar{C}_{3,2}$	$1.417152872119 \times 10^{-5}$
$\bar{S}_{3,2}$	$4.877963012362 \times 10^{-6}$
$\bar{C}_{3,3}$	$1.227495055506 \times 10^{-5}$
$\bar{S}_{3,3}$	$-1.774395591200 \times 10^{-6}$

Table 5.1: Normalized gravity coefficients up to order $n = 3$, from the GRAIL Gravity Model (GL0660B) [24].

where the term of degree $n = 0$, i.e., μ/r has been left out since it is already included in (5.2). While the terms of order $n = 1$ are not included because the corresponding coefficients $C_{1,0}$, $C_{1,1}$, $S_{1,0}$, $S_{1,1}$ are all equal to zero, since the coordinate system's origin is chosen to coincide with center of mass of the Moon [24, 11]. Often (5.19) is rewritten introducing the notation $C_{n,0} = -J_n$, and $P_{n,0} = P_n$, i.e.,

$$\begin{aligned}\mathcal{V}(\boldsymbol{\sigma}) = &-\frac{\mu}{r}\sum_{n=2}^{\infty}\left(\frac{R_M}{r}\right)^n J_n P_n(\sin\phi) \\ &+\frac{\mu}{r}\sum_{n=2}^{\infty}\sum_{m=1}^{n}\left(\frac{R_M}{r}\right)^n \big(C_{n,m}\cos m\lambda + S_{n,m}\sin m\lambda\big) P_{n,m}(\sin\phi).\end{aligned} \tag{5.20}$$

The gravitational field coefficients J_n, $C_{n,m}$ and $S_{n,m}$ are usually referred with the following special names:

- $J_n = -C_{n,0}$, are the zonal coefficients,
- $C_{n,m}$, $S_{n,m}$ for $n = m$, are the sectorial coefficients,
- $C_{n,m}$, $S_{n,m}$ for $n \neq m$, are the tesseral coefficients.

The J_n notation is the one used historically in satellite geodesy, while most modern references often use exclusively the $C_{n,m}$, $S_{n,m}$ nomenclature [11]. Notice that the gravitational field coefficients must be used together with the specific gravitational parameter μ and reference radius R_M, for which the coefficients are calibrated, in order to obtain the correct results [11]. In practice the expansion in spherical harmonics of the potential given in (5.19), is truncated up to some maximum values for degree n and order m, and we will refer to this truncation as the $n \times m$ gravitational field expansion.

The gradient of the potential can be computed as:

$$\nabla\mathcal{U}^*(x, y, z) = \nabla\mathcal{U}(x - 1 + \mu, y, z; 1 - \mu) + \nabla\mathcal{V}(x, y, z), \tag{5.21}$$

where the components of $\nabla\mathcal{U}$ are given in equations (2.41 – 2.43), while to obtain the components of $\nabla\mathcal{V}(\boldsymbol{r}) = \partial\mathcal{V}/\partial\boldsymbol{r}$, we first compute the gradient in spherical coordinates, this is given by [41]:

$$\nabla\mathcal{V}(\boldsymbol{\sigma}) = \frac{\partial\mathcal{V}}{\partial r}\hat{r} + \frac{1}{r}\frac{\partial\mathcal{V}}{\partial\phi}\hat{\phi} + \frac{1}{r\cos\phi}\frac{\partial\mathcal{V}}{\partial\lambda}\hat{\lambda}, \tag{5.22}$$

where $\hat{r}$, $\hat{\phi}$, $\hat{\lambda}$ are the spherical coordinates unit vectors. Notice the presence of the longitudinal singularity at the poles, i.e., at $\phi = \pm\pi/2$. This of course is only an artifact due to the spherical coordinates representation, and can be addressed this as described in [41]. Then, recalling that

$$\frac{\partial r^{-n}}{\partial r} = -\frac{n}{r^2}\left(\frac{1}{r}\right)^{n-1}, \tag{5.23}$$

we can compute the partial derivatives with respect to the spherical coordinates, i.e., $\partial\mathcal{V}/\partial\boldsymbol{\sigma}$, that are given by [7, 41]:

$$\frac{\partial\mathcal{V}}{\partial r} = -\frac{\mu}{r^2}\sum_{n=2}^{\infty}\sum_{m=0}^{n}(n+1)\left(\frac{R_M}{r}\right)^n\big(C_{n,m}\cos m\lambda + S_{n,m}\sin m\lambda\big)P_{n,m}(\sin\phi), \tag{5.24}$$

$$\frac{\partial\mathcal{V}}{\partial\phi} = \frac{\mu}{r}\sum_{n=2}^{\infty}\sum_{m=0}^{n}\left(\frac{R_M}{r}\right)^n\big(C_{n,m}\cos m\lambda + S_{n,m}\sin m\lambda\big)\frac{d}{d\phi}P_{n,m}(\sin\phi), \tag{5.25}$$

$$\frac{\partial\mathcal{V}}{\partial\lambda} = \frac{\mu}{r}\sum_{n=2}^{\infty}\sum_{m=0}^{n}\left(\frac{R_M}{r}\right)^n m\big(S_{n,m}\cos m\lambda - C_{n,m}\sin m\lambda\big)P_{n,m}(\sin\phi). \tag{5.26}$$

Finally we can transform the gradient back into into Cartesian coordinates as in [45], using:

$$\begin{pmatrix}\partial\mathcal{V}/\partial x\\ \partial\mathcal{V}/\partial y\\ \partial\mathcal{V}/\partial z\end{pmatrix} = \begin{pmatrix}\cos\phi\cos\lambda & -\sin\phi\cos\lambda & -\sin\lambda\\ \cos\phi\sin\lambda & -\sin\phi\sin\lambda & \cos\lambda\\ \sin\phi & \cos\phi & 0\end{pmatrix}\begin{pmatrix}\partial\mathcal{V}/\partial r\\ (1/r)\partial\mathcal{V}/\partial\phi\\ (1/(r\cos\phi))\partial\mathcal{V}/\partial\lambda\end{pmatrix}. \tag{5.27}$$

It is worth noting that the following recurrence relation holds [45]:

$$\sin m\lambda = 2\cos\lambda\sin(m-1)\lambda - \sin(m-2)\lambda, \tag{5.28}$$

$$\cos m\lambda = 2\cos\lambda\cos(m-1)\lambda - \cos(m-2)\lambda. \tag{5.29}$$

which can be used together with (5.17) to compute the terms corresponding to $m \geq 2$ inside (5.19).

5.1.1 Legendre polynomials and associated Legendre functions

We denote the associated Legendre function of degree n, and order m, by $P_{n,m}$. The associated Legendre functions of order zero, which we denote by $P_n = P_{n,0}$, are known as the Legendre polynomials. The Legendre polynomials and associated Legendre functions, are defined by the equations:

$$P_n(x) = \frac{1}{2^n n!}\frac{d^n}{dx^n}(x^2-1)^n, \tag{5.30}$$

$$P_{n,m}(x) = (1-x^2)^{m/2}\frac{d^m}{dx^m}P_n(x). \tag{5.31}$$

$n\backslash m$	0	1	2	3
0	1			
1	x	$\sqrt{1-x^2}$		
2	$\frac{1}{2}(3x^2-1)$	$3x\sqrt{1-x^2}$	$3(1-x^2)$	
3	$\frac{1}{2}(5x^3-3x)$	$\frac{3}{2}(5x^2-1)\sqrt{1-x^2}$	$15x(1-x^2)$	$15(1-x^2)^{3/2}$

Table 5.2: Associated Legendre functions $P_{n,m}(x)$ up to order $n = 3$.

The definition (5.30) is known as Rodrigues' formula. One can easily see from these definitions that, for $m > n$, $P_{n,m}$ must be identically zero. Note that sometimes authors use a different definition of $P_{n,m}$, which differs from (5.31) by a factor $(-1)^m$, known as Condon-Shortley phase.

For practical purposes the Legendre associated functions can be computed more conveniently by using the following recursion formulas:

$$P_{m,m}(\sin\phi) = (2m-1)\cos\phi P_{m-1,m-1}(\sin\phi), \tag{5.32}$$

$$P_{n,m}(\sin\phi) = \frac{2n-1}{n-m}\sin\phi P_{n-1,m}(\sin\phi) - \frac{n+m-1}{n-m}P_{n-2,m}(\sin\phi), \quad n \neq m. \tag{5.33}$$

The explicit expressions of $P_{n,m}$ of low degree and order given in Table 5.2 can be used to start the recursion formulas. The recurrence relation (5.33) for $m = 0$, i.e., for the Legendre polynomial P_n, is known as Bonnet's recursion formula.

The first order derivative of the associated Legendre functions $dP_{n,m}/dx$ can be obtained using the following recursion formula:

$$(1-x^2)\frac{d}{dx}P_{n,m}(x) = \sqrt{1-x^2}P_{n,m+1}(x) - mxP_{n,m}(x). \tag{5.34}$$

Then using the chain rule and (5.34), we can write:

$$\frac{d}{d\phi}P_{n,m}(\sin\phi) = P_{n,m+1}(\sin\phi) - m\tan\phi P_{n,m}(\sin\phi), \tag{5.35}$$

that is the expression needed to evaluate (5.25). The expression for the second order derivative of the associated Legendre functions can be derived as in [41], and it is:

$$\frac{d^2}{d\phi^2}P_{n,m}(\sin\phi) = P_{n,m+2}(\sin\phi) - (2m+1)\tan\phi P_{n,m+1}(\sin\phi) \tag{5.36}$$

$$+ m(m\tan^2\phi - \sec^2\phi)P_{n,m}(\sin\phi). \tag{5.37}$$

5.1.2 Normalization

The gravity coefficients become very small as the degree increases. For the most part this is due to the fact that the associated Legendre functions $P_{n,m}$ tend to large values as the degree n increases. Then for numerical reasons it is good practice to normalize both the Legendre functions and the gravity coefficients. The normalization is achieved by multiplying the gravitational field coefficients by scale factor $\alpha_{n,m}$ that depends on the degree and order of the coefficients. The associated Legendre functions are normalized

by the corresponding inverse factor $1/\alpha_{n,m}$. Then if we denote the normalized coefficients by $\bar{J}_n$, $\bar{C}_{n,m}$, $\bar{S}_{n,m}$, we can write their relationship with the unnormalized ones as [23]:

$$\begin{pmatrix} \bar{C}_{n,m} \\ \bar{S}_{n,m} \end{pmatrix} = \sqrt{\frac{(n+m)!}{(2-\delta_{m,0})(2n+1)(n-m)!}} \begin{pmatrix} C_{n,m} \\ S_{n,m} \end{pmatrix} = \alpha_{n,m} \begin{pmatrix} C_{n,m} \\ S_{n,m} \end{pmatrix}, \tag{5.38}$$

where $\delta_{m,0}$ is the Kronecker delta, i.e., it is equal to unity if $m = 0$, and it is zero otherwise. Recalling that $J_n = -C_{n,0}$ we can write also $J_n = \alpha_{n,0}\bar{J}_n$. The corresponding associated Lagrange functions are normalized by the inverse factor, denoting the normalized associated Lagrange functions by $\bar{P}_{n,m}$ we have:

$$\bar{P}_{n,m} = \frac{P_{n,m}}{\alpha_{n,m}}. \tag{5.39}$$

We can now write the normalized version of (5.19), that is:

$$\mathcal{V}(\boldsymbol{\sigma}) = \frac{\mu}{r} \sum_{n=2}^{\infty} \sum_{m=0}^{n} \left(\frac{R_M}{r}\right)^n \left(\bar{C}_{n,m} \cos m\lambda + \bar{S}_{n,m} \sin m\lambda\right) \bar{P}_{n,m}(\sin\phi). \tag{5.40}$$

5.2 Differential corrections revisited

The differential correction techniques of Section 3.3 exploited the symmetries of the families of periodic orbits. The presence of the lunar gravitational field in the equations of motion forces us to introduce new strategies to find periodic orbits in the nonsymmetric case. We proceed as in [45], by using directly the Jacobi constant $\mathcal{C}^*$ as the continuation parameter to generate the families of periodic orbits. Moreover, the technique presented in [45], employs the singular value decomposition to tackle the issue of the degenerate Jacobian associated to a periodic orbit, also in the specific case of a bifurcation orbit, in which case the Jacobian contains an additional degenerate direction that leads to a new periodic orbit [45]. To reduce the dimension of the problem we will always start from an initial guess on the xy plane, therefore it is useful to introduce the reduced state vector $\boldsymbol{\xi}$ that is obtained removing the variable z, i.e.,

$$\boldsymbol{\xi} = (x, y, \dot{x}, \dot{y}, \dot{z}), \tag{5.41}$$

and stopping the integration at the n-th crossing with the xy plane, the crossing time t_f is computed as we have already discussed in Section 3.1.1. In the following we will use the notation $\boldsymbol{\xi}(t_f) = \boldsymbol{\xi}_f$. Suppose now that we want to compute a periodic orbit at a given value of the Jacobi constant $\mathcal{C}^*$, and that the initial dynamical state of a near periodic initial guess at time t_0 is given by $\boldsymbol{\xi}(t_0) = \boldsymbol{\xi}_0$. We define the constraint vector:

$$K = \begin{pmatrix} \boldsymbol{\xi}_f - \boldsymbol{\xi}_0 \\ \mathcal{C}_0^* - \mathcal{C}^* \end{pmatrix}_{6\times 1}, \tag{5.42}$$

where $\mathcal{C}^*(t_0) \equiv \mathcal{C}_0^* = \mathcal{C}^*(t_f) \equiv \mathcal{C}_f^*$, denotes the current value of the Jacobi constant of the orbit. Our aim is to drive K to zero, in order to do so we need iteratively modify the initial conditions, at each iteration the variation of the initial dynamical state is given by $\Delta\boldsymbol{\xi}_0$, that is the solution of the linear system:

$$\frac{dK}{d\boldsymbol{\xi}_0} \Delta\boldsymbol{\xi}_0 = -K. \tag{5.43}$$

Notice that (5.43) is an overconstrained linear system. It is possible to reformulate the problem to have an equal number of constraints and unknowns, here instead we proceed as in [45], where a least square method is proposed in order to enforce the constraint on the solution regardless of the number of unknowns. The 6×5 Jacobian matrix of K admits the following singular value decomposition (SVD):

$$\frac{\partial K}{\partial \boldsymbol{\xi}_0} = UDV^T, \tag{5.44}$$

where U and V are square orthogonal matrices of dimensions 6 and 5, respectively, and D is a 6×5 diagonal matrix. The diagonal elements of D are non negative and are called the singular values of the Jacobian. [45]. Consider now the pseudoinverse of the Jacobian matrix of K, i.e.,

$$\left(\frac{\partial K}{\partial \boldsymbol{\xi}_0}\right)^+ = VSU^T, \quad S_{i,i} = \begin{cases} 1/D_{i,i}, & \text{if } \varepsilon > 0, \\ 0, & \text{if } \varepsilon < 0, \end{cases} \tag{5.45}$$

Furthermore when one or more the singular values are zero (or $< \varepsilon$), the least squares solution with the smallest magnitude is given by [27, 45]:

$$\Delta \boldsymbol{\xi}_0 = -\left(\frac{\partial K}{\partial \boldsymbol{\xi}_0}\right)^+ K \tag{5.46}$$

The Jacobian of K can be computed from:

$$\frac{\partial K}{\partial \boldsymbol{\xi}_0} = \begin{pmatrix} \frac{\partial \boldsymbol{\xi}_f}{\partial \boldsymbol{\xi}_0} - I_{5\times 5} \\ \frac{\partial \mathcal{C}_0^*}{\partial \boldsymbol{\xi}_0} \end{pmatrix}_{6\times 5}, \tag{5.47}$$

where the derivative of the Jacobi constant with respect to $\boldsymbol{\xi}_0$ is given by:

$$\frac{\partial \mathcal{C}_0^*}{\partial \boldsymbol{\xi}_0} = \left(2\frac{\partial \mathcal{U}^*}{\partial x}, 2\frac{\partial \mathcal{U}^*}{\partial y}, -2\dot{x}, -2\dot{y}, -2\dot{z}\right)\Big|_{\boldsymbol{x}=\boldsymbol{x}_0}. \tag{5.48}$$

Finally we need to address the computation of

$$\frac{\partial \boldsymbol{\xi}_f}{\partial \boldsymbol{\xi}_0} = \Phi^*(t_f, t_0)_{i\neq 3,\, j\neq 3} - \frac{1}{\dot{z}_f}\dot{\boldsymbol{\xi}}_f \Phi^*(t_f, t_0)_{i=3,\, j\neq 3}, \tag{5.49}$$

where the sate transition matrix $\Phi^*(t_f, t_0)^*$, is defined analogously to what we have done in (3.4), as:

$$\Phi^*(t_f, t_0) = \frac{\partial \varphi^*(\boldsymbol{x}_0, t_f)}{\partial \boldsymbol{x}_0} =, \tag{5.50}$$

The state transition matrix $\Phi(t_f, t_0)^*$ obeys the differential equation:

$$\frac{d\Phi^*(t, t_0)}{dt} = \Lambda^*(\boldsymbol{x})\Phi(t, t_0), \quad \Phi^*(t_0, t_0) = I_{6\times 6}, \tag{5.51}$$

where $\Lambda^*(\boldsymbol{x})$ is the 6×6 matrix defined as:

$$\Lambda^*(\boldsymbol{x}) = \frac{\partial g^*(\mu, \boldsymbol{x})}{\partial \boldsymbol{x}} = \begin{pmatrix} 0_{3\times 3} & I_{3\times 3} \\ \mathcal{U}^*_{\mathbf{rr}} & 2\Omega \end{pmatrix}, \quad \mathcal{U}^*_{\mathbf{rr}} = \begin{pmatrix} \mathcal{U}^*_{xx} & \mathcal{U}^*_{xy} & \mathcal{U}^*_{xz} \\ \mathcal{U}^*_{xy} & \mathcal{U}^*_{yy} & \mathcal{U}^*_{yz} \\ \mathcal{U}^*_{xz} & \mathcal{U}^*_{yz} & \mathcal{U}^*_{zz} \end{pmatrix}. \tag{5.52}$$

Notice that

$$\mathcal{U}^*_{\mathbf{rr}}(x,y,z) = \mathcal{U}_{\mathbf{rr}}(x-1+\mu,y,z;1-\mu) + \mathcal{V}_{\mathbf{rr}}(x,y,z), \tag{5.53}$$

therefore we need to compute the second order partial derivatives of $\mathcal{V}$. Consider first the chain rule, which can be written as:

$$\frac{\partial(\cdot)}{\partial\alpha} = \frac{\partial(\cdot)}{\partial r}\frac{\partial r}{\partial\alpha} + \frac{\partial(\cdot)}{\partial\phi}\frac{\partial\phi}{\partial\alpha} + \frac{\partial(\cdot)}{\partial\lambda}\frac{\partial\lambda}{\partial\alpha}, \qquad \alpha = x,y,z. \tag{5.54}$$

Then applying (5.54) to $\mathcal{V}$ twice, yields the general expression for the components of $\mathcal{V}_{\mathbf{rr}}$. Let $\alpha,\beta = x,y,z$, then we can write:

$$\begin{aligned}\mathcal{V}_{\alpha\beta} = \frac{\partial^2\mathcal{V}}{\partial\alpha\partial\beta} = {}& \frac{\partial^2\mathcal{V}}{\partial r^2}\frac{\partial r}{\partial\alpha}\frac{\partial r}{\partial\beta} + \frac{\partial^2\mathcal{V}}{\partial r\partial\phi}\frac{\partial r}{\partial\alpha}\frac{\partial\phi}{\partial\beta} + \frac{\partial^2\mathcal{V}}{\partial r\partial\lambda}\frac{\partial r}{\partial\alpha}\frac{\partial\lambda}{\partial\beta} \\ &+ \frac{\partial^2\mathcal{V}}{\partial\phi\partial r}\frac{\partial\phi}{\partial\alpha}\frac{\partial r}{\partial\beta} + \frac{\partial^2\mathcal{V}}{\partial\phi^2}\frac{\partial\phi}{\partial\alpha}\frac{\partial\phi}{\partial\beta} + \frac{\partial^2\mathcal{V}}{\partial\phi\partial\lambda}\frac{\partial\phi}{\partial\alpha}\frac{\partial\lambda}{\partial\beta} \\ &+ \frac{\partial^2\mathcal{V}}{\partial\lambda\partial r}\frac{\partial\lambda}{\partial\alpha}\frac{\partial r}{\partial\beta} + \frac{\partial^2\mathcal{V}}{\partial\lambda\partial\phi}\frac{\partial\lambda}{\partial\alpha}\frac{\partial\phi}{\partial\beta} + \frac{\partial^2\mathcal{V}}{\partial\lambda^2}\frac{\partial\lambda}{\partial\alpha}\frac{\partial\lambda}{\partial\beta} \\ &+ \frac{\partial\mathcal{V}}{\partial r}\frac{\partial^2 r}{\partial\alpha\partial\beta} + \frac{\partial\mathcal{V}}{\partial\phi}\frac{\partial^2\phi}{\partial\alpha\partial\beta} + \frac{\partial\mathcal{V}}{\partial\lambda}\frac{\partial^2\lambda}{\partial\alpha\partial\beta}.\end{aligned} \tag{5.55}$$

The explicit expressions of the six distinct partial derivatives with respect to the spherical coordinates, that appear in (5.55), is the following [41]:

$$\frac{\partial^2\mathcal{V}}{\partial r^2} = \frac{\mu}{r^3}\sum_{n=2}^{\infty}\sum_{m=0}^{n}(n+1)(n+2)\left(\frac{R_M}{r}\right)^n\big(C_{n,m}\cos m\lambda + S_{n,m}\sin m\lambda\big)P_{n,m}(\sin\phi), \tag{5.56}$$

$$\frac{\partial^2\mathcal{V}}{\partial r\partial\phi} = -\frac{\mu}{r^2}\sum_{n=2}^{\infty}\sum_{m=0}^{n}(n+1)\left(\frac{R_M}{r}\right)^n\big(C_{n,m}\cos m\lambda + S_{n,m}\sin m\lambda\big)\frac{d}{d\phi}P_{n,m}(\sin\phi), \tag{5.57}$$

$$\frac{\partial^2\mathcal{V}}{\partial r\partial\lambda} = -\frac{\mu}{r^2}\sum_{n=2}^{\infty}\sum_{m=0}^{n}(n+1)\left(\frac{R_M}{r}\right)^n m\big(S_{n,m}\cos m\lambda - C_{n,m}\sin m\lambda\big)P_{n,m}(\sin\phi), \tag{5.58}$$

$$\frac{\partial^2\mathcal{V}}{\partial\phi^2} = \frac{\mu}{r}\sum_{n=2}^{\infty}\sum_{m=0}^{n}\left(\frac{R_M}{r}\right)^n\big(C_{n,m}\cos m\lambda + S_{n,m}\sin m\lambda\big)\frac{d^2}{d\phi^2}P_{n,m}(\sin\phi), \tag{5.59}$$

$$\frac{\partial^2\mathcal{V}}{\partial\phi\partial\lambda} = \frac{\mu}{r}\sum_{n=2}^{\infty}\sum_{m=0}^{n}\left(\frac{R_M}{r}\right)^n m\big(S_{n,m}\cos m\lambda - C_{n,m}\sin m\lambda\big)\frac{d}{d\phi}P_{n,m}(\sin\phi), \tag{5.60}$$

$$\frac{\partial^2\mathcal{V}}{\partial\lambda^2} = -\frac{\mu}{r}\sum_{n=2}^{\infty}\sum_{m=0}^{n}\left(\frac{R_M}{r}\right)^n m^2\big(S_{n,m}\sin m\lambda + C_{n,m}\cos m\lambda\big)P_{n,m}(\sin\phi). \tag{5.61}$$

The first order partial derivatives of the spherical coordinates with respect to the Cartesian ones are given by [41]:

$$\frac{\partial r}{\partial x} = \frac{x}{r}, \qquad \frac{\partial r}{\partial y} = \frac{y}{r}, \qquad \frac{\partial r}{\partial z} = \frac{z}{r}, \tag{5.62}$$

$$\frac{\partial\phi}{\partial x} = \frac{-xz}{r^2\sqrt{x^2+y^2}}, \qquad \frac{\partial\phi}{\partial y} = \frac{-yz}{r^2\sqrt{x^2+y^2}}, \qquad \frac{\partial\phi}{\partial z} = \frac{1-z^2/r^2}{\sqrt{x^2+y^2}}, \tag{5.63}$$

$$\frac{\partial\lambda}{\partial x} = \frac{-y}{x^2+y^2}, \qquad \frac{\partial\lambda}{\partial y} = \frac{x}{x^2+y^2}, \qquad \frac{\partial\lambda}{\partial z} = 0. \tag{5.64}$$

While the second order partial derivatives are given by:

$$\frac{\partial^2 r}{\partial x^2} = \frac{y^2+z^2}{r^3}, \qquad \frac{\partial^2 r}{\partial y^2} = \frac{x^2+z^2}{r^3}, \qquad \frac{\partial^2 r}{\partial z^2} = \frac{x^2+y^2}{r^3}, \tag{5.65}$$

$$\frac{\partial^2 r}{\partial x \partial y} = -\frac{xy}{r^3}, \qquad \frac{\partial^2 r}{\partial x \partial z} = -\frac{xz}{r^3}, \qquad \frac{\partial^2 r}{\partial y \partial z} = -\frac{yz}{r^3}, \tag{5.66}$$

$$\frac{\partial^2 \lambda}{\partial x^2} = \frac{2xy}{(x^2+y^2)^2}, \qquad \frac{\partial^2 \lambda}{\partial x \partial y} = \frac{y^2-x^2}{(x^2+y^2)^2}, \qquad \frac{\partial^2 \lambda}{\partial x \partial z} = 0, \tag{5.67}$$

$$\frac{\partial^2 \lambda}{\partial y^2} = -\frac{2xy}{(x^2+y^2)^2}, \qquad \frac{\partial^2 \lambda}{\partial y \partial z} = 0, \qquad \frac{\partial^2 \lambda}{\partial z^2} = 0. \tag{5.68}$$

$$\frac{\partial^2 \phi}{\partial x^2} = \frac{z(2x^4+x^2y^2-y^2(y^2+z^2))}{r^4(x^2+y^2)^{3/2}}, \qquad \frac{\partial^2 \phi}{\partial x \partial y} = \frac{xyz(3x^2+3y^2+z^2)}{r^4(x^2+y^2)^{3/2}}, \tag{5.69}$$

$$\frac{\partial^2 \phi}{\partial x \partial z} = -\frac{x(x^2+y^2-z^2)}{r^4\sqrt{x^2+y^2}}, \qquad \frac{\partial^2 \phi}{\partial y^2} = -\frac{z(x^4+x^2(z^2-y^2)-2y^4)}{r^4(x^2+y^2)^{3/2}}, \tag{5.70}$$

$$\frac{\partial^2 \phi}{\partial y \partial z} = -\frac{y(x^2+y^2-z^2)}{r^4\sqrt{x^2+y^2}}, \qquad \frac{\partial^2 \phi}{\partial z^2} = -\frac{2z\sqrt{x^2+y^2}}{r^4}, \tag{5.71}$$

5.2.1 The osculating orbital elements

Recall that an unperturbed Keplerian orbit can be determined, although not always unambiguously [7], by a set of six parameters that uniquely determine the orbit, which we refer to as the orbital elements. Here we will use the set of orbital elements: $(a, e, i, \Omega, \omega, M_0)$. These are defined as follows.

- **Semi-major axis**, a: this element defines the size of the orbit. For an elliptical orbit, it is the distance from the center of the ellipse to the furthest point on the perimeter, i.e., either the apocenter or pericenter of the orbit.
- **Eccentricity**, e: this element defines the shape of the orbit. The value $e = 0$ corresponds to a circular orbit, values of the eccentricity in the range $0 < e < 1$ correspond to increasingly elongated ellipses. Here we are interested only in the elements of a closed orbit, however for the sake of completeness we must note that the limiting case $e = 1$ corresponds to a parabola (if the angular momentum is non-zero, otherwise it corresponds to radial motion), and for $e > 1$ the trajectory is a hyperbola.
- **Inclination**, i: this is the tilt of the orbit, or the angle between the plane of the orbit and the reference plane, which for our purposes is the Moon's orbital plane, i.e., the xy plane.
- **Longitude of the ascending node**, Ω: this is the angle between a given reference direction, e.g., the x axis, and the point where the orbit crosses the reference plane from South to North, hence the name.
- **Argument of pericenter**, ω: this is the angle between the ascending node and the orbit's point of closest approach to the central body, i.e. the pericenter of the orbit.

- **Mean anomaly at epoch**, M_0: the mean anomaly $M = n(t - \tau)$, is the angle swept by the radius vector of a fictitious body which orbits the ellipse at a constant angular velocity equal to the mean motion $n = 2\pi/T$, since the passage from pericenter τ. Thus the mean anomaly at epoch can be written as

$$M_0 = n(t_0 - \tau), \tag{5.72}$$

  where the epoch t_0 is the reference time to which the orbital elements are referred.

Additionally we define the true anomaly f, as the angle between the periapsis of the orbit and the radius vector of the orbiting body as it moves along its path. The elements a, e, and M_0 are known as the phoronomic elements, while i, Ω, and ω are known as the angular elements [7]. An orbiting object is considered to be in direct motion if its inclination is $i < 90°$. Conversely, its motion is regarded as retrograde if $90° < i \leq 180°$. A polar orbit describes the boundary case when $i = 90°$. In the special cases of $i = 0°, 180°$ the orbit is referred to as direct equatorial or retrograde equatorial, respectively [7]. The uniqueness of the representation of the dynamical state through the Keplerian elements does not hold when the orbit is circular, i.e., $e = 0$, and/or when $i = 0$. Indeed in the first case the argument of pericenter ω loses its meaning and consequently also the instant of passage through the pericenter, while in the second case the longitude of the ascending node Ω loses its meaning [7]. Note that other parametrizations are often used, for instance the argument of pericenter ω, can be replaced by the longitude of the pericenter $\tilde{\omega} = \omega + \Omega$. This is especially convenient when the inclination is close to zero, i.e., when the line of nodes becomes nearly indeterminate [7]. Note also that for parabolic orbits, $e = 1$, the elements a and e can be replaced by the focal distance q, thereby reducing the number of orbital elements required to describe the orbit to five.

For a purely Keplerian elliptic orbit, the orbital elements are constants. This is a consequence of the fact, that in the Two-Body Problem, the shape, size, and orientation of the orbit remain unchanged with time. While this fails to be true when purturbative terms are introduced, for a perturbed non Keplerian orbit we can still define its osculating orbital elements, these are defined as the instantaneous orbital elements, that a Keplerian orbit would have, if it had the same position and velocity of the perturbed orbit at some specified point in time.

In order to compute the orbital elements, we first have to move to a quasi-inertial, reference frame, i.e., a non rotating frame whose origin coincides with the central body of interest, i.e., the Moon. Let $\boldsymbol{x} = (\boldsymbol{r}, \boldsymbol{v})$ be the Cartesian state vector of a spacecraft in the quasi-inertial reference frame, and relabel for the moment the usual state vector in the synodic reference frame by $\boldsymbol{x}_s = (\boldsymbol{r}_s, \boldsymbol{v}_s)$. In practice, $\boldsymbol{x}$ can be obtained using the following transformations. First we need to perform a translation from the Moon-centered synodic reference frame, in which the equation of motion (5.4) are given, to the center-of-mass synodic reference frame, subsequently apply the transformation to obtain the state vector in the inertial reference frame with origin in the center of mass, $\boldsymbol{x}_i = (\boldsymbol{r}_i, \boldsymbol{v}_i)$, i.e.,

$$\boldsymbol{r_i} = R\boldsymbol{r}_s, \quad \boldsymbol{v_i} = R\boldsymbol{v}_s + \dot{R}\boldsymbol{r}_s, \tag{5.73}$$

where R is the rotation matrix, about a vertical axis passing though the center of mass of the Earth-Moon system, i.e., the z axis. This is given by

$$R(t) = \begin{pmatrix} \cos t & -\sin t & 0 \\ \sin t & \cos t & 0 \\ 0 & 0 & 1 \end{pmatrix}. \tag{5.74}$$

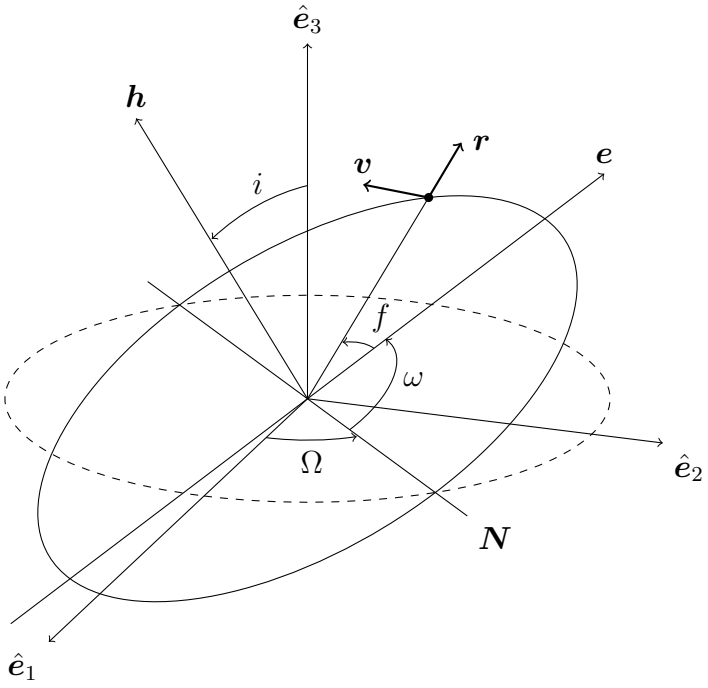

Figure 5.1: Visualization of an elliptic orbit and its orbital elements.

Notice that in (5.74), we used the fact that the Earth-Moon system has unit angular velocity in the normalized coordinates. The same transformation can be then applied to obtain the state vector of the Moon in the inertial frame, which we denote by $\boldsymbol{x}_M = (\boldsymbol{r}_M, \boldsymbol{v}_M)$. Lastly, the state vector of the spacecraft in the quasi-inertial frame is obtained by taking the relative position and velocity with respect to the Moon in the inertial frame, i.e.,

$$\boldsymbol{x} = \boldsymbol{x}_i - \boldsymbol{x}_M. \tag{5.75}$$

It's worth noting that the same result could have been achieved without converting from the Moon-centered synodic frame to the center-of-mass synodic frame, which would also eliminate the need for the final conversion (5.75). At this point let us denote the specific angular momentum vector by $\boldsymbol{h} = \boldsymbol{r} \times \boldsymbol{v}$, and its magnitude by $h = \|\boldsymbol{h}\|$, and let $r = \|\boldsymbol{r}\|$, $v = \|\boldsymbol{v}\|$. In the following we will denote the unit vectors of the quasi-inertial Cartesian reference frame by:

$$\hat{\boldsymbol{e}}_1 = (1,0,0)^T, \quad \hat{\boldsymbol{e}}_2 = (0,1,0)^T, \quad \hat{\boldsymbol{e}}_3 = (0,0,1)^T. \tag{5.76}$$

This last definition shall not arise confusion with the eccentricity vector $\boldsymbol{e}$. Finally we are ready to state the transformation between Cartesian state vector in the quasi-inertial frame and the osculating elements, i.e.,

$$\boldsymbol{e} = \frac{1}{\mu}\left(v^2 - \frac{\mu}{r}\right)\boldsymbol{r} - \frac{\boldsymbol{r}\cdot\boldsymbol{v}}{\mu}\boldsymbol{v}, \quad e = \|\boldsymbol{e}\|, \tag{5.77}$$

$$a = -\frac{\mu}{2}\left(\frac{v^2}{2} - \frac{\mu}{r}\right), \tag{5.78}$$

$$i = \cos^{-1}\left(\frac{\boldsymbol{h}\cdot\hat{\boldsymbol{e}}_3}{h}\right). \tag{5.79}$$

Now let $\boldsymbol{N} = \hat{\boldsymbol{e}}_3 \times \boldsymbol{h}$, be the vector defining the direction of the line of nodes. Then the longitude of the ascending node and the argument of pericenter of the orbit are given by

$$\Omega = \begin{cases} \cos^{-1}(\frac{\boldsymbol{N}\cdot\hat{\boldsymbol{e}}_1}{\|N\|}), & \boldsymbol{N}\cdot\hat{\boldsymbol{e}}_2 \geq 0, \\ 2\pi - \cos^{-1}(\frac{\boldsymbol{N}\cdot\hat{\boldsymbol{e}}_1}{\|N\|}), & \boldsymbol{N}\cdot\hat{\boldsymbol{e}}_2 < 0, \end{cases} \tag{5.80}$$

$$\omega = \begin{cases} \cos^{-1}(\frac{\boldsymbol{N}\cdot\boldsymbol{e}}{\|N\|e}), & \boldsymbol{e}\cdot\hat{\boldsymbol{e}}_3 \geq 0, \\ 2\pi - \cos^{-1}(\frac{\boldsymbol{N}\cdot\boldsymbol{e}}{\|N\|e}), & \boldsymbol{e}\cdot\hat{\boldsymbol{e}}_3 < 0. \end{cases} \tag{5.81}$$

Moreover we can obtain the following expression for the true anomaly:

$$f = \begin{cases} \cos^{-1}(\frac{\boldsymbol{e}\cdot\boldsymbol{r}}{r\,e}), & \boldsymbol{r}\cdot\boldsymbol{v} \geq 0, \\ 2\pi - \cos^{-1}(\frac{\boldsymbol{e}\cdot\boldsymbol{r}}{r\,e}), & \boldsymbol{r}\cdot\boldsymbol{v} < 0. \end{cases} \tag{5.82}$$

This can be used to compute the eccentric anomaly E, trough the relationships

$$\sin E = \frac{\sqrt{1-e^2}\sin f}{1+e\cos f}, \quad \cos E = \frac{e+\cos f}{1+e\cos f}. \tag{5.83}$$

Finally the mean anomaly M can be computed from the well-known Kepler's equation:

$$M = E - \sin E. \tag{5.84}$$

It is worth mentioning that while computing the mean anomaly given the eccentric anomaly is straightforward, the Kepler equation is transcendental in the unknown E, and lacks a closed-form solution. Then a solution for E can be expressed as a series expansion or computed numerically using one of a wide range of available methods, a Newton-Rhaphson's method being the simplest approach.

5.3 Repeating Ground Track orbits

Orbits that cover periodically the same ground track over the central body have applications in many different missions. This are usually known as Repeating Ground Track (RGT) orbits. Since we assumed that the Moon's rotational period is synchronously locked with its orbital period, i.e., the rotation rate is equal to the orbital mean motion, the periodic orbits in the present model are indeed RGT orbits [45]. As in the standard CR3BP, these periodic orbits exists in families that are parametrized by the Jacobi constant $\mathcal{C}^*$. In the case of high-altitude nearly polar RGT, varying $\mathcal{C}^*$ across a family of orbits has the effect of varying the average inclination i of the orbit, which happens to be very convenient, since i is a fundamental parameter in the process of mission design [45]. In particular both the period T of the orbit and its average inclination i increase monotonically in the same direction of the Jacobi constant $\mathcal{C}^*$, as can be seen in the bottom panel of Figure 5.3. Additionally the period of the repeating orbit is given by $T = 2\pi + \Delta\Omega$. With $\Delta\Omega$ being the total change in the longitude of the ascending node during one period of the spacecraft orbit [45].

A natural way of classifying the families of RGT orbits is the number of revolutions n that the massless body, i.e., a spacecraft, completes in a full repeat period. Accordingly, the families will be referred as the $n-$cycle families of RGT orbits. Modifying the parameter n allows to vary the altitude of the orbits in the $n-$cycle family in discrete steps, with higher values corresponding to lower altitudes [45].

In order to compute families of RGT orbits in the C3BP with the addition of the lunar gravitational field, the following algorithm can be employed [45]:

- Select the discrete number of cycles n of the RGT orbit family to be computed.
- Provide an initial guess $\boldsymbol{x}_0$ for a nearly polar. It will be enough to compute the initial conditions for a polar orbit around the point-mass Moon in the Two-Body Problem starting in the plane of the Moon's equator, i.e., the xy plane, for a polar orbit that completes n revolutions during one lunar revolution, i.e., in a time interval of length $T = 2\pi$. The two-body orbit is usually a good approximation at nearly polar inclination and will usually converge in the perturbed model [45].
- Use the initial guess $\boldsymbol{x}_0$ in conjunction with the differential correction scheme described in Section 5.2 to converge on a periodic orbit of the $n-$cycle RGT family. Since this is the first orbit of the family, we can simply remove the constraint corresponding to the Jacobi constant in equations (5.42) and (5.47).
- Select a small step $\Delta\mathcal{C}^*$, and use the differential correction scheme to converge on a new orbit of the RGT family imposing in (5.42) that the target Jacobi constant $\mathcal{C}^*$ equals the Jacobi constant of the last converged solution increased by $\Delta\mathcal{C}^*$.

In order to asses convergence we check the normalized miss distance defined as [45]:

$$d = \frac{\|\boldsymbol{r}(t_0) - \boldsymbol{r}(t_f)\|}{\|\boldsymbol{r}(t_0)\|} + \frac{\|\dot{\boldsymbol{r}}(t_0) - \dot{\boldsymbol{r}}(t_f)\|}{\|\dot{\boldsymbol{r}}(t_0)\|} + \left|\frac{\mathcal{C}_0^* - \mathcal{C}^*}{\mathcal{C}^*}\right|. \tag{5.85}$$

The value of ε in (5.45) affects the convergence of the differential correction scheme. If ε is too large, the algorithm will overconstrain the search space and d will stabilize at a larger value. On the other hand, if ε is too small, the algorithm will underconstrain

the search space causing d to oscillate indefinitely [45]. Here we use values in the range $\varepsilon \in [10^{-6}, 10^{-4}]$ as suggested in [45]. The integration of the equations of motion (5.4), is performed using a Runge-Kutta 9(8) integrator and the relative and absolute tolerances are chosen so that the Jacobi constant $\mathcal{C}^*$ is conserved to at least 12 digits over the course of a full orbital period, i.e., about 27.3 days, even with the inclusion of the lunar gravitational field truncated to degree and order 8×8.

When only the third-body perturbations are included, i.e., $n = m = 0$, we are able to generate families of $n-$cycle RGT orbits, using values up $n = 330$, corresponding to an altitude of just 112 km over lunar surface. The orbits in this families vary in inclination and starting from a polar initial guess we are able to continue the families up to very low inclinations. For instance we generated orbits of the 100−cycle RGT family, with inclinations as low as 1° and as high as 175° (see Figure 5.3). When only third body perturbations are considered, convergence is achieved with normalized miss distance on the order $d \approx 10^{-11}$, which corresponds to just a few millimeters in position, or lower. We must note however that when a realistic Moon's gravitational field is included, the convergence precision decreases substantially for orbits with higher or lower than polar inclination. For $n = 100$, at the polar inclination, we are able to achieve convergence on the order $d \approx 10^{-11}$ with a lunar gravitational field truncated at degree and order 8×8 (see Figure 5.4). To achieve this level of precision, the Two-Body polar initial guess, needs to be first corrected into a polar RGT orbit in the CR3BP, then an increasingly extended gravitational field is used to reach convergence to a new RGT orbit that will serve as the initial guess for the successive step, up to the desired values of degree and order of the gravitational field. An alternative method would be that of using a continuation process in the gravitational field parameters $C_{n,m}$ and $S_{n,m}$.

In Figures 5.4 − 5.8 we show the plots of the orbits and orbital elements of selected from the 100, 200 and 300−cycle RGT orbit families, at different inclinations. Lastly, in Figures 5.9 − 5.13 we show the evolution of the eccentricity vector over one period of the same selected orbits.

5.3.1 Polar initial guess

Here we show how the initial conditions of the initial guess for a polar orbit in the Two-Body Problem can be derived. Since we are interested in the $n-$cycle RGT family, the polar orbit needs to complete n revolutions per synodic period. Thus, in normalized units, the period of one single revolution must be $T = 2\pi/n$. The semi-major axis can then be determined using Kepler's third law, and it is

$$\frac{a^3}{T^2} = \frac{\mu}{4\pi^2}. \tag{5.86}$$

Solving for a, and substituting the expression for a single revolution period, we find an expression for the semi-major axis as a function of the number of revolutions n:

$$a = \left(\frac{T^2 \cdot \mu}{4\pi^2}\right)^{1/3} = \left(\frac{\mu}{n^2}\right)^{1/3}. \tag{5.87}$$

Then we can compute the velocity v of the body using the vis-viva equation,

$$v^2 = \mu\left(\frac{2}{r} - \frac{1}{a}\right). \tag{5.88}$$

For a circular orbit, the distance from the focus to the body, i.e., the radial distance r, is equal to the semi-major axis a at all times, thus for a circular orbit, we can impose $r = a$, and equation (5.88), reduces to

$$v = \sqrt{\frac{\mu}{a}}, \tag{5.89}$$

More in general, for an eccentric orbit, i.e. $e \neq 0$, the radial distance depends on the true anomaly f. In particular it is

$$r = \frac{a(1-e^2)}{1+e\cos f}. \tag{5.90}$$

Finally, assuming the initial conditions are taken on the xy plane, the initial velocity must be oriented in the z direction for the orbit to be polar, i.e., $i = 90°$. Then we can set the initial conditions for a polar orbit with longitude of the ascending node Ω, as

$$\boldsymbol{x}_0 = (\boldsymbol{r}_0, \dot{\boldsymbol{r}}_0), \quad \boldsymbol{r}_0 = (r\cos\Omega, r\sin\Omega, 0)\,, \quad \dot{\boldsymbol{r}}_0 = (0, 0, v). \tag{5.91}$$

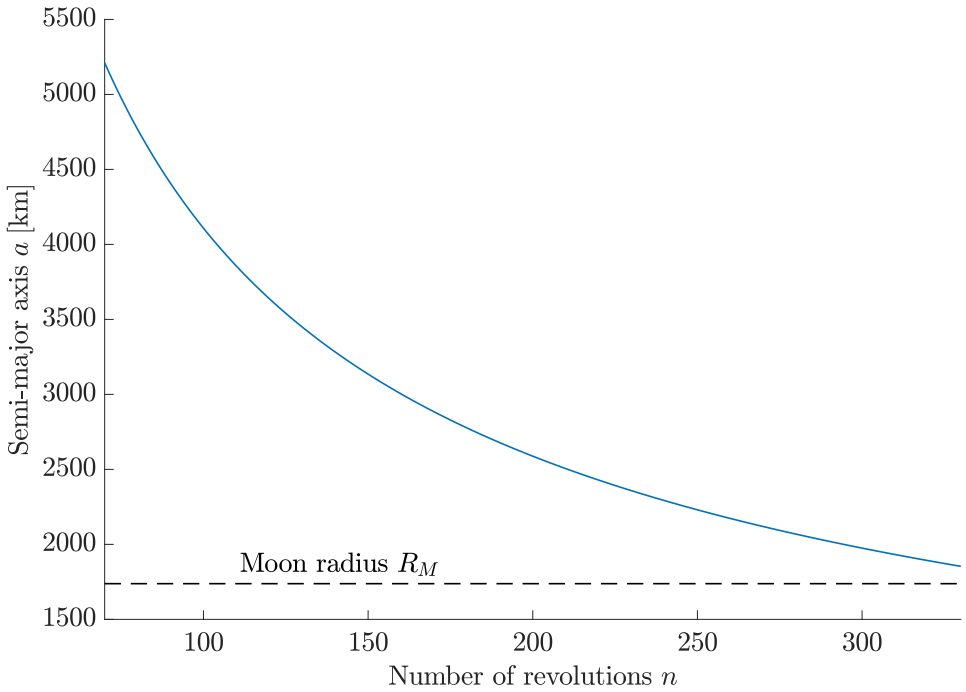

Figure 5.2: Semi-major axis of the $n-$cycle RGT polar orbits as a function of the number of revolutions n per synodic period, computed from equation (5.87).

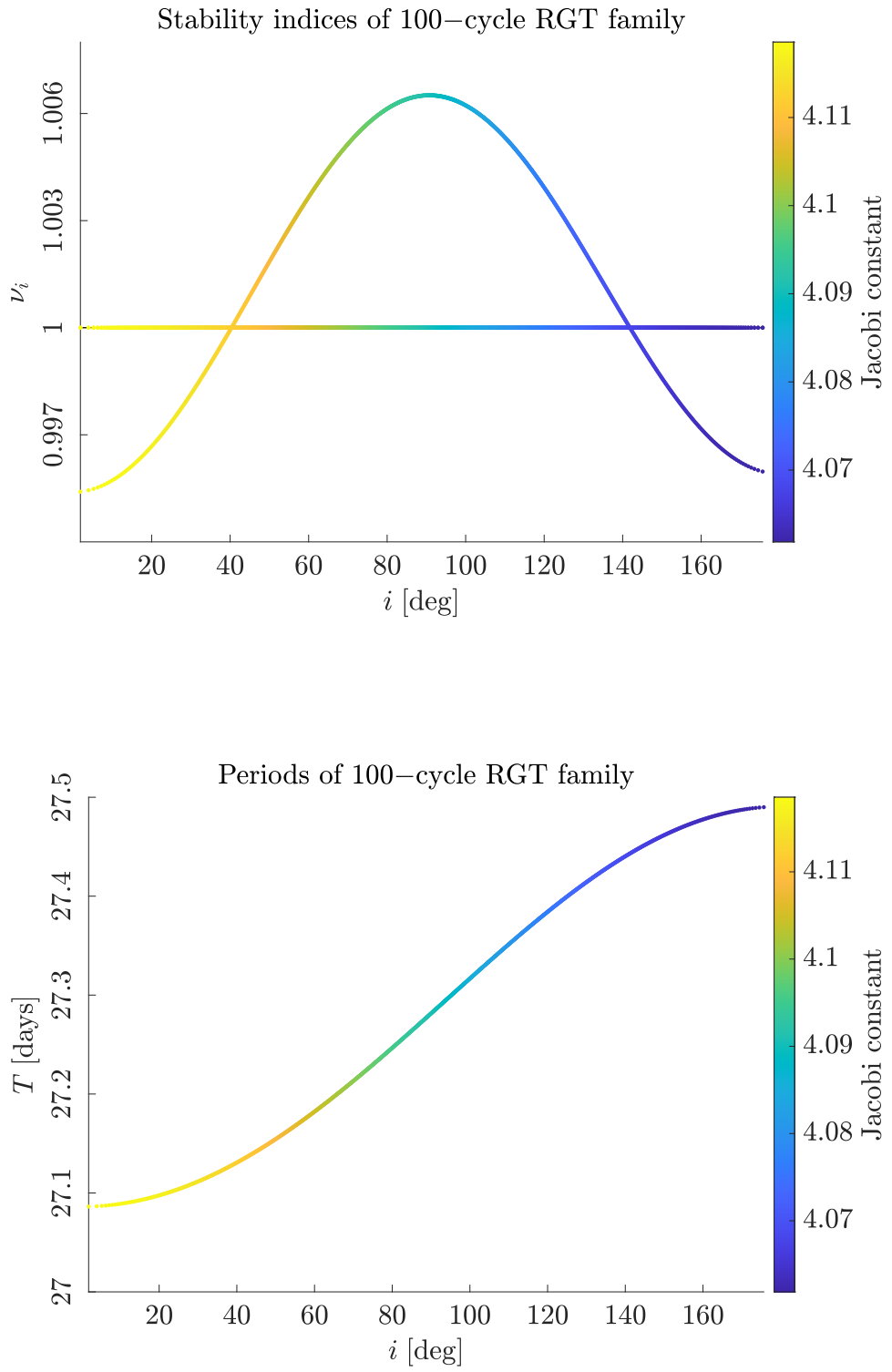

Figure 5.3: Plots showing the stability indices (top), and period (bottom) of the 100−cycle RGT family as a function of the inclination. Recall that the period is given by $T = 2\pi + \Delta\Omega$.

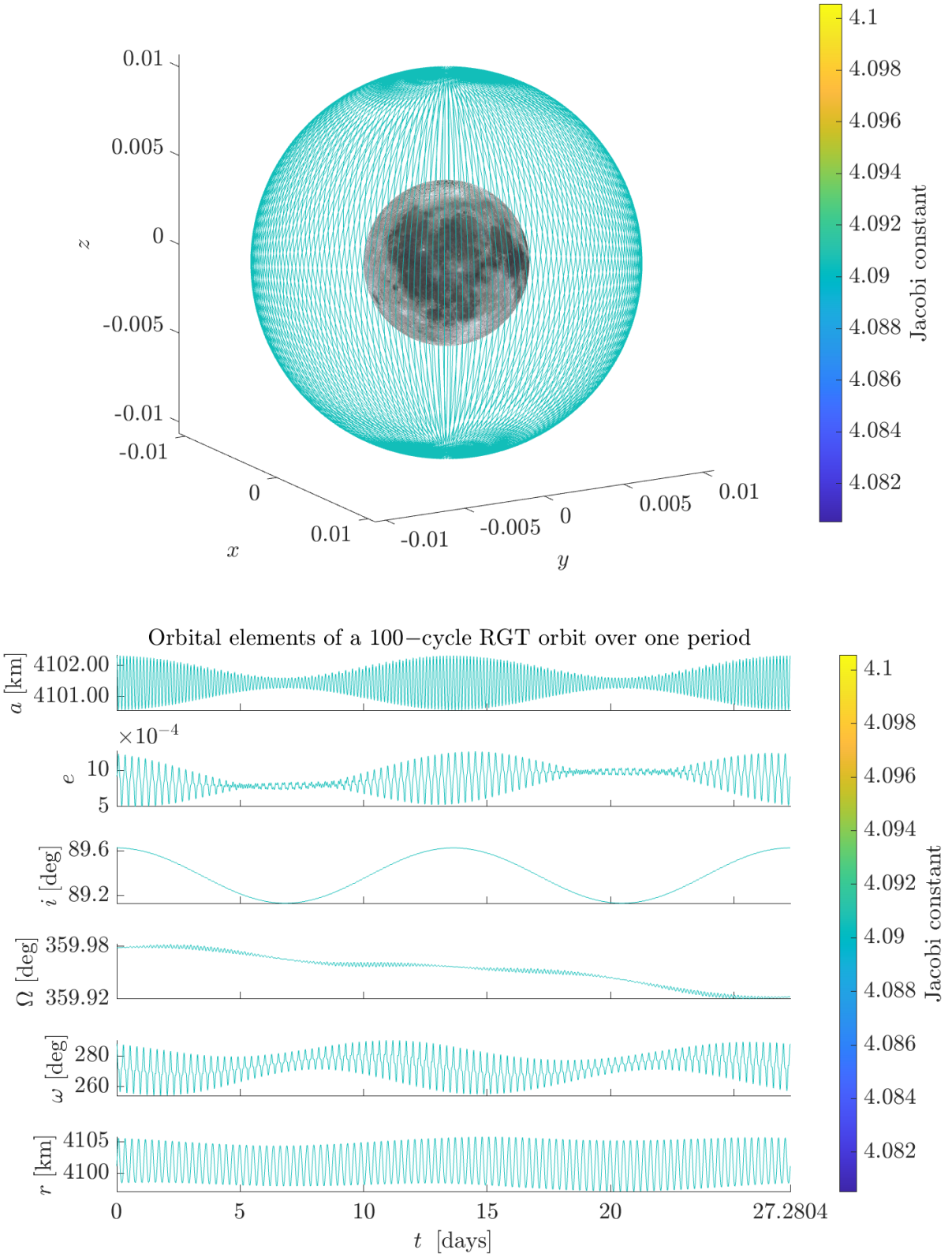

Figure 5.4: Example of an orbit of the 100−cycle RGT family, with initial inclination $i_0 = 90°$, computed in the CR3BP with an 8×8 lunar gravitational field expansion. Convergence is achieved with normalized miss distance $d \approx 10^{-11}$.

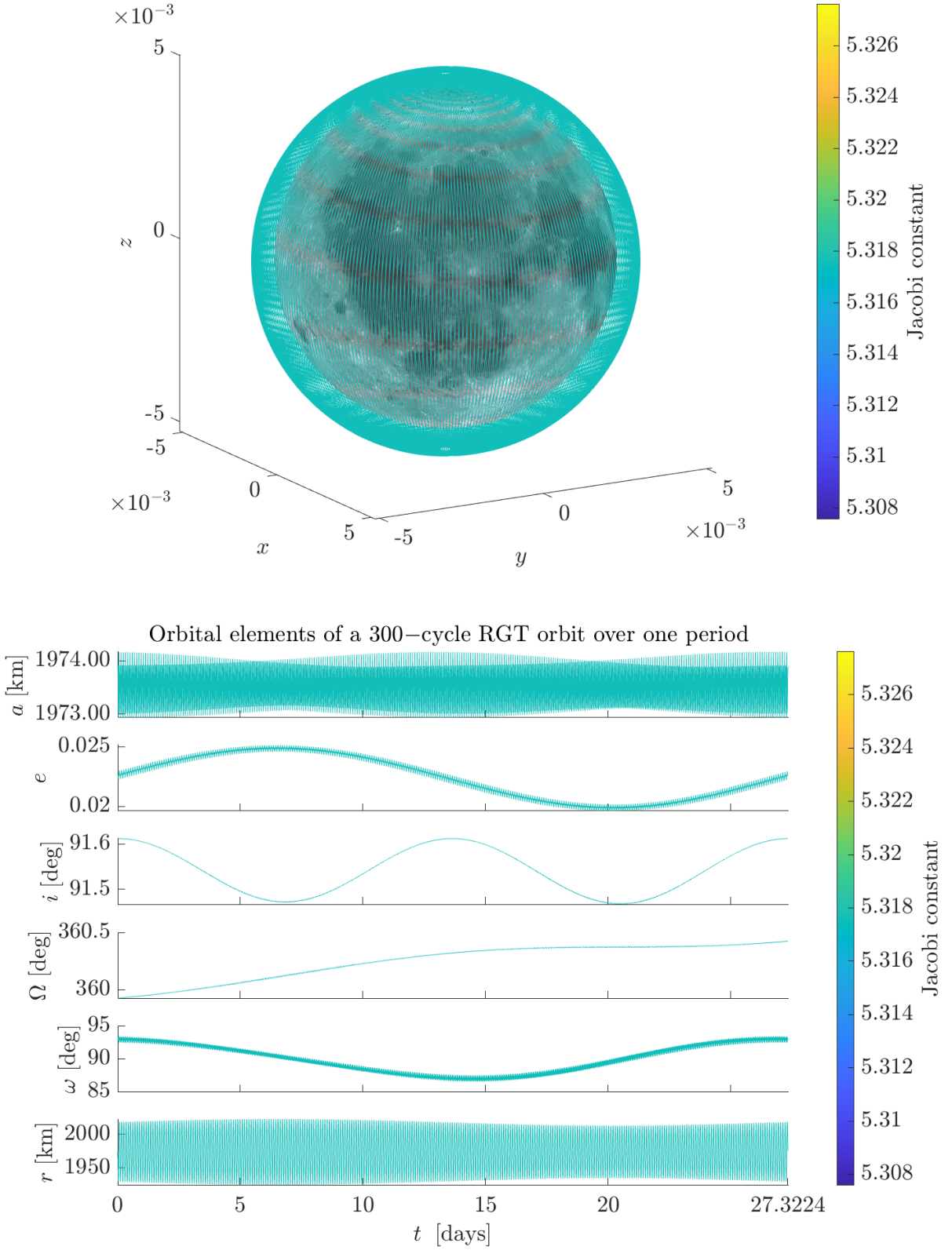

Figure 5.5: Example of an orbit of the 300−cycle RGT family, with initial inclination $i_0 = 91°$, computed in the CR3BP with an 8×0 lunar gravitational field expansion.

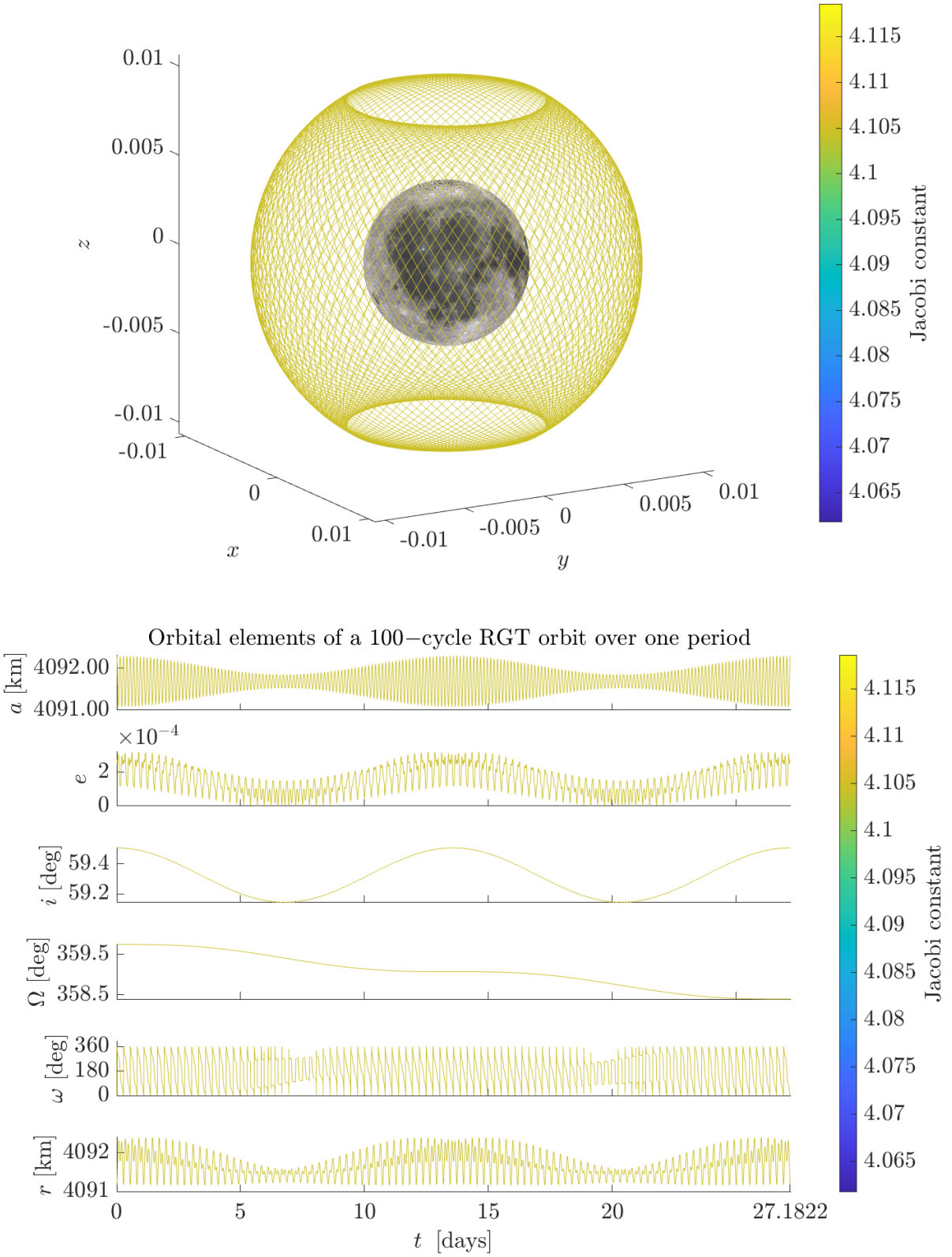

Figure 5.6: Example of an orbit of the 100−cycle RGT family, with initial inclination $i_0 = 60°$, computed in the CR3BP.

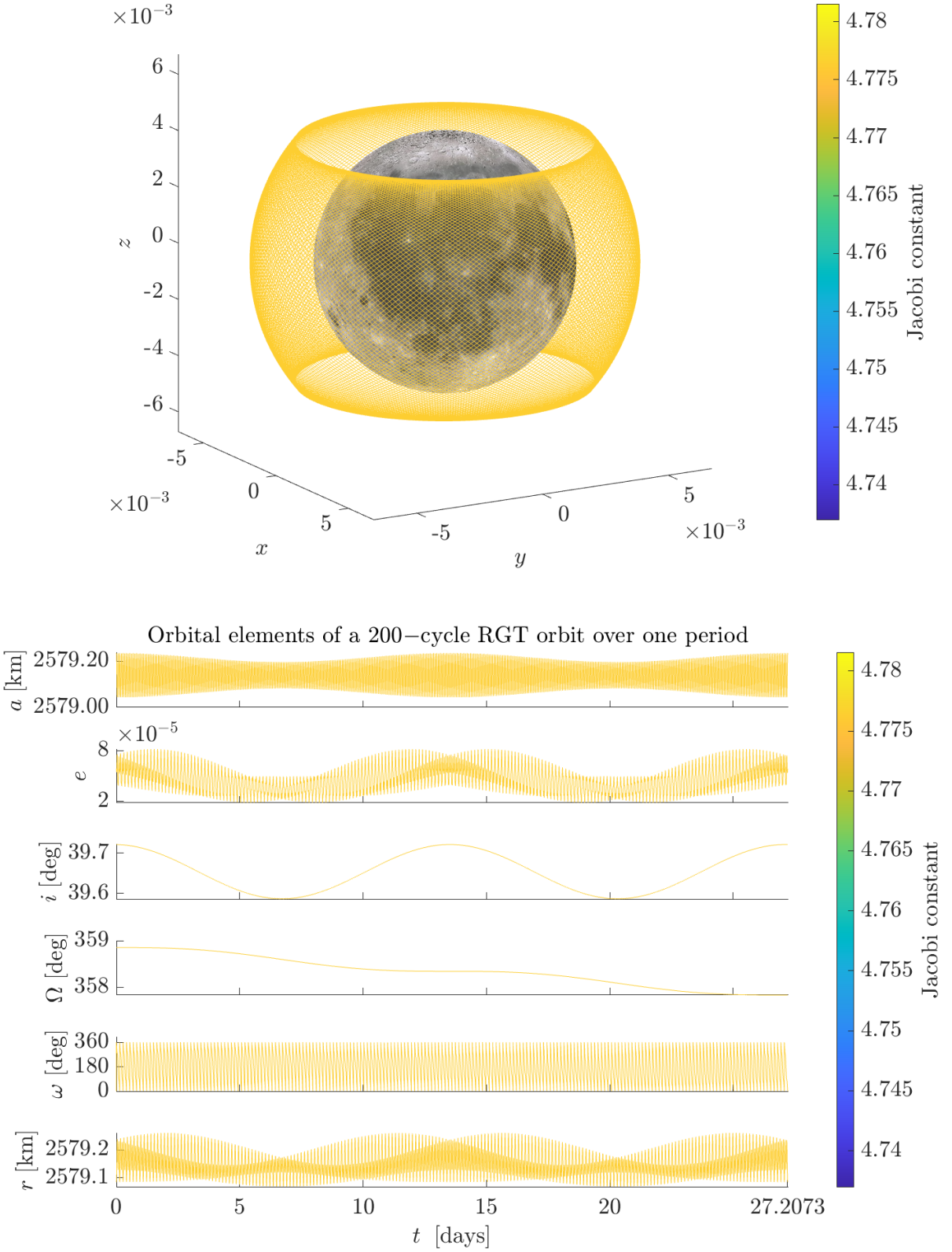

Figure 5.7: Example of an orbit of the 200−cycle RGT family, with initial inclination $i_0 = 40°$, computed in the CR3BP.

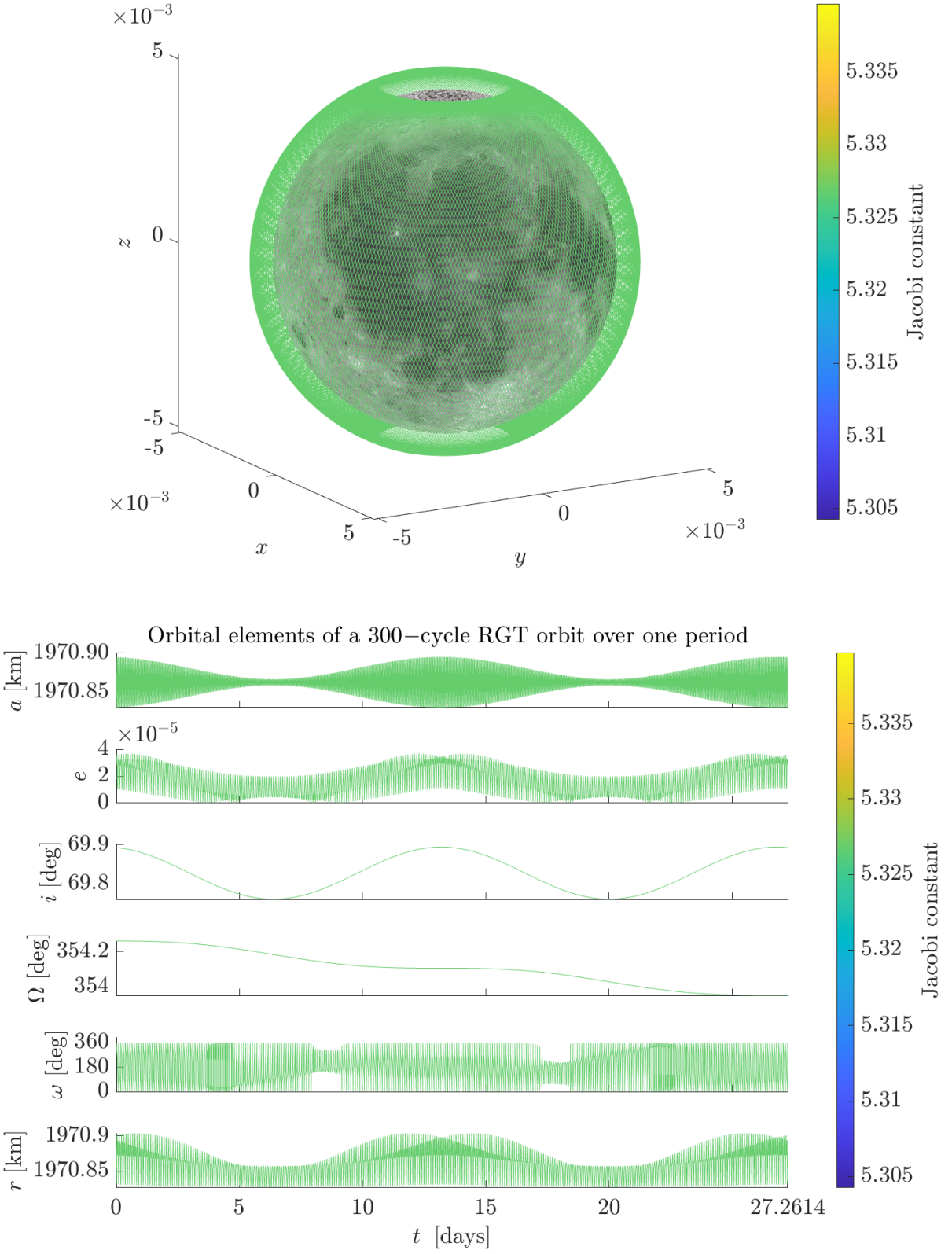

Figure 5.8: Example of an orbit of the 300−cycle RGT family, with initial inclination $i_0 = 70°$, computed in the CR3BP.

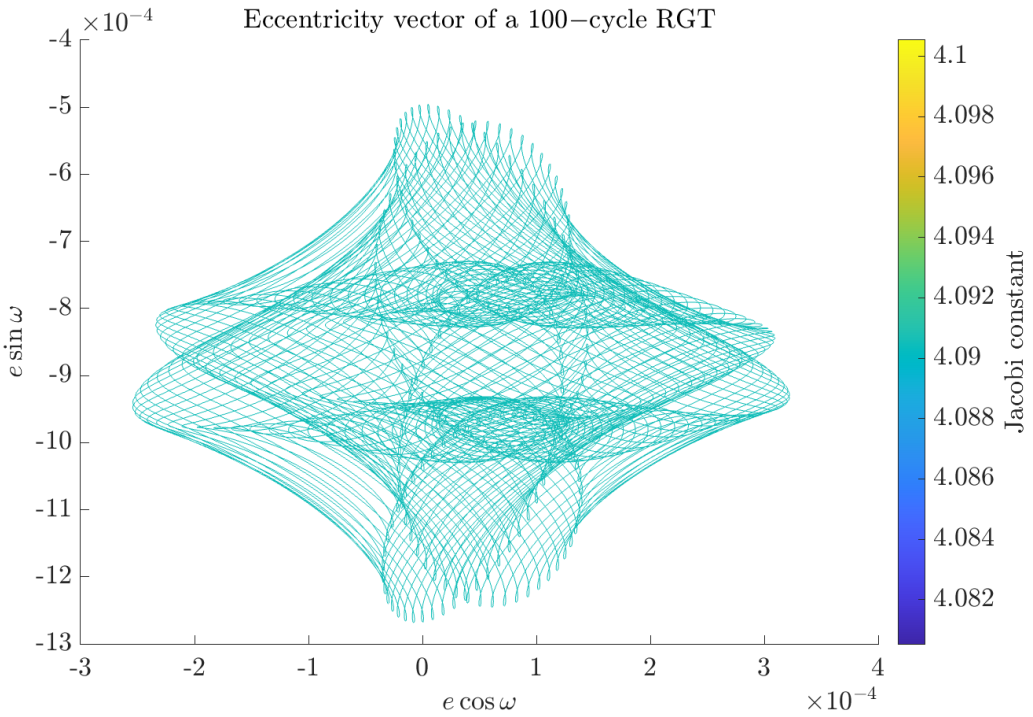

Figure 5.9: Eccentricity vector of the 100−cycle RGT family, with initial inclination $i_0 = 90°$, computed in the CR3BP with an 8×8 lunar gravitational field expansion, shown in Figure 5.4.

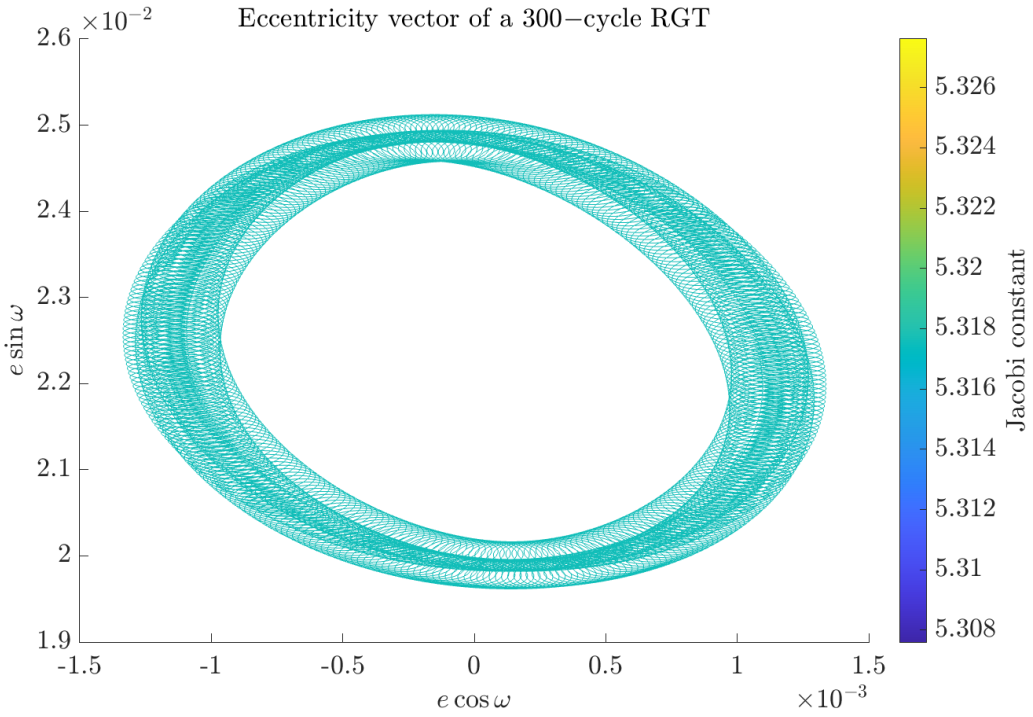

Figure 5.10: Eccentricity vector of the 300−cycle RGT family, with initial inclination $i_0 = 91°$, computed in the CR3BP with an 8×0 lunar gravitational field expansion, shown in Figure 5.5.

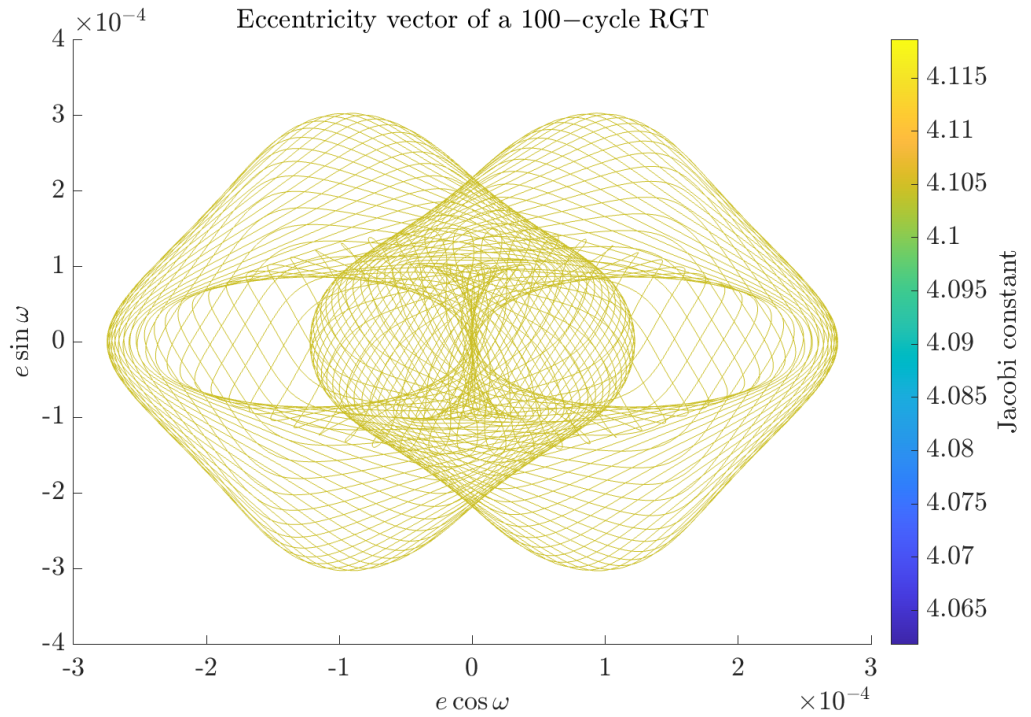

Figure 5.11: Eccentricity vector of the 100−cycle RGT family, with initial inclination $i_0 = 60°$, shown in Figure 5.6.

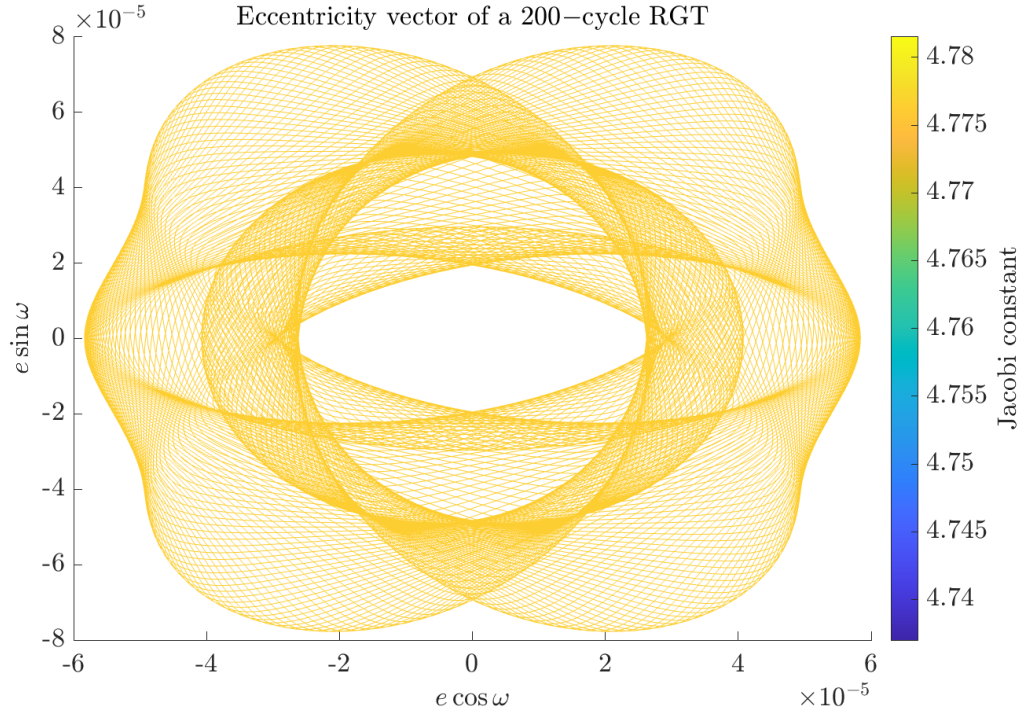

Figure 5.12: Eccentricity vector of the 200−cycle RGT family, with initial inclination $i_0 = 40°$, shown in Figure 5.7.

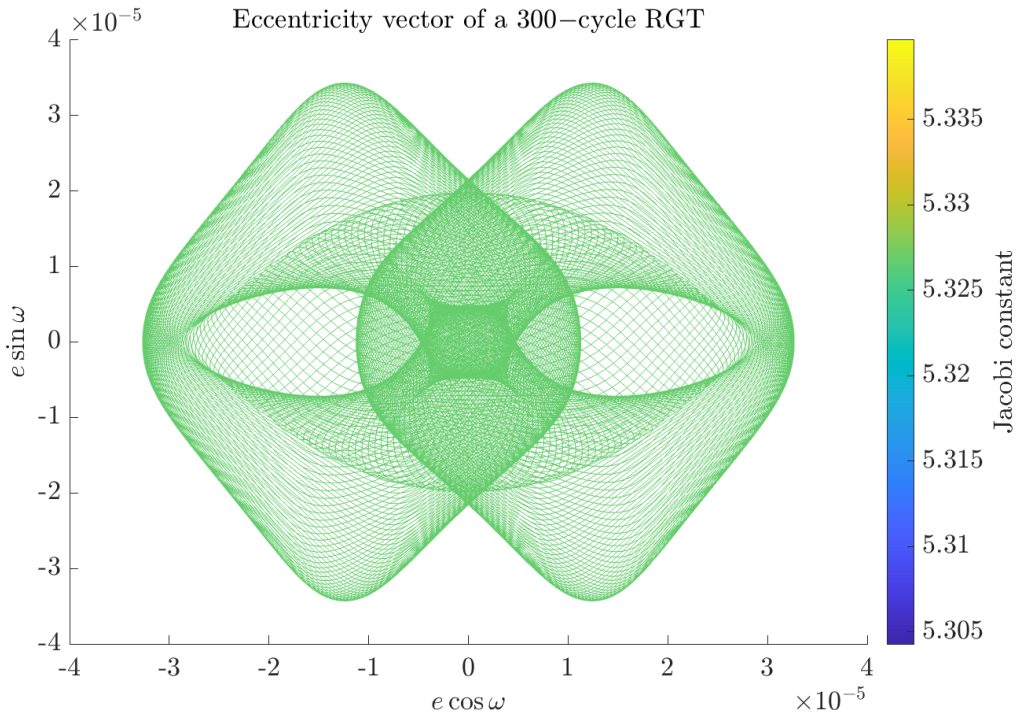

Figure 5.13: Eccentricity vector of the 300−cycle RGT family, with initial inclination $i_0 = 70°$, shown in Figure 5.8.

5.4 Transfers from an NRHO to a Lunar RGT Orbit

We are interested in computing impulsive transfers from a Near Rectilinear Halo Orbit (NRHO) to a Repeat Ground Track (RGT) orbit around the Moon. In particular we will focus on RGT orbits with nearly polar inclinations, since these are the ones of most practical interest because of their global coverage properties. The transfer will be computed assuming a 2-impulse maneuver. We proceed as in Section 4.0.1, by computing the unstable eigenvectors of the selected NRHO. It is worth noting that for the NRHOs the unstable eigenvectors are close to unity. In practice, this translates to trajectories that require a considerable amount of time to leave the orbit, especially for low values of the parameter ε in (3.27). In order to reduce the time of transfer we have to choose relatively large values of ε. However, bear in mind that when working with relatively large values of ε, a significant displacement in position also occurs when approximating the unstable manifold. As a workaround, we modify (3.27) to give the perturbation not in the direction of the full unstable eigenvector $\boldsymbol{v}_u$, but rather in its velocity space components only. The projection is obtained by simple scalar multiplication with the vector $\boldsymbol{w} = (0, 0, 0, 1, 1, 1)^T$, i.e.,

$$\boldsymbol{x}_u = \boldsymbol{x} + \varepsilon \boldsymbol{v}_u \cdot \boldsymbol{w}. \tag{5.92}$$

At this point the main goal remains that of minimizing the energy cost of the transfer, which we measure in terms of the total required ΔV. The minimum ΔV transfer is sought using a grid search algorithm. The procedure is outlined as follows:

- Select an NRHO, for example, the $4:1$ or the $9:2$ resonant L_2 Southern NRHO.

- Select a value for n and one target orbit from the $n-$cycle RGT family, for instance, based on the target inclination.
- Select a number k of points, equispaced in time, from the selected NRHO and integrate the trajectories departing from the NRHO in the unstable direction for a range of j equispaced values of ε in a given range, e.g., $\varepsilon \in (10^{-2}, 10^{-1})$, and compute the cost of the first maneuver as:

$$\Delta V_A = \|\varepsilon \boldsymbol{v}_u \cdot \boldsymbol{w}\|. \tag{5.93}$$

- Find the trajectories that approach the target RGT orbit in physical space within a certain threshold, for instance $d = 1$ km, and save the time spent on the transfer trajectory Δt from the ΔV_A maneuver up to closest approach. In this phase it may be necessary to exclude those trajectories that impact the Moon prior to closest approach.
- Compute the second ΔV_B for the orbits of the preceding step as:

$$\Delta V_B = \| \left(\boldsymbol{x}_u(\Delta t) - \boldsymbol{x}_{\mathrm{RGT}}(\Delta t)\right) \cdot \boldsymbol{w}\|, \tag{5.94}$$

  where $\boldsymbol{x}_{\mathrm{RGT}}(\Delta t)$ denotes the dynamical state of the RGT orbit corresponding to the closest approach with the transfer trajectory.
- Choose the trajectories that satisfy the requirements relative to the total time of transfer and select the one that minimizes the total $\Delta V = \Delta V_A + \Delta V_B$.

Recall that the periodic orbits obtained in Chapter 2 were computed in the center-of-mass synodic reference frame, with the Earth being placed on the negative side of the x axis, to the left of the Moon. That convention differs from the one that we use to compute the families of RGT orbits. In fact, to accommodate for the inclusion of the spherical harmonic expansion of the lunar gravitational field, the new reference frame is the Moon-centered synodic frame, and this time the Earth is located to the right of the Moon along the x axis. However in order to obtain the initial conditions of any periodic orbits with the present convention it will be enough to apply the transformation (2.56) to account for the fact that the Earth is now on the right side of the x axis with respect to the Moon, i.e., at $P_1 = (1, 0, 0)$, followed by a translation to account for the shift in the origin of the reference frame that is now the center of the Moon, i.e., $P_2 = (0, 0, 0)$. Moreover recall that the initial conditions of a Northern Halo orbit can be mapped into those of the Southern Halo family with the same Jacobi constant by using the symmetry transformation (2.54).

5.4.1 Lower bound for the transfer cost

The velocity impulse at the second injection point, i.e., ΔV_B, is considerably larger than the first impulse along the unstable manifold. This is a simple consequence of the presence of the factor ε in (5.92). Here we are interested in making an estimate of the lower bound for ΔV_B. This can be computed by considering the difference in the Jacobi constant of the transfer trajectory, $\mathcal{C}_u^* = \mathcal{C}(\boldsymbol{x}_u)$, and the that of the target RGT orbit, which we denote

by $\mathcal{C}^*_{\text{RGT}} = \mathcal{C}(\boldsymbol{x}_{\text{RGT}})$. Introducing the notation, $\boldsymbol{x}_u = (\boldsymbol{r}_u, \dot{\boldsymbol{x}}_u)$, and $\boldsymbol{x}_{\text{RGT}} = (\boldsymbol{r}_{\text{RGT}}, \dot{\boldsymbol{r}}_{\text{RGT}})$, we can write

$$\Delta\mathcal{C}^*_B \equiv \mathcal{C}^*_{\text{RGT}} - \mathcal{C}^*_u = \left[2\mathcal{U}^*(\boldsymbol{r}_{\text{RGT}}) - \dot{\boldsymbol{r}}^2_{\text{RGT}}\right] - \left[2\mathcal{U}^*(\boldsymbol{r}_{\boldsymbol{u}}) - \dot{\boldsymbol{r}}^2_u\right]. \tag{5.95}$$

Since at injection point the orbits intersect in physical space, in particular it must be $\mathcal{U}^*(\boldsymbol{r}_u) = \mathcal{U}^*(\boldsymbol{r}_{\text{RGT}})$. Then (5.95) can be rewritten as

$$\dot{\boldsymbol{r}}^2_{\text{RGT}} - \dot{\boldsymbol{r}}^2_u = \Delta\mathcal{C}^*_B. \tag{5.96}$$

Note that the l.h.s. of (5.96) can be decomposed as

$$\dot{\boldsymbol{r}}^2_{\text{RGT}} - \dot{\boldsymbol{r}}^2_u = (\dot{\boldsymbol{r}}_{\text{RGT}} - \dot{\boldsymbol{r}}_u) \cdot (\dot{\boldsymbol{r}}_{\text{RGT}} + \dot{\boldsymbol{r}}_u) \tag{5.97}$$

The norm of the sum of the velocities in the r.h.s. of (5.97) can be rewritten as

$$\|\dot{\boldsymbol{r}}_{\text{RGT}} + \dot{\boldsymbol{r}}_u\| = \sqrt{\dot{\boldsymbol{r}}^2_{\text{RGT}} + \dot{\boldsymbol{r}}^2_u + 2\|\dot{\boldsymbol{r}}_{\text{RGT}}\|\|\dot{\boldsymbol{r}}_u\|\cos\delta_B}. \tag{5.98}$$

Moreover, since it is $\Delta V_B = \|\dot{\boldsymbol{r}}_{\text{RGT}} - \dot{\boldsymbol{r}}_u\|$, taking the norm of the r.h.s. of equation (5.96), applying the Cauchy-Schwartz inequality and then rearranging, we obtain

$$\Delta V_B \geq \frac{|\Delta\mathcal{C}^*_B|}{\sqrt{\dot{\boldsymbol{r}}^2_{\text{RGT}} + \dot{\boldsymbol{r}}^2_u + 2\|\dot{\boldsymbol{r}}_{\text{RGT}}\|\|\dot{\boldsymbol{r}}_u\|\cos\delta_B}} \tag{5.99}$$

Then a lower bound for ΔV_B can be determined by minimizing the r.h.s. of (5.99), or equivalently by maximizing the term at the denominator. Inspecting the quantities in the denominator of (5.99), we find that this is maximized for $\cos\delta_B = 1$, i.e., $\delta_B = 0°$. As we might have expected, this happens when the velocity vectors, $\dot{\boldsymbol{r}}_u$ and $\dot{\boldsymbol{r}}_{\text{RGT}}$, are aligned and point in the same direction. Finally we can express the lower bound as

$$\Delta V_B \geq \min_{\delta_B} \Delta V_B = \frac{|\Delta\mathcal{C}^*_B|}{\sqrt{\dot{\boldsymbol{r}}^2_{\text{RGT}} + \dot{\boldsymbol{r}}^2_u + 2\|\dot{\boldsymbol{r}}_{\text{RGT}}\|\|\dot{\boldsymbol{r}}_u\|}}. \tag{5.100}$$

5.4.2 Outcomes

In Table 5.3 we show the costs in terms of ΔV relative to the 2-impulse transfers departing from 9 : 2 and 4 : 1 Southern NRHOs towards orbits that belongs to the 100, 200 and 300−cycle RGT families at different inclinations. As already mentioned, we are mainly interested in RGT orbits at nearly polar inclinations because of their global coverage properties, thus only inclinations as low as $i = 70°$ are considered.

It appears evident that a relationship is present between the inclination, i, and the total change in velocity, ΔV, required for the transfer. However this should not be a surprise, and a very rough explanation is given by the fact that the NRHOs — object of this study — are nearly polar, so that the higher amount of ΔV, required to transfer towards an RGT with relatively low inclination, must account for the change in inclination as well. More specifically, this can be understood in terms of equation (5.99), where the relationship between the cost of ΔV_B and the angle between the velocity along the transfer trajectory and that of the RGT orbit at the second injection point, appears.

The RGT families are associated with significantly higher values of the Jacobi constant (see Tables A.16 – A.18), when compared with those of the NRHOs (see Table A.8).

Moreover the Jacobi constant of the 4 : 1 NRHO is slightly higher that of the 9 : 2 NRHO, hence closer to that of a RGT orbit. Consequently, (5.99) suggests that the required ΔV should be lower for a transfer departing from the 4 : 1 NRHO with respect to that of the 9 : 2 NRHO, towards the same target RGT orbit. However such a difference in Table 5.3, appears evident only in the transfers towards the higher altitude, 100−cycle RGT orbits.

The cost of the second transfer, ΔV_B, is found to be around 10% to 20% higher than the lower bound of equation (5.100), for small values of δ_B corresponding to near polar inclinations, e.g., $i_0 > 85°$. However, the lower bound is surpassed by up to 40%, at the lower than polar inclinations, as correspondingly we find an increase in the δ_B angle.

In our numerical experiments we find significant variations in the total time of transfer Δt for the selected trajectories, which appear to be uncorrelated to both inclination and altitude. However this is a consequence of the fact that for this investigation we have chosen the total ΔV cost as the sole optimization parameter. Indeed we find that optimal transfer corresponding for different choices of the initial NRHO and the target RGT orbit, lead to transfer trajectories that vary in geometry as they depart on different points along the NRHO, as indicated by the parameter τ. This parameter is defined as $\tau = t/T$, where T is the period of the corresponding NRHO, and t is the time needed to reach the insertion point corresponding to ΔV_A, starting from the initial state $\boldsymbol{x}_0$, i.e., the apolune of the NRHO.

We should note that the outcomes of this study may exhibit slight variations depending on the dimension of the parameter space being utilized. In other words, slight improvements could be found if we considered a greater number of test trajectories along the unstable manifold. The number of the test trajectories is essentially the product of the number of points that discretize the selected NRHO, in this case, $k = 10^2$, and the number j, of equally spaced values for $\varepsilon \in (10^{-2}, 10^{-1})$. For this study we used $j = 10$. Therefore the number of test trajectories for each NRHO and RGT orbit transfer pair is $j \times k = 10^3$.

In Figures 5.14 − 5.19 we show the trajectories of sample transfers selected from Table 5.3. We observe that the geometry of the transfer trajectory can significantly vary depending on the characteristics of the target RGT orbit, i.e., inclination and number of revolutions, as well as the chosen initial NRHO.

$p:q$	n	τ	i_0 [deg]	Δt [days]	ΔV [m/s]	ΔV_A [m/s]	ΔV_B [m/s]	δ_A [deg]	δ_B [deg]
		0.5001	90.0000	7.1531	546.3307	61.3146	485.0161	2.2834	10.5134
		0.6901	85.0435	25.1229	494.4779	17.3146	477.1633	3.1050	10.1198
	100	0.3201	80.0377	19.5498	603.3343	30.5479	572.7864	1.9764	17.6198
		0.2400	75.0468	21.8260	891.9938	5.4155	886.5783	0.9151	35.3598
		0.3401	70.0332	19.4721	849.1826	24.5647	824.6179	1.2455	32.1728
		0.4001	90.0000	19.8364	591.7332	9.5217	582.2115	0.3873	7.4464
		0.8902	84.9058	4.5768	758.9467	59.1323	699.8144	23.9902	15.5061
4 : 1	200	0.5901	80.0233	24.5987	757.2337	19.6741	737.5596	1.9443	17.7144
		0.9902	75.0606	9.8481	1067.0184	26.4347	1040.5838	10.0035	31.6840
		0.0500	69.9742	9.3647	1180.6326	25.8234	1154.8093	8.4286	36.5424
		0.0700	90.0000	2.8259	835.7723	24.7618	811.0105	8.9789	15.7855
		0.2901	85.0432	13.4892	907.7479	54.2404	853.5075	5.8088	17.9842
	300	0.3301	80.0468	13.3724	819.2955	31.6652	787.6302	1.8215	14.7446
		0.9202	74.9683	10.5249	1328.9162	49.0835	1279.8328	22.2848	34.8190
		0.6601	70.0723	24.3058	1298.8591	27.3236	1271.5356	4.1389	34.5378
		0.5901	90.0000	6.9988	539.6553	48.5815	491.0738	3.7153	10.7826
		0.7902	85.0435	3.9024	763.1652	47.7217	715.4435	14.4961	26.3058
	100	0.0600	80.0377	2.7538	807.5109	19.4438	788.0672	7.8200	30.1883
		0.1400	75.0468	2.4038	985.5890	38.7126	946.8764	16.4561	38.7152
		0.6101	70.0332	6.6745	979.2114	47.1918	932.0195	4.0416	37.5313
		0.6101	90.0000	6.3662	593.8873	37.7535	556.1339	3.2896	3.4706
		0.3301	84.9058	0.9410	794.7517	62.5758	732.1759	4.2916	17.0458
9 : 2	200	0.1300	80.0233	27.0043	818.4677	22.5188	795.9490	9.9474	20.7064
		0.7201	75.0606	13.0934	1070.4049	73.0802	997.3246	10.4672	29.6635
		0.1000	69.9742	26.8678	1191.6394	6.9254	1184.7140	3.3717	37.8862
		0.6901	90.0000	5.6407	686.6940	39.6214	647.0726	5.1973	4.4433
		0.7401	85.0432	5.3654	908.8207	48.3521	860.4686	8.3339	18.0759
	300	0.1800	80.0468	26.0470	934.9298	39.9717	894.9581	13.6716	19.8014
		0.8602	74.9683	3.9668	1255.6864	14.4203	1241.2661	5.9370	33.4428
		0.2000	70.0723	19.6953	1367.4012	14.3466	1353.0546	3.8720	37.5878

Table 5.3: Parameters of different 2-impulse transfers from a $p:q$ resonant NRHO to a lunar n-cycle RGT orbit. The table specifies the initial inclination i_0 of the RGT orbit, the total time of transfer, Δt, the magnitude of the total ΔV required for the transfer, the magnitudes of ΔV_A and ΔV_B, as well as the angles, δ_A and δ_B, that are between the velocity vectors before and after each the impulsive maneuvers at the injection points A and B respectively. The maximum Δt is constrained to one synodic period $T \approx 27.3$ days.

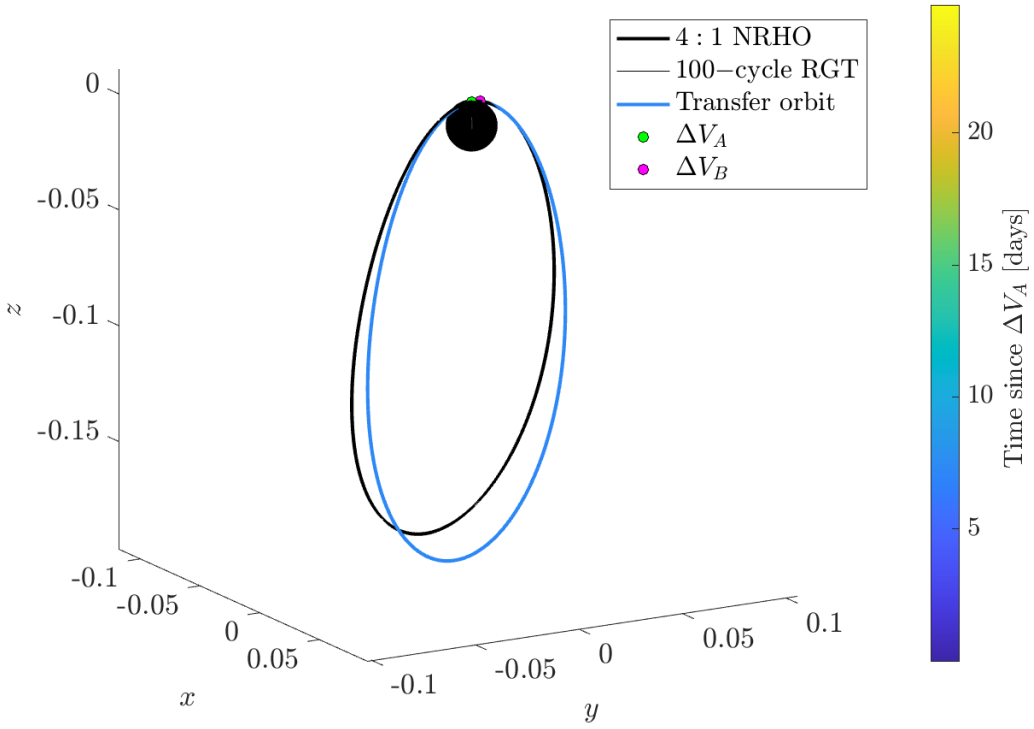

Figure 5.14: Sample of a 2-impulse minimum ΔV transfer from the $4:1$ Southern NRHO to a $100-$cycle RGT with initial inclination $i_0 = 90°$.

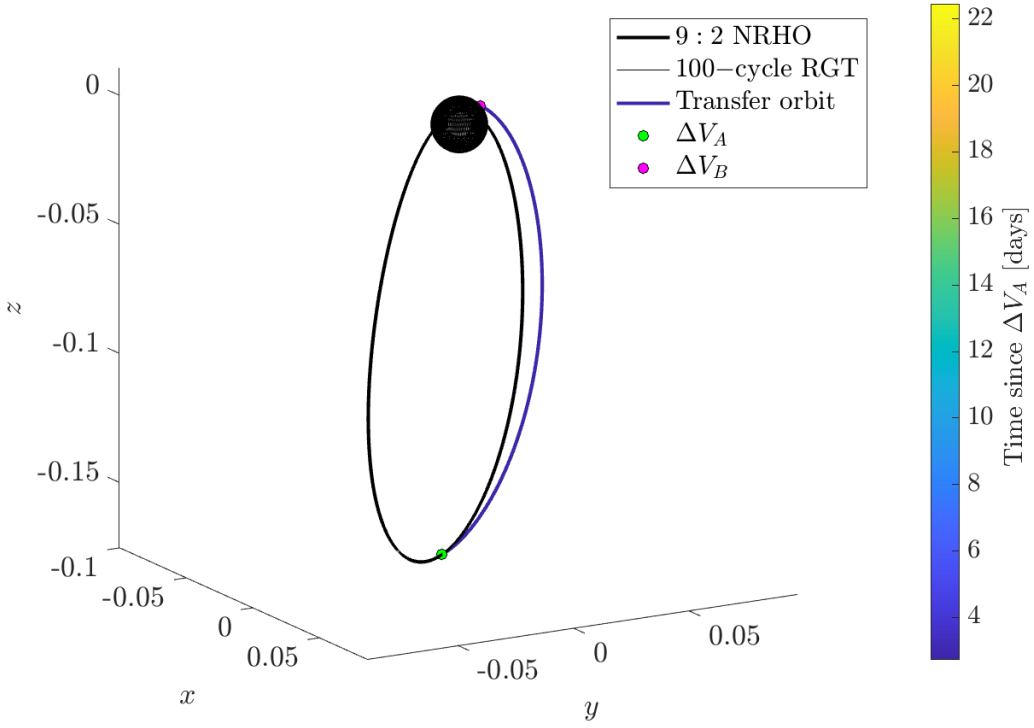

Figure 5.15: Sample of a 2-impulse minimum ΔV transfer from the $9:2$ Southern NRHO to a $100-$cycle RGT with initial inclination $i_0 = 90°$.

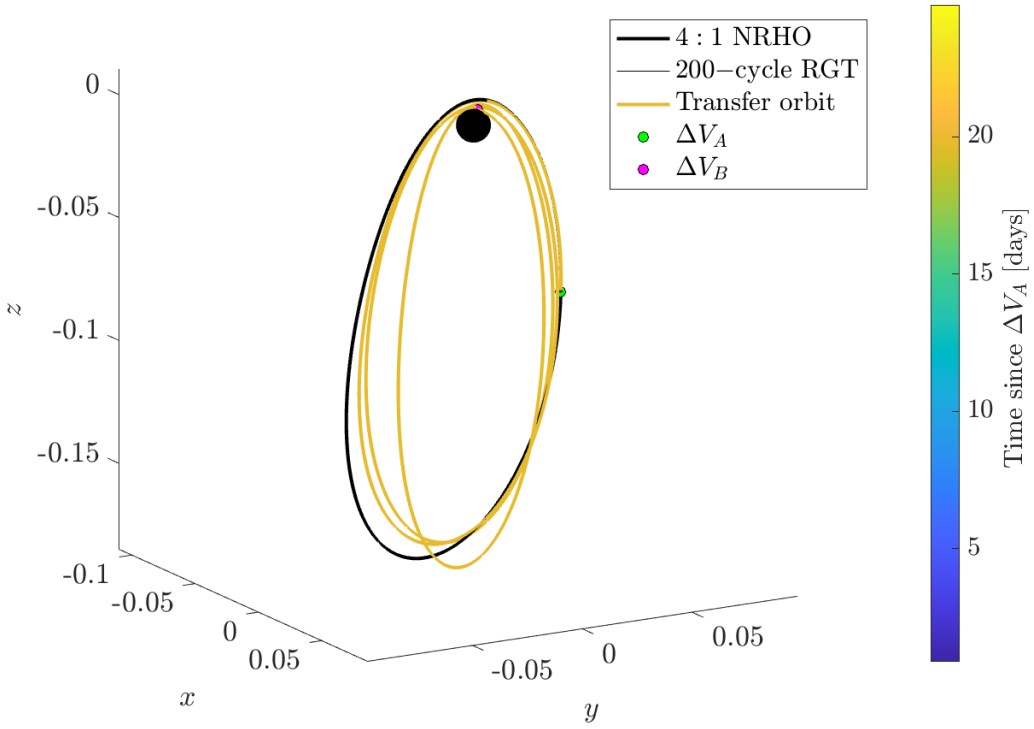

Figure 5.16: Sample of a 2-impulse minimum ΔV transfer from the $4:1$ Southern NRHO to a $200-$cycle RGT with initial inclination $i_0 = 90°$.

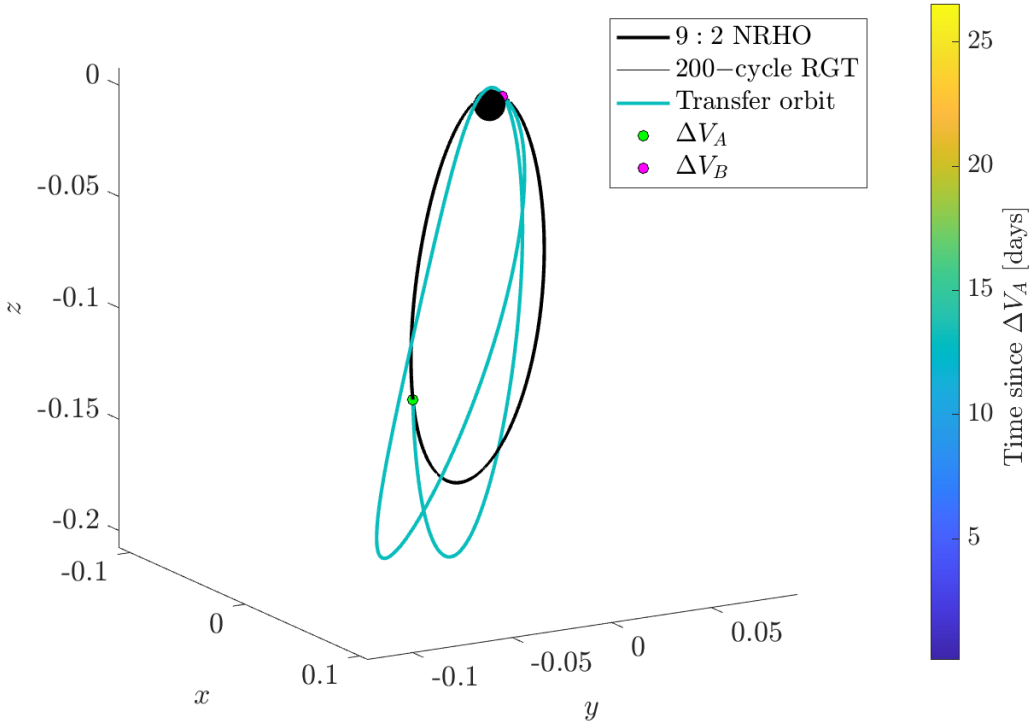

Figure 5.17: Sample of a 2-impulse minumum ΔV trasnfer from the $9:2$ Southern NRHO to a $200-$cycle RGT with initial inclination $i_0 = 75°$.

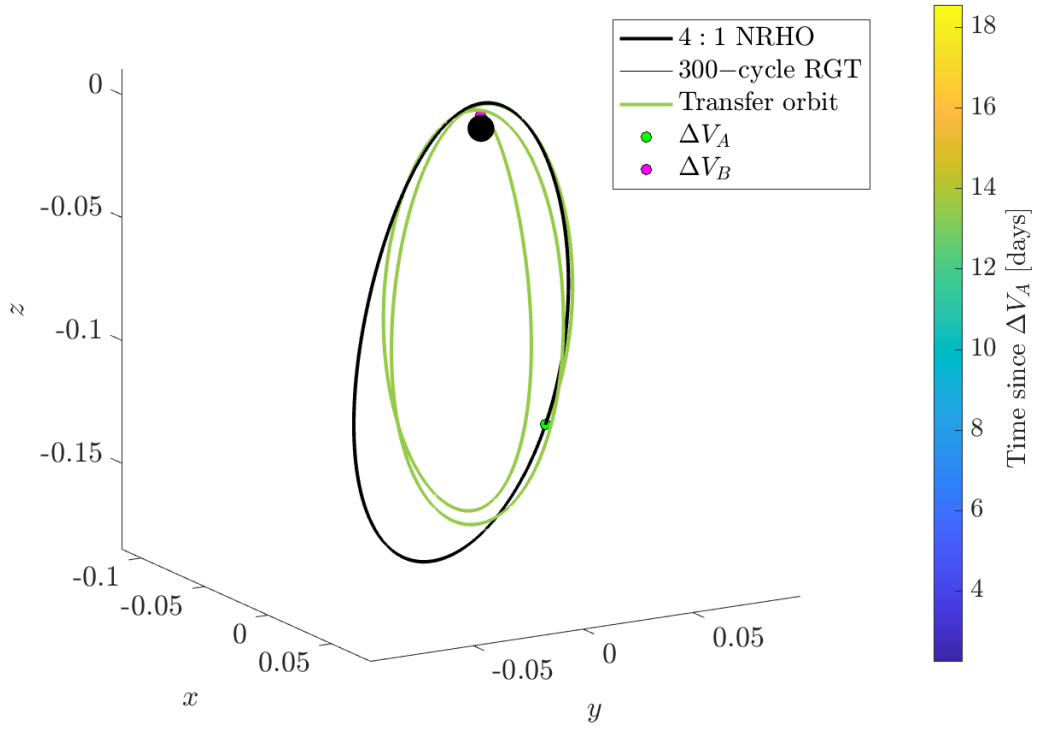

Figure 5.18: Sample of a 2-impulse minimum ΔV transfer from the $4:1$ Southern NRHO to a $300-$cycle RGT with initial inclination $i_0 = 85°$.

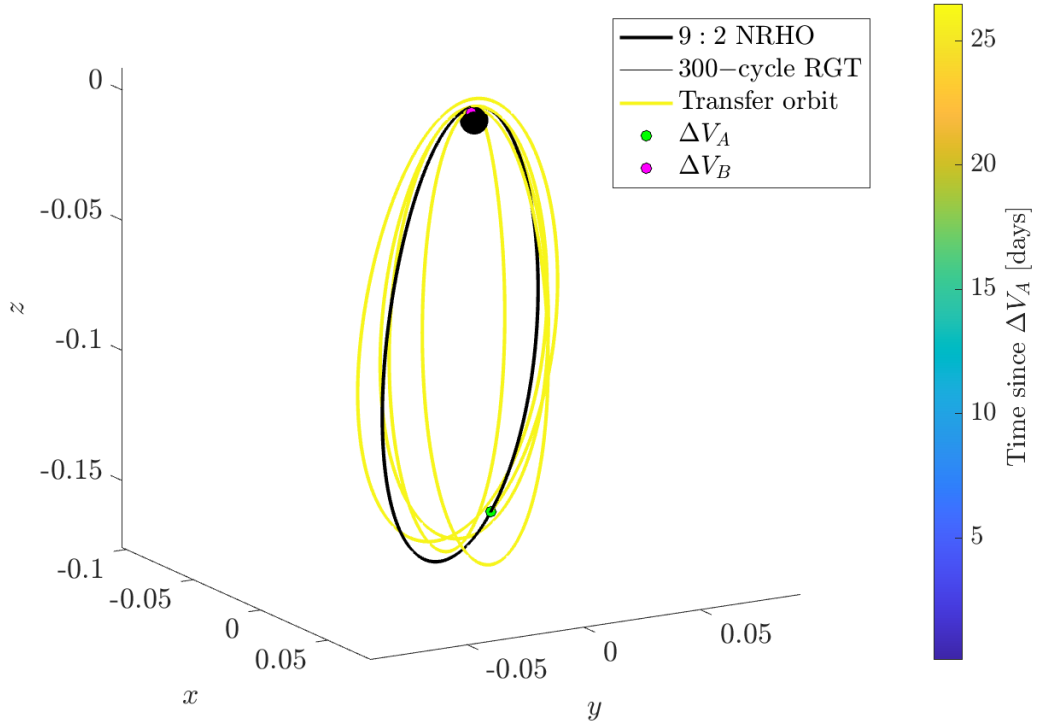

Figure 5.19: Sample of a 2-impulse minumum ΔV trasnfer from the $9:2$ Southern NRHO to a $300-$cycle RGT with initial inclination $i_0 = 80°$.

Chapter 6

Conclusions and Future Prospects

This thesis set out on an explorative journey into the Circular Restricted Three-Body Problem (CR3BP), and how its understanding can facilitate the design of efficient spacecraft trajectories, particularly in the context of lunar missions. Through various sections, we delved into the fundamentals of the CR3BP, studied periodic orbits, explored differential corrections, investigated invariant manifolds, and examined potential applications in lunar mission planning. In the initial sections, we laid the foundation by discussing core concepts such as the Jacobi constant, zero-velocity surfaces, and the five Lagrangian equilibrium points. These concepts are critical to understanding the behavior of bodies under the gravitational influence of two primary bodies. Subsequently, we delved into the fascinating realm of periodic orbits. Through differential correction techniques that exploit different symmetries, we managed to compute and characterize families of periodic orbits like the Lyapunov, Halo, Axial, Vertical, Distant Prograde Orbits, Distant Retrograde Orbits, and Low Prograde Orbits. We introduced methods that can be used to examine the stability of these orbits and the detect different types of bifurcations using Broucke diagrams. However, the differential techniques we presented are limited by their very nature, and can be used only for obtaining periodic orbits that posses some kind of symmetry, e.g., with respect to the xz plane or the x axis (see Section 3.3). In order to compute non-symmetric periodic orbits, such as the L_4 and L_5 Planar families of orbits, we need to resort to a different approach. One alternative, although not the only one, is that of using a correction scheme based on the singular value decomposition of the Jacobian, like the one that we later used for generating the Repeating Ground Track (RGT) orbit families (see Section 5.2). Another option for computing branches of periodic orbit families is the use of pseudo-arclength continuation methods, such as the one implemented in the software AUTO [10]. These methods can be more robust for cases where the solution curve exhibits bifurcations, and also to avoid issues related to the geometry of the family of periodic orbits in consideration, such as those that we encountered with the Halo orbit families. In that case, for instance, as the family of periodic orbits grows out-of-plane direction, we are required to manually change the mapping technique to address the specific geometric constraints.

A pivotal concept in our study was that of invariant stable and unstable manifolds. Through these manifolds, we identified paths for spacecraft where energy requirements for orbital maneuvers are minimized. We demonstrated that by using Poincaré maps and sections, homoclinic and heteroclinic transfers between L_1 and L_2 Lyapunov orbits can be engineered with minimal thrust, which has significant implications for the efficiency

of spacecraft trajectories, especially in the Earth-Moon system. In this investigation we limited our attention to planar transfers. In a future research phase a natural goal would be to expand the methods presented here to three-dimensional orbits. This will come with additional complications, indeed a direct extension of the techniques that we presented in this thesis to compute different types of planar heteroclinic and homoclinic transfers (see Sections 4.0.1 and 4.0.2), would lead us to look for intersections between the stable and unstable manifolds not in a two dimensional section in phase space, but on a four-dimensional surface, with the two additional dimensions corresponding to the degrees of freedom associated with out of plane motion. Some research in this direction has been carried out, for instance, in [52].

To incorporate higher fidelity modeling of lunar gravity, we introduced a CR3BP model enhanced with the spherical harmonic expansion of the lunar full-potential using the GRAIL Gravity Model (GL0660B). This high-fidelity model enabled us to compute families of lunar Repeat Ground Track (RGT) orbits, which are particularly relevant for missions requiring persistent monitoring of the lunar surface. Indeed RGT orbits, especially those with nearly polar inclinations, could be instrumental in missions that require comprehensive lunar surface coverage. For instance a Synthetic Aperture Radar (SAR) on an RGT orbit can enable high-resolution radar imaging, offering detailed insights into the lunar surface, including topography, mineralogy, and ice-water distribution. A highlight of this study was examining the prospects of utilizing Near Rectilinear Halo Orbits (NRHOs) as conduits for spacecraft transfers to RGT orbits, exploiting once again the presence of unstable manifolds for constructing efficient transfer trajectories. In particular we focused on the $4:1$ and $9:2$ resonant NRHOs. The latter constitutes the reference trajectory for the NASA Gateway, a fundamental component of the ongoing Artemis program, whose aim is that of establishing a permanent base on the Moon, with the ultimate goal of facilitating the feasibility of human missions to Mars.

It is crucial to recognize that the transfer trajectories that we constructed within this investigation should be treated as initial guesses, serving as starting points for further optimization in higher-fidelity, ephemeris models (see e.g., [37]). These models would necessitate the specification of the mission's intended launch date and include, alongside an high-degree and -order expansion of the lunar gravitational field, the accurate position of the Earth, the Sun, and the gravitational influence of other planets in the solar system, along with the solar radiation pressure perturbations. Furthermore, the study of effective orbit maintenance strategies would be indispensable to secure the long-term success of the mission.

Appendix A

Tables of initial conditions

The following appendices provide a collection of tables that outline the initial conditions for selected orbits that belongs to the Lyapunov, Halo, Axial and Vertical families, as well as the DRO, DPO and LPO families, that were computed in Section 3. For each of the selected orbit we show the relevant initial conditions, i.e., the nonzero phase space coordinates in initial dynamical state $\boldsymbol{x}_0$, given in the synodic frame with origin in the center of mass of the system. We include also the period T, in normalized units, and the Jacobi constant $\mathcal{C}$. Additionally, the nontrivial stability indices ν_i, $i = 1, 2$ of the selected orbits are included as well, and the presence of the most relevant bifurcations have been highlighted. Finally we show the initial conditions, starting on the xy plane in the Moon centered synodic frame, of selected orbits belonging to the 100, 200 and 300−cycle RGT families computed only with third body perturbations, i.e., in the CR3BP. Along the Jacobi constant, period in normalized units and the stability indices we provide also the initial inclination i_0 of the orbit.

Family	x_0	$\dot{y}_0$	T	$\mathcal{C}$	$\lvert\nu_1\rvert$	$\lvert\nu_2\rvert$	
	0.8327	0.0366	2.6956	3.1872	0.9857	1324.3917	
	0.8235	0.1253	2.7422	3.1746	0.9997	1182.9324	
	0.8234	0.1263	2.7430	3.1548	1.0000	1183.2789	L_1 Halo
	0.8225	0.1358	2.7516	3.1721	1.0025	1156.8706	
	0.8021	0.3428	3.2491	3.0831	1.1066	456.7727	
	0.7919	0.4026	3.6091	3.0462	1.0982	285.5306	
L_1 Lyapunov	0.7817	0.4428	3.9465	3.0216	1.0015	201.0126	
	0.7816	0.4432	3.9500	3.0216	1.0000	200.2815	L_1 Axial
	0.7793	0.4507	4.0218	3.0170	0.9666	187.4602	
	0.6977	0.6435	5.8763	2.9398	1.5075	60.3354	
	0.6569	0.7359	6.4245	2.9164	2.7228	53.8590	
	0.5753	0.9401	7.0627	2.8694	4.7833	61.0470	
	0.4937	1.1769	7.3471	2.8136	7.3117	81.5920	

Table A.1: Initial conditions, period T, Jacobi constant $\mathcal{C}$, and modulus of the stability indices ν_i, $i = 1, 2$ of selected Lyapunov orbits.

Family	x_0	$\dot{y}_0$	T	$\mathcal{C}$	$\lvert\nu_1\rvert$	$\lvert\nu_2\rvert$	
	1.1618	-0.0341	3.3750	3.1713	0.9683	721.0569	
	1.1784	-0.1382	3.4054	3.1566	0.9924	631.5058	
	1.1808	-0.1553	3.4152	3.1523	1.0000	606.9093	L_2 Halo
	1.1950	-0.2740	3.5549	3.1069	1.0817	387.6062	
	1.2192	-0.4250	4.2871	3.0153	1.0146	130.5768	
	1.2200	-0.4277	4.2871	3.0153	1.0000	127.7214	L_2 Axial
L_2 Lyapunov	1.2768	-0.5410	5.7582	2.9544	1.0880	58.7355	
	1.3432	-0.6394	6.9339	2.9215	3.1540	49.7617	
	1.4760	-0.8306	8.3306	2.8661	2.5756	78.1626	
	1.5424	-1.0198	6.0671	2.6538	0.1153	0.9906	
	1.6088	-1.1312	6.1553	2.5666	0.2181	0.9971	
	1.7416	-1.3619	6.2490	2.3373	0.3715	1.0001	
	1.8080	-1.4832	6.2737	2.1842	0.4370	1.0002	

Table A.2: Initial conditions, period T, Jacobi constant $\mathcal{C}$, and modulus of the stability indices ν_i, $i = 1, 2$ of selected Lyapunov orbits.

Family	x_0	$\dot{y}_0$	T	$\mathcal{C}$	$\lvert\nu_1\rvert$	$\lvert\nu_2\rvert$	
	-1.0176	0.0254	6.2184	3.0120	0.9995	1.6766	
	-1.0836	0.1560	6.2186	3.0056	0.9995	1.6733	
	-1.1166	0.2199	6.2189	2.9989	0.9995	1.6699	
	-1.1496	0.2831	6.2192	2.9898	0.9995	1.6653	
	-1.1826	0.3456	6.2196	2.9783	0.9995	1.6595	
	-1.3422	0.6403	6.2227	2.8875	0.9996	1.6138	
L_3 Lyapunov	-1.4742	0.8780	6.2271	2.7636	0.9998	1.5523	
	-1.6062	1.1149	6.2333	2.5858	0.9999	1.4644	
	-1.6966	1.2794	6.2391	2.4237	1.0000	1.3830	L_3 Halo
	-1.7382	1.3566	6.2424	2.3348	1.0000	1.3368	
	-1.8702	1.6156	6.2572	1.9596	1.0001	1.1189	
	-1.8966	1.6723	6.2617	1.8575	1.0000	1.0487	L_3 Axial
	-1.9118	1.7064	6.2647	1.7918	0.9998	0.9999	

Table A.3: Initial conditions, period T, Jacobi constant $\mathcal{C}$, and modulus of the stability indices ν_i, $i = 1, 2$ of selected Lyapunov orbits.

Family	x_0	$\dot{y}_0$	T	$\mathcal{C}$	$\lvert\nu_1\rvert$	$\lvert\nu_2\rvert$
	0.9798	1.2340	0.0412	4.4343	0.9991	0.9992
	0.9014	0.4780	1.2504	3.0277	0.3205	0.5221
	0.8230	0.5006	2.8583	2.9398	0.0826	0.6467
	0.7446	0.6097	4.2791	2.8934	0.4021	0.7293
	0.6662	0.7652	5.1888	2.8465	0.4849	0.7669
	0.5878	0.9543	5.6850	2.7888	0.2074	0.9243
DRO	0.5094	1.1756	5.9516	2.7167	0.0029	0.9768
	0.4310	1.4356	6.1002	2.6272	0.1515	0.9934
	0.3526	1.7501	6.1867	2.5168	0.2613	0.9985
	0.2742	2.1517	6.2388	2.3799	0.3497	1.0000
	0.1958	2.7138	6.2709	2.2069	0.4282	1.0002
	0.1174	3.6494	6.2909	1.9780	0.5062	1.0002
	0.0390	6.0375	6.3031	2.2289	0.6277	0.9996

Table A.4: Initial conditions, period T, Jacobi constant $\mathcal{C}$, and modulus of the stability indices ν_i, $i = 1, 2$ of selected DRO orbits.

Family	x_0	$\dot{y}_0$	T	$\mathcal{C}$	$\lvert\nu_1\rvert$	$\lvert\nu_2\rvert$
	0.9800	-1.2363	0.0399	4.5191	0.9992	0.9992
	0.9524	-0.5518	0.4064	3.3365	0.9114	0.9309
	0.9248	-0.3821	1.0479	3.2033	0.4114	0.8602
Western LPO	0.8972	-0.2341	1.2707	3.1909	0.0548	0.9081
	0.8696	-0.1263	1.6525	3.1864	0.4290	0.7283
	0.8578	-0.0952	2.0782	3.1846	0.7437	0.9771
	0.8543	-0.0951	2.4226	3.1830	0.5260	7.3773
	0.9305	-0.4507	1.3433	3.1827	0.0791	1.0007
	0.9394	-0.5287	1.4145	3.1808	0.0407	0.8377
Eastern LPO	0.9482	-0.6268	1.5830	3.1771	0.3190	0.5691
	0.9571	-0.7560	1.8950	3.1731	0.1087	0.7643
	0.9659	-0.9447	2.4263	3.1703	0.7593	0.9713
	0.9748	-1.2833	3.0644	3.1674	0.1624	8.5695
	0.9818	-1.9459	3.4424	3.1614	0.5043	34.5451

Table A.5: Initial conditions, period T, Jacobi constant $\mathcal{C}$, and modulus of the stability indices ν_i, $i = 1, 2$ of selected Western LPO.

Family	x_0	$\dot{y}_0$	T	$\mathcal{C}$	$\lvert\nu_1\rvert$	$\lvert\nu_2\rvert$
	1.0635	0.3787	2.1648	3.1456	0.7345	9.3820
	1.0485	0.5171	3.3433	3.0954	0.9382	163.5741
	1.0335	0.6551	4.1374	3.0607	0.4627	456.5749
	1.0185	0.8497	5.1642	3.0252	1.0852	901.1284
	1.0145	0.9216	5.5252	3.0153	1.9453	1042.4225
	1.0127	0.9606	5.7156	3.0105	2.4637	1111.6428
DPO	1.0108	1.0038	5.9216	3.0055	3.0679	1182.1496
	1.0089	1.0520	6.1453	3.0005	3.7653	1253.6836
	1.0070	1.1066	6.3892	2.9953	4.5576	1326.0971
	1.0052	1.1692	6.6565	2.9900	5.4347	1399.5564
	1.0033	1.2422	6.9506	2.9845	6.3660	1474.9350
	1.0014	1.3292	7.2753	2.9787	7.2868	1554.5161
	0.9995	1.4355	7.6350	2.9726	8.0830	1643.5066

Table A.6: Initial conditions, period T, Jacobi constant $\mathcal{C}$, and modulus of the stability indices ν_i, $i = 1, 2$ of selected DPO orbits.

Family	x_0	z_0	$\dot{y}_0$	T	$\mathcal{C}$	$\lvert\nu_1\rvert$	$\lvert\nu_2\rvert$	
	0.8234	0.0000	0.1263	2.7430	3.1548	1.0000	1182.9324	L_1 Lyapunov
	0.8235	0.0350	0.1444	2.7510	3.1641	0.9675	987.5838	
	0.8249	0.0700	0.1823	2.7705	3.1363	0.7793	588.6324	
	0.8287	0.1050	0.2206	2.7870	3.0971	0.2448	255.7307	
	0.8496	0.1750	0.2631	2.5606	3.0084	0.8663	11.6417	
	0.8844	0.1949	0.2157	2.0756	2.9992	0.6227	1.2448	
Northern L_1 Halo	0.9194	0.2122	0.1375	1.8075	3.0032	1.0794	2.4515	
	0.9334	0.2472	0.0905	1.9227	2.9806	1.3619	2.8702	
	0.9308	0.2822	0.0819	2.1057	2.9514	1.1881	1.9208	
	0.9292	0.2912	0.0817	2.1453	2.9436	0.6525	1.0000	L_1 Axials
	0.9233	0.3172	0.0838	2.2688	2.9207	2.9102	2.9102	
	0.9129	0.3522	0.0908	2.4057	2.8886	6.3163	6.3163	
	0.9003	0.3872	0.1010	2.5191	2.8548	10.5010	10.5010	

Table A.7: Initial conditions, period T, Jacobi constant $\mathcal{C}$, and modulus of the stability indices ν_i, $i = 1, 2$ of selected Northern Halo orbits.

Family	x_0	z_0	$\dot{y}_0$	T	$\mathcal{C}$	$\lvert\nu_1\rvert$	$\lvert\nu_2\rvert$	
	1.1808	0.0000	0.1553	3.4152	3.1523	1.0000	606.9093	L_2 Lyapunov
	1.1803	0.0240	0.1591	3.4108	3.1496	0.9908	580.2584	
	1.1785	0.0480	0.1679	3.3965	3.1423	0.9570	509.2933	
	1.1696	0.0960	0.1935	3.3350	3.1151	0.7324	300.4808	
	1.1618	0.1200	0.2063	3.2820	3.0964	0.4749	198.5540	
	1.1513	0.1440	0.2172	3.2038	3.0751	0.0715	114.8364	
Northern L_2 Halo	1.1368	0.1680	0.2244	3.0782	3.0517	0.4798	53.9435	
	1.1151	0.1908	0.2234	2.8382	3.0276	0.9744	16.1721	
	1.1091	0.1948	0.2210	2.7605	3.0232	1.0000	11.1979	Dragonfly
	1.0911	0.2014	-0.2088	2.5056	3.0159	0.8199	2.8524	
	1.0431	0.1936	-0.1448	1.7952	3.0293	0.3908	1.6888	
	1.0191	0.1800	-0.0968	1.4727	3.0495	0.7109	1.2391	
	1.0118	0.1739	-0.0799	1.3743	3.0316	0.4414	1.0000	Butterfly
Southern L_2 Halo	1.0265	0.1850	-0.1129	1.5708	3.0422	0.6337	1.4400	4 : 1
	1.0134	0.1754	-0.0837	1.3963	3.0560	0.7576	1.0559	9 : 2

Table A.8: Initial conditions, period T, Jacobi constant $\mathcal{C}$, and modulus of the stability indices ν_i, $i = 1, 2$ of selected Northern Halo orbits.

Family	x_0	z_0	$\dot{y}_0$	T	$\mathcal{C}$	$\lvert\nu_1\rvert$	$\lvert\nu_2\rvert$	
	-1.6966	0.0000	1.2794	6.2391	2.4237	1.0000	1.3830	L_3 Lyapunov
	-1.6882	0.1920	1.2730	6.2390	2.4096	1.0000	1.3796	
	-1.6623	0.3840	1.2531	6.2386	2.3680	0.9999	1.3697	
	-1.6184	0.5760	1.2196	6.2378	2.2987	0.9999	1.3536	
	-1.5553	0.7680	1.1715	6.2366	2.2020	0.9997	1.3314	
	-1.4713	0.9600	1.1076	6.2347	2.0783	0.9995	1.3039	
Northern L_3 Halo	-1.3631	1.1520	1.0257	6.2318	1.9280	0.9992	1.2720	
	-1.2252	1.3440	0.9219	6.2271	1.7520	0.9987	1.2370	
	-1.0484	1.5348	0.7891	6.2192	1.5529	0.9979	1.2003	
	-0.8564	1.6913	0.6448	6.2068	1.3725	0.9965	1.1671	
	-0.6644	1.8059	0.4999	6.1877	1.2304	0.9944	1.1350	
	-0.4724	1.8837	0.3541	6.1543	1.1268	0.9898	1.0983	
	-0.2804	1.9225	0.2083	6.0779	1.0636	0.9759	1.3080	

Table A.9: Initial conditions, period T, Jacobi constant $\mathcal{C}$, and modulus of the stability indices ν_i, $i = 1, 2$ of selected Northern Halo orbits.

Family	x_0	$\dot{y}_0$	$\dot{z}_0$	T	$\mathcal{C}$	$\lvert\nu_1\rvert$	$\lvert\nu_2\rvert$	
	0.7816	0.4432	0.0000	3.9500	3.0216	1.0000	201.0126	L_1 Lyapunov
	0.7820	0.4415	0.0370	3.9511	3.0211	1.0040	200.8604	
	0.7833	0.4364	0.0740	3.9543	3.0202	1.0155	202.3969	
	0.7855	0.4277	0.1110	3.9597	3.0187	1.0328	204.9465	
	0.7886	0.4153	0.1480	3.9673	3.0167	1.0532	208.4898	
	0.7928	0.3990	0.1850	3.9769	3.0141	1.0731	212.9936	
L_1 Axial	0.7980	0.3783	0.2220	3.9885	3.0111	1.0886	218.4022	
	0.8044	0.3527	0.2590	4.0018	3.0076	1.0957	224.6193	
	0.8121	0.3214	0.2960	4.0166	3.0038	1.0912	231.4764	
	0.8214	0.2830	0.3330	4.0320	3.0000	1.0740	238.6745	
	0.8325	0.2354	0.3700	4.0470	2.9962	1.0463	245.6801	
	0.8459	0.1745	0.4070	4.0594	2.9932	1.0161	251.5234	
	0.8623	0.0917	0.4430	4.0652	2.9918	1.0000	254.2394	L_1 Vertical

Table A.10: Initial conditions, period T, Jacobi constant $\mathcal{C}$, and modulus of the stability indices ν_i, $i = 1, 2$ of selected L_1 Axial orbits.

Family	x_0	$\dot{y}_0$	$\dot{z}_0$	T	$\mathcal{C}$	$\lvert\nu_1\rvert$	$\lvert\nu_2\rvert$	
	1.2200	-0.4277	0.0000	4.2871	3.0153	1.0000	127.7223	L_2 Lyapunov
	1.2192	-0.4250	0.0000	4.2871	3.0153	1.0146	130.5768	
	1.2191	-0.4261	0.0360	4.3119	3.0131	1.0132	128.5384	
	1.2121	-0.4147	0.1080	4.3233	3.0077	1.0998	133.4866	
	1.2061	-0.4046	0.1440	4.3328	3.0033	1.1511	137.4383	
	1.1984	-0.3914	0.1800	4.3446	2.9980	1.1900	142.0502	
	1.1892	-0.3750	0.2160	4.3581	2.9922	1.2059	147.0358	
L_2 Axial	1.1787	-0.3550	0.2520	4.3725	2.9862	1.1945	152.0896	
	1.1544	-0.3033	0.3240	4.4004	2.9752	1.1086	161.1361	
	1.1411	-0.2706	0.3600	4.4115	2.9710	1.0570	164.5121	
	1.1274	-0.2322	0.3960	4.4190	2.9682	1.0172	166.7602	
	1.1134	-0.1865	0.4320	4.4221	2.9671	1.0002	167.6629	
	1.1123	-0.1823	0.4350	4.4222	2.9671	1.0000	167.6713	L_2 Vertical

Table A.11: Initial conditions, period T, Jacobi constant $\mathcal{C}$, and modulus of the stability indices ν_i, $i = 1, 2$ of selected L_2 Axial orbits.

Family	x_0	$\dot{y}_0$	$\dot{z}_0$	T	$\mathcal{C}$	$\lvert\nu_1\rvert$	$\lvert\nu_2\rvert$	
	-1.8966	1.6723	0.0000	6.2617	1.8575	1.0000	1.0487	L_3 Lyapunov
	-1.8924	1.6744	0.0720	6.2617	1.8315	1.0000	1.0567	
	-1.8803	1.6831	0.1440	6.2619	1.7479	1.0002	1.0758	
	-1.8578	1.6965	0.2160	6.2623	1.6054	1.0003	1.1034	
	-1.8208	1.7123	0.2880	6.2629	1.4013	1.0004	1.1325	
	-1.7629	1.7253	0.3600	6.2637	1.1386	1.0005	1.1541	
L_3 Axial	-1.6774	1.7272	0.4320	6.2645	0.8393	1.0006	1.1606	
	-1.5649	1.7100	0.5040	6.2653	0.5526	1.0005	1.1527	
	-1.4386	1.6749	0.5760	6.2659	0.3274	1.0004	1.1390	
	-1.3140	1.6303	0.6480	6.2663	0.1770	1.0002	1.1272	
	-1.2000	1.5834	0.7200	6.2665	0.0887	1.0001	1.1195	
	-1.0988	1.5379	0.7920	6.2666	0.0447	1.0000	1.1155	
	-1.0010	1.4903	0.8720	6.2666	0.0307	1.0000	1.1142	L_3 Vertical

Table A.12: Initial conditions, period T, Jacobi constant $\mathcal{C}$, and modulus of the stability indices ν_i, $i = 1, 2$ of selected L_3 Axial orbits.

Family	x_0	$\dot{y}_0$	$\dot{z}_0$	T	$\mathcal{C}$	$\lvert\nu_1\rvert$	$\lvert\nu_2\rvert$	
	0.8379	0.0017	0.0763	2.7896	3.1825	0.9772	1599.4160	
	0.8623	0.0917	0.4430	4.0652	2.9918	1.0000	254.2394	L_1 Axial
	0.8653	0.0989	0.5420	5.0251	2.8951	2.4009	169.5561	
	0.8744	-0.0298	0.7310	5.8518	2.6720	6.1431	189.2101	
	0.8957	-0.5156	1.0436	6.2114	1.8872	8.8669	164.5771	
	0.9007	-0.7046	1.0932	6.2420	1.5632	8.9253	141.3930	
L_1 Vertical	0.9050	-0.8936	1.1111	6.2607	1.2333	8.7748	117.2399	
	0.9085	-1.0826	1.0984	6.2730	0.8992	8.4419	93.3395	
	0.9116	-1.2716	1.0536	6.2817	0.5617	7.9089	70.4504	
	0.9144	-1.4606	0.9719	6.2881	0.2216	7.1198	49.1705	
	0.9169	-1.6496	0.8424	6.2930	-0.1208	5.9624	30.0823	
	0.9192	-1.8386	0.6363	6.2968	-0.4651	4.2059	13.8757	
	0.9213	-2.0276	0.1740	6.2998	-0.8110	1.2107	1.6710	

Table A.13: Initial conditions, period T, Jacobi constant $\mathcal{C}$, and modulus of the stability indices ν_i, $i = 1, 2$ of selected Vertical orbits.

Family	x_0	$\dot{y}_0$	$\dot{z}_0$	T	$\mathcal{C}$	$\lvert\nu_1\rvert$	$\lvert\nu_2\rvert$	
	1.1551	-0.0013	0.0475	3.5209	3.1699	0.9606	973.5467	
	1.1124	-0.1763	0.4320	4.3839	2.9717	0.9664	171.2133	
	1.1119	-0.1813	0.4360	4.4236	2.9669	1.0000	167.5494	L_2 Axial
	1.0973	-0.3513	0.6414	5.8165	2.6721	6.1075	221.0354	
	1.0849	-0.5263	0.8296	6.1197	2.2631	9.0291	237.8383	
	1.0780	-0.7013	0.9379	6.2008	1.8724	9.6352	207.8020	
	1.0734	-0.8763	0.9990	6.2373	1.4904	9.5202	169.9207	
L_2 Vertical	1.0701	-1.0513	1.0238	6.2578	1.1128	9.0613	132.7773	
	1.0676	-1.2263	1.0162	6.2707	0.7378	8.3798	99.0989	
	1.0656	-1.4013	0.9763	6.2796	0.3644	7.5114	69.8735	
	1.0640	-1.5763	0.9001	6.2860	-0.0078	6.4470	45.4274	
	1.0627	-1.7513	0.7774	6.2908	-0.3794	5.1336	25.8093	
	1.0616	-1.9263	0.5796	6.2945	-0.7504	3.4394	10.9857	
	1.0608	-2.1013	0.0737	6.2975	-1.1210	0.9643	1.1060	

Table A.14: Initial conditions, period T, Jacobi constant $\mathcal{C}$, and modulus of the stability indices ν_i, $i = 1, 2$ of selected Vertical orbits.

Family	x_0	$\dot{y}_0$	$\dot{z}_0$	T	$\mathcal{C}$	$\lvert\nu_1\rvert$	$\lvert\nu_2\rvert$	
	-1.0050	0.0063	0.1128	6.2499	2.9994	0.9995	1.6816	
	-1.0041	0.1813	0.5767	6.2504	2.6467	0.9995	1.6097	
	-1.0032	0.3563	0.7684	6.2510	2.2948	0.9995	1.5391	
	-1.0024	0.5313	0.8867	6.2518	1.9436	0.9995	1.4698	
	-1.0016	0.7063	0.9593	6.2528	1.5931	0.9995	1.4018	
	-1.0009	0.8813	0.9961	6.2542	1.2432	0.9995	1.3352	
	-1.0003	1.0563	1.0012	6.2561	0.8940	0.9996	1.2699	
L_3 Vertical	-1.0000	1.2313	0.9750	6.2589	0.5454	0.9997	1.2060	
	-1.0000	1.4063	0.9151	6.2633	0.1971	0.9999	1.1435	
	-1.0010	1.4903	0.8720	6.2666	0.0307	1.0000	1.1142	L_3 Axial
	-1.0045	1.7563	0.6548	6.2920	-0.5013	1.0011	1.0236	
	-1.0255	1.9313	0.3888	6.3920	-0.8678	0.9569	1.0059	
	-1.1707	2.1063	0.0000	7.0168	-1.3495	0.5352	0.9602	

Table A.15: Initial conditions, period T, Jacobi constant $\mathcal{C}$, and modulus of the stability indices ν_i, $i = 1, 2$ of selected Vertical orbits.

Family	x_0	y_0	$\dot{x}_0$	$\dot{y}_0$	$\dot{z}_0$	i_0 [deg]	T	$\mathcal{C}$	$\lvert\nu_1\rvert$	$\lvert\nu_2\rvert$
	0.0106	-0.0003	0.0315	1.0581	0.0342	1.8500	6.2375	4.1185	0.9954	1.0000
	0.0106	-0.0001	0.0084	0.8801	0.5918	33.9159	6.2449	4.1138	0.9988	1.0000
	0.0106	-0.0001	0.0045	0.7019	0.7969	48.6249	6.2524	4.1091	1.0000	1.0016
	0.0106	-0.0000	0.0023	0.5241	0.9252	60.4712	6.2599	4.1044	1.0000	1.0037
	0.0107	-0.0000	0.0010	0.3465	1.0067	71.0052	6.2675	4.0997	1.0000	1.0053
	0.0107	-0.0000	0.0002	0.1693	1.0524	80.8600	6.2751	4.0950	1.0000	1.0062
100−cycle RGT	0.0107	-0.0002	-0.0002	-0.0075	1.0672	90.4034	6.2828	4.0903	1.0000	1.0065
	0.0106	-0.0008	-0.0138	-0.1834	1.0526	99.9129	6.2905	4.0856	1.0000	1.0062
	0.0107	-0.0008	-0.0277	-0.3590	1.0074	109.6675	6.2983	4.0809	1.0000	1.0054
	0.0107	-0.0008	-0.0409	-0.5343	0.9275	120.0156	6.3061	4.0762	1.0000	1.0039
	0.0107	-0.0008	-0.0532	-0.7093	0.8027	131.5425	6.3140	4.0715	1.0000	1.0019
	0.0107	-0.0008	-0.0638	-0.8840	0.6063	145.6270	6.3220	4.0668	0.9993	1.0000
	0.0107	-0.0007	-0.0645	-1.0592	0.1738	170.6979	6.3300	4.0621	0.9962	1.0000

Table A.16: Initial conditions, period T, Jacobi constant $\mathcal{C}$, and modulus of the stability indices ν_i, $i = 1, 2$ of selected 100−cycle RGT.

Family	x_0	y_0	$\dot{x}_0$	$\dot{y}_0$	$\dot{z}_0$	i_0 [deg]	T	$\mathcal{C}$	$\lvert\nu_1\rvert$	$\lvert\nu_2\rvert$
	0.0067	-0.0004	0.0799	1.3318	0.1183	5.0684	6.2602	4.7815	0.9989	1.0000
	0.0067	-0.0002	0.0263	1.1120	0.7478	33.9113	6.2640	4.7778	0.9997	1.0000
	0.0067	-0.0001	0.0140	0.8905	1.0027	48.3883	6.2677	4.7741	1.0000	1.0004
	0.0067	-0.0001	0.0070	0.6691	1.1633	60.0912	6.2715	4.7704	1.0000	1.0009
	0.0067	-0.0000	0.0029	0.4479	1.2659	70.5170	6.2753	4.7667	1.0000	1.0013
	0.0067	-0.0000	0.0007	0.2268	1.3244	80.2819	6.2791	4.7630	1.0000	1.0015
300−cycle RGT	0.0067	-0.0000	0.0000	0.0060	1.3444	89.7458	6.2829	4.7593	1.0000	1.0016
	0.0067	-0.0000	-0.0009	-0.2087	1.3290	98.9245	6.2866	4.7557	1.0001	1.0016
	0.0067	-0.0001	-0.0034	-0.4291	1.2758	108.5889	6.2905	4.7520	1.0001	1.0014
	0.0067	-0.0001	-0.0079	-0.6492	1.1801	118.8195	6.2943	4.7483	1.0003	1.0010
	0.0067	-0.0001	-0.0150	-0.8691	1.0299	130.1630	6.2982	4.7446	1.0005	1.0008
	0.0067	-0.0002	-0.0269	-1.0887	0.7955	143.8536	6.3021	4.7409	0.9999	1.0000
	0.0067	-0.0003	-0.0581	-1.3072	0.3297	165.8586	6.3059	4.7372	0.9991	1.0000

Table A.17: Initial conditions, period T, Jacobi constant $\mathcal{C}$, and modulus of the stability indices ν_i, $i = 1, 2$ of selected 200−cycle RGT.

Family	x_0	y_0	$\dot{x}_0$	$\dot{y}_0$	$\dot{z}_0$	i_0 [deg]	T	$\mathcal{C}$	$\lvert\nu_1\rvert$	$\lvert\nu_2\rvert$
	0.0051	-0.0003	0.1010	1.5239	0.1561	5.8346	6.2678	5.3397	0.9995	1.0000
	0.0051	-0.0005	0.1150	1.2907	0.8243	32.4608	6.2701	5.3367	0.9999	1.0000
	0.0051	-0.0005	0.0994	1.0599	1.1078	46.1398	6.2724	5.3338	1.0000	1.0001
	0.0051	-0.0005	0.0804	0.8295	1.2914	57.1635	6.2747	5.3308	1.0000	1.0004
	0.0051	-0.0005	0.0597	0.5994	1.4146	66.9341	6.2771	5.3279	1.0000	1.0005
	0.0051	-0.0005	0.0379	0.3696	1.4926	76.0227	6.2794	5.3249	1.0000	1.0006
300−cycle RGT	0.0051	-0.0005	0.0151	0.1400	1.5322	84.7508	6.2817	5.3220	1.0000	1.0007
	0.0051	-0.0000	-0.0000	-0.0899	1.5366	93.3475	6.2840	5.3190	1.0000	1.0007
	0.0051	-0.0000	-0.0001	-0.3203	1.5061	102.0076	6.2863	5.3161	1.0000	1.0007
	0.0051	-0.0000	-0.0002	-0.5507	1.4386	110.9459	6.2887	5.3131	1.0000	1.0006
	0.0051	-0.0000	-0.0002	-0.7809	1.3285	120.4462	6.2910	5.3102	1.0000	1.0004
	0.0051	-0.0000	-0.0003	-1.0109	1.1638	130.9780	6.2934	5.3072	1.0000	1.0002

Table A.18: Initial conditions, period T, Jacobi constant $\mathcal{C}$, and modulus of the stability indices ν_i, $i = 1, 2$ of selected 300−cycle RGT.

Acknowledgements

Firstly, I want to express my deep gratitude to my thesis advisor, Prof. Stefano Casotto, for guiding me through every step of this project. Your knowledge, dedication and patience have been fundamental in the completion of this thesis, and for that, I am truly grateful. Thank you also for constantly proposing me new challenges and ideas, you have been a constant source of motivation and encouragement, allowing me to surpass my own expectations.

I would also like to express my sincere gratitude to my co-supervisor, Dr. Nicola Baresi. Your insightful suggestions, constructive comments, and critical perspectives have been extremely formative for me and have deeply contributed to the quality of this work. Thank you for the invaluable time you have dedicated to me and to this project.

Additionally, I want to thank all the important people in my life who have always believed in me and encouraged me through this journey. Your support has meant a lot to me.

Lastly and most importantly, to my girlfriend, Fabiana; this wouldn't have been possible without you. You are my endless source of inspiration, a bright light when things seem dark, and an even brighter one in the good times. For your infinite love and support, for being always there for me, thank you!

Bibliography

[1] N. Bosanac. *Leveraging natural dynamical structures to explore multi-body systems*. PhD thesis, Purdue University, West Lafayette, Indiana, 2016.

[2] N. Bosanac, K. C. Howell, and E. Fischbach. Stability of orbits near large mass ratio binary systems. *Celestial Mechanics and Dynamical Astronomy*, 122(1):27–52, May 2015.

[3] J. V. Breakwell and J. V. Brown. The 'Halo' family of 3-dimensional periodic orbits in the Earth-Moon restricted 3-body problem. *Celestial Mechanics*, 20(4):389–404, November 1979.

[4] R. Broucke. Stability of periodic orbits in the elliptic, restricted three-body problem. *AIAA Journal*, 7:1003–1009, January 1969.

[5] E. Campbell. *Bifurcations from families of periodic solutions in the circular restricted problem with application to trajectory design*. Phd dissertation, Purdue University, West Lafayette, Indiana, 1999.

[6] E. Canalias and J. Masdemont. Homoclinic and heteroclinic transfer trajectories between planar lyapunov orbits in the sun-earth and earth-moon systems. *Discrete and Continuous Dynamical Systems - A*, 14(2):261–279, 2006.

[7] S. Casotto. Lecture Notes on Celestial Mechanics. University of Padua, 2022.

[8] B. Cheetham, T. Gardner, A. Forsman, E. Kayser, and M. Clarkson. *CAPSTONE: A Unique CubeSat Platform for a Navigation Demonstration in Cislunar Space*.

[9] A. Chenciner and R. Montgomery. A remarkable periodic solution of the three-body problem in the case of equal masses. *Annals of Mathematics*, 152(3):881–901, 2000.

[10] E. Doedel, A. Champneys, T. Fairgrieve, Y. Kuznetsov, B. Sandstede, and X. Wang. Auto 97: Continuation and bifurcation software for ordinary differential equations (with homcont). 06 1999.

[11] R. A. Eckman, A. J. Brown, D. R. Adamo, and R. G. Gottlieb. Normalization and implementation of three gravitational acceleration models. NASA Technical Paper 2016-218604, National Aeronautics and Space Administration, Johnson Space Center, Houston, TX, 2016. Revision A, Final.

[12] G. Gomez, A. Jorba, J. Masdemont, and C. Simo. Study of the transfer from the Earth to a halo orbit around the equilibrium point L_1. *Celestial Mechanics and Dynamical Astronomy*, 56(4):541–562, August 1993.

[13] G. Gomez, J. Llibre, R. Martinez, and C. Simo. *Dynamics and Mission Design Near Libration Points, Volume I: Fundamentals: The Case of Collinear Libration Points*. World Scientific Monograph Series in Mathematics 2. World Scientific Publishing Company, 2001.

[14] D. Grebow. Generating periodic orbits in the circular restricted three-body problem with applications to lunar south pole coverage. Master's thesis, School of Aeronautics and Astronautics, Purdue University, West Lafayette, Indiana, 2006.

[15] D. Grebow. *Trajectory design in the Earth–Moon system and lunar south pole coverage*. Phd dissertation, Purdue University, West Lafayette, Indiana, 2010.

[16] J. Guckenheimer and P. Holmes. *Nonlinear Oscillations, Dynamical Systems, and Bifurcations of Vector Fields*. Applied Mathematical Sciences (Switzerland) №42. Springer, 1st edition, 1983.

[17] M. Guzzo. Dynamical Systems. University of Padua, 2020.

[18] D. C. Heggie. A new outcome of binary–binary scattering. *Monthly Notices of the Royal Astronomical Society*, 318, 2000.

[19] K. C. Howell. Three-Dimensional Periodic Halo Orbits. *Celestial Mechanics*, 32(1):53, January 1984.

[20] K. C. Howell and J. V. Breakwell. Almost Rectilinear Halo Orbits. *Celestial Mechanics*, 32(1):29–52, January 1984.

[21] V. S. Kalantonis. Numerical investigation for periodic orbits in the hill three-body problem. *Universe*, 6(6), 2020.

[22] T. Kapela and C. Simó. Computer assisted proofs for nonsymmetric planar choreographies and for stability of the eight. *Nonlinearity*, 20:1241 – 1255, 2007.

[23] W. M. Kaula. *Theory of Satellite Geodesy: Applications of Satellites to Geodesy*. Blaisdell Publishing, 1966.

[24] A. S. Konopliv, R. S. Park, D. N. Yuan, S. W. Asmar, M. M. Watkins, J. G. Williams, E. Fahnestock, G. Kruizinga, M. Paik, D. Strekalov, N. Harvey, D. E. Smith, and M. T. Zuber. The JPL lunar gravity field to spherical harmonic degree 660 from the GRAIL Primary Mission. *Journal of Geophysical Research (Planets)*, 118(7):1415–1434, July 2013.

[25] W. S. Koon, M. W. Lo, J. E. Marsden, and S. D. Ross. *Dynamical Systems, the Three-Body Problem, and Space Mission Design*. SIAM, Philadelphia, PA, 3rd edition, 2011.

[26] M. Lara, R. Russell, and B. Villac. Classification of the distant stability regions at europa. *Journal of Guidance, Control, and Dynamics*, 30(2):409–418, 2007.

[27] D. C. Lay, S. R. Lay, and J. McDonald. *Linear Algebra and Its Applications*. Pearson, 2015.

[28] Q. Li, Y. Tao, and F. Jiang. Orbital stability and invariant manifolds on distant retrograde orbits around ganymede and nearby higher-period orbits. *Aerospace*, 9:454, 08 2022.

[29] J. Llibre, R. Martínez, and C. Simó. Tranversality of the invariant manifolds associated to the Lyapunov family of periodic orbits near L_2 in the restricted three-body problem. *Journal of Differential Equations*, 58(1):104–156, January 1985.

[30] M. W. Lo. Halo orbit generation using the center manifold. *Advances in the Astronautical Sciences*, 97:105, 1997.

[31] K. R. Meyer and G. R. Hall. *Introduction to Hamiltonian Dynamical Systems and the N-Body Problem*. Applied Mathematical Sciences (Switzerland) №90. Springer, 1992.

[32] A. Moccia. *Synthetic Aperture Radar*. John Wiley & Sons, Ltd, 2010.

[33] NASA. Orion Will Go the Distance in Retrograde Orbit During Artemis I, 2023. Accessed: June 28, 2023.

[34] NASA Artemis Team. Flight Day 10: Orion Enters Distant Retrograde Orbit, 11 2022. Accessed: June 28, 2023.

[35] NASA Solar System Exploration. ISEE-3 / ICE In Depth, 2023. Accessed: June 28, 2023.

[36] I. Newton. *Philosophiae naturalis principia mathematica*. W. Dawson, 1687.

[37] K. Oguri, K. Oshima, S. Campagnola, K. Kakihara, N. Ozaki, N. Baresi, Y. Kawakatsu, and R. Funase. EQUULEUS Trajectory Design. *Journal of the Astronautical Sciences*, 67(3):950–976, January 2020.

[38] L. Perko. *Differential Equations and Dynamical Systems*. Springer, 3rd edition, 2006.

[39] H. Poincaré. *Science and Method*. T. Nelson, London, 1914.

[40] N. Pushparaj, N. Baresi, and Y. Kawakatsu. Transfers and orbital maintenance of spatial retrograde orbits for Phobos exploration. *Acta Astronautica*, 189:452–464, December 2021.

[41] J. L. Read, A. B. Younes, B. Macomber, J. Turner, and J. L. Junkins. State transition matrix for perturbed orbital motion using modified chebyshev picard iteration. *The Journal of the Astronautical Sciences*, 62(2):148–167, 2015.

[42] R. B. Roncoli. Lunar constants and models document. NASA Technical Report JPL D-32296, Jet Propulsion Laboratory, Pasadena, CA, 9 2005.

[43] A. E. Roy. *Orbital Motion*. CRC Press, 4th edition, 2005.

[44] A. E. Roy and M. W. Ovenden. On the occurrence of commensurable mean motions in the solar system. The mirror theorem. *MNRAS*, 115:296, January 1955.

[45] R. Russell and M. Lara. Long-lifetime lunar repeat ground track orbits. *Journal of Guidance Control and Dynamics*, 30:982–993, 07 2007.

[46] D. J. Scheeres. *Orbital Motion in Strongly Perturbed Environments*. Springer, New York, 2012.

[47] R. Seydel. *Practical Bifurcation and Stability Analysis*. Springer, New York, 3rd edition, 2010.

[48] K. F. Sundman. Mémoire sur le problème des trois corps. *Acta Mathematica*, 36:105 – 179, 1913.

[49] V. Szebehely. *Theory of Orbit*. Academic Press, 1967.

[50] B. Tapley, B. Schutz, and G. Born. *Statistical orbit determination*. AP, 2004.

[51] F. Topputo. Fast numerical approximation of invariant manifolds in the circular restricted three-body problem. *Communications in Nonlinear Science and Numerical Simulations*, 32:89–98, March 2016.

[52] T. M. Vaquero Escribano. *Spacecraft Transfer Trajectory Design Exploiting Resonant Orbits in Multi-Body Environments*. PhD thesis, Purdue University, August 2013.

[53] V. A. Yakubovich and V. M. Starzhinskii. *Linear Differential Equations With Periodic Coefficients, volume 1*. John Wiley and Sons, 1975.

[54] L. H. Zhang, L. Xiong, J. Sun, S. Gao, X. L. Wang, and A. B. Zhang. Technical characteristics of the relay communication satellite "queqiao" for chang'e-4 lunar farside exploration mission. *SCIENTIA SINICA Technologica*, 49(2):138–146, 2019.

[55] E. Zimovan, K. C. Howell, and D. Davis. Near rectilinear halo orbits and nearby higher-period dynamical structures: orbital stability and resonance properties. *Celestial Mechanics and Dynamical Astronomy*, 132, 06 2020.

[56] E. M. Zimovan-Spreen, K. C. Howell, and D. C. Davis. Dynamical Structures Nearby NRHOs with Applications to Transfer Design in Cislunar Space. *Journal of the Astronautical Sciences*, 69(3):718–744, June 2022.